ABSTRACT

Title of Dissertation:	CRYSTAL WET MILLING IN ROTOR-STATOR MIXERS
Author:	Kanan Ghaderzadeh Doctor of Philosophy, 2018
Directed by:	Professor Richard V. Calabrese Department of Chemical and Biomolecular Engineering

Wet milling in rotor-stator mixers to reduce crystal size is an emerging practice with significant potential in crystallization and milling of active pharmaceutical ingredients. The complexities of crystal breakage behavior, the turbulent nature of flow, and multiscale geometry in rotor-stator mixers have limited the understanding of the milling process in these devices. The purpose of this work is to investigate the effect of milling conditions, crystal physical properties, and mixer geometry on the milling behavior of crystals, and to introduce a mechanistic framework on which to base mill design, scale up, and operating strategies.

A Silverson L4R rotor-stator mixer with a square-hole stator head was used to conduct systematic wet milling experiments. Three mill head geometries were studied. There are inline units with a standard shear gap (clearance between rotor and stator) and an enlarged shear gap, and a batch unit with a standard shear gap. Three different crystals with different elastic modulus, hardness, and fracture toughness were milled in an anti-solvent. Rotor speed and volumetric throughput were adjusted independently to vary energy input and mill head residence time. The milling rate was found to increase with

higher rotor speed and lower throughput, while the ultimate particle size (maximum particle size at the end of milling) was only dependent on rotor speed. The effects of fluid agitation, particle-particle collisions, and particle-wall collisions on crystal breakage were assessed by changing particle concentration, coating the stator surfaces, and reducing rotor diameter. It was found that the concentration of particles in the slurry has a limited effect on milling rate and negligible effect on ultimate particle size. The effect of higher power input and smaller dispersion zone volume (the volume of the shear gap and stator hole regions), through changes to the mixing head geometry, showed to be more successful in concentrating the energy input, and hence, leads to higher milling rates and smaller ultimate particle size.

To quantitatively explain the experimental results, a class of mechanistic models for crystal breakage were developed that consider the influence of plastic deformation, elastic deformation, and fracture toughness on breakage resistance. These models are in agreement with classical grinding theories. Based on the particle size scale, two classes of disruptive forces were studied considering either macroscale velocity (proportional to rotor tip speed) or inertial subrange turbulent eddy velocity (given by Kolmogorov's inertial subrange model). Four cohesive force definitions were studied, each with different dependence on physical properties and particle size. The disruptive and cohesive forces were employed to construct eight different correlations for ultimate crystal size and its rate of approach. Model discrimination is based on comparison to the wet milling experimental data. The best-fitting model was based on the combination of inertial subrange model as the disruptive force and elastic-plastic deformation model as the cohesive force.

For geometrically similar devices, a dimensionless comminution number was developed (ratio of disruptive to cohesive forces) to aid physical interpretation and scale up/down efforts. For devices without geometric similarity, the concept of local energy dissipation rate, defined as the power draw of the mixer per mass of fluid in shear gap and stator slot regions (calculated through computational fluid dynamics simulations), was introduced and exploited to compare the data from different mixers with different geometries. This approach was successful in correlating the maximum stable particle size resulting from wet milling of different crystals in a Silverson L4R inline mixer with standard and enlarged shear gap, and in a Silverson L4R batch mixer at different rotor speeds.

The mechanistic theory is further utilized to provide breakage kernels based on probability of collision and collision rate theories. Application of the breakage functions to predict the milling rate as well as their implementation within a population balance framework is discussed.

CRYSTAL WET MILLING IN ROTOR-STATOR MIXERS

By

Kanan Ghaderzadeh

Dissertation submitted to the Faculty of the Graduate School of the
University of Maryland, College Park, in partial fulfillment
of the requirements for the degree of
Doctor of Philosophy
2018

Advisory Committee:
Professor Richard V. Calabrese, Chair
Professor Akua A. Asa-Awuku
Professor Panagiotis Dimitrakopoulos
Professor Kenneth T. Kiger
Professor Michael R. Zachariah

Table of Contents

List of Tables

List of Figures

Nomenclature

σ	- stress $[N/m^2]$
σ_f	- stress at fracture $[N/m^2]$
a	- flaw length $[m]$
a_f	- flaw length at fracture $[m]$
E	- elastic or Young's modulus $[N/m^2]$
Γ	- surface energy $[J/m^2]$
K	- stress intensity factor $[N/m^{3/2}]$
K_c	- critical stress intensity factor or fracture toughness $[N/m^{3/2}]$
G	- shear modulus $[N/m^2]$
K	- bulk modulus $[N/m^2]$
v	- Poisson ratio [-]
H	- hardness $[Pa]$
E_{sp}	- specific energy $[J/kg]$
x	- particle length $[m]$
l_i	- fractured fragment length $[m]$
m	- particle mass $[kg]$
n	- number of particles
u	- impact velocity $[m/s]$
ρ_P	- particle density $[kg/m^3]$
u_{tip}	- rotor tip speed $[m/s]$
ρ_f	- fluid density $[kg/m^3]$
ϵ	- energy dissipation rate $[J/kg.s]$
N	- rotor speed $[1/s]$
D	- rotor diameter $[m]$
ΔV	- fractured fragment volume $[m^3]$
V	- particle initial volume $[m^3]$
τ_c	- cohesive stress $[N/m^2]$

τ_D - disruptive stress [N/m^2]

We - Weber number [-]

Co - comminution number [-]

T - time constant [s]

D100 - largest particle size of the sample [m]

D95 - size at which 95% (by volume) of particles in the sample are smaller [m]

D90 - size at which 90% (by volume) of particles in the sample are smaller [m]

D80 - size at which 80% (by volume) of particles in the sample are smaller [m]

D50 - size at which 50% (by volume) of particles in the sample are smaller [m]

D10 - size at which 10% (by volume) of particles in the sample are smaller [m]

D_{43} - Debroukere mean diameter [m]

D_{32} - Sauter mean diameter [m]

D_{10} - arithmetic mean diameter [m]

API - active pharmaceutical ingredient

IPA - isopropyl alcohol

CFD - computational fluid dynamics

RANS - Reynolds-average Navier-Stokes

FBRM - focused beam reflectance method

PVM - particle vision method

ASTM - American society of testing materials

SEM - scanning electron microscopy

TEM - transmission electron microscopy

RBI - relative backscatter index

Chapter 1: Introduction

1.1 –Motivation and Purpose

Size reduction and comminution is a critical step in many particulate processes, e.g., dry milling, wet milling, mineral processing, ceramic processing, mining and crystallization. It is used to create particles with specific size distribution and morphology to enhance product design, stability, solubility, and so on. Milling processes can be categorized to two broad categories: dry milling and wet milling. Wet milling has specific advantages over dry milling such as reducing number of operational steps, better control of heat generation and crystal morphology, reduced exposure to milling dust. Furthermore, it can be utilized in series with unit operations such as crystallization to ensure robust product delivery.

Despite the increasing industrial interest, there are currently few studies to describe the wet milling of active pharmaceutical ingredients (APIs) or other crystalline substances, particularly in high shear rotor-stator mixers. Furthermore, no mechanistic framework has been developed to address the effect of different milling variables, particle mechanical properties, or mixer geometry/scale on wet milling performance. Consequently, the design and scale up of wet milling processes in high shear rotor-stator mixers is still predominantly based on experience and trial and error.

The purpose of this study is to investigate the effect of milling conditions, crystal physical properties, and mixer geometry on milling behaviour of crystals; and to introduce a class of mechanistic models for breakage and attrition of crystals in

rotor-stator mixers based on elastic-plastic deformation and fracture mechanics concepts. The ultimate goal is to develop mechanistic correlations that lead to general laws for scaling up particle size from the laboratory to the industrial scale. Three steps are required to achieve this goal: 1) Conduct definitive wet milling experiments in a rotor-stator mixer to investigate the effect of milling conditions, mixer geometry, and particle physical properties on ultimate particle size and particle breakage kinetics; 2) resolve the complex flow in the high shear mixer to identify the extend of the particle-fluid, particle-particle, and particle-rotor interactions; and 3) identify the comminution mechanisms and important physical properties in particle breakage.

1.2 –Approach

In experimental part of this study, a set of systematic experiments were performed in a Silverson L4R inline rotor-stator mixer with a standard shear gap (clearance between rotor and stator) and an enlarged shear gap, and in a Silverson L4R batch rotor-stator mixer to investigate the effect of milling conditions, mixer geometry, and particle physical properties on ultimate particle size (maximum stable particle size at equilibrium) and particle breakage rate. Rotor speed and volumetric throughput were adjusted to independently vary energy input and mill head residence time. To vary crystal physical properties (i.e. elastic modulus, hardness, fracture toughness), three different crystalline materials, sucrose, glycine, and ascorbic acid, were milled in isopropyl alcohol (IPA) as an anti-solvent. Using an anti-solvent allows discrimination between mechanical size reduction and solubility effects. The effects of fluid shear, particle-particle collisions, and particle-wall collisions on crystal breakage were assessed by changing particle concentration; coating the stator surfaces, and small geometric changes. Since the initial crystal size (before milling) is

greater than the standard shear gap width, the inline mixer rotor was modified to an enlarged shear gap to study the effect of shear gap width on milling performance. In addition, wet milling experiments in a Silverson L4R batch mixer were performed for the sucrose-IPA system at different rotor speeds. The batch mixer has a smaller mixing head and different power draw, so different milling behaviour was observed compared to the inline mixer.

In the modelling part of this study, a class of mechanistic models was developed to interpret and correlate the data obtained in wet milling experiments. These models consider the influence of plastic deformation, elastic deformation, and fracture resistance of a crystal during breakage. The cohesive forces resisting particle breakage were found to be a function of particle elastic modulus, hardness, fracture toughness, and size. Each mechanistic model predicts different relative importance of the material properties and particle size in resisting breakage. Therefore, different expressions for cohesive force were developed dependent on the particle deformation mechanics and breakage behavior. The disruptive forces that contribute to particle breakage were found to be a function of particle velocity magnitude at impact with surfaces and other crystals. While previous studies have related the disruptive force to macroscale velocity, particle sizes are such that they should be influenced by eddy encounters in the inertial subrange of turbulence. Therefore, two expressions for disruptive force were developed dependent on macroscale velocity, based on rotor tip speed, and eddy velocity given by Kolmogorov inertial subrange model. These cohesive and disruptive forces were employed to construct different correlations for maximum stable crystal size and the rate of approach to ultimate size. Model discrimination was based on comparison to the wet milling experimental data.

According to the proposed mechanistic models, power draw or energy dissipation rate data are required to collapse the milling data for different mixer geometries. These data are available in the literature for the Silverson L4R batch mixer but not for inline mixer. This gives rise to the numerical part of this study, in which a three-dimensional computational fluid dynamics (CFD) simulation was performed to investigate the effect of shear gap width on power draw and local velocity field in the Silverson L4R inline rotor-stator mixer. The Reynolds-Average Navier-Stokes (RANS) equations, with the realizable k-ε turbulence model and enhanced wall functions, were used to model the complex turbulent flow pattern generated by this mixer. The integral of the total moment exerted by pressure and viscous forces on the moving surfaces of the rotor was calculated to determine the torque and power draw of the mixer at different rotor speeds. It was found that the mixer with wider shear gap has a slightly better pumping number compared to mixer with standard shear gap whereas the later results in higher energy dissipation rates and hence better milling performance. The simulation results showed that the configuration with narrow shear gap draw significantly more power and power draw decreases with increasing the shear gap width.

Finally, the aforementioned wet milling experimental data, mechanistic models of breakage, and power draw data were utilized to develop a dimensionless comminution number for geometrically similar devices, to aid physical interpretation and scale up/down efforts. For devices without geometric similarity, the concept of local energy dissipation rate (defined as the power draw of the mixer per mass of fluid in shear gap and stator slot regions) was introduced and exploited to compare the data from the different mixer geometries. This approach was successful in correlating the maximum stable particle size resulting from wet milling of different crystalline

materials in a Silverson L4R inline mixer with standard and enlarged shear gap, and a Silverson L4R batch mixer at different rotor speeds. The mechanistic theory is further utilized to provide breakage rate kernels based on probability of collision and collision rate theories. Application of the breakage functions to predict the attrition rate as well as their implementation within a population balance framework is discussed.

The results of this study are not restricted to rotor-stator mixers; the scaling laws, non-dimensional correlations, and breakage functions developed herein can be applied to other processes in which particle breakage occurs according to the same mechanism(s).

1.3 –Organization of the Dissertation

This dissertation is divided into 7 chapters. Chapter 1, the current chapter, comprises the general outlines of the study. Chapter 2 focuses on the characterization of size distribution and physical properties of the particles. Various size measurement methods that are relevant to this study are discussed, which include: sieving, microscope-based image analyzing, laser diffraction, focused beam reflectance method (FBRM), and particle vision method (PVM). The measurement of particle physical properties (i.e., elastic modulus, hardness, and fracture toughness) using a nanoindentation method is discussed.

Chapter 3 provides an introduction to fracture mechanics and development of mechanistic models for particle breakage. Particle breakage behavior based on indentation, elastic, plastic, and elastic-plastic deformation mechanisms are discussed. The functional forms of these models and their similarities with classical

comminution theories are presented and discussed. Different cohesive and disruptive forces that are relevant in wet milling process are presented, and different scale-up strategies for rotor-stator mixers are provided.

Chapter 4 provides the results of wet milling experiments in the Silverson L4R inline mixers with standard and enlarged shear gap, and in the Silverson L4R batch mixer. The experiment setups and procedures for batch and inline modes are shown. The size measurement obtained from laser diffraction method is compared to FBRM and PVM results. The effect of milling conditions including rotor speed and volumetric throughput on ultimate particle size and particle breakage rate are presented. The effect of particle physical properties is discussed by presenting the experiment results for wet milling of different crystal-antisolvent systems (sucrose, glycine, ascorbic acid in IPA). Furthermore, the effect of solid concentration and mixer geometry on wet milling of sucrose-IPA system is presented and discussed.

Chapter 5 reports the suitability of different mechanistic models that are presented in Chapter 3 to predict the wet milling data provided in Chapter 4. A definition for the dimensionless comminution number is presented and the scale up strategy for geometrically similar mixers is discussed. Furthermore, the concept of local energy dissipation rate is presented and a general scale up strategy is provided.

Chapter 6 is concerned with calculation of power draw for the Silverson inline mixer with different shear gaps. The CFD simulation of Silverson L4R inline mixer is discussed and the geometry details, grid generation strategy, and numerical solution method is provided. The simulation results including the velocity field within the mixer, turbulent kinetic energy distribution, and total energy dissipation rate are

presented. The fluctuation of power draw with respect to rotor position is presented and discussed.

Chapter 7 presents the conclusions of each portion of this study, summarizes the findings, and proposes recommendations for future work that would further improve the understanding of the wet milling processes in rotor-stator mixers.

Chapter 2: Particle Size and Physical Property Measurements

This chapter provides a brief overview on various particle size definitions, size distributions, sampling errors, and size measurement techniques that are used in this study to characterize the milling performance of rotor-stator mixers. In addition, particle physical properties that play an important role in particle breakage are presented and their measurement method using a nanoindentation technique is discussed.

2.1 –Particle Size

Determination of particle sizes and size distribution of suspensions, emulsions, slurries, powders, granules, sprays, and aerosols is a critical step in many manufacturing and processing operations. Particle size and size distribution influence various properties of particulate materials such as stability in suspension, packing density and porosity, dissolution rate, reactivity, flowability and so on. For example:

- In the pharmaceutical industry, the size of API controls their dissolution and absorption rates.

- In the paint industry, the size of pigments affects appearance of the coated surface (matt, semi-glass, and glass finishes), depth of color, and rheological properties of the paint.

- In the food processing industry, particle size can change the product flavor and texture, e.g., the size of coffee grinds affects the flavors released in the brewing process.

- In polymer processing, particle size distribution of catalysts influences the shape and molecular weight distribution of the polymer.

Accurate definition and measurement of particle size can lead to a better understanding of the process dynamic and better control of the product quality.

In quiescent liquid-liquid and gas-liquid processes, the resultant droplets and bubbles are usually spherical and their size can be fully described by their radius or diameter; whereas, in solid processing applications, the resultant particles usually have irregular shapes, and therefore the proper definition of their size is more challenging. One would need to store many data points to fully describe the particle's irregular shape and various dimensions.

In order to avoid the complexity of reporting various sizes for a single particle, it is preferred to report one diameter as the representative of the particle size. This is usually done by measuring a related size-dependent property and reducing it to a single linear dimension, dictated by the measurement technique. For example, image analysing techniques characterize the particles based on their surface area (projection area), and therefore the diameter of a sphere having the same surface area as the particle can be used to characterize the particle size. Table 2.1 summarizes some of the popular size definitions based on equivalent sphere diameter. It is important to note that these equivalent diameters provide a simple and acceptable result for particles with low aspect ratios, but problems can arise for needle and plate shaped particles in which the aspect ratios are high.

Table 2.1 -Definitions of the equivalent diameters based on measured properties of the particle

Equivalent diameter	Definition
Projected area diameter	Diameter of a circle having the same area as the projected area of the particle
Surface diameter	Diameter of a sphere having the same surface area as the particle
Volume diameter	Diameter of a sphere having the same volume as the particle
Surface volume diameter	Diameter of a sphere having the same surface to volume ratio as the particle
Sieve diameter	Diameter of the sphere that can pass the sieve aperture
Stokes' diameter	Diameter of a sphere having the same settling velocity as the particle under laminar flow condition

There are other size measures which can be used to quantify particle size such as Martin diameter, Feret diameter (including the maximum and minimum Feret diameter), and chord length. These diameters can be obtained using image analyzing methods. The Martin diameter is the length of the chord dividing the projected particle area into two equal halves. A Feret diameter (or calliper diameter) is the perpendicular distance between parallel tangents touching opposite sides of the particle's projected area. Chord length is the length of a line segment whose

endpoints lie on the circumference of the projected area of the particle. Figure 2.1 shows a graphical representation of these statistical diameters.

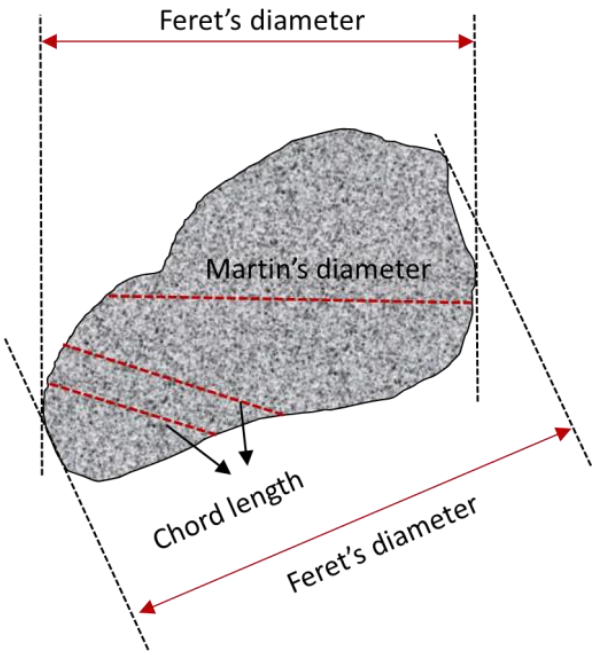

Figure 2.1-Definition of statistical diameters representing different dimensions of the particle

As mentioned earlier, there are an infinite number of linear dimensions to describe the particle size for irregular shaped particles. Moreover, the orientation of irregular particles during measurement can have a significant effect on the measurement result. Therefore, to have a statistically meaningful size, a large number of particles (from couple of hundred to several thousand particles) need to be analysed depending on the extent of the particle irregularity and the type of measurement technique. Given the vast variety of particle size definitions, it is important to note that the conversion from one size representing a dimension of the particle to that representing another dimension should be conducted with a careful consideration of the particle shape.

In this study, different measures of particle size are used to characterize the data from different measurement techniques. The sieving data are characterized by sieve diameter, laser diffraction data are characterized by volume diameter, image analysis uses projected area diameter, and FBRM uses the chord length as defined in Table 2.1 and Figure 2.1.

2.2 –Particle size distribution

Particle populations are usually poly-dispersed, consisting of particles of different size. It is common practice to specify the size of these poly-dispersed particle populations in the form of either a frequency distribution, or a cumulative (undersize) frequency distribution. Frequency distribution is a two-dimensional representation of the particle sizes and the number of reoccurrence of each size. The number of reoccurrence of each particle size can be represented in different ways with respect to the weighting of individual particles based on their number, mass, volume, surface area, or other properties that is usually dictated by the measurement technique, e.g., mass distribution can be determined by the sieving technique, volume distribution by the laser diffraction method, and number distribution by microscopy methods. Each of these different distributions is advantageous for certain application. For example, in dry and wet milling processes, a volume distribution is a better measure for product evaluation compared to a number distribution because of the extensive generation of fine particles during milling that obscure the effect of larger particles on the number-based size distribution.

It is important to note that it is mathematically possible to convert a distribution from one base to another (e.g., number distribution to mass or volume distribution)

but it requires the assumption that the particles have a specific shape, and thus can introduce significant error for irregular shaped particles.

2.3 –Distribution Statistics

It is common practice to define different distribution statistics and measures in order to compare different size distributions. This is especially useful when monitoring particulate process dynamics or comparing the products of different processes. It is important to note that a single measure cannot adequately describe a size distribution and usually different statistics of a distribution are reported together to give a better understanding of the size distribution. The type of process and the intended application is considered when choosing the appropriate distribution measures. Some of the frequently used distribution statistics are:

- *Mode:* one of the popular measures of a size distribution is the mode of the distribution. It is defined as the size at which the frequency distribution is maximum (i.e., it is a measure of the particle size with maximum probability of occurrence in a size distribution).

- *Median:* the median is the 50% size on a cumulative distribution. It is a measure of the particle size at which half the distribution population has particle sizes smaller than this size, and half has particle sizes larger than this size.

- *Mean*: the mean is usually defined as the arithmetic average of a number based size distribution as:

$$\bar{x} \; or \; D_{10} = \frac{\sum n_i x_i}{\sum n_i} \qquad (2.1)$$

where n_i is the number of particles with size x_i, and $\bar{x}$ is the mean. This is also called number weighted average size and shown as D_{10}. It is important to note that for a normal distribution, the mean, the median, and the mode are all equivalent.

- *Weighted average:* different weighted average sizes are defined to accommodate different type of processes and applications. In chemical reaction or dissolution problems, for example, the available surface area of the particles is important and therefore a surface area weighted average size is more relevant and can be defined as:

$$D_{32} = \frac{\sum n_i {x_i}^3}{\sum n_i {x_i}^2} \qquad (2.2)$$

where D_{32} is the surface area weighted average size. It is also called the Suater mean diameter. Another popular size measure is the volume weighted average size, D_{43}. It is defined as:

$$D_{43} = \frac{\sum n_i {x_i}^4}{\sum n_i {x_i}^3} \qquad (2.3)$$

It is also called the De Brouckere mean diameter. This mean value is heavily weighted toward the large particles of the distribution and is a good measure for the processes that are sensitive to the presence of large particles.

- *Cumulative percentile*: the cumulative percentile indicates the number of particles in a population whose size is smaller than a given size. For example, the D90 is the particle size at which 90% (by mass or volume) of the particles have sizes smaller than this value. They are also called D-values. Different D-values are representative of different aspects of a size distribution, e.g., D10 is a representative of the size of fine particles, D50 is the median, and D90 is a representative of the size of large particles in the distribution. Figure 2.2 and Figure 2.3 show a unimodal distribution and a bimodal distribution that are obtained during the wet milling of sucrose in IPA and measured by a laser diffraction method. The volume frequency and cumulative volume percentage of the distributions are illustrated along with the corresponding D10, D50, and D90 values.

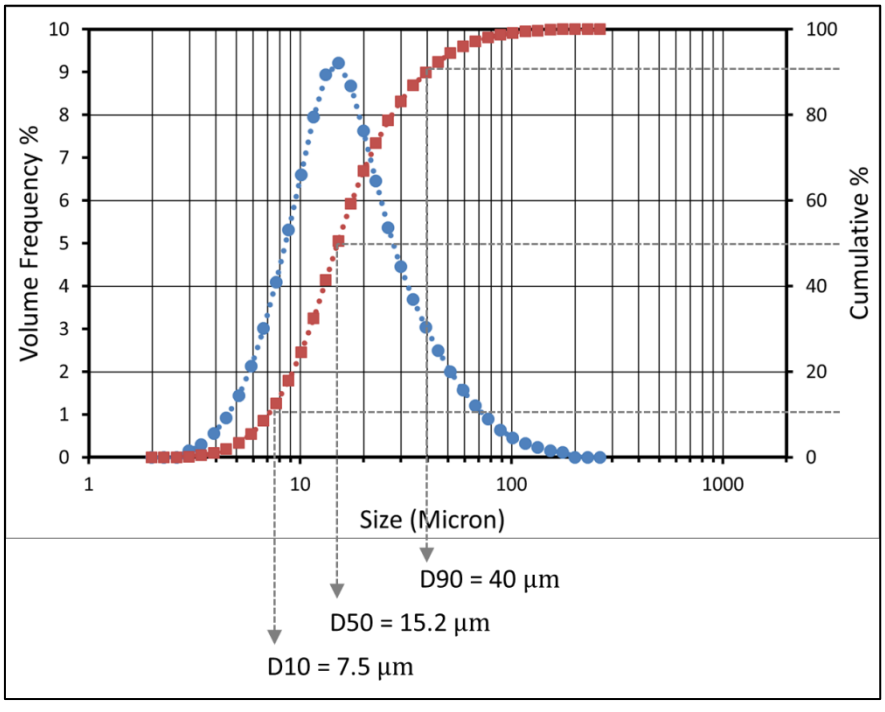

Figure 2.2 -Unimodal frequency and cumulative size distribution obtained during wet milling (L4R batch mixer at 8000 rpm) of sucrose in IPA and its corresponding D10, D50, and D90 values measured by laser diffraction method

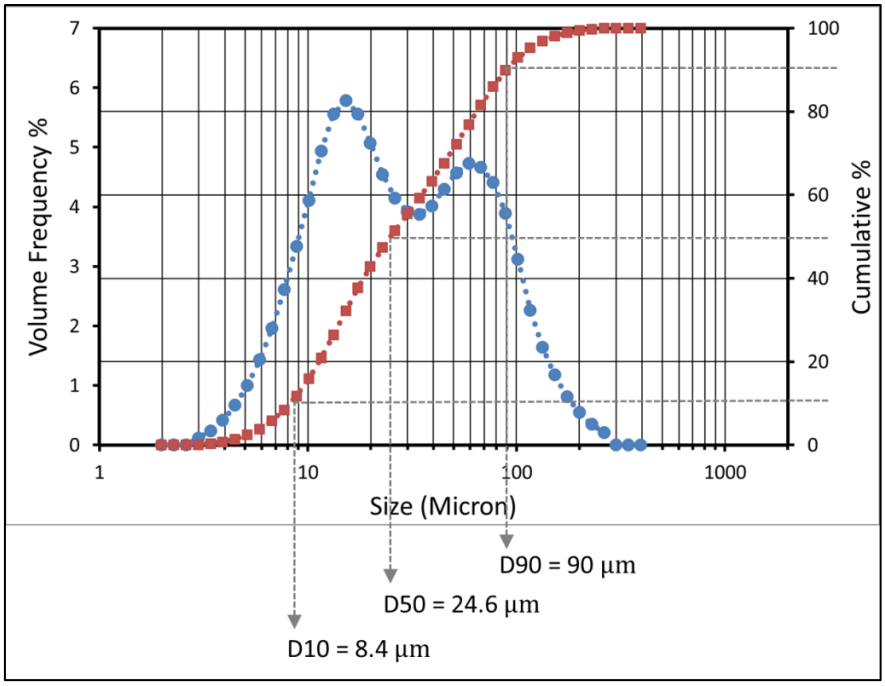

Figure 2.3 -Bimodal frequency and cumulative size distribution obtained during wet milling (L4R batch mixer at 8000 rpm) of sucrose in IPA and its corresponding D10, D50, and D90 values measured by laser diffraction method

2.4 –Sampling

Particulate systems consist of a large population of particles with different sizes. It is not feasible to characterize the size of each and every particle in the entire population, so sampling is performed to obtain a sample with smaller fraction of the population. Special care must be taken in sampling steps to obtain a sample whose size distribution would be representative of that of the entire population; an incorrect and non-representative sampling can result in poor process characterization.

The accuracy of a size distribution measurement depends on sampling errors, errors in measurement procedures (proper dispersion in measurement cell), operator errors (poor calibration), and the instrument limitations. Sometimes, the sample acquired in one sampling step is too large and must be further sub-divided to give an appropriate sample size for measurement. Sampling itself is prone to two types of

errors: one arises from a non-representative sample due to inhomogeneous bulk materials and lack of proper mixing and dispersion, the other is due to statistical errors with random fluctuations around the mean value [1]. In order to establish homogeneity, it is necessary to measure the size distribution of the different samples taken from the different regions of the bulk; the homogeneity is established if the variability of the size distribution between different samples is sufficiently small. The random fluctuation of the size distribution data around a mean value is a characteristic of a random process and cannot be completely suppressed; however, it is possible to reduce these fluctuations by increasing the sample size or sampling time.

Proper mixing and dispersion in solid-liquid suspensions requires some mode of agitation. The agitation creates a turbulent flow field in which solid particles are dispersed and distributed throughout the liquid. The properties of both the liquid and the solid particles, holding vessel geometry, and agitation parameters influence the homogeneity of the suspension. The degree of dispersion can be classified into three levels of partial suspension, complete suspension, and uniform suspension as shown in Figure 2.4 [2]. Uniform suspension is the desired result at which particle concentration and size distribution are practically homogeneous throughout the holding vessel. In this study, to establish a uniform crystal-antisolvent suspension, the size and aspect ratio of the holding tank, impeller blades, and baffles are carefully selected and the agitation rate is adjusted to enhance the top-bottom mixing without aeration. The homogeneity of the sampling was examined by inline and offline measurement of samples acquired from different regions of the crystal-antisolvent suspension in the sampling/holding tank (see Chapter 4 for details).

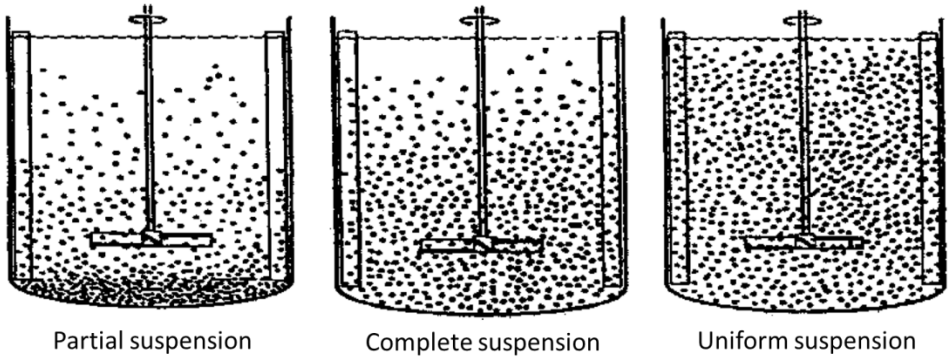

Figure 2.4 - Degrees of dispersion - partial suspension: some particles rest on the bottom of the tank for short periods; complete suspension: all particles are off the bottom of the vessel; uniform suspension: particle concentration and size distribution are practically homogeneous throughout the vessel [2].

2.5 –Particle Size Measurement Techniques

Particle size and size distribution can be determined using different measurement techniques such as sieving, sedimentation, microscopy and image analysis, electron zone sensing, laser diffraction, dynamic light scattering, focused beam reflectance method (FBRM), particle video microscopy (PVM) and many other techniques. Some of these techniques can be used inline (integrated into the process) with a fast response rate and some has to be used in an offline mode with a batch analysis procedure. The number of sampling steps, the required concentrations of the samples, and the size range capabilities are different in different techniques. The general factors that should be considered before selecting a measurement technique are:

- Size range
- The technique needs to generate size data in a form that is relevant to the process in hand (i.e., number based measurement, volume based measurement, and so on)
- Accuracy and reproducibility

- Amount of sample available for analysis
- Response rate of the measurement including sample preparation, measurement, and reporting, e.g., online methods usually have a faster response rate compared to off-line techniques
- Cost of the instruments

It is important to note that the resulting size distribution should be based in the format of the primary result for a given technique, e.g., laser diffraction technique generates results based on volume distributions and any specification should be volume based; conversion to another basis such as number can introduce significant errors.

2.5.1 –Sieving

Sieving is widely used in different disciplines and industries due to its relative simplicity, low cost, and high reliability in determining particle size distribution over a wide size range. It can characterize the dry powders as well as the slurries by shaking the sample through a stacked series of sieves with decreasing mesh size. The mesh size is defined as the number of wires per linear inch of the sieve. A variety of sieves with different aperture sizes are available. For woven wire sieves, the mesh size ranges from 5 inch mesh with 125 mm of aperture size to No. 635 mesh with 20 μm of aperture size based on the American Society of Testing Materials (ASTM) standards. The electroformed sieves can have smaller aperture sizes down to 1 μm. Particles having two dimensions smaller than the aperture opening will pass through, whereas larger particles will be retained. The resulting data can be reported as a mass based size distribution or cumulative mass percentage. The resolution is bounded by

the aperture opening of the sieves and varies from 10s of mm for coarse sizes to 10s of μm for fine particles. Some of the limitations of this technique include the long analysis times, the shaking action may cause agglomeration or fracture of particles during the analysis, and type and duration of the mechanical shaking and blockage of apertures during sieving can affect the reproducibility of the results.

In this study, in order to obtain a consistent initial particle size distribution for milling experiments, batches of 100 grams of crystals were sieved using a vibratory sieve shaker (WS Tyler RX-29 Roto Tap) that provided motion in both horizontal and vertical axes with variable amplitude for 20 minutes (until less than 0.5% of the sample passes through in any 10 minutes sieving period based on the ASTM standard). A fraction of particles retained between No. 40 and No. 60 sieves (250-420 μm) was collected and used as the feed for the wet milling experiments.

2.5.2 –Image Analysis

Image analysis provides a direct and powerful tool to characterize size, shape, surface texture, and degree of dispersion of the particles. The images of the particles are usually magnified by an optical lens, captured by a digital camera, and analyzed by image analysis techniques. The required magnification depends on the size of the particles being studied and the extent of the resolution that is desired. Optical light microscopes, scanning electron microscopes (SEM), and transmission electron microscopes (TEM) can be used to obtain higher resolution images.

Optical light microscopes are used to analyze particle size in the range from 3μm to 150 μm [1]. The lower limit is due to diffraction of light passing through the camera aperture and causes a fuzzy edge surrounded by circles of light for fine

particles. The upper limit is due to narrow depth of field so that, for a sample having a wide range of sizes, only a portion of particles are in focus in any field of view. The particles larger than 150 μm can be removed using a sieving method and their image can be captured using a simple magnifying glass. The size distribution of particles with sizes smaller than 1 μm can be characterized by using higher magnification microscopes such as SEM and TEM.

In image analysis step, the captured images are usually converted to gray-scale images to enhance the contrast between the particles and the background. The images are then set to a specific threshold so that, all the pixels that have a grayscale value above the threshold are converted to black, and those with grayscale below the threshold are converted to white. The projected area of the particles in the image is then calculated by counting the number of pixels with black identifiers at each particle region. Figure 2.5 shows a sample of a raw image obtained using optical microscopy and the processed image identified via ImageJ software [3]. The border particles are removed because their size/shape cannot be meaningfully described.

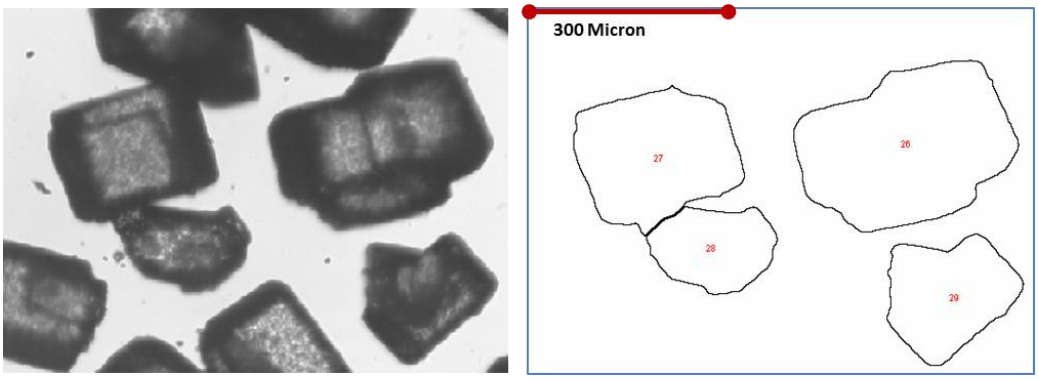

Figure 2.5 -A microscope image of sucrose particles and its processed version using ImageJ image processing software

In this study, image analysis is primarily used as an off-line method to monitor the particle size and shape in small batches to confirm the size data obtained by other devices. It was also used to monitor the samples for agglomerate formation.

2.5.3 –Laser Diffraction

Laser diffraction is one of the popular techniques for measuring particle size distribution because of its capability in analyzing broad range of materials with wide range of size distributions, ease of use, and high speed of measurement. The underlying principle of measurement is the difference in the scattering light from particles with different sizes and materials. The theory of light scattering by small particles has been developed by many authors and the fundamentals can be found in standard texts, e.g., Bohren and Huffman (1983). The theory is mathematically complex and computationally expensive to apply to non-spherical particles, therefore most of the laser diffraction methods assume that the particles are spherical and provide corresponding equivalent spherical diameters. This assumption can lead to biases and erroneous data when measuring the size distribution of particles with high aspect ratios. Another limitation of this method is due to multiple scattering where light scattered from one particle encounters with another particle and gets scattered again. To overcome to this problem, the concentration of particles in the sample should be diluted to reduce the probability of multiple scattering phenomena. The concentration limit depends on the design of the instrument, the nature of the incident light source, optical geometry, and light detection system.

To use laser diffraction method (based on Mie theory), the refractive indices of the particles and the dispersing medium need to be known. These indices are used to

predict the amount of absorption and refraction of the light passing through the particle. This is especially important for fine particles with sizes close to wavelength of the laser source. For fine particles, the refractive index is usually a complex quantity with a real and an imaginary part. The real part describes the refractive properties of the particle, while the imaginary part describes the light absorbing properties. For opaque, non-spherical particles with sizes much larger than the wavelength of the laser source, the refractive index can be adequately quantified by a real number (zero imaginary part).

The Horiba, LA950, laser diffraction instrument was used in this study as shown in Figure 2.6. It can measure wet and dry samples with size range of 10 nm to 3 mm [4]. This device consists of:

- Two light sources: a 5 mW 650 nanometers red laser diode and a 3 mW 405 nanometers blue light emitting diode. The smaller wavelength light is used to extend the lower detection limit of the technique.

- A beam expander to produce a uniform parallel beam for illuminating the sample volume.

- A sample cell with transparent flat windows and capacity of 10 mL to introduce the sample and control the interaction of particles and the incident light. The cell is mounted at a slight angle to the beam to eliminate the back reflections.

- The cell is stirred with a magnetic stirrer to keep the particles suspended. The size and rotational speed of the magnetic bar is carefully adjusted to ensure a uniform suspension of crystal-antisolvent system in the sample cell. This is particularly

important for measuring the samples taken at the early stages of the milling where there are larger particles with higher settling velocities.

- The scattered light from the sample passes through several optical lenses, and forms a scattering pattern onto 87 silicon photodiode array detectors at different light scattering angles.

- The detected signals are digitalized and compiled with Horiba software that controls the system during the measurement process and analyzes the light scattering data. The software utilizes Mie theory to convert the light scattering data to volume-based size distribution data.

One cycle of measurement including loading the sample cell, measurement, saving the data, and rinse typically takes less than 5 minutes to complete.

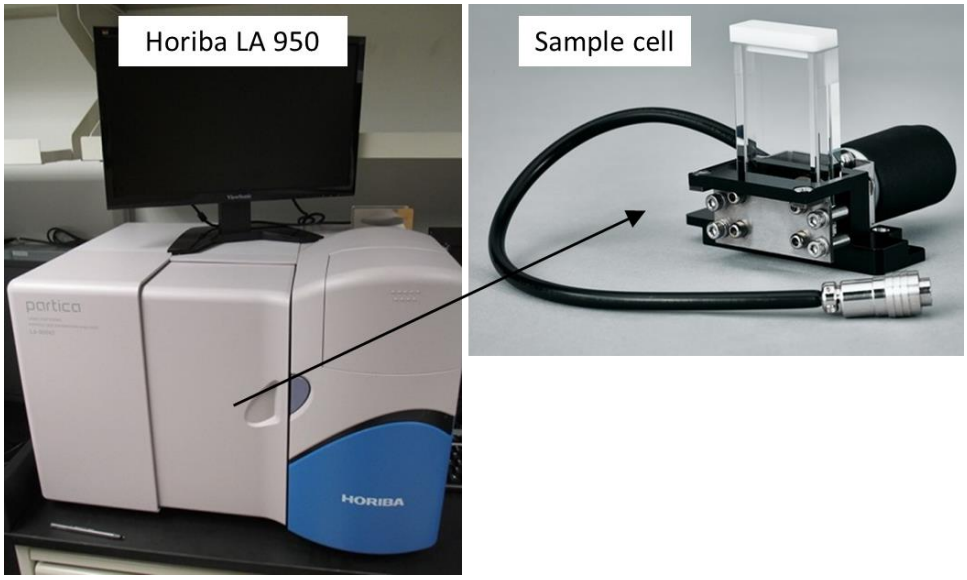

Figure 2.6 -Horiba LA 950 laser diffraction instrument and its sampling cell

2.5.4 –Focused Beam Reflectance Measurement (FBRM)

The FBRM device is an in-situ probe to characterize the chord length distributions of particulate samples. The probe projects a focused laser beam to its tip where a rotating optical lens deflects the laser. The beam is focused to a fine point close the probe's window and traces a circular path as shown in Figure 2.7. When the probe is inserted into a system of particles, the laser is reflected as it scans across the surface of a particle. The probe measures the reflectance time and determines the chord length by the product of the reflectance time and the laser scan-speed. Depending on the concentration of the particles, thousands of particles are usually counted during one measurement and the results are presented as a chord length distribution of particles.

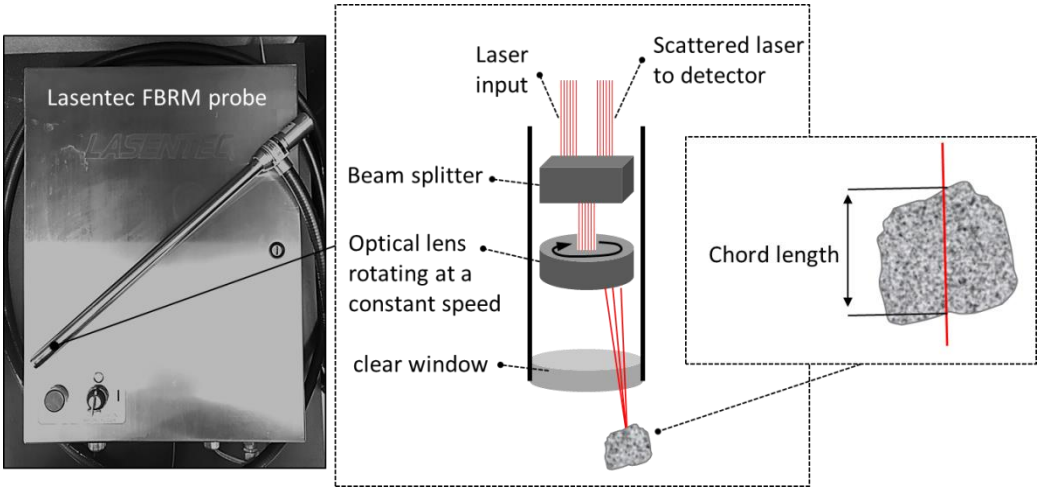

Figure 2.7 -Lasentec D600 FBRM probe and schematic of probe internal parts showing the laser crossing a particle surface

Considerable efforts have been made to find numerically robust solutions to reconstruct the size distribution from a chord length distribution, but for non-spherical particles, the results are unreliable due to ill-posed nature of this inverse problem. Despite this drawback, the chord length distribution data obtained by a FBRM probe

can be used to qualitatively monitor the dynamic changes in particulate processes. Moreover, process control strategies may be correlated directly with chord lengths and chord length distribution.

In this study, FBRM probe, a Mettler-Toledo Lasentec D600 particle size analyzer, was used in situ for inline measurement of chord length distribution as well as evaluation of complete solid suspension in the holding vessel of inline setup (see Chapter 4 for details). It utilizes a laser with power of 3 mW, wavelength of 790 nanometers, and rotation speed of 2 m/s. It is capable to measure the chord length of particles between 1 μm and 2 mm [5]. The instrument was calibrated using a standard sample provided by Mettler-Toledo Autochem.

2.5.5 –Particle Vision Measurement (PVM)

A PVM probe, Particle View V19 from Mettler-Toledo Autochem as shown in Figure 2.8, was also used in this study to monitor the particle shape during the milling. PVM is an in situ video microscope that can be integrated to the system as an inline measurement technique. It uses 6 near infrared laser sources to illuminate a small area in front of the probe window (within the slurry). An integrated CCD camera records digital images of the illuminated area with a 826 μm × 619 μm field of view and rate of up to 10 images per second [6]. Particles larger than 20 μm can be identified from the PVM images; below this size scale, it can be difficult to distinguish individual particles.

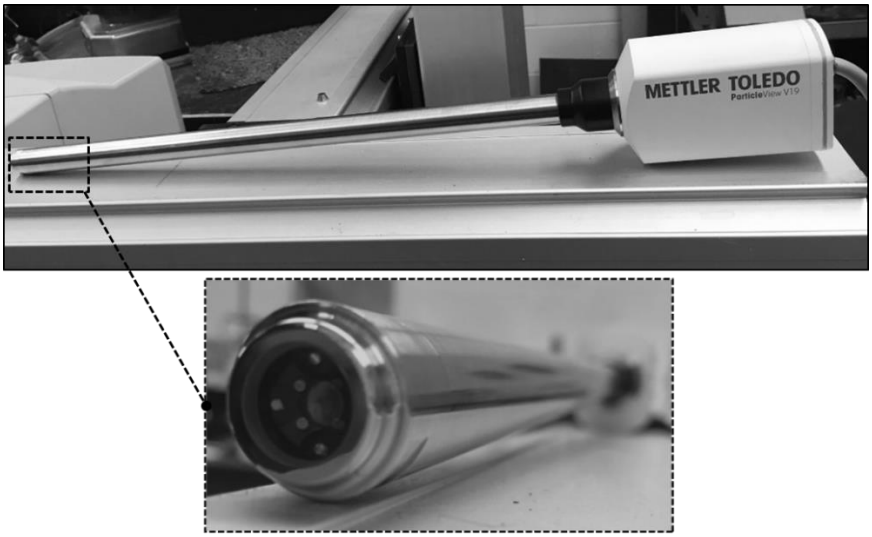

Figure 2.8 -Particle Vision Measurement (PVM) probe, Particle View V19 from Mettler-Toledo Autochem and schematic of probe tip

Using image analysis techniques to obtain quantitative information from PVM images is challenging. The images have non-uniform intensity with poorly defined particle outlines. The image processing problem is further complicated by particle overlap and presence of large number of fine particles that scatter the input light and saturate the images. Despite this drawback, a relative backscatter index (RBI) is defined by Mettler-Toldeo that can be used to qualitatively monitor the dynamic changes of particle size and concentration in the process. The RBI is a function of particle size, shape, concentration, brightness, and refractive index. It is defined as:

$$RBI = \frac{image\ brightness}{intensity\ of\ light\ input} \tag{2.4}$$

RBI decreases as the particles get finer and as the concentration of particles increases, i.e., image brightness decreases. An example of images captured by PVM probe and corresponding RBI during a wet milling experiment are given in Figure 2.9.

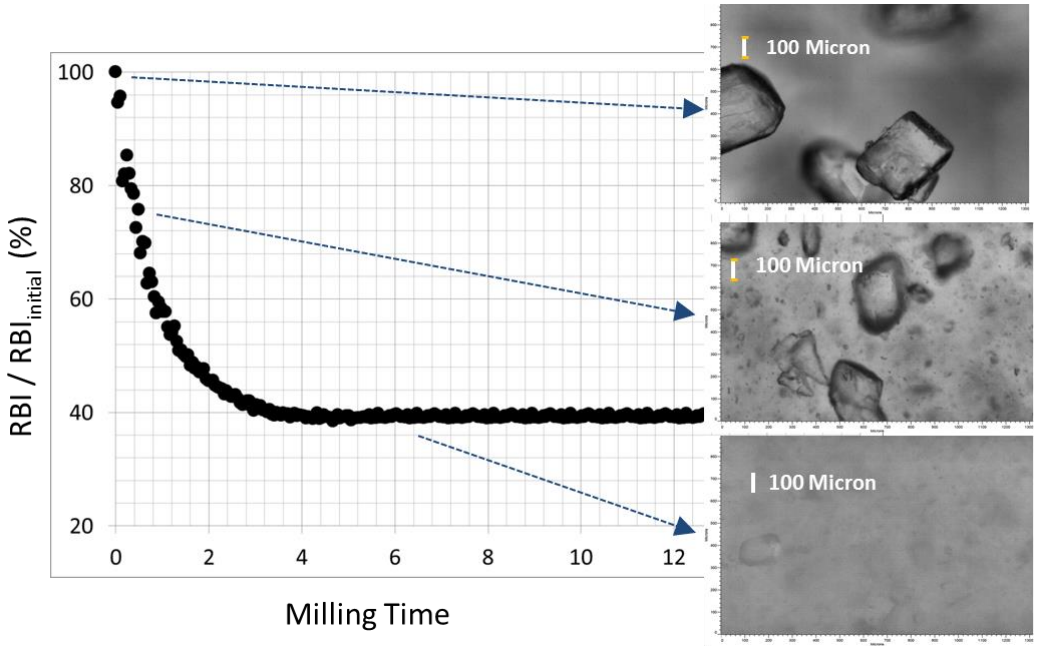

Figure 2.9 -PVM images of sucrose crystals in IPA captured inline during wet milling (L4R inline mixer with standard shear gap), RBI of images are calculated at different milling times

2.6 –Particle Physical Properties

All solid materials deform under the application of force or stress. Depending on the characteristics of this deformation, the process is classified as elastic or plastic. The characteristics of this deformation primarily depend on physical properties of the material, temperature, and magnitude of the applied load. An elastic deformation is a type of process in which the original size and shape can be recovered once the load is removed. This type of deformation involves stretching of the atomic bonds of the material. The atoms keep their original bonds and restore their original positions when the load is removed. If the loads are increased beyond a certain limit (yield strength) then the particle goes through a plastic deformation. The plastic deformation involves the breaking of a limited number of atomic bonds (e.g. the movement of dislocations). The required force to break the bonds of all the atoms in a crystal plane is very great. However, the movement of dislocations allows atoms in crystal planes to slip past one

another at a much lower stress levels. Since the energy required to move is lowest along the densest planes of atoms, dislocations have a preferred direction of travel within a grain of the material. In this case the particle cannot recover its original shape when the loads are removed.

2.6.1 –Young's Modulus

For combined stress states that have a combination of tensile, compression, and shear stresses, the elastic behavior of a material is defined through the Young's modulus (is also known as elastic modulus, E), the shear modulus (G), the bulk modulus (B), and Poisson's ratio (ν). For an isotropic material, these properties are related to each other according to:

$$E = 2G(1 - \nu) \tag{2.5}$$

$$G = \frac{E}{2(1+\nu)} \tag{2.6}$$

$$B = \frac{E}{3(1-2\nu)} \tag{2.7}$$

$$\nu = \frac{E-2G}{2G} \tag{2.8}$$

For many materials, B ~ E, $G \sim \frac{3}{8}$ E, and ν ~ 0.33 [7]. Low modulus materials are pliable, and stretch a lot when they are pulled. High modulus materials are the opposite; they stretch very little when pulled. Elastic modulus is related to the atomic binding energy for the case of inorganic materials or molecular binding energy for organic solids. As shown in Figure 2.10, the stronger the bond of a material, the higher the resistance to bond stretching and hence a higher Young's modulus of the

material. This material property can be obtained by several methods; a nanoindentation technique is used here.

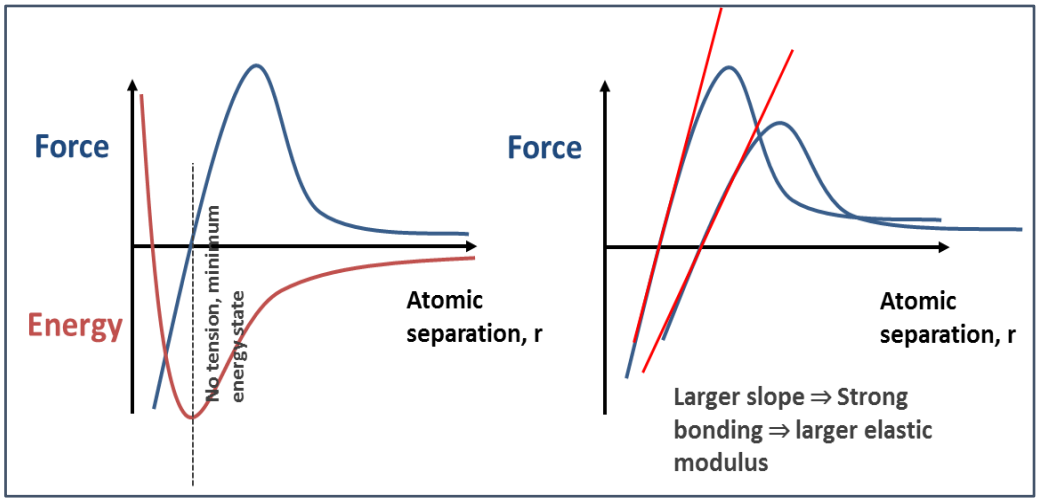

Figure 2.10- Elastic modulus is related to the atomic bonding forces; the higher atomic bonds (sharper slope), higher the elastic modulus

2.6.2 –Hardness

The resistance of a material to plastic deformation can be characterized using the concept of hardness. Mohs [8] introduced a qualitative hardness scale based on the scratch resistance of a material relative to diamond. Tabor [9] developed an indentation technique to quantitatively characterize the hardness of different materials. For fine particulate solids, which is the case in this study, the standard indentation method is not possible due to size constraint and the most appropriate technique is the nanoindentation.

2.6.3 –Fracture Toughness

The fracture toughness or critical stress intensity factor (K_c) is a material property that represents the material resistance to crack growth. It is originally developed for isotropic, linearly elastic materials subjected to small deformations.

American engineer and physicist George R. Irwin [10] did a major work to predict crack growth under loading based on stress intensity factor. He showed that the fracture toughness can provide a proper characterization of crack tip stressing even when linear elastic theory is not applicable to the process. (see Chapter 3 for more details).

2.7 –Indentation Test

Indentation testing is a mechanical testing process designed to determine the properties of materials by putting an indentation in the surface of a material sample. An indenter with a well-defined geometry is pressed on the surface of a sample using a known test load. The stress-strain history and the indent size and depth can be obtained as the indenter penetrates into and is withdrawn from the sample.

Nanoindentation is an indentation test in which the length scale of the penetration is in nanometers rather than microns or millimeters. In nanoindentation tests, the size of the residual impression is of the order of microns and it can be obtained by measuring the depth of penetration of the indenter into the specimen surface. The measured depth of the indentation together with the known geometry of the indenter can be used to calculate the hardness of the material.

2.7.1 –Measurements of Particle Mechanical Properties

By placing a load F on the indenter tip, it penetrates into the specimen to a measurable depth. At this point, the load may be held constant for a period or removed. The Young's modulus can be estimated from stress-strain graph during the loading and unloading process. The hardness (H) can be calculated by

$$H = F/(2a^2) \qquad (2.9)$$

where F is the applied load and a is the diagonal length of indentation as shown in Figure 2.11.

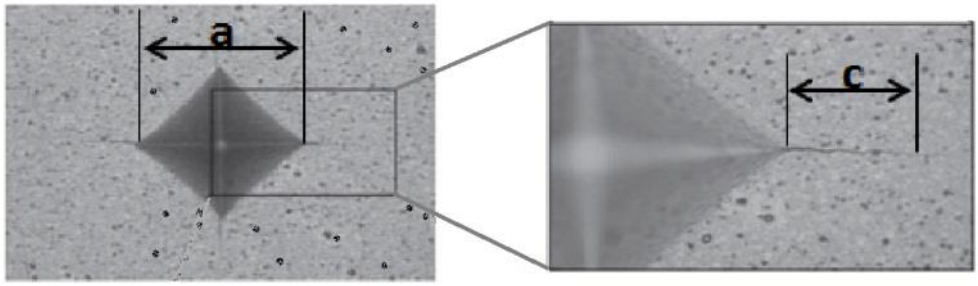

Figure 2.11- Indentation area and crack propagation in an indentation test

Stress intensity factor (K_c) describes the ability of a material containing a crack to resist fracture, and is estimated as

$$K_c = \xi\,(\mathrm{E/H})^2\,(\mathrm{F/c^{1.5}}) \qquad (2.10)$$

where ξ is a calibration factor (=0.016 ± 0.004), E is elastic modulus, H is hardness, F is applied load, and c is the radial crack [11].

The penetration depth can be in the order of μm or nm: micro-indentation and nano-indentation respectively. In this work, indentation tests were performed using a TI 950 Hysitron TriboIndenter (Figure 2.12) with load resolution of 1 nN and displacement resolution of 0.02 nm.

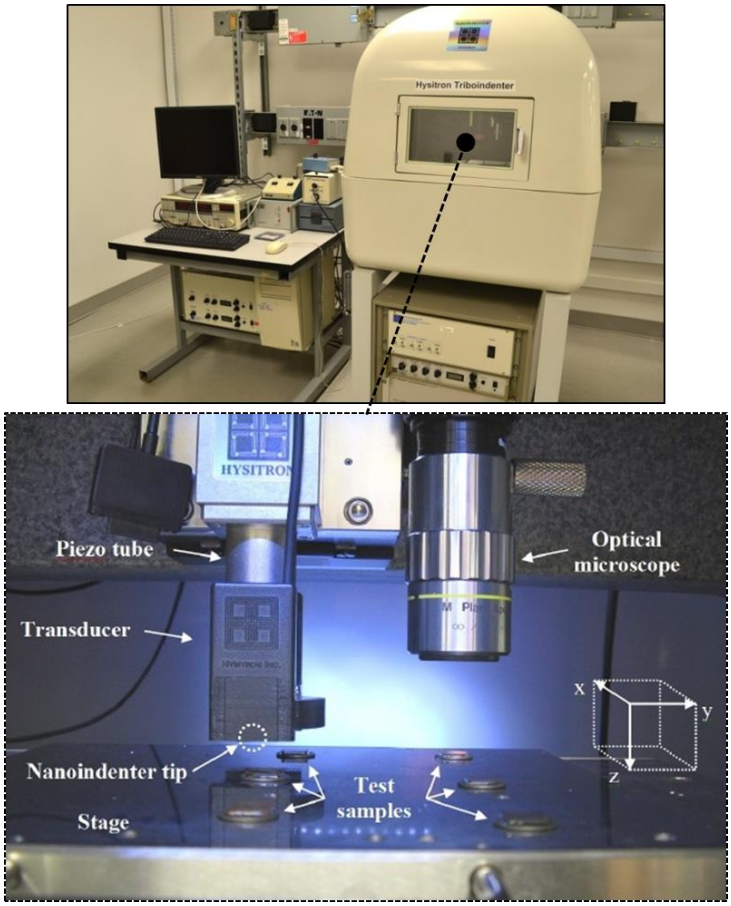

Figure 2.12 - TI 950 Hysitron nanoindentation device used in this study to measure elastic modulus, hardness, and fracture toughness of different crystals

2.8 –Summary

- Various size measurement methods that are used in this study were discussed including sieving, microscope-based image analyzing, laser diffraction, FBRM, and PVM.

- It was shown that a number based measurement technique can be overwhelmed and saturated by the large number of fine particles that are generated via attrition during a milling process. Therefore, to consider the maximum stable particle size, a volume or surface based measurement technique is preferred in size distribution measurement of milling processes.

- Mechanical properties of crystals that are important during breakage were discussed including, Young's/elastic modulus, hardness, and fracture toughness. A nanoindentation technique was introduced to measure these properties at the scale of the crystals.

Chapter 3: Comminution Theories and Mechanistic Models for Particle Breakage

Comminution is a generic term for processes in which solid particles are mechanically broken into smaller particles and fragments (i.e., size reduction, milling, grinding, and crushing). It is used to create particles of certain size distribution and shape to enhance product design, stability, solubility, and so on. Despite widespread application, comminution is one the least energy efficient unit operation processes [12]; only small amount of the energy delivered to the process is used to reduce particle size and create new surfaces. Therefore, the power requirement is one of the major considerations in designing comminution processes. There have been considerable research efforts to explain the actual energy input necessary in size reduction processes. Comminution theories explain the energy consumption as a function of size reduction, but do not consider the physics of the particle breakage and physical properties of the materials. Mechanistic models, on the other hand, use the concepts of solid and fracture mechanics to predict the milling performance.

3.1 –Classical Comminution Theories

Classical theories attempt to model the milling process by empirically relating the energy requirements to size reduction. They have been the topic of extensive research in different fields of engineering; yet, they are empirical laws that do not take into account the physics of the breakage and physical properties of the materials. These so called laws can be generalized as [13]:

$$dE_{sp} = -c\,\frac{dx}{x^n} \qquad (3.1)$$

where E_{sp} is specific (per unit mass or volume) energy consumption, x is particle size, c is a dimensional constant and n is a dimensionless constant.

3.1.1 –Rittinger's Law

Rittinger's model (1867) suggests that the energy consumption is related to the amount of fresh surface produced; therefore $n=2$:

$$dE_{sp} = -c_R \frac{dx}{x^2} \tag{3.2}$$

where c_R is the Rittinger's constant. This equation can be integrated (with boundary condition of $E_{sp} = 0 \; at \; x = x_{initial}$) to give:

$$E_{sp} = c_R \left(\frac{1}{x_{product}} - \frac{1}{x_{initial}} \right) \tag{3.3}$$

In the grinding process, even if the initial size of particles is $x_{initial}$, i.e., monodispersed particles, the products will have a distribution of sizes. It is possible to use certain statistics of the distribution to overcome this problem. Since $E_{sp} \propto 1/x$, a mean diameter can be defined based on -1 moments of the distribution as:

$$\frac{1}{\bar{x}} = \int_0^{x_{max}} \frac{P(x,t)dx}{x} \tag{3.4}$$

where $P(x,t)$ is the cumulative fraction of the size distribution. Furthermore, it is possible to assume that the energy input rate to mill is constant, so that the fresh surface area production is proportional to milling time [13].

3.1.2 –Kick's Law

Kick's model (1885) states that for geometrically similar size reduction, the energy required for comminution is proportional to particle volume and therefore *n=1*:

$$dE_{sp} = -c_K \frac{dx}{x} \tag{3.5}$$

where c_K is the Kick's constant. This equation can be integrated (with boundary condition of $E_{sp} = 0 \; at \; x = x_{initial}$) to give:

$$E_{sp} = c_K \log\left(\frac{x_{product}}{x_{initial}}\right) \tag{3.6}$$

Similar to previous section, in order to consider the distribution of particles with different sizes, it is possible to use a certain statistic of the distribution. Here, a mean particle size, $\bar{x}$, can be defined as:

$$\log\left(\frac{\bar{x}}{x_{initial}}\right) = \int_0^{x_{max}} \log\left(\frac{x}{x_{initial}}\right) P(x,t)dx \tag{3.7}$$

where $P(x,t)$ is the cumulative fraction of the size distribution.

3.1.3 –Bond's Law

Bond (1952) has argued that neither the Rittinger theory, which relates only to surface area, nor the Kick theory, which relates only to particle volume, can adequately describe the grinding results. Size reduction is related to both surface and volume; the amount of impact energy is related to particle volume, but breakage starts with a crack, created by concentration of stresses on the surface.

Bond's third law of grinding suggested to use n=3/2 which falls between the two previous models [15–19].

$$dE_{sp} = -c_B \frac{dx}{x^{\frac{3}{2}}} \tag{3.8}$$

where c_B is the Bond's constant. It integrates to give:

$$E_{sp} = c_B \left(\frac{1}{\sqrt{x_{product}}} - \frac{1}{\sqrt{x_{initial}}} \right) \tag{3.9}$$

The third theory of comminution is further developed by Bond to introduce a work index for different materials and different milling operations. The commonly used form of the equation is:

$$W = 10\, Wi \left(\frac{1}{\sqrt{P}} - \frac{1}{\sqrt{F}} \right) \tag{3.10}$$

where

W = Predicted mill energy consumption in kWh/tone

Wi = Bond's work index in kWh/tone

P = D80 of the product (80% passing size in μm of the product)

F = D80 of the feed (80% passing size in μm of the feed)

This theory is a widely used method in milling processes and has become an accepted approach for designing comminution processes [13,20]. It is important to note that this equation lumps particle mechanical properties as well as the energy delivery capacity of the milling device in one parameter, which is called work index.

3.1.4 –Size Range Applicability of Comminution Laws

Application of Kick's and Rittinger's theories has been met with varied success and is not realistic for designing many industrial size reduction processes. Instead, Bond's model is the most widely used method in milling processes and has become a standard design approach for milling processes [20]. It has been suggested that the three approaches to prediction of energy requirements mentioned above are each applicable to a different range of product size. It is common practice to assume that Kick's proposal is applicable for large particle size (coarse crushing and crushing), Rittinger's for very small particle size (ultra-fine grinding) and the Bond formula being suitable for intermediate particle size (the most common range for many industrial milling processes). This is shown in Figure 3.1, in which specific energy requirement is plotted against particle size on logarithmic scales [21].

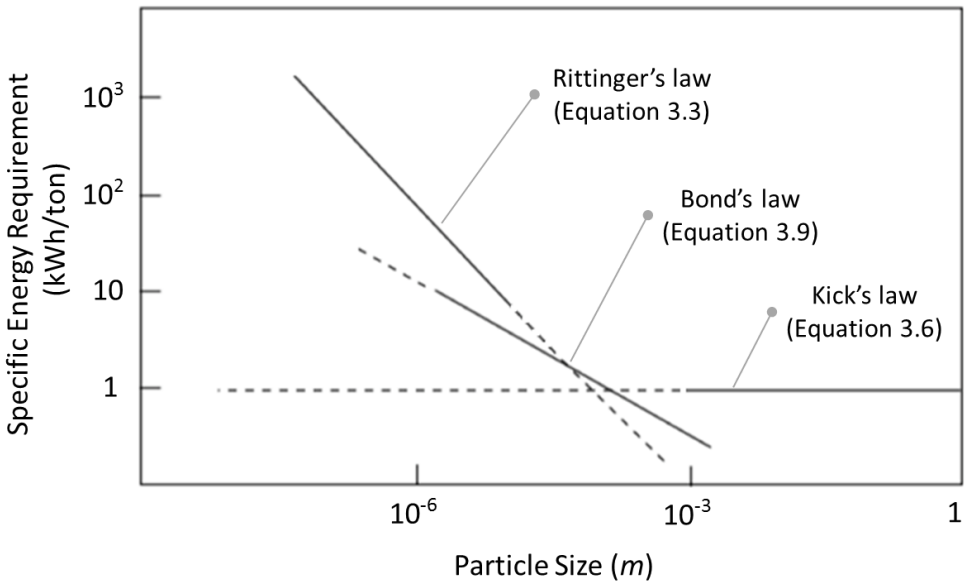

Figure 3.1- Size range applicability of grinding laws in a log-log representation [21]: Kick's theory is applicable for large particle size, Rittinger's for very small particle size, and the Bond's work index is suitable for intermediate particle size

3.2 –Fracture Mechanics

Prior to the research of Griffith (1921), the general assumption was that in order to break a solid material, the atomic bonds of the material had to be overcome. However, Griffith found that the fracture strength from known physical parameters of molecular structure led to values that are orders of magnitude larger than that one experience in laboratory measurements, i.e., the stress needed to fracture glass fibers, depending on their size, is 10 to 100 times smaller than the theoretical stress needed for breaking glass atomic bonds. A theory was needed to reconcile these apparently contradictory results. Griffith proposed that the low fracture resistance observed in experiments, as well as the size-dependence of strength, was due to the presence of microscopic cracks in the bulk material. The presence of cracks changes the stress field in the material causing high stress concentration. Depending on the crack length and crack tip radius, the stress at the crack tip can be orders of magnitude higher than the applied stress as shown in Figure 3.2. This concentration of stresses can exceed the atomic bonding energy, resulting in crack propagation and fracture.

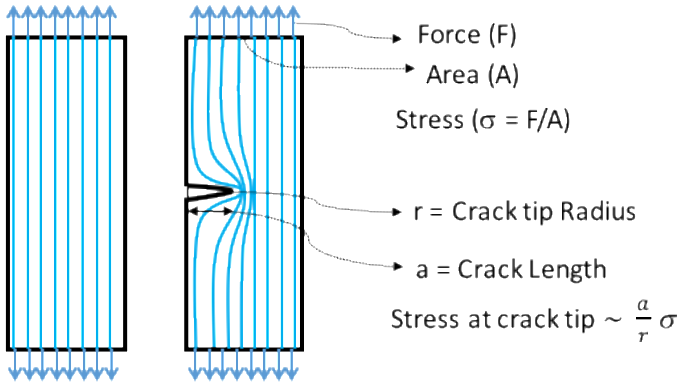

Figure 3.2- Stress concentration near the crack tip of a solid under stress

Based on linear elastic theory, Inglis (1913) developed a mathematical framework for the stress field surrounding an ellipse to prove that the presence of

cracks in a solid under strain could lead to stress concentration at the crack tip. Based on this mathematical approach, Griffith showed that the product of the square root of the flaw length, a_f, and the stress at fracture, σ_f, was nearly constant and that constant can be estimated from a thermodynamic energy approach (with plane stress assumption):

$$\sigma_f \sqrt{\pi\, a_f} = \sqrt{E\, \Gamma} \qquad (3.11)$$

Equation 3.11 relates the stress at fracture to the size of crack. The left side of this equation states that fracture will occur when stress magnitude or/and crack size reaches their critical value. The term $\sigma \sqrt{\pi\, a}$ appears frequently in fracture mechanics and it is usually abbreviated to a single symbol *K*, called the stress intensity factor. The right side depends on material properties only: *E* is the elastic modulus and Γ is the energy required to generate a unit area of crack (surface tension). Therefore, fracture occurs when $K = K_c$ where $K_c \left(= \sqrt{E\, \Gamma}\right)$ is the critical stress intensity factor, more usually called the fracture toughness (Table 3.1).

Table 3.1- Definition of stress intensity factor and critical stress intensity factor

Γ	Energy Required to Generate a Unit Area of Crack	$J\, m^{-2}$
$K_c \ \left(= \sqrt{E\, \Gamma}\right)$	Fracture Toughness or Critical Stress Intensity Factor	$N\, m^{-3/2}$
$K \ (= \sigma \sqrt{\pi\, a})$	Stress Intensity Factor	$N\, m^{-3/2}$

Griffith's analysis introduced fracture toughness into fracture mechanics literature as an important property of the material which quantifies the resistance of the particle against fracture [24]. This property can be used with elastic theory to

quantify brittle breakage. The brittle fracture mode happens when a particle breaks before reaching the yield stress and therefore no plastic deformation is presented. However, most of the particulate solid materials, as well as the crystals used in this study, break in a semi-brittle (elastic-plastic) mode [25–28].

Semi-brittle materials experience a plastic deformation at the crack tip before fracture (stress at the crack tip exceeds the yield strength). In the vicinity of the crack front, a region is formed where weakening and rupture of cohesive bonds occur. This region is enclosed by a zone of plastically deformed material. The deformations in this zone govern the processes of fracture and define the modes of fracture of a body. Thus, studies of plastic deformations around cracks are of fundamental importance for describing the process of fracture [29].

Irwin's (1957) studies extended Griffith's energy theory to accommodate this inelastic yielding that precedes the crack propagation. He showed that the critical stress intensity factor (K_c), that is defined based on elastic theory and experiments on brittle material i.e. glass, can characterize crack stressing for semi-brittle materials as well. For the semi-brittle failure mode, the prevailing stresses reach the yield stress, and hence plastic deformation precedes the crack propagation. The important particle physical properties in this failure mode are the elastic modulus, hardness (H), and fracture toughness (Kc).

Depending on the loading condition, particles can experience a combination of tensile, compression, and shear stresses. The elastic behaviour of a material under these stresses is defined through Young's modulus (is also known as elastic modulus, E), bulk modulus (B), shear modulus (G), and Poisson's ratio (ν). For an isotropic

material, these properties are related to each other and for many materials $B \sim E$, $G \sim \frac{3}{8} E$, and $\nu \sim 0.33$ [7]. Hardness represents the resistance of a material to plastic deformation. The mechanistic basis for characterization of hardness has been developed by Tabor (1996), based on the indentation technique. In Chapter 2, the measurement of elastic modulus, hardness, and fracture toughness of different crystals using a nanoindentation technique is discussed.

It is important to note that, in the other side of brittleness spectrum, ductile materials consume all the receiving energy in the form of plastic deformation. The size reduction in these materials can be achieved in very high strain rates or very low temperatures. Figure 3.3 shows how failure mode can change under different condition [30].

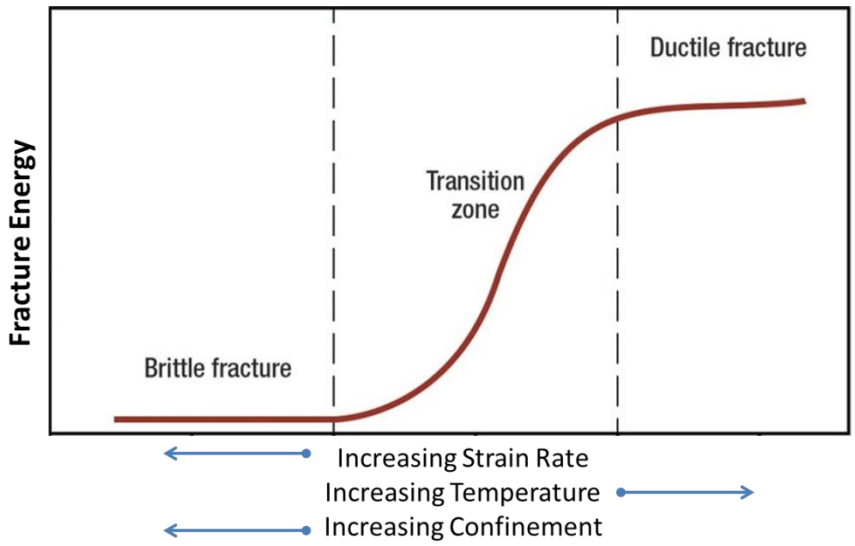

Figure 3.3 -Fracture behavior of materials under different process conditions (confinement is the geometric constraints on the surface of the particle) [7]

3.3 –Mechanistic Breakage and Attrition Theories

Despite the popular energy-size theories for comminution, there are few publications on quantifying the milling behaviour of materials according to their mechanical properties. Lawn and Marshal (1979) used indentation mechanics to study the breakage mechanism. Gahn and Mersmann (1995, 1997, 1999) developed a mechanistic model for attrition loss for crystals undergoing elastic deformation in suspension crystallizers. Attrition occurs at lower stress levels compared to those necessary for comminution, although the mechanism of both processes is similar: the propagation of cracks under impact. Another mechanistic model was developed by Ghadiri and Zhang [26] to relate the attrition of materials undergoing plastic deformation in single particle impact experiments to their physical properties measured from indentation tests. These studies will be explained in next sections under the title of mechanistic models based on indentation, elastic, and plastic mechanisms.

Rumpf (1973) presented a scaling analysis to correlate the energy consumption to particle size. They showed that to obtain a similar fracture pattern the following conditions must meet:

$$\frac{energy\ consumption}{particle\ volume} \times particle\ size = const. \qquad (3.12)$$

$$\frac{crack\ or\ flaw\ size}{particle\ size} = const. \qquad (3.13)$$

They observed that the constant in equation 3.13 depends on particle size and, based on experimental data, they showed that fractured surface area per utilized energy input increases (fracture energy decreases) monotonically with particle size.

This means more energy is required to break smaller particles because the initial flaw pattern is less favourable for fracture propagation.

Vogel and Peukert (2003, 2005) developed a model based on Rumpf's approach to predict the particle impact behaviour in impact mills. They divided the milling process into a machine function and a material function. The machine function describes the type of mill and the operational parameters, and the material function comprises the material properties. They proposed a form of breakage probability based on Weibull statistics as:

$$S = 1 - e^{-f_{Mat}\, k\, x\, (W_{kin} - W_{Mat,min})} \qquad (3.14)$$

In this equation the number of impacts, *k*, and the specific impact energy, $W_{kin,}$ are the machine functions. The material functions are f_{Mat}, a measure for the resistance of the material against fracture, and $W_{Mat,min}$, characterizes the specific energy which a particle can take up without comminution. They obtained these parameters experimentally by single particle impact tests. Meier and Peukert (2009) correlated these empirical parameters to the material properties, i.e. *H* and K_c, based on Rumpf dimensional analysis approach.

3.3.1 –Indentation Mechanism

Based on indentation measurements, Lawn and Marshal (1979) proposed an index of brittleness in terms of hardness and fracture toughness parameters. This index is defined as:

$$Index\ of\ Brittleness = {}^{H}/_{K_c} \qquad (3.15)$$

They measured the minimum crack size and minimum crack load of different materials and concluded that the materials with higher brittleness index are easier to break. It is reported that the brittleness index is successful in ranking the breakage behavior of several different pharmaceutical materials [27]. Taylor et al. (2004) found good correlation between brittleness index and the size reductions of five pharmaceutical materials in a pilot-plant scale Apex hammer mill.

3.3.2 –Elastic Deformation Mechanism

Gahn and Mersmann (1995, 1997, 1999) developed a mechanistic model for attrition lost occurring in suspension crystallizers. They assumed that attrition happens only at the contact of a crystal corner with flat impeller surface. The mechanical properties of the crystals are assumed to be independent of strain rate and are described by average isotropic values. For Poisson's ratio, a constant value of 0.25 is assumed. Furthermore, they assumed that formation and propagation of the cracks occurs instantaneously.

They considered a cone shape particle colliding with impeller surface as shown in Figure 3.4. They assumed that the stresses vary inversely as the square of the distance from the point of application of the impact force as proposed by Michell (1900). By integrating the elastic stress over the volume with elastic deformation, they obtained the average elastic energy per unit volume as:

$$W_{elastic\ per\ unit\ volume} \sim \frac{H^2\, a^4}{G\, l_i^{\,4}} \qquad (3.16)$$

where H is hardness, a is plastic deformation length scale, G is shear modulus, and l_i is elastic deformation length scale.

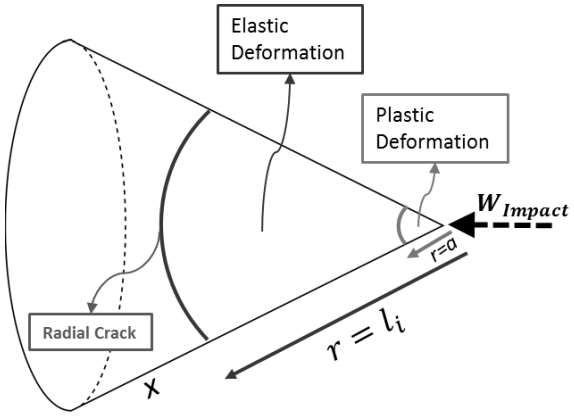

Figure 3.4 - Illustration of cone shape particle under impact energy as shown in Gahn and Mersmann (1997) for derivation of mechanistic model based on elastic mechanism

They assumed that the elastic energy obtained in Equation 3.16 is utilized to break the particle (which equates the elastic deformation length scale and the fracture length scale). Considering the plastic deformation mechanics and definition of the hardness, they obtained an expression to relate plastic deformation length scale, a, to plastic deformation energy, $W_{plastic}$, and hardness, H, as:

$$W_{plastic} \sim H\, a^3 \tag{3.17}$$

Considering the relationship between impact energy, elastic deformation energy, and plastic deformation energy, they reasoned that the elastic energy contributes by less than 15% to the total impact energy and therefore assumed that the plastic energy is approximately equal to impact energy. Based on this assumption, Equation 3.17 becomes:

$$W_{impact} \sim H\, a^3 \tag{3.18}$$

Combining Equations 3.16 and 3.18 gives:

$$W_{elastic\ per\ unit\ volume} \sim \frac{H^{2/3}\ {W_{impact}}^{4/3}}{G\ {l_i}^4} \qquad (3.19)$$

This elastic energy is assumed to be the source for the fracture and a thermodynamic surface energy approach is used to give:

$$W_{elastic\ per\ unit\ volume}\ l_i \sim \Gamma \qquad (3.20)$$

where $w_{elastic\ per\ unit\ volume}$ is the elastic energy stored in a fragment with size l_i, and Γ is the particle surface energy. Combining Equations 3.19 and 3.20 gives:

$$\frac{H^{2/3}\ {W_{impact}}^{4/3}}{G\ {l_i}^3} \sim \Gamma \qquad (3.21)$$

Finally, substituting the fractured fragment volume as $\Delta V = {l_i}^3$ in Equation 3.21, they proposed the following model for fractional loss under impact:

$$\Delta V \sim \frac{H^{2/3}\ {W_{impact}}^{4/3}}{G\ \Gamma} \qquad (3.22)$$

It is important to note that this model employs a surface energy approach to quantify the resistance against the fracture and does not account for stress concentration due to presence of cracks in the material. Consequently, plastic deformation at the crack tip is not considered in this model. In the remaining of this subsection, Equation 3.22 will be further established to give a comparable expression to other models presented in the next sections.

Equation 3.22 can be written in terms of collision or impact velocity, u, by substituting W_{impact} as:

$$W_{impact} = mu^2 \tag{3.23}$$

where m is particle mass. Based on Equation 2.6 and constant Poisson ratio assumption (ν = 0.25), shear modulus, G, can be substituted by elastic modulus, E. Furthermore, using the definition of fracture toughness, $K_c = \sqrt{E\,\Gamma}$, Equation 3.22 becomes:

$$\Delta V \sim \frac{H^{2/3}\, m^{4/3}\, u^{8/3}}{{K_c}^2} \tag{3.24}$$

By dividing the both sides of Equation 3.24 by the parent particle volume ($V = x^3$), and substituting particle mass as $m = \rho_p V$, the final expression can be written as:

$$\frac{\Delta V}{V} \sim \frac{{\rho_p}^{4/3}\, u^{8/3}\, x\, H^{2/3}}{{K_c}^2} \tag{3.25}$$

Where ΔV is fractured volume, V is initial or parent volume, ρ_p is particle density, u is impact velocity, x is particle size, H is hardness, and K_c is critical stress intensity factor (fracture toughness). Several studies used this model to address the attrition behavior of crystals under impact condition similar to those found in stirred tank crystallizers [40–43].

3.3.3 –Plastic Deformation Mechanism

Another mechanistic model was developed by Ghadiri and Zhang [26] to relate the attrition of materials in single particle impact experiments to their physical properties measured from indentation tests. They assume that the fracture time scale is the same as plastic deformation time scale. Furthermore, they assumed that the

breakage of the particle is due to the formation of the subsurface lateral cracks induced by plastic deformation.

Considering a single fragment being detached from a corner of the particle, they assumed an ideal geometry as shown in Figure 3.5. The volume of the fragment lost per impact is:

$$\frac{\Delta V}{V} = \frac{{l_i}^2 a}{x^3} \tag{3.26}$$

where l_i is the lateral crack length and a is the plastic deformation length scale.

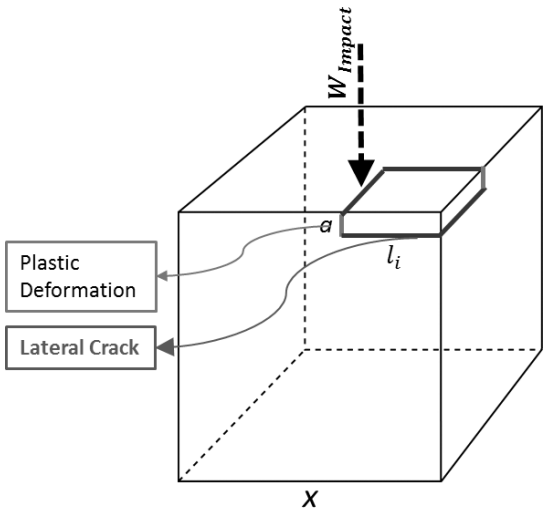

Figure 3.5 - Illustration of cubic shape particle under impact energy as shown in Ghadiri and Zhang (2002) for derivation of mechanistic model based on plastic mechanism

In order to estimate the crack length, l_i, they used the halfpenny crack model in the generic form of $K_c = kP/{l_i}^{3/2}$ [11], where K_c is the fracture toughness, k is a proportionality constant, and P is the applied load that can be calculated from hardness data as $P = Ha^2$. Combining these two equations to eliminate P gives:

$$l_i \sim (\frac{Ha^2}{K_c})^{2/3} \quad (3.27)$$

They assumed that the impact energy is completely dissipated in the form of plastic deformation ($H \sim \rho_p u^2$) and estimated its time scale as:

$$t_p \sim \sqrt{\rho_p / H}\ x \quad (3.28)$$

Based on Newton's law, the relationship between applied load and plastic deformation time scale is:

$$P = m\frac{du}{dt} \sim \rho_p x^3 \frac{u}{t_p} \quad (3.29)$$

Using the definition of the hardness as $H = P/a^2$ the above equation can be written as:

$$H\ a^2 \sim \rho_p x^3 \frac{u}{t_p} \quad (3.30)$$

Combining Equations 3.28 and 3.30 to eliminate t_p gives:

$$a \sim x u^{1/2} (\frac{\rho_p}{H})^{1/4} \quad (3.31)$$

Ultimately, combining Equations 3.26, 3.27, and 3.31, they proposed the following model for fractional loss under impact condition:

$$\frac{\Delta V}{V} \sim \frac{\rho_p\, u^2\, x\, H}{{K_c}^2} \quad (3.32)$$

where ΔV is the fractured volume, V is the initial volume, ρ_p is the particle density, u is the impact velocity, x is the particle size, H is the hardness, and K_c is the critical

stress intensity factor (fracture toughness). As seen in the Gahn and Mersmann model, Equation 3.25, particle breakage is related to the same parameters, but with different dependencies.

Zhang and Ghadiri (2002) showed that this model can predict the single particle impact experiment results accurately up to a certain impact velocity. Several researchers used this model to quantify the attrition in different milling processes (Taylor et al. 2004; Bentham et al. 2004; Yang et al. 2007; Olusanmi et al. 2011).

3.4 –Breakage Model Based on Elastic-Plastic Deformation Mechanism

The aforementioned mechanistic models consider either elastic or plastic deformation. In reality, both mechanisms contribute to particle breakage. Assume a cubic particle collides with a hard surface at its corner with velocity *u* as shown in Figure 3.6. It was considered that the impact surface has a high elastic modulus (hard surface) and therefore all the kinetic energy of the impact is being transferred to the particle. The impact energy dissipates in two ways: elastic deformation and plastic deformation of the particle (Equation 3.33). The plastic deformation length scale is *a*, and the elastic deformation length scale in the fractured volume is l_i.

$$W_{impact} \sim W_{elastic} + W_{plastic} \tag{3.33}$$

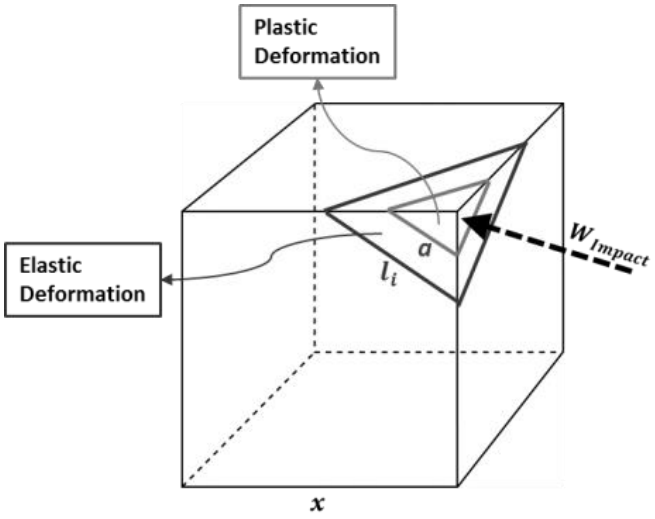

Figure 3.6- Illustration of plastic and elastic deformation of a particle under impact at its corner, *a* is plastic deformation length scale, l_i is elastic deformation length scale in fractured volume, and *x* is initial particle size

The impact energy can be estimated as $W_{impact} \sim mu^2$ (Equation 3.23) where *m* is particle mass, and *u* is impact velocity. Plastic deformation energy can be calculated as [25]:

$$W_{plastic} \sim H\, a^3 \tag{3.34}$$

where *a* is plastic deformation length scale and *H* is hardness. And finally, the elastic deformation energy can be estimated as [32,49]:

$$W_{elastic} \sim \frac{H^2}{E} a^3 \tag{3.35}$$

where *E* is elastic modulus. The Poisson ratio was considered that of an isotropic crystal with ν=0.33 and hence the elastic behaviour of the crystal under different strain conditions can be evaluated using only the elastic modulus (shear modulus and bulk modulus are linearly related to elastic modulus). Combining equations 3.23 and 3.33-35 gives:

$$a^3 \sim \frac{mu^2}{H+\frac{H^2}{E}} \tag{3.36}$$

The key observation here is that the plastic energy is consumed and dissipated to deform the particle permanently with the length scale of *a*, but, elastic energy is propagated through the particle and is the available source of energy for the breakage. By combining equations 3.35 and 3.36, the available elastic energy in the particle under impact can be written as:

$$W_{elastic} \sim \frac{H^2}{E} \frac{mu^2}{H+\frac{H^2}{E}} \tag{3.37}$$

In order for breakage to happen, $W_{elastic}$ needs to be great enough to produce enough stress, σ_f that, based on Griffith's theory, $\sigma_f \sqrt{\pi\, a_f}$ reaches the limit of $K_c \left(= \sqrt{E\, \Gamma}\right)$ as:

$$\sigma_f \sqrt{\pi\, a_f} = K_c \tag{3.38}$$

where σ_f is stress at fracture and a_f is flaw length scale, K_c is stress intensity factor (fracture toughness), E is elastic modulus, and Γ is surface energy. The stress at fracture can be estimated as:

$$\sigma_f \sim \frac{W_{elastic}}{{l_i}^3} \sim \frac{1}{{l_i}^3} \frac{H^2}{E} \frac{mu^2}{H+\frac{H^2}{E}} \tag{3.39}$$

For brittle and semi-brittle particles, the pre-existing cracks and flaws are always presented in the particle. The larger the particle, the larger the flaws and smaller stress needed for crack propagation. Therefore, the flaw length scale can be written as a function of particle size, *x*, as:

$$a_f = f(x) \tag{3.40}$$

The simplest functionality would be a linear functionality. A linear relationship between flaw size and the range of particle size is assumed here as:

$$a_f \propto x \tag{3.41}$$

Substituting σ_f and a_f from Equations 3.39 and 3.41, Equation 3.39 gives:

$$\frac{H^2}{E}\ \frac{mu^2}{H+\frac{H^2}{E}}\ \frac{\sqrt{x}}{{l_i}^3}\ \sim K_c \tag{3.42}$$

Substituting particle mass as $m = \rho_p V$, dividing the both sides of Equation 3.42 by the parent particle volume ($V = x^3$), and substituting the fracture volume as $\Delta V \sim {l_i}^3$, an expression for fracture volume can be obtained as:

$$\frac{\Delta V}{V} \sim \frac{\rho_p\, u^2\ H^2\sqrt{x}}{E\, K_c \left(H+\frac{H^2}{E}\right)} \tag{3.43}$$

Generally $\frac{H^2}{E} < 0.1\ H$ [32] and the final model can be approximated as:

$$\frac{\Delta V}{V} \sim \frac{\rho_p\, u^2\ H\sqrt{x}}{E\, K_c} \tag{3.44}$$

Equation 3.44 relates the fractional loss during the impact to kinetic energy of the impact, square root of the particle size, and mechanical properties of the particle. The plastic, elastic, and fracture behavior of the particle are important in fracture process and they are represented in the model by hardness, elastic modulus, and fracture toughness respectively. It is important to note that the stress concentration due to presence of cracks in the material as well as the plastic deformation at the crack

tip is considered via adopting Griffith fracture theory and employing the concept of fracture toughness in deriving the Equation 3.44.

3.5 –Similarities between Comminution Laws and Mechanistic Models

By some manipulation, it can be shown that the classical theories of comminution can be translated to mechanistic models. This discovery is particularly important in bridging the existing studies on particle fracture and milling in different disciplines and therefore be able to interpret the data from different experiments.

3.5.1 –Lawn and Marshal Approach Compared to Kick's Law

Lawn and Marshal classified the brittleness as the ratio of hardness to critical stress intensity factor. Classifying the brittleness index as H/K_c without taking into account the effect of particle size, is similar to Kick's law. Kick assumes that the energy required for size reduction is proportional to volume ratio of feed and produced particle:

$$E_{sp} \sim \log\left(\frac{product\ volume}{initial\ volume}\right) \qquad (3.45)$$

Based on this model the energy required to reduce size from 100 to 10 is equal to the energy required for size reduction from 10 to 1. In other word, the particle size effect is not seen in Kick's law.

3.5.2 –Ghadiri and Zhang Model Compared to Rittinger's Law

By setting the specific energy as $E_{sp} = u^2$ and rearranging the Ghadiri and Zhang model, equation 3.32, we obtain

$$E_{sp} = u^2 \sim \frac{{K_c}^2 \Delta V}{\rho_p \, H \, x \, V} \tag{3.46}$$

where $\Delta V \sim dx^3$ and $V \sim x^3$. Differentiating the both sides of Equation 3.46 and considering $dx^3 \sim x^2 dx$, we obtain

$$dE_{sp} \sim \frac{{K_c}^2}{\rho_p \, H} \frac{dx}{x^2} \tag{3.47}$$

This matches to Rittinger's law as:

$$dE_{sp} = -c_R \frac{dx}{x^2} \quad , \quad c_R \sim -{K_c}^2 / \rho_p \, H \tag{3.48}$$

It is found that Rittinger's constant can be expressed in terms of mechanical properties of the material.

3.5.3 –Gahn and Mersmann Model Compared to Bond's and Rittinger's Law

Setting the specific energy as $E_{sp} = u^2$ and rearranging the Gahn and Mersmann model, equation 3.25, gives:

$$E_{sp} = u^2 \sim \left(\frac{{K_c}^2 \Delta V}{{\rho_p}^{\frac{4}{3}} H^{\frac{2}{3}} \, x \, V} \right)^{3/4} \tag{3.49}$$

Differentiating the both sides gives:

$$dE_{sp} \sim \frac{{K_c}^{3/2}}{\rho_p \, H^{1/2}} \frac{dx}{x^{7/4}} \tag{3.50}$$

This is analogized to an energy model in between Rittinger's ($n = 2$) and Bond's law ($n = 3/2$) with exponent $n = 7/4$ as:

$$dE_{sp} = -c\,\frac{dx}{x^{\frac{7}{4}}} \quad , \quad c \sim -{K_c}^{3/2}/\rho_p\, H^{1/2} \tag{3.51}$$

3.5.4 –Current Study's Model Compared to Bond's Law

Setting the specific energy as $E_{sp} = u^2$ and rearranging the current study's model, equation 3.44, gives:

$$E_{sp} = u^2 \sim \frac{E\,K_c\,\Delta V}{\rho_p\, H\sqrt{x}\; V} \tag{3.52}$$

Differentiating the both sides gives,

$$dE_{sp} \sim \frac{E\,K_c}{\rho_p\, H}\,\frac{dx}{x^{3/2}} \tag{3.53}$$

This translates to the Bond's law as:

$$dE_{sp} = -c_B\,\frac{dx}{x^{\frac{3}{2}}} \quad , \quad c_B \sim -E\,K_c/\rho_p\, H \tag{3.54}$$

Based on this result, Bond's constant can be expressed in terms of mechanical properties of the material.

3.6 –Mechanistic Models for Wet Milling in Rotor Stator Mixers

The forces acting on the particle in a wet milling process can be divided into two opposing forces: a cohesive force and a disruptive force. The cohesive force is a function of particle size and mechanical properties and acts to oppose the particle fracture. The disruptive force acts on a particle to break it and depends on the type of mill as well as the operating conditions. It is possible to estimate theses opposing

forces based on the aforementioned mechanistic models. This procedure is described in the following sections.

3.6.1 –Disruptive Forces

In the experimental part of this study, Chapter 4, it is concluded that the impact energy imparted to the particles due to particle-particle and particle-wall collisions is primarily important in breakage of particles. Given the highly turbulent flow field Re>10,000 in rotor-stator mixers, both macroscale turbulence and inertial subrange turbulence models were used to determine the collision velocities as summarized in Table 3.2. For particle collisions governed by the macroscale turbulence velocity (macroscale turbulence with length scale ℓ), it is reasonable to consider that the largest disruptive force available for breakage is proportional to rotor tip velocity, u_{tip}. On the other hand, turbulent eddy fluctuations determine the velocity at which particle-particle and particle-wall collisions happen in the turbulent flow. It is reasonable to assume the velocity of a particle with size x is proportional to velocity of the eddy with the same length scale. In the rotor-stator mixers, the Kolmogorov length scale (η ~ 1 - 10 μm) is at least one order of magnitude smaller than the mean particle size. Therefore, the inertial subrange model can be used to calculate the average magnitude of eddy fluctuation velocity ($\sqrt{\overline{u(x)'}^2}$). The Inertial subrange model estimates that the kinetic energy of eddies with size x is equal to energy dissipation rate (ϵ) at size x with the power of 2/3. By substituting $\epsilon \sim N^3D^2$ and $ND \sim u_{tip}$, the expression in the third row of Table 3.2 is obtained. It is important to note that u_{tip} can be used to compare the data in the case of geometrically similar systems, although local energy dissipation rate, which depends on the power draw and

geometry of the mill, is a better measure to compare the data between different mills with different geometries.

Table 3.2- Disruptive stress, $\tau_D \sim \rho_p u^2$ predicted by different models: macroscale turbulence and inertial subrange turbulence models

Model	Macroscale turbulence $x \sim \ell$	Inertial subrange turbulence $\eta < x < \ell$
Collision speed	~ Tip speed	~ Eddy velocity on length scale of x
Disruptive stress	$\rho_p {u_{tip}}^2$ $(u = u_{tip})$	$\rho_P \overline{u(x)'}^2 \sim \rho_P (\epsilon x)^{\frac{2}{3}} \sim \rho_p {u_{tip}}^2 \left(\frac{x}{D}\right)^{\frac{2}{3}}$ (u = $\sqrt{\overline{u(x)'}^2}$)

3.6.2 –Cohesive Forces

The cohesive forces that oppose the particle's breakage can be estimated using the mechanistic models presented above. It is reasonable to assume that the size of fractured volume is proportional to corresponding disruptive and cohesive forces. This can be expressed as:

$$\frac{\Delta V}{V} = \frac{Disruptive\ Stress}{Cohesive\ Stress} \tag{3.56}$$

Rearranging the model based on plastic mechanism, equation 3.32, gives:

$$\frac{\Delta V}{V} \sim \frac{\rho_p\, u^2}{{K_c}^2/Hx} \tag{3.57}$$

By comparing equations 3.56 and 3.57, we can extract the cohesive stress as:

$$\tau_c = \frac{{K_c}^2}{H\,x} \tag{3.58}$$

Similarly, a cohesive stress can be extracted from the elastic mechanism model by rearranging equation 3.25 as:

$$\left(\frac{\Delta V}{V}\right)^{3/4} \sim \frac{\rho_p\, u^2}{{K_c}^{3/2}/H^{1/2}\, x^{3/4}} \tag{3.59}$$

And by comparing to equation 3.56, the cohesive stress can be written as:

$$\tau_c = \frac{{K_c}^{3/2}}{H^{1/2}\, x^{3/4}} \tag{3.60}$$

In the same way, a cohesive stress can be extracted from the elastic-plastic model, equation 3.44, by rearranging it as:

$$\frac{\Delta V}{V} \sim \frac{\rho_p\, u^2}{E\, K_c/H\, x^{1/2}} \tag{3.61}$$

And the cohesive stress can be determined as:

$$\tau_c = \frac{E\, K_c}{H\, x^{1/2}} \tag{3.62}$$

As shown above, each of these different models predicts different relative importance of the material physical properties and particle size in breakage process. Table 3.3 summarizes these different cohesive stresses.

Table 3.3-Cohesive stresses, τ_C, resisting particle breakage predicted by different mechanisms: indentation, elastic, plastic, and elastic-plastic models

Model	Cohesive Stress ($\boldsymbol{\tau_C}$)
Indentation Mechanism*	$c\ \frac{K_c}{H}$
Elastic Mechanism	$\frac{{K_c}^{3/2}}{H^{1/2}\ x^{3/4}}$
Plastic Mechanism	$\frac{{K_c}^{2}}{H\ x}$
Elastic-Plastic Mechanism	$\frac{EK_c}{H\ x^{1/2}}$

*c is a dimensional constant (Pa/$m^{1/2}$)

3.6.3 –Breakage Model

Breakage occurs when the particles are exposed to disruptive stresses that exceed the cohesive stresses. Thus, by comparing the disruptive and cohesive stresses, a criterion can be specified for the occurrence of breakage and predicting the largest particle size that can survive. That is to say, the maximum stable particle size, *x*, exists when the disruptive stress balances the cohesive stress ($\tau_C \sim \tau_D$). As has been noted, 2 different disruptive stresses (Table 3.2) and 4 different cohesive stresses (Table 3.3) are present in the wet milling process, and as a result 2×4=8 different mechanistic models can be predicted Table 3.4 and Table 3.5 summarize the different breakage models based on rotor tip speed and energy dissipation rate respectively.

Table 3.4- Breakage models: mechanistic correlations for maximum stable particle size (x_{max} or $D100$) obtained by a balance between the cohesive and disruptive stresses

Cohesive Stress Model	Disruptive Stress Model	Correlation for Maximum Stable Particle Size
Indentation Mechanism	MT†	$\frac{x}{D} \sim \frac{1}{D}\, e^{-\frac{\rho_P H}{cK_c} {u_{tip}}^2}$
	IST‡	$\frac{x}{D} \sim \left(\frac{cK_c}{\rho_P H}\right)^{3/2} \frac{1}{{u_{tip}}^3}$
Plastic Mechanism	MT	$\frac{x}{D} \sim \frac{{K_c}^2}{\rho_P HD} \frac{1}{{u_{tip}}^2}$
	IST	$\frac{x}{D} \sim \left(\frac{{K_c}^2}{\rho_P HD}\right)^{3/5} \frac{1}{{u_{tip}}^{6/5}}$
Elastic Mechanism	MT	$\frac{x}{D} \sim \left(\frac{{K_c}^{\frac{3}{2}}}{\rho_P H^{\frac{1}{2}} D^{\frac{3}{4}}}\right)^{4/3} \frac{1}{{u_{tip}}^{8/3}}$
	IST	$\frac{x}{D} \sim \left(\frac{{K_c}^{\frac{3}{2}}}{\rho_P H^{\frac{1}{2}} D^{\frac{3}{4}}}\right)^{12/17} \frac{1}{{u_{tip}}^{24/17}}$
Elastic-Plastic Mechanism	MT	$\frac{x}{D} \sim \left(\frac{EK_c}{\rho_P HD^{\frac{1}{2}}}\right)^2 \frac{1}{{u_{tip}}^4}$
	IST	$\frac{x}{D} \sim \left(\frac{EK_c}{\rho_P HD^{\frac{1}{2}}}\right)^{6/7} \frac{1}{{u_{tip}}^{12/7}}$

†MT = Macroscale Turbulence ‡IST = Inertial Subrange Turbulence

Table 3.5- Breakage models based on energy dissipation rate (disruptive stresses are calculated based on inertial subrange turbulence)

Cohesive Stress Model	Disruptive Stress Model	Correlation for Maximum Stable Particle Size
Indentation mechanism	Inertial Subrange Turbulence	$x \sim (\frac{cK_c}{\rho_P H})^{3/2} \frac{1}{\varepsilon}$
Plastic mechanism	Inertial Subrange Turbulence	$x \sim (\frac{{K_c}^2}{\rho_P H})^{3/5} \frac{1}{\varepsilon^{2/5}}$
Plastic mechanism	Inertial Subrange Turbulence	$x \sim (\frac{{K_c}^{\frac{3}{2}}}{\rho_P H^{\frac{1}{2}}})^{12/17} \frac{1}{\varepsilon^{8/17}}$
Elastic-plastic mechanism	Inertial Subrange Turbulence	$x \sim (\frac{EK_c}{\rho_P H})^{6/7} \frac{1}{\varepsilon^{4/7}}$

Here *D* is the rotor diameter; *x* is the maximum stable particle size (*D100*) that can survive under the disruptive force that is dictated by the milling operational conditions, i.e. rotor tip speed, $u_{tip} \sim ND$ (N is rotor speed and D is rotor diameter). In practice, *D95*, *D90*, or *D80* of the size distribution are used instead of largest particle size, because of statistical considerations and the high scatter in *D100* measurements. In this study, D90 is considered as the representative of the largest particle size and it is shown that D95 and D80 are linearly correlated to D90.

Again, each of these different models predicts different relative importance of the material physical properties and energy input to the breakage process. The validity of these models needs to be assessed by comparison to experimental data. In Chapter 4, the detailed description of the experiment's setup and procedure are given and the

experimental data for wet milling of different materials in different rotor-stator mixers are presented.

3.7 –Dimensionless Number for Particle Breakage in Geometrically Similar Systems

Analogous to the Weber number in drop breakup, a new dimensionless number for solid fracture was developed. It is the ratio of inertial force to cohesive force of solid particles, and it is called the Comminution number (Co):

$$Co = \frac{Inertial\ force}{Solid\ cohesive\ force} \tag{3.63}$$

In section 3.6, the solid cohesive stresses are obtained using different mechanistic models. Using these different models, different Comminution numbers can be defined. Table 3.6 summarizes the Comminution numbers and corresponding breakage models. The use of Comminution number will allow the important task of scale up/down in milling processes as well as data reduction of similar problems.

Table 3.6- Comminution number for geometrically similar systems: definition and application in different mechanistic models

Model	Co Number	Correlation for Maximum Stable Particle Size based on Co Number
Indentation Mechanism	$Co_I = \frac{\rho_P \, {u_{tip}}^2}{\frac{\alpha \, K_c}{H}}$	$\frac{x}{D} \sim (Co_I)^{-3/2}$
Elastic Mechanism	$Co_E = \frac{\rho_P \, {u_{tip}}^2}{\frac{{K_c}^{\frac{3}{2}}}{H^{\frac{1}{2}} \, \mathrm{D}^{\frac{3}{4}}}}$	$\frac{x}{D} \sim (Co_E)^{-12/17}$
Plastic Mechanism	$Co_P = \frac{\rho_P \, {u_{tip}}^2}{\frac{{K_c}^2}{\mathrm{H} \, D}}$	$\frac{x}{D} \sim (Co_P)^{-3/5}$
Elastic-Plastic Mechanism	$Co_{EP} = \frac{\rho_P \, {u_{tip}}^2}{\frac{E \, K_c}{H \mathrm{D}^{\frac{1}{2}}}}$	$\frac{x}{D} \sim (Co_{EP})^{-6/7}$

The proposed mechanistic models and equations in this chapter were assessed in Chapter 5 using the experimental data. As described in Chapter 4, these data were obtained in wet milling of different crystal-anti-solvent systems in both the Silverson L4R inline and batch mixers. The inline mixer was further modified to study the effect of the shear gap width on milling performance. The detailed summary of the experiment results and procedure is given in Chapter 4.

3.8 –Summary

- A class of mechanistic models for breakage and attrition of crystals and particulate solids have been developed based on elastic-plastic deformation and fracture mechanics concepts. These mechanistic models were further analyzed to give four

different forms of cohesive forces resisting the particle breakage under different deformation stresses based on elastic deformation, plastic deformation, and elastic-plastic deformation mechanisms. Furthermore, two different scales of velocities were identified for collision intensity based on macroscale turbulence and inertial subrange turbulence theories. Based on these 2 different disruptive stresses and 4 different cohesive stresses, $2\times4=8$ different mechanistic correlations for maximum stable particle size were introduced.

- The proposed mechanistic models show that the breakage of a particle is a function of its mechanical properties, size, and the impact energy. Most of the impact energy usually consumed to plastically deform the particle and only small portion propagate as elastic energy.

- The functional form of these models was shown to agree with classical comminution theories where the size reduction is empirically related to power consumption.

- Based on the mechanistic models, a dimensionless comminution number is developed (ratio of disruptive to cohesive forces) to aid physical interpretation and scale up/down efforts for geometrically similar devices

- In this study, the characteristic velocity of rotor-stator mixers, $u_{tip} = ND$, is used to describe the particle collision velocity and to construct the mechanistic models of milling. However, these mechanistic models can be utilized in other milling devices by substituting the appropriate characteristic velocity, e.g., jet velocity in

impinging jets, superficial velocity in valve homogenizers, and impact velocity of milling balls in ball mills.

Chapter 4: Wet Milling Experiments in Rotor Stator Mixers

4.1 –Introduction

Wet milling involving high shear rotor-stator mixers to reduce crystal size is an emerging practice with significant potential in crystallization and milling of active pharmaceutical ingredients (API). It has certain advantages such as smaller footprint, higher yield, lower cost, and better control of heat generation and crystal morphology when compared to dry milling. Despite the increasing industrial interest, there are few works to address wet milling of API or other solid particles in high shear mixers.

Lee et al. (2004) conducted wet milling experiments in a lab scale rotor-stator inline mixer with different crystal-antisolvent systems. The effect of concentration of slurry (14 to 20% by weight), morphology of crystals, rotor speed, and flow rate were studied on milling performance. They reported that the wet milling performance is relatively independent of slurry concentration and flow rate when operating the mixer in a free pumping mode. They stated that the shear frequency, defined as the product of rotation rate, number of slots on rotor, and number of slots on stator, can be used to scale up rotor –stator wet mills from lab to pilot scale manufacturing. Kamahara et al. (2007) studied a semi-batch crystallizer using a rotor-stator device to generate fine particles as a source of secondary crystallization and they concluded that a constant rotor tip speed is a criterion for scale up. Harter et al. (2013) conducted an experimental study to evaluate the effect of flow rate, slurry solids concentration, and starting particle size distribution in wet milling performance and terminal particle size. They concluded that by maintaining constant tip speed comparable terminal particle size could be achieved. In addition, they developed an empirical model to

incorporate the critical geometric parameters by considering the frequency and the probability of a slot event to account for geometrical differences of the mill heads across the scales. Engstrum et al. (2013) studied particle size reduction in two different lab scales and one pilot scale rotor-stator mixers. They assumed that the dominant mechanism of size reduction is rotor-particle collisions and influence of particle-particle collisions and fluid shear forces have a comparatively negligible effect. They introduced a scaling approach to correlate API particle size reduction to energy input normalized for rotor-stator mixers by accounting for mill geometry, tip speed, and mill head residence time. Luciani et al. (2015) presented a modelling-aided approach to scale-up high-shear rotor−stator wet milling processes for pharmaceutical applications. A population balance equation was used to provide insight into the significance of different scale-up factors. They concluded that the specific breakage rate in population balance equations can be correlated to shear rate, particle-wall collisions, and frequency of rotor-stator events.

Given the relatively small amount of the current research on wet milling of crystalline materials in rotor-stator mixers, there is clearly a need for more investigation to address the effect of different milling variables, particle mechanical properties, and mixer geometry/scale on wet milling performance. Apart from limited amount of literature, the major shortcoming of the existing research summarized above is that they do not consider the effects of particle size and physical properties on milling performance. Consequently, the proposed correlations and scale up strategies are not mechanistic and remain case dependent.

Other than wet milling of crystalline materials, incorporation of nanoparticles in the liquid phase, deagglomeration of nanoparticle clusters and stabilization are also

carried out in rotor-stator mixers. Despite the similarities in particle attrition and erosion mechanisms, the cohesive forces resisting the deagglomeration of nanoparticle clusters are different than those resisting the particle fracture. Therefore, a different approach is required to study the deagglomeration processes.

Baldyga et al. (2008) utilized a two-stage rotor-stator inline mixer to study break up of fumed silica clusters. They reasoned that erosion is the dominant breakup mechanism and concluded that the breakup occurs when the hydrodynamic stresses in turbulent flow, based on Kolmogorov theory, are larger than the bonding forces forming the agglomerates. Padron et al. (2008) studied the effect of rotor speed, flow rate, particle properties, and rheology of dispersions on the breakup of hydrophobic and hydrophilic fumed silica nanoparticle clusters in an inline rotor-stator mixer. They showed that the breakup occurs through erosion and smaller aggregates are gradually eroded from large clusters over a period. They concluded that rotor speed has a stronger effect on cluster breakup when compared to flowrate effect. Furthermore, they concluded that at higher concentrations the rate of fine generation of hydrophobic particles are higher and it can be due to difference in hydrogen bond and rheology of dispersions.

In this chapter, the results of wet milling experiments performed in the Silverson L4R rotor-stator inline mixer with the standard and enlarged shear gap, and in the batch mixer are presented. These experiments are conducted to investigate the effect of milling conditions, mixer geometry, and particle physical properties on ultimate particle size and particle breakage rate.

4.2 –Rotor-Stator Mixer Geometry

In mixing processes, there is generally a trade-off between the required power input and the resultant particle size distribution. The maximum particle size obtained at equilibrium is a function of maximum local energy dissipation rate rather than the average energy dissipation rate in the mixing head. The advantage of rotor-stator mixers is their capacity to concentrate most of the supplied power in the mixing head creating a high local energy dissipation region which enhance the mixing performance [57–59]. Furthermore, an in-line rotor–stator mixer can be used in a continuous process by placing the mixing head in a recirculation loop of a stirred vessel.

Silverson rotor-stator L4R inline and batch mixers were used in this study. They have a 250 W, 110 Volt, single phase, 60 Hz motor with nominal maximum speed of 9000 rpm. The rotor is a radial 4-blade impeller that rotates inside a stator with square holes as shown in Figure 4.1. The rotor moves the slurry radially out of the mixer head through the 4 rows of holes in the stator. The mixing capacity of the batch unit depends on the slurry viscosity. In the inline assembly, the centrifugal action of the rotor generates a pumping action which gives a throughput up to 12 litres/minute (lpm), reducing as the viscosity increases. A valve, in the pipeline on the outlet side of the mixer, is used to control the throughput independent of the rotor speed.

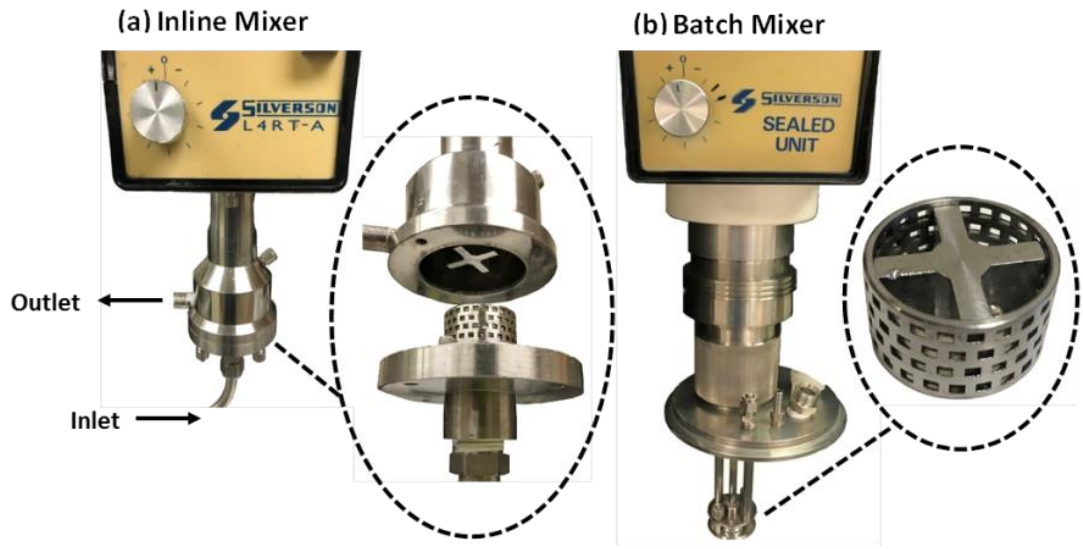

Figure 4.1- Silverson L4R Rotor Stator Mixers with Square Hole Stator (a) Inline mixer, (b) Batch mixer

Most of the experiments were carried out in the inline mixer with the standard shear gap of 0.2 mm (clearance between rotor and stator). Since the initial crystal size is greater than the shear gap width, the rotor was modified to have a larger shear gap of 1.7 mm, and to study the effect of shear gap width on milling performance. The milling experiments were also performed in the batch mixer to investigate the effect of scale/geometry on particle breakage in terms of power draw and the volume of the dispersion zone. The lab scale Silverson L4R batch mixer has a smaller mixing head compared with the lab scale Silverson L4R inline mixer. Geometry details for the different mixers are listed in Table 4.1.

Table 4.1- Silverson L4R inline and batch mixer geometry details

Mixer Dimensions	Inline Mixer		Batch Mixer
	Standard Shear Gap	Enlarged Shear Gap	Standard Shear Gap
Rotor Diameter	31.1 mm	28.2 mm	28.1 mm
Shear Gap Width	0.2 mm	1.7 mm	0.2 mm
Square Hole Stator	104 Square Hole Slots		92 Square Hole Slots
Size of Stator Slots	2.4 mm×2.4 mm×2.0 mm		2.6 mm×2.4 mm×1.6 mm
Thickness of Stator Ring	2.0 mm		2.0 mm
Height of Stator Ring	18.9 mm		18.9 mm
Inner Diameter of Stator Ring	31.5 mm		28.5 mm

4.3 –Experiment Setup

4.3.1 –Inline Mixer Setup

Rotor-stator mixer is fed through a recirculation loop in line with a stirred vessel as shown in Figure 4.2. The experimental rig consists of a 3 litres glass vessel to hold the solid suspension. The holding vessel is fitted with a down pumping pitched blade turbine ($D = 0.5T$, blades inclined at 45°, $C = T/4$) rotated at 900 rpm (using Waverly OS20 overhead stirrer) to ensure complete solids dispersion [60,61]. Four baffles were mounted close to the wall of the vessel to promote better top to bottom mixing. The uniform dispersion state was verified by sampling different

vertical locations within the holding vessel in situ using the FBRM probe and offline by the laser diffraction method.

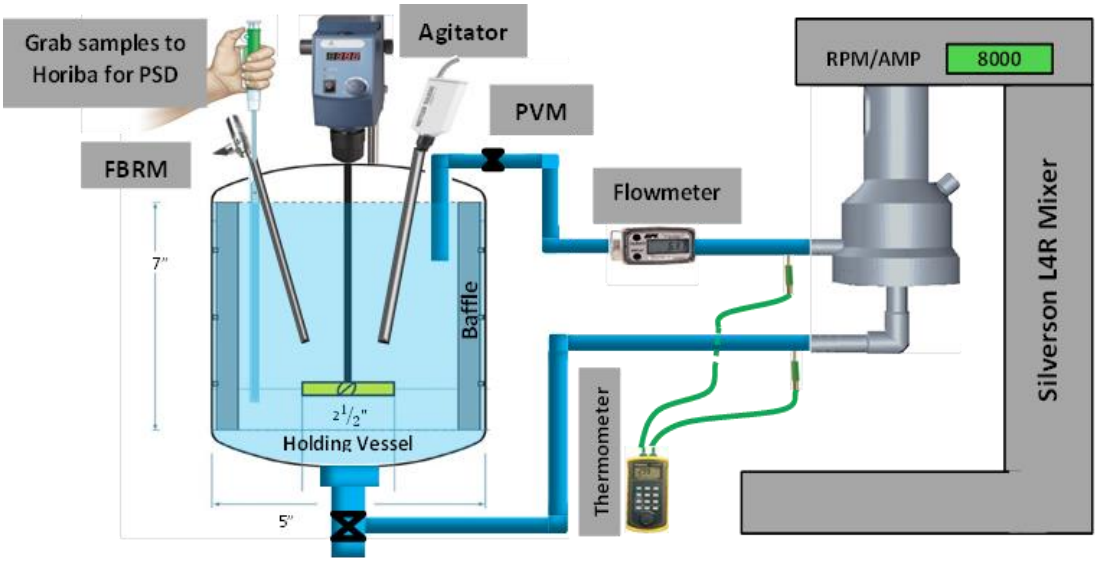

Figure 4.2- Experimental setup of Silverson inline rotor-stator mixer feed through a recirculation loop in line with a stirred vessel

The slurry from the holding vessel was pumped via a 1/2 inch PTFE tube to an inline L4R Silverson high shear rotor–stator mixer. The mixer head used in this work was a one-stage rotor-stator design with the square-hole stator and the four-blade rotor. The rotor is driven by a motor controlled by a frequency inverter and may be run to a maximum rotor speed of 10,000 rpm with 100 rpm intervals. The holding vessel was charged with 2 litres of antisolvent (isopropyl alcohol) and left for half an hour to reach thermal equilibrium at a given rotor speed. The slurry was maintained at room temperature by running water as a cooling fluid over the mixer head. The temperature change was monitored by a differential thermometer before and after the mixer head to ensure zero net heat generation. A diaphragm valve was installed in the outlet (recycle) tube to control the flow rate. The time zero is taken when the crystals were added to the holding vessel. Experiments were carried out over a range of independently controlled flow rates and rotor speeds.

The samples removed from the holding vessel at different times during the milling, were analysed offline by Horiba LA-950 laser diffraction and video microscopy techniques. Furthermore, particle chord length and shape were continuously monitored in the holding vessel by two particle size analysis probes, a FBRM and a PVM probe. They were positioned at an angle to the horizontal (as suggested by the manufacturer) at a height just above the axial centre of the impeller for the best performance. In addition, the FBRM measurement confirmed that the crystals were uniformly suspended in the holding vessel.

4.3.2 –Batch Mixer Setup

A schematic of the batch mixer setup is shown in Figure 4.3. A 2 litres glass vessel was charged with antisolvent (isopropyl alcohol). It was then attached to the mixer, and left for half an hour to reach thermal equilibrium at a given rotor speed. The time zero is taken when the crystals were added to the mixing vessel. The slurry temperature was measured and maintained at room temperature by using a cooling unit, HAAKE Phoenix II C35P, with a model predictive control strategy. The samples removed from the holding vessel at different times during the milling, were analysed offline with the Horiba LA-950 laser diffraction and video microscopy techniques. Furthermore, particle chord length was monitored online in the batch vessel with the FBRM probe. The milling is continued up to 90 minutes, at which point no further change in size distribution is observed.

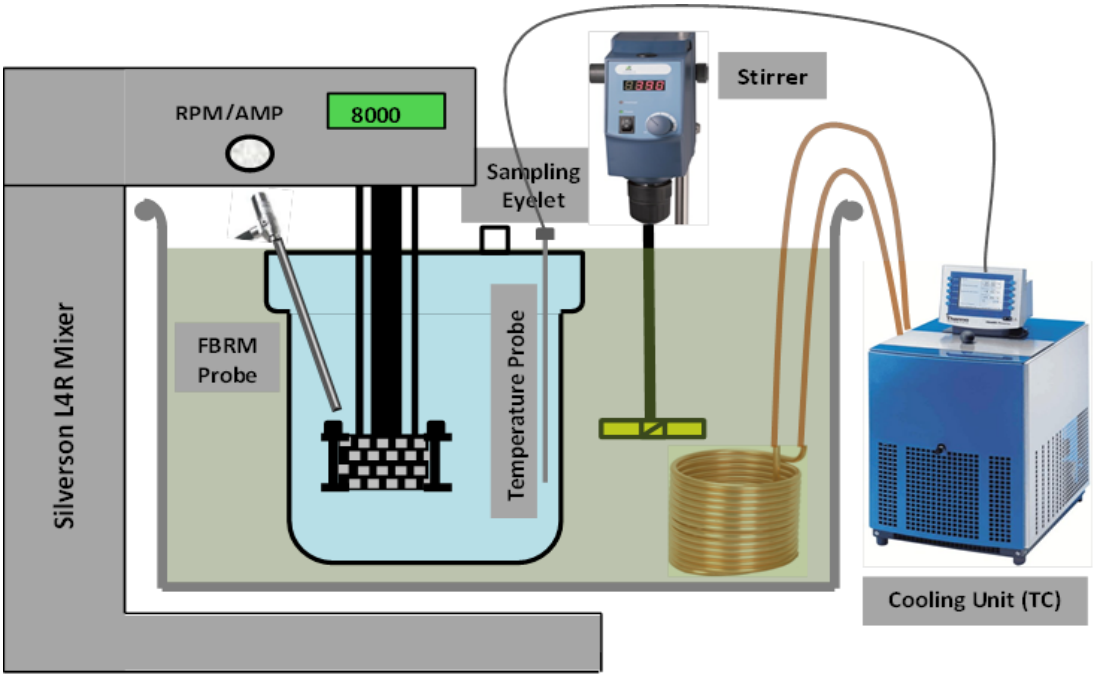

Figure 4.3- Experimental setup of Silverson batch mixer in a glass vessel immersed in a cooling bath

4.4 –Particle Size Measurement Procedure

In order to perform different experiments with a consistent initial particle size distribution, the crystals were sieved using a vibratory sieve shaker. A fraction of 250-420 μm was collected and used as the feed for the wet milling experiments. Different techniques were used to measure the size distribution and shape of the particles during the milling. An FBRM probe, a Mettler-Toledo Lasentec D600 particle size analyser, was used in situ for inline measurement of size as well as evaluation of complete solid suspension in the holding vessel of inline setup. In addition, a PVM probe is used in situ for online monitoring of particle shape. Also from Metller-Toledo, it records digital images with a field of view of 826 micron by 619 microns.

A laser diffraction device is used off line to measure the particle size distribution of samples taken from the holding vessel at different times of the milling. Horiba Partica LA-950 provides a volume based particle size distribution in range of

0.01 micron to 3 mm. The 10 mL sample removed from holding vessel was added to 30 mL antisolvent (1:4 dilution). A fraction of the diluted slurry sample was transferred to the laser diffraction measurement cuvette. A magnetic stirrer bar is used to stir the slurry and keep the particles dispersed in the cuvette. Dispersion of particles larger than 400 microns in the measurement cuvette was challenging and a larger stirrer bar is used with a higher stirring rate to obtain a uniform suspension of crystals in the test sample. No sonication was applied to prevent undesired particle breakage [4].

4.5 –Mechanical Properties Measurement Procedure

Indentation tests were performed using a TI 950 Hysitron TriboIndenter to obtain the mechanical properties for 3 different crystals, sucrose, glycine, and ascorbic acid that are used in wet milling experiments. These crystals are primarily selected for milling experiments because they have different elastic modulus, hardness, and fracture toughness but similar morphology as shown in the microscopy images in Figure 4.4. Crystals with size range of 500-700 μm are selected for the indentation test. For each material, 10 different crystals are tested. Different mechanical properties, elastic modulus, hardness, and fracture toughness are obtained based on the indentation data and corresponding equations given in Chapter 2.

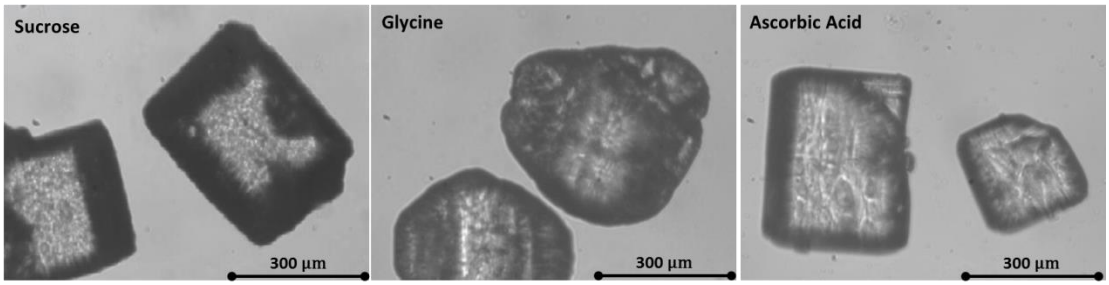

Figure 4.4 - Microscope images of sucrose, glycine, and ascorbic acid before milling

The mechanical properties as well as the brittleness indices (defined in chapter 3) are provided in Table 4.2. The brittleness indices are not very different because these crystals have similar crystalline structure. Nevertheless, different brittleness indices are obtained for different materials, e.g., sucrose has a higher brittleness index compared to glycine, and therefore we expect more brittle behaviour from sucrose.

Table 4.2- Mechanical Properties of Crystals and Brittleness Indices

	Young's Modulus	**Hardness**	**Fracture Toughness**	**Brittleness Index**
	E (GPa)	H (MPa)	K_c (MPa $m^{½}$)	H/K_c (10^{-3} $m^{-½}$)
Sucrose	21.1	1105	0.097	11.3
Glycine	28.6	887	0.089	9.9
Ascorbic Acid	32.2	1059	0.069	12.2

It is important to mention that the indentation data for ascorbic acid have large scatter (up to 35% of mean value) due to anisotropic nature of ascorbic acid crystals, i.e., the hardness and fracture toughness are different for the same sample measured in different orientations.

4.6 –Experiment Procedure

Crystals with 10% by weight, dispersed in 2 litres IPA, were fed to the Silverson mixer at a series of flow rates 2.1, 3, and 4.2 L/min in the inline setup and rotor speeds 5000, 6500, and 8000 rpm in both the inline and batch setups. The samples were taken from the sampling point in the glass vessels at predefined time intervals to investigate particle size reduction. Extra milling time was provided to

ensure that all particles experienced the regions with maximum local energy dissipation rate multiple times and the pseudo steady state [62] is achieved.

Here tank turnover is used as the time scale of the process. The tank turnover is the number of times the slurry in the holding vessel is passed through the mixer at a certain time and can be calculated as:

$$Number\ of\ tank\ turnover = \frac{t}{V/_{Q_v}} \tag{4.1}$$

Where t is the milling time, V is the volume of the slurry in holding vessel, and Q_v is the flow rate. The time scale can also be expressed as the mill head passes. The mill head passes can be calculated using the same equation by substituting V as the volume of the slurry in mill head. Since volume of the slurry in holding vessel (2000 ml) is 25.3 times larger than mill head (79 ml), 1 tank turnover is equal to 25.3 mill head passes.

4.7 –Size Distribution Considerations

The particle size used to compare the data from different milling conditions is D90, based on cumulative volume percentage. D90s, obtained from wet milling of sucrose-IPA system in the Silverson inline mixer with the standard shear gap at different rotor speeds and flowrates, are plotted against other relevant sizes to determine the relationship between D90 and other measures of particle size. As shown in Figure 4.5 and Figure 4.6, D95 and D80 are linearly correlated to D90 whereas D50, D10, D_{43}, D_{32}, and D_{10} do not show a linear relationship. These correlations are shown for sucrose-IPA system but assumed to apply more generally. It is important to

note that the values of maximum stable particle size, D100, were not used directly because of the statistical considerations and the high scatter in D100 measurement.

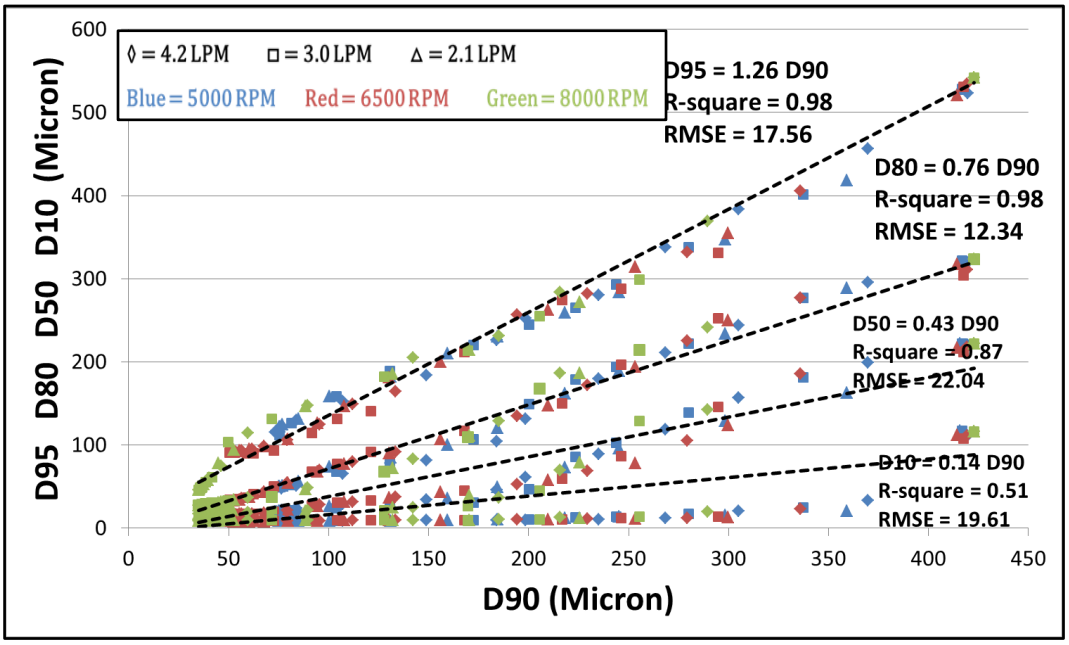

Figure 4.5- Relationship between D90 and other cumulative particle sizes – data are from wet milling of sucrose/IPA in the Silverson L4R inline mixer with the standard shear gap at different rotor speeds and flow rates

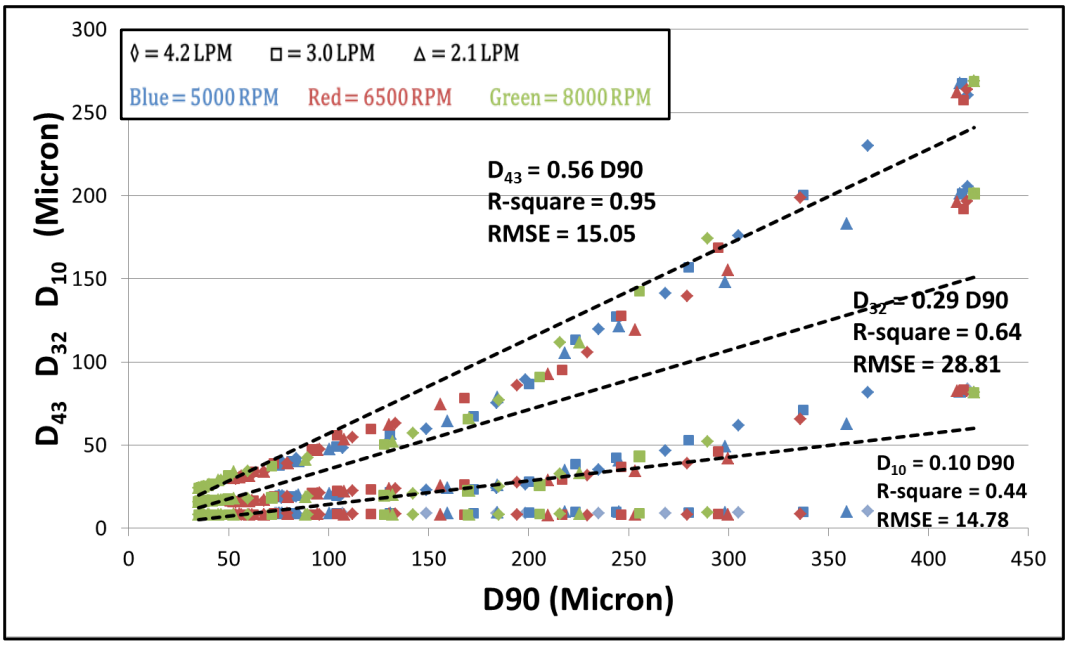

Figure 4.6 - Relationship between D90 and mean particle sizes – data are from wet milling of sucrose/IPA in the Silverson L4R inline mixer with the standard shear gap at different rotor speeds and flow rates

4.8 –Experiment Results

4.8.1 –Silverson L4R inline mixer with standard shear gap

Wet milling experiments were conducted in the Silverson inline mixer with the standard shear gap to investigate the effect of rotor speed, throughput, particle physical properties, slurry concentration (particle-particle collisions), and particle-wall collisions on particle size reduction as summarized in Table 4.3.

Table 4.3 - The matrix of different experiments performed in the Silverson L4R inline mixer with the standard shear gap

	5000 rpm	6000 rpm	6500 rpm	8000 rpm
2.1 lpm	○ △ □	○	○	○
3.0 lpm	○	○	○ △ □ ⊘ ◍ ◍ ◍	○ △ □
4.2 lpm	○ △ □	○ △ □	○ △ □	○ △ □

○ sucrose-IPA
△ glycine-IPA
□ ascorbic acid-IPA
◍ 20% weight
○ 10% weight
⊘ 5% weight
◍ 2% weight
◍ particle-wall collision

Figure 4.7 to Figure 4.12 show the change in the particle size distribution from the initial distribution (obtained by sieving) to the final distribution for wet milling of sucrose-IPA system at 8000 rpm and 3.0 lpm measured with the laser diffraction method. It is important to note that the initial and the final distributions are unimodal; however, the intermediate distributions are bimodal. This is the characteristic of the wet milling processes in rotor-stator mixers where transition from initial to final distribution occurs through the bimodal or polymodal distributions. The PVM images

of the sucrose crystals at different milling times were taken in situ as shown in Figure 4.13 to Figure 4.18. As the number of small particles increases during the milling, the laser input scatters significantly and does not reflect back to the sensor. As a result, the contrast and resolution of the PVM images decreases as the sensor becomes increasingly saturated. Despite this shortcoming, the images can be used to qualitatively monitor the particle size and shape changes during the milling. The scanning electron microscopy images of sucrose before and after milling are shown in Figure 4.19 for comparison with PVM images.

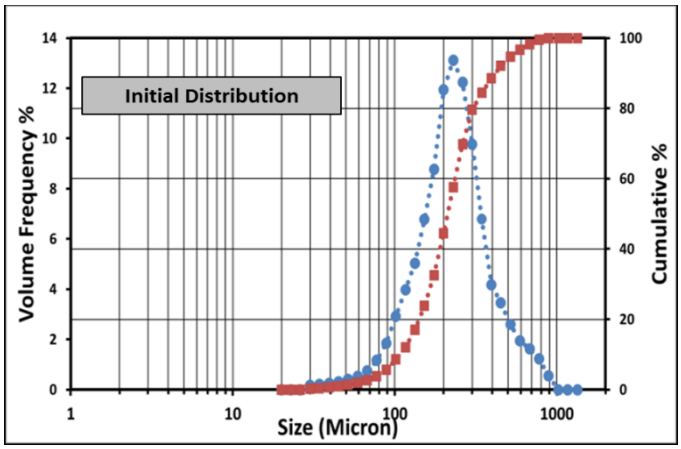

Figure 4.7 - Initial size distribution (obtained by sieving), measured with the laser diffraction method - wet milling of sucrose in IPA at 8000 rpm and 3.0 lpm – Silverson L4R inline mixer with standard shear gap

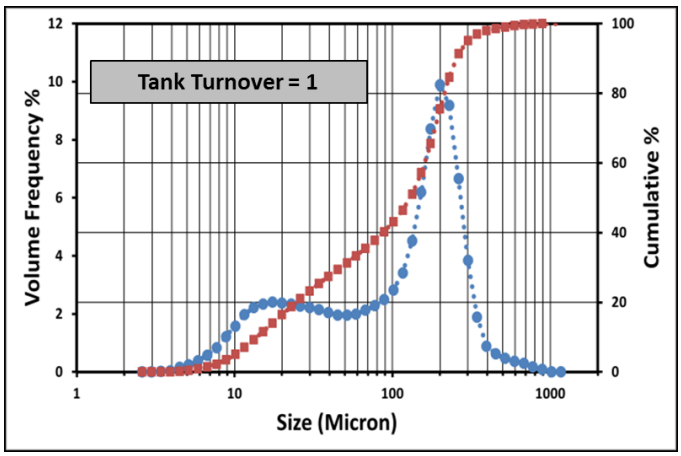

Figure 4.8 – Particle size distribution, measured with the laser diffraction method, resulted from wet milling of sucrose in IPA at 8000 rpm and 3.0 lpm after 1 tank turnover – Silverson L4R inline mixer with standard shear gap

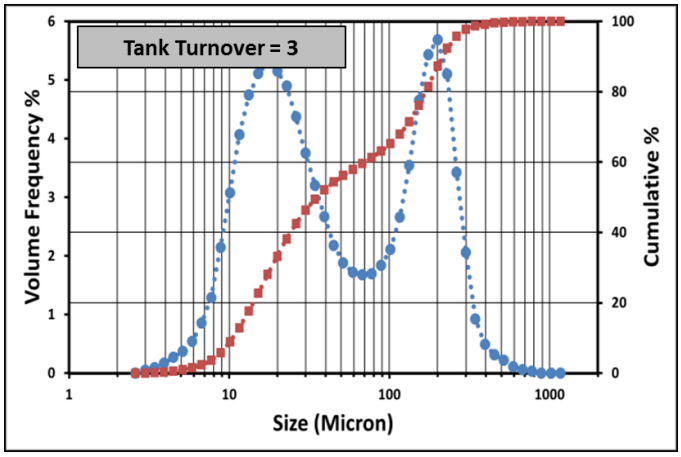

Figure 4.9 - Particle size distribution, measured with the laser diffraction method, resulted from wet milling of sucrose in IPA at 8000 rpm and 3.0 lpm after 3 tank turnovers – Silverson L4R inline mixer with standard shear gap

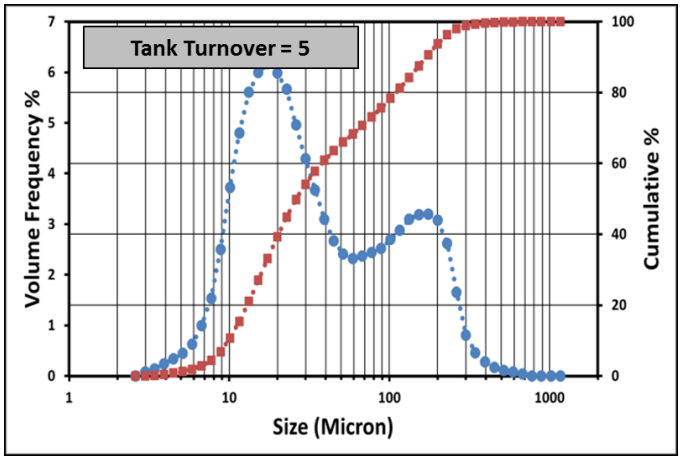

Figure 4.10 - Particle size distribution, measured with the laser diffraction method, resulted from wet milling of sucrose in IPA at 8000 rpm and 3.0 lpm after 5 tank turnovers – Silverson L4R inline mixer with standard shear gap

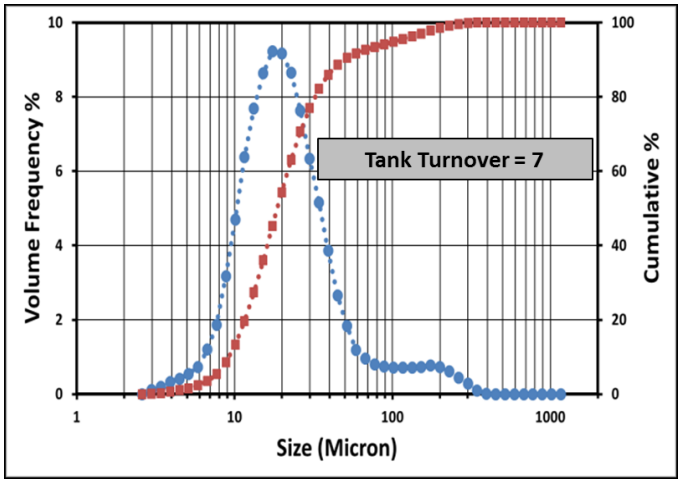

Figure 4.11 - Particle size distribution, measured with the laser diffraction method, resulted from wet milling of sucrose in IPA at 8000 rpm and 3.0 lpm after 7 tank turnovers – Silverson L4R inline mixer with standard shear gap

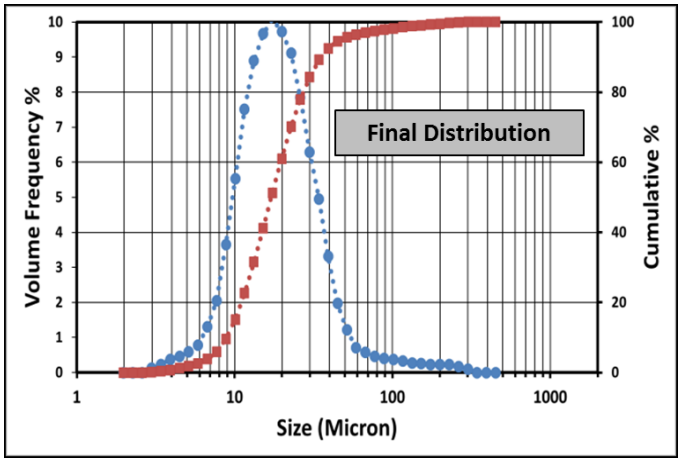

Figure 4.12 - Final size distribution, measured with the laser diffraction method, resulted from wet milling of sucrose in IPA at 8000 rpm and 3.0 lpm – Silverson L4R inline mixer with standard shear gap

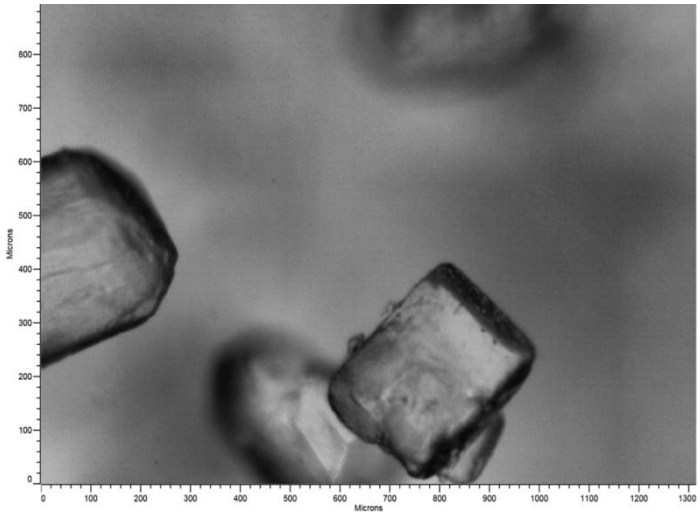

Figure 4.13 - Online PVM images of sucrose in IPA at initial size distribution - wet milling at 8000rpm and 3.0 lpm - Silverson L4R inline mixer with standard shear gap

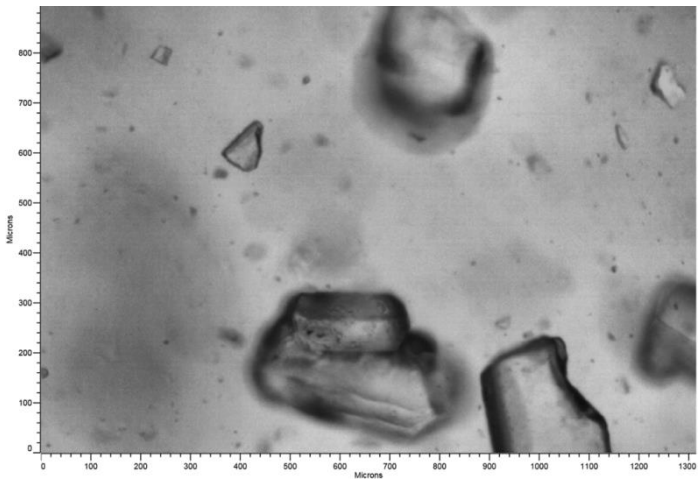

Figure 4.14 - Online PVM images of sucrose in IPA after 1 tank turnover - wet milling at 8000rpm and 3.0 lpm - Silverson L4R inline mixer with standard shear gap

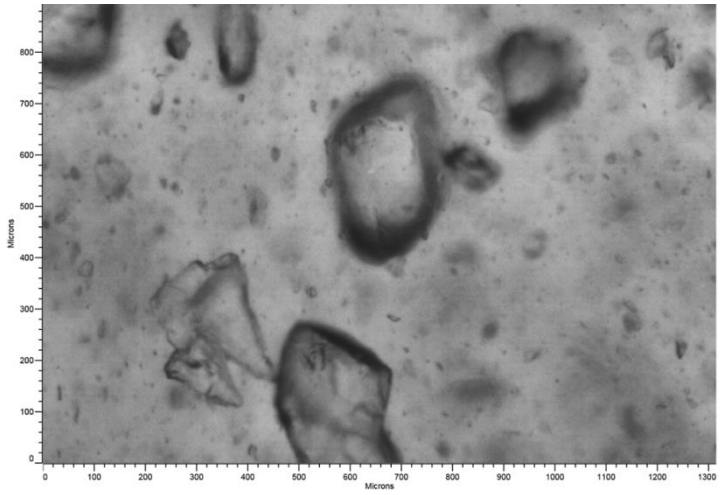

Figure 4.15 - Online PVM images of sucrose in IPA after 3 tank turnovers - wet milling at 8000rpm and 3.0 lpm - Silverson L4R inline mixer with standard shear gap

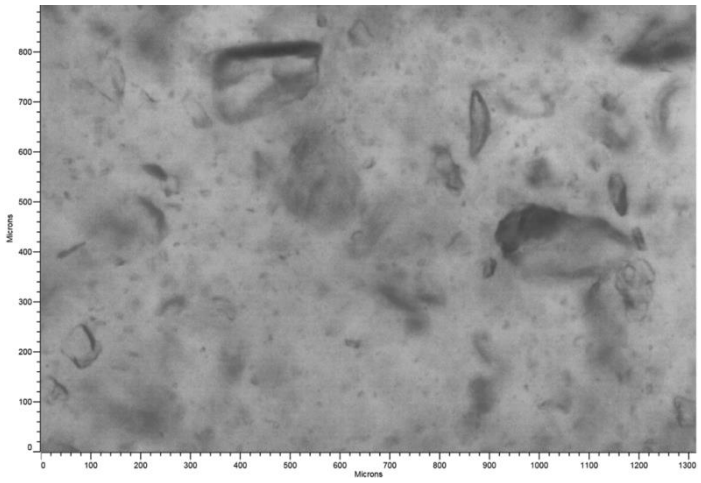

Figure 4.16 - Online PVM images of sucrose in IPA after 5 tank turnovers - wet milling at 8000rpm and 3.0 lpm - Silverson L4R inline mixer with standard shear gap

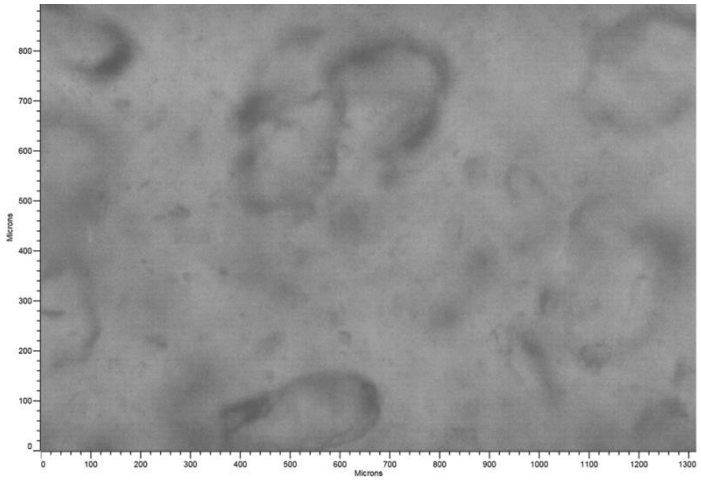

Figure 4.17 - Online PVM images of sucrose in IPA after 11 tank turnovers - wet milling at 8000rpm and 3.0 lpm - Silverson L4R inline mixer with standard shear gap

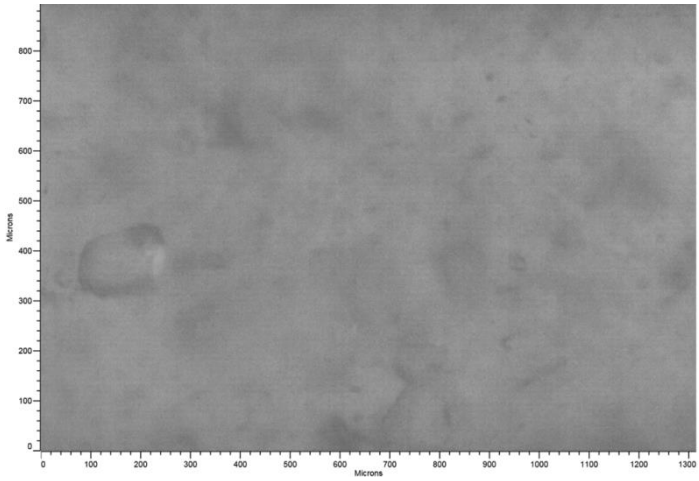

Figure 4.18 - Online PVM images of sucrose in IPA after 15 tank turnovers - wet milling at 8000rpm and 3.0 lpm - Silverson L4R inline mixer with standard shear gap

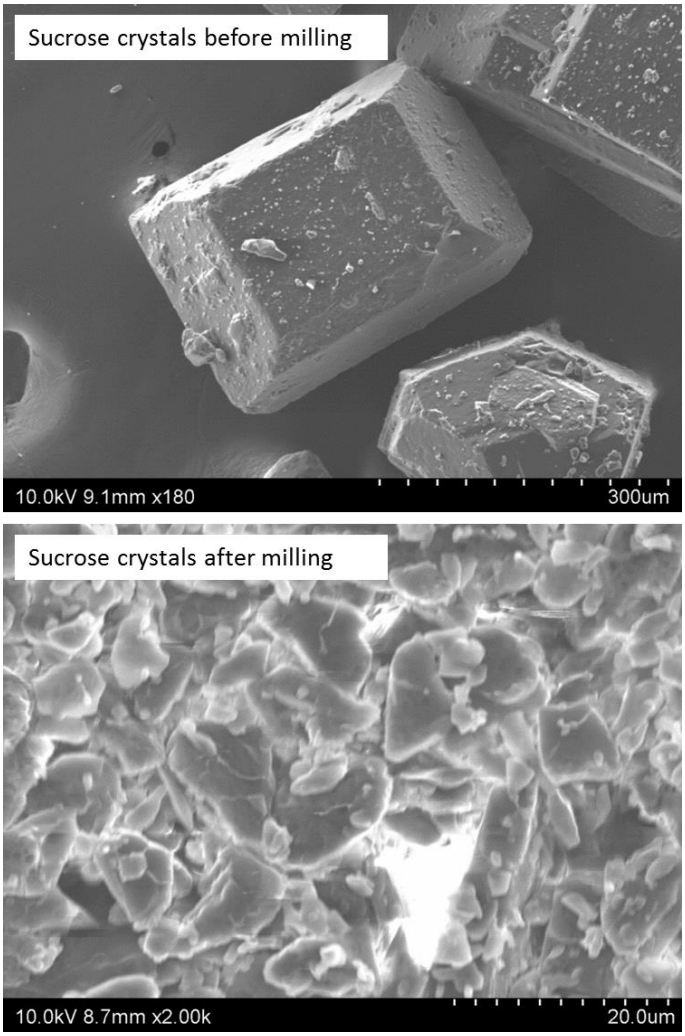

Figure 4.19- SEM images of sucrose before and after milling at 8000 rpm and 3.0 lpm – Silverson L4R inline mixer with standard shear gap

4.8.1.1 –Rotor speed effect on particle size reduction in the Silverson L4R inline mixer with the standard shear gap

Sucrose wet milling experiments were conducted to find the effect of rotor speed on particle size reduction at constant flow rate. All the variables held constant except for rotor speed; enough time is allowed to establish the equilibrium. As shown in Figure 4.20 and Figure 4.21, the rotor speed has a strong effect on the rate of size reduction as well as the ultimate equilibrium size. Furthermore, a sharp breakage rate at the beginning followed by slow changes is observed in the particle breakage data. The sharp breakage slope is due to fracture mode which refers to the breakage of a particle into fragments of comparable size. The slow breakage part is due to an attrition mechanism by which small fragments are chipped off from larger particles.

This can be explained based on fracture mechanics: larger particles have lower cohesive stress (Table 3.3) and are easier to break but once they are broken down to a critical particle size, further breakage cannot occur for a given rotor speed. Furthermore, the shear gap geometry can be important since milling starts with particle sizes larger than shear gap and ends with particles smaller than shear gap. The wet milling experiment results for other measures of the size distribution as well as different rotor speed conditions for sucrose-IPA system are given in Appendix A.

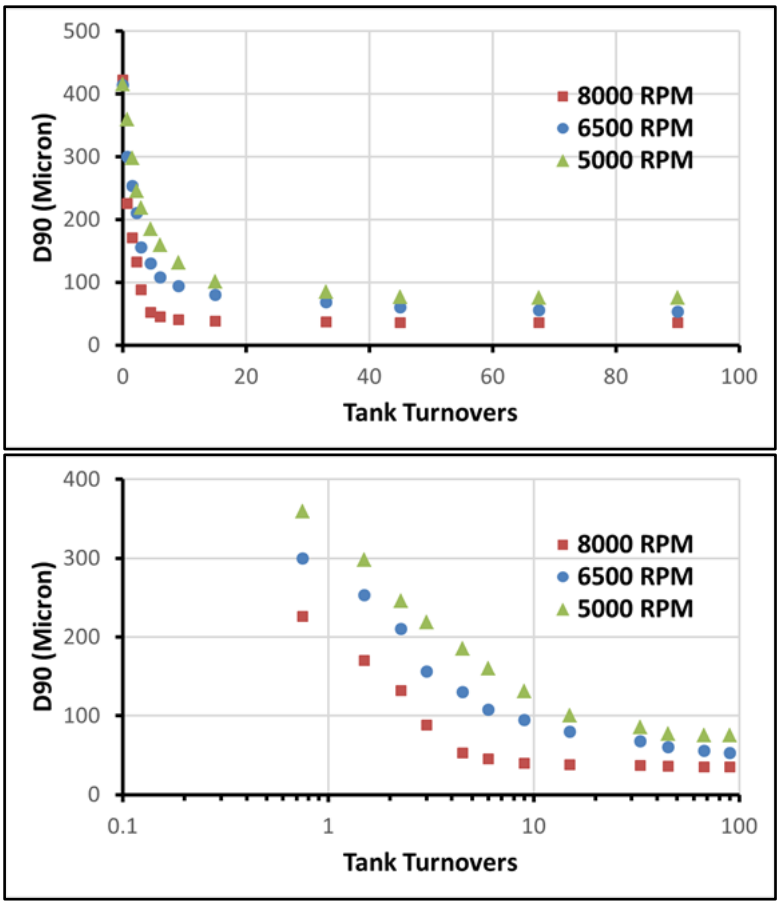

Figure 4.20 - Rotor speed effect on sucrose breakage (laser diffraction measurements) – The flow rate is fixed at 2.1 lpm – lower graph is log-normal representation of the data in upper graph – Silverson L4R inline mixer with standard shear gap

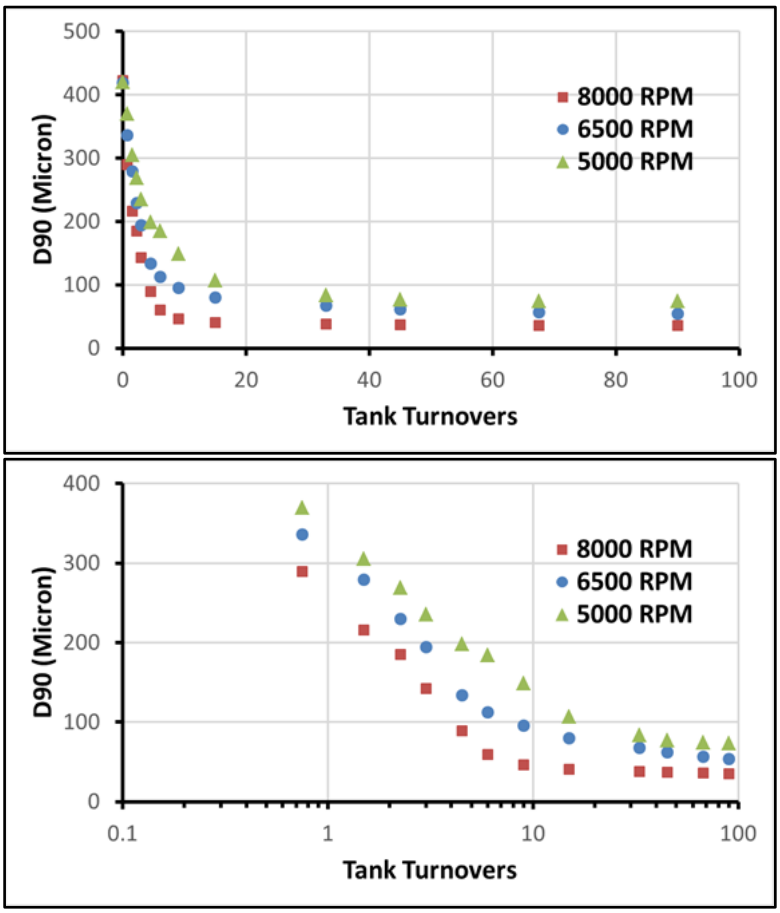

Figure 4.21 - Rotor speed effect on sucrose breakage (laser diffraction measurements) – The flow rate is fixed at 4.2 lpm – lower graph is log-normal representation of the data in upper graph – Silverson L4R inline mixer with standard shear gap

4.8.1.2 –Flowrate effect on particle size reduction in the Silverson L4R inline mixer with the standard shear gap

The number of "high shear events" depends on the residence time distribution of the particles in the mill. The lower residence time means fewer impacts and therefore less breakage. Figure 4.22 and Figure 4.23 present the particle size as a function of flow rate at constant rotor speeds of 5000 and 8000 rpm respectively. The final attainable particle size is not different for different flowrates; however, the rate of approach to the final equilibrium size is faster with lower flow rates. This is because the mill head residence time per tank turnover for the lower flow rates is higher.

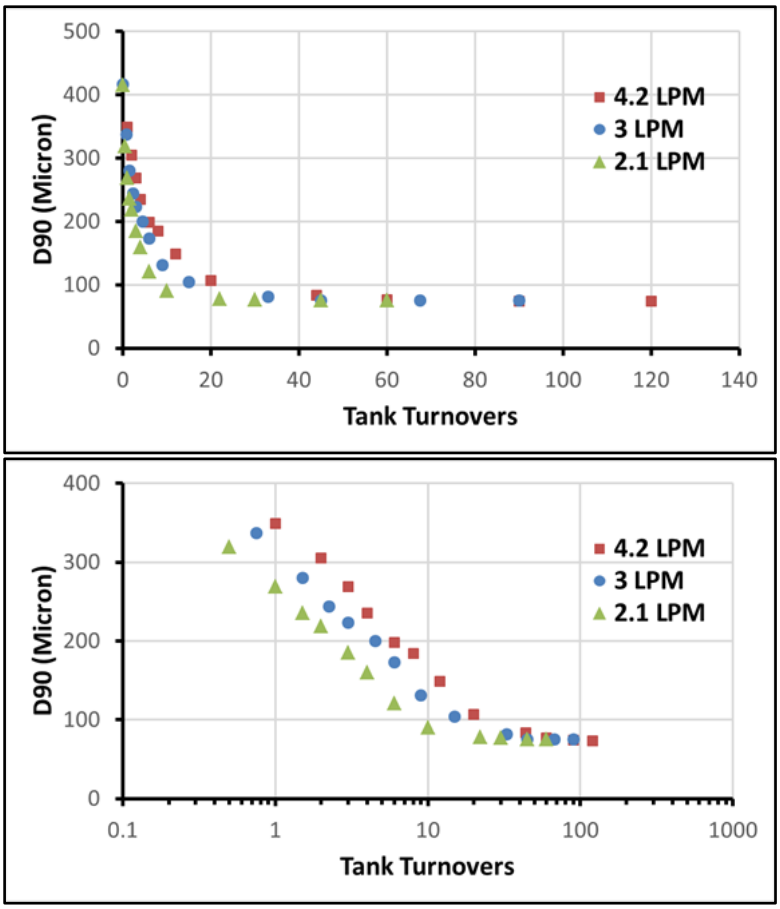

Figure 4.22 - Flow rate effect on particle breakage (laser diffraction measurements) - The rotor speed is fixed at 5000 rpm – lower graph is log-normal representation of the data in upper graph - Silverson L4R inline mixer with standard shear gap

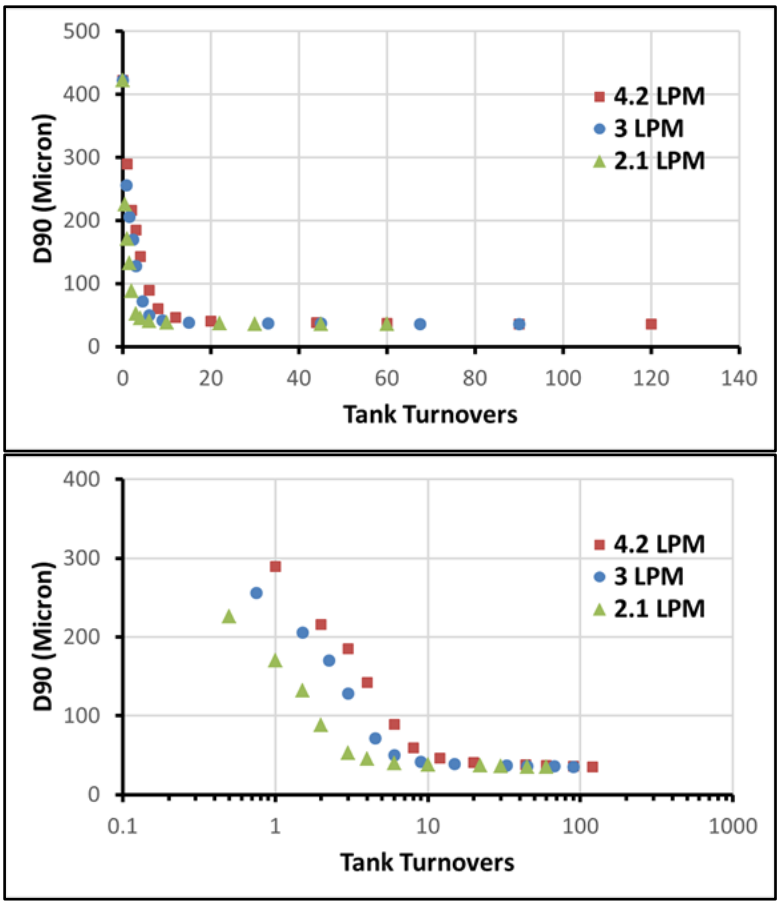

Figure 4.23 - Flow rate effect on particle breakage (laser diffraction measurements) - The rotor speed is fixed at 8000 rpm – lower graph is log-normal representation of the data in upper graph - Silverson L4R inline mixer with standard shear gap

The effect of rotor speed and flowrate on breakage rate is also exploited in situ in the holding vessel by the FBRM and the PVM probes. However, the difficulty is that the measurements are in terms of the chord length and not the size; one gets a distribution of chord length even for mono-sized spherical particles. Since FBRM is a number based measurement technique, Sauter mean diameter (D32) of the chord length distribution is used here to compare the milling performances.

The digital images that are recorded using a PVM probe can be analysed and a relative backscatter index (RBI) can be defined for each image. As it is discussed in Chapter 2, RBI is the ratio of image brightness to intensity of light output. It is a function of particle size, particle shape, and concentration. A higher RBI is associated

to a larger particle size; an increase in number concentration of particles, as a result of reduction in particle size, decreases the RBI values.

In spite of different measurement mechanisms, both FBRM and PVM show the right trend for wet milling of sucrose as shown in Figure 4.24 and Figure 4.25 respectively; by increasing rotor speed and decreasing flow rate the milling performance improves. However, the measurement of the ultimate particle sizes is not precise. As the number of small particles increases during the milling, the contrast and resolution of the measurement decreases and eventually the sensor becomes saturated. This saturation causes a false detection of the time required to reach the equilibrium. For example, the PVM probe shows that the wet milling at 8000 rpm and 2.1 lpm reaches the final size distribution after 4 tank turnovers whereas the data obtained with the laser diffraction method shows the equilibrium condition after 10 tank turnovers. In Figure 4.24 and Figure 4.25, the initial D32 for FBRM data is 180 ± 12 μm and initial RBI for PVM data is 4.2 ± 0.3. Several chord length distributions measured with the FBRM probe during wet milling of sucrose-IPA system are provided in Appendix D.

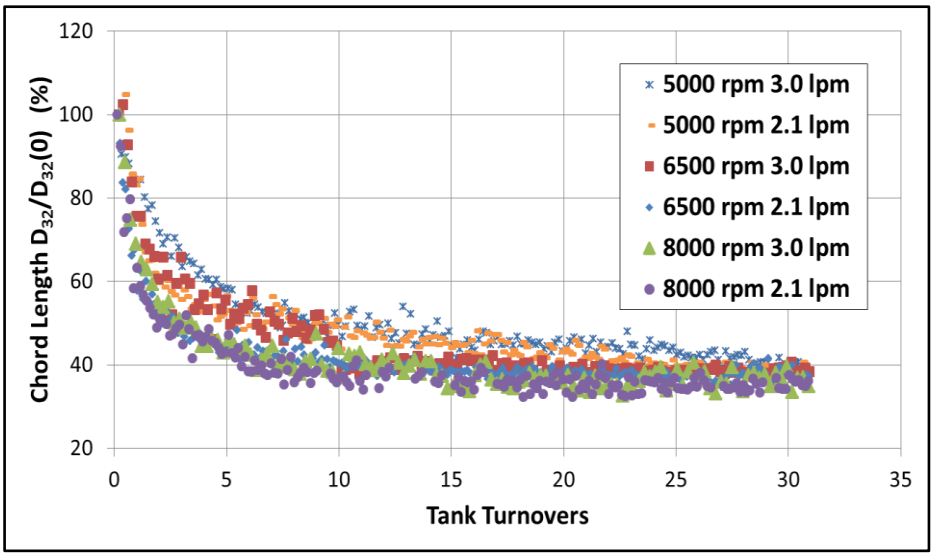

Figure 4.24 - Rotor speed and flow rate effect on wet milling of sucrose in IPA; chord length measurement by FBRM - Silverson L4R inline mixer with standard shear gap

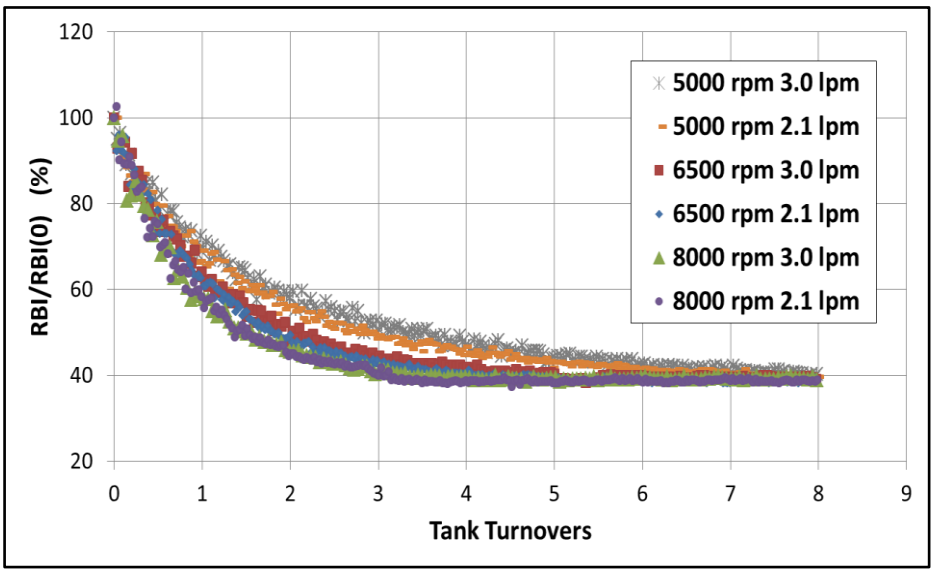

Figure 4.25 - Rotor speed and flow rate effect on wet milling of sucrose in IPA; RBI measurement by PVM - Silverson L4R inline mixer with standard shear gap

4.8.1.3 –The effect of particle physical properties on particle size reduction in the Silverson L4R inline mixer with the standard shear gap

Three crystals, glycine, sucrose, and ascorbic acid were milled to investigate the effect of mechanical properties on the milling behavior. The refractive indices for sucrose, glycine, and ascorbic acid are 1.51, 1.46, and 1.71 respectively. The laser diffraction device corrects the readings based on refractive indices. The rotor speed and the flow rate held constant; enough time is allowed to establish the equilibrium.

Figure 4.26 and Figure 4.27 show the extent of influence of physical properties on size reduction of these three materials (additional wet milling data for glycine-IPA and ascorbic acid-IPA systems are in Appendix B and C). Each figure shows different rotor speed and flow rate scenarios. The brittleness index defined by Lawn and Marshal's model predicts a larger brittleness index for sucrose compared with glycine. This means that the sucrose crystals are more susceptible to breakage compared with glycine. This observation is in agreement with the experiment results in which the sucrose shows a higher rate of breakage and the ultimate size (D90) of sucrose crystals is smaller than the glycine at the end of milling process.

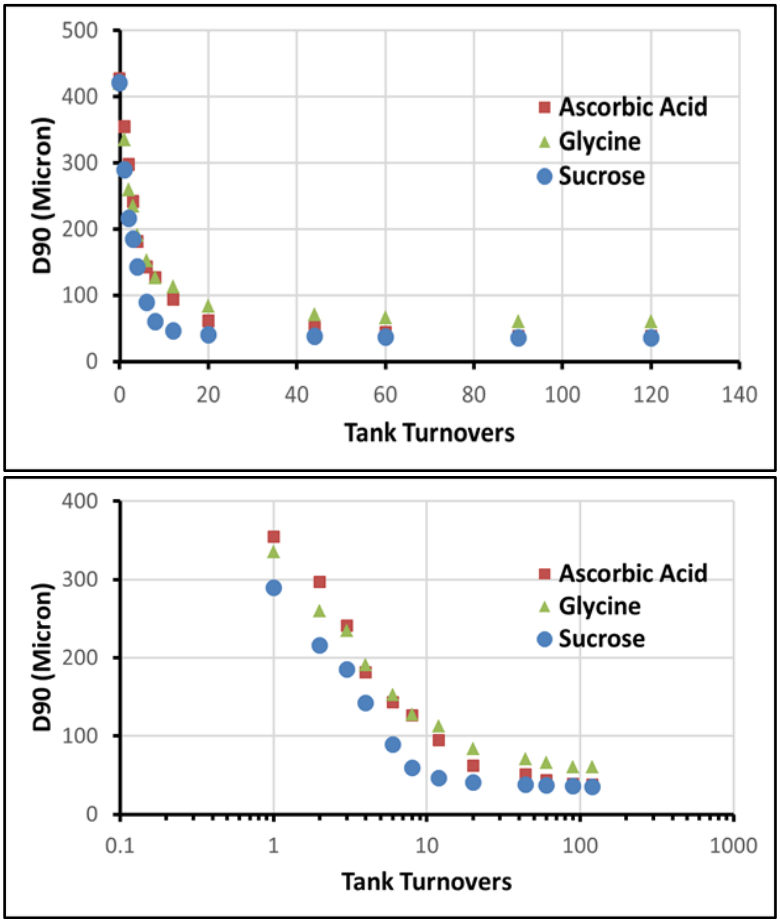

Figure 4.26 - Wet milling of different crystals, ascorbic acid, glycine, and sucrose (laser diffraction measurements) - 8000 rpm and 4.2 lpm – lower graph is log-normal representation of the data in upper graph - Silverson L4R inline mixer with standard shear gap

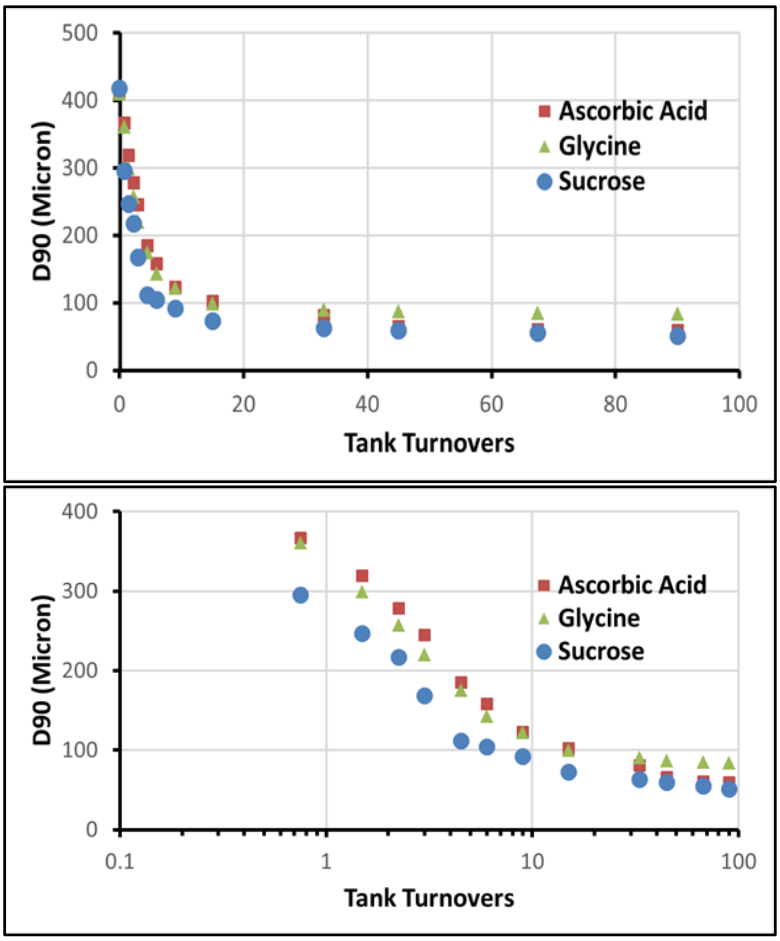

Figure 4.27 - Wet milling of different crystals, ascorbic acid, glycine, and sucrose (laser diffraction measurements) - 6500 rpm and 3.0 lpm – lower graph is log-normal representation of the data in upper graph - Silverson L4R inline mixer with standard shear gap

Difference in physical properties of these crystals can also explain the difference in size of chips and attrition products. A simple explanation is sketched in Figure 4.28; a higher brittleness index results in a larger chip size as represented by D10 or D_{10}. Figure 4.29 and Figure 4.30 show that the chip size D10 (10% cumulative size) and D_{10} (arithmetic or number based mean) of sucrose is larger than that of glycine. As it mentioned before, the indentation data for ascorbic acid shows its anisotropic nature. Therefore, the brittleness index of this material is not successful in predicting its milling behaviour.

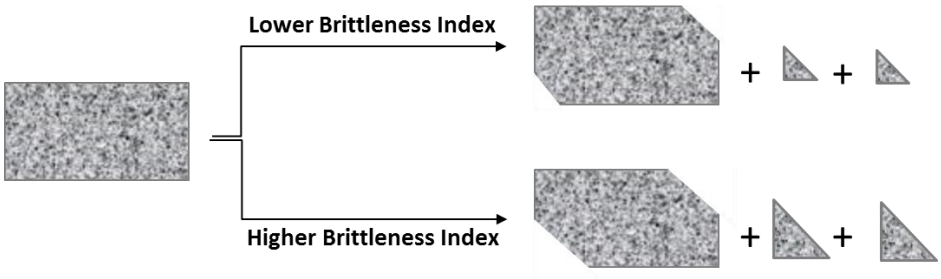

Figure 4.28- A particle with higher brittleness index breaks down to smaller D90 and larger D10

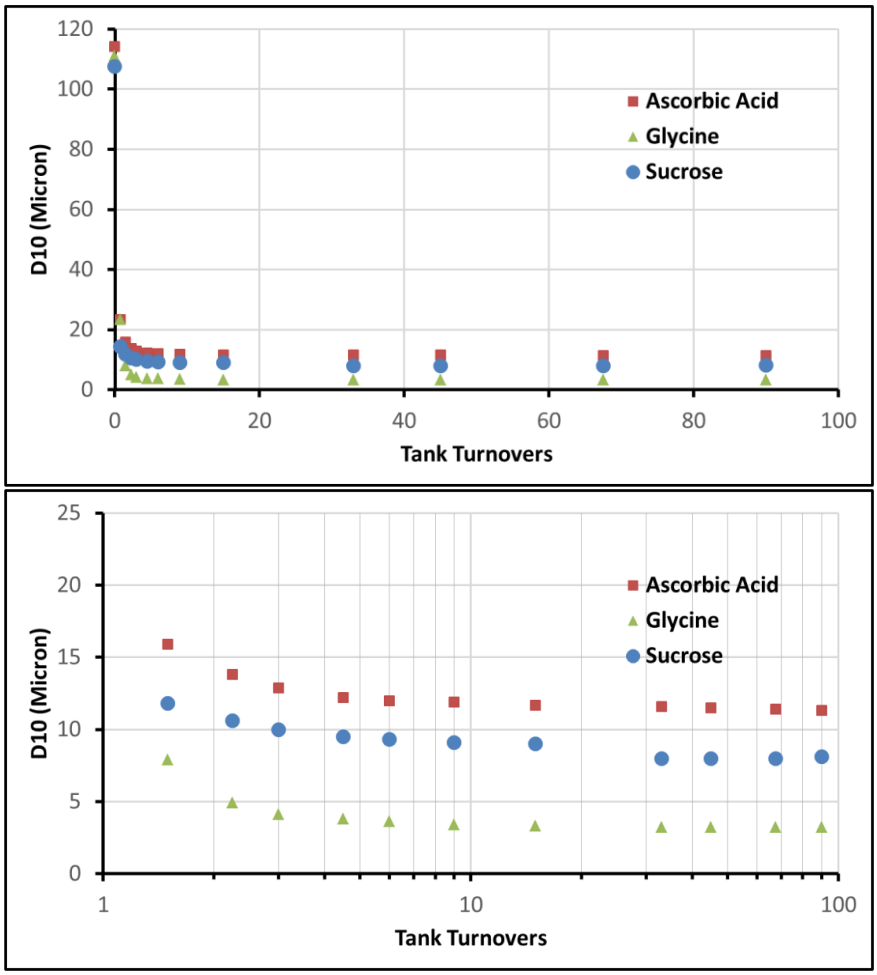

Figure 4.29 - Size of attrited small chips in milling of different crystals, ascorbic acid, glycine, and sucrose, at 6500 rpm and 3.0 lpm (D10 is 10% cumulative size measured by laser diffraction method); lower graph is log-normal representation of the data in upper graph - Silverson L4R inline mixer with standard shear gap

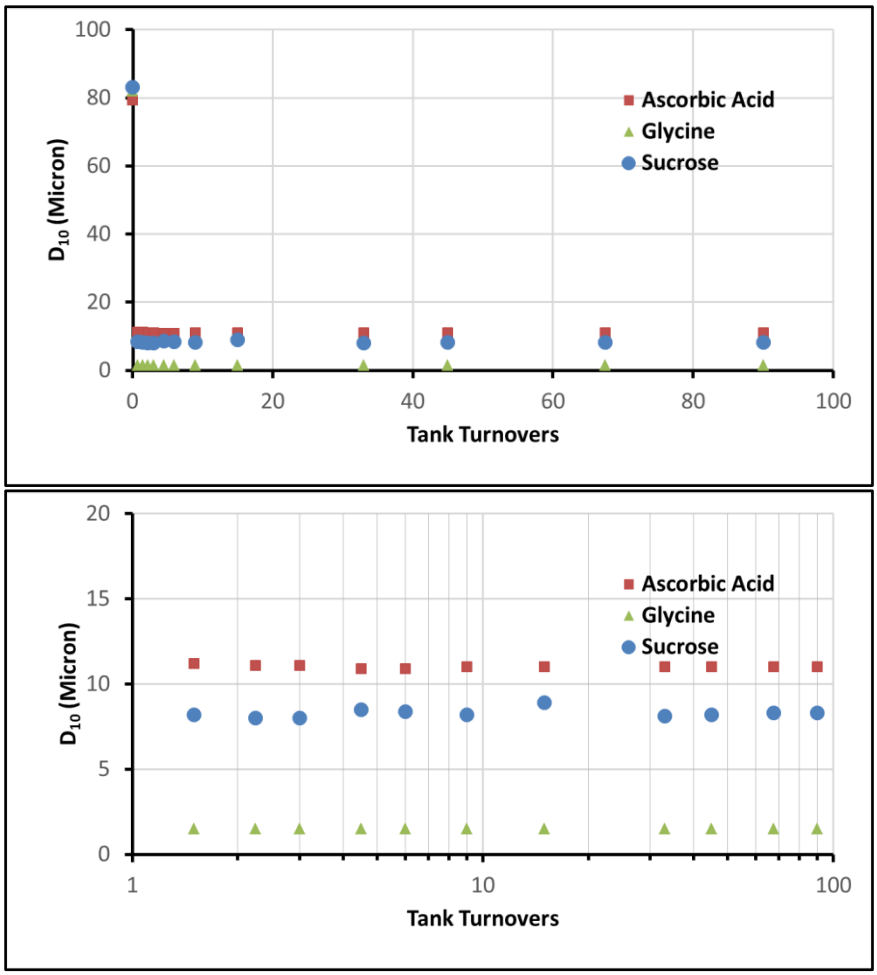

Figure 4.30 - Size of attrited small chips in milling of different crystals at 6500 rpm and 3.0 lpm (D_{10} is the arithmetic or number mean measured by laser diffraction method); lower graph is log-normal representation of the data in upper graph - Silverson L4R inline mixer with standard shear gap

4.8.1.4 –The effect of slurry concentration (particle-particle collision) on particle size reduction in the Silverson L4R inline mixer with the standard shear gap

The breakage can happen as a result of particle-particle collision, particle-wall collision, and/or fluid shear effects. Several experiments were carried out to explore the scope of each mechanism on the particle breakage. Extend of particle-particle collision was examined by milling different concentration of the sucrose in IPA. It was reasoned that by increasing the concentration, the probability of particle-particle collisions increases with a power of 2 whereas the particle-wall collisions increase

proportionally. So if the mechanical energy for breakage is coming from particle-particle collisions, then it should significantly change the milling behavior.

It is important to note that in all other experiments presented in this study, the concentration of slurry is set to 10% by weight. Here, different concentrations of sucrose in IPA were milled using inline mixer at 6500 rpm and 3.0 lpm. The experiment results, as shown in Figure 4.31, do not show a strong dependency toward concentration. This suggests that the particle-particle effects are not strong when compared to energy input (rotor speed) or residence time (flow rate) effects. This is in agreement with experimental evidence from literature that particle size reduction in rotor-stator wet mills is mostly independent of slurry concentration [53].

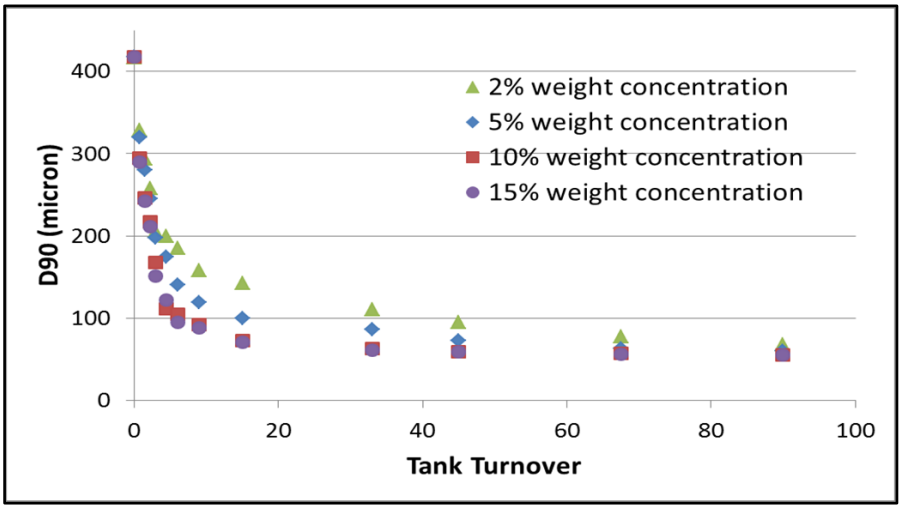

Figure 4.31- Concentration effect on wet milling performance – 6500 rpm and 3.0 lpm - Silverson L4R inline mixer with standard shear gap (laser diffraction measurements)

Another experiment was designed to investigate the significance of particle-wall collisions. In this experiment, several coats of primer and paint were applied to the stator walls and enough time was allowed, ensuring that the paint is dry. The slotted head stator was used because of its larger openings which give better access to apply consistent layers of coating. It was then assembled to the mixer and milling

experiment was run with pure IPA for an hour. At this point no sign of paint removal was observed in stator. Subsequently, the experiment was repeated with 10 percent weight sucrose in IPA for another hour. If the paint is removed from stator walls during the milling, then it may be implied that particle-wall collisions are prevailing in breaking the particles. As it is shown in Figure 4.32, the paint on the inside wall of stator and the walls of the approach edges of the slots were removed. This observation suggests that the particle-wall collisions are important in wet milling processes and they might be the dominant mechanism causing the breakage.

Figure 4.32- Particle-wall collisions cause the removal of paint coatings on inside wall and approach edges of the stator slots - Silverson L4R inline mixer with the standard shear gap

4.8.2 –Silverson L4R Inline Mixer with Enlarged Shear Gap

Power draws in rotor-stator mixers vary with the geometry, the rotor size, the rotor speed, flowrate, and properties of the process fluids. In the case of batch mixers, power draw is also a function of the vessel size and structure (baffles, obstacles). In this part, the effect of shear gap width on the milling performance of Silverson L4R inline mixer is investigated. Figure 4.33 shows the schematic geometries of the standard and enlarged shear gaps. The difference between these two geometries is the size of the rotor which in turn results in difference in width of the shear gap.

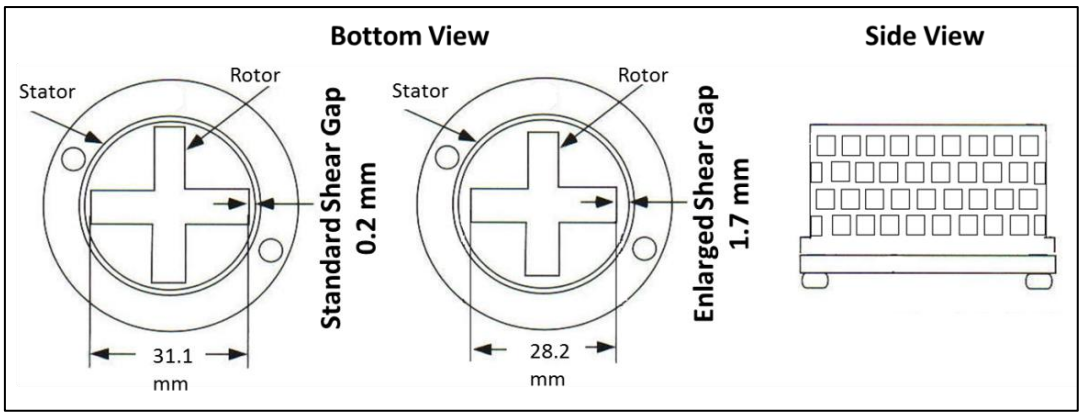

Figure 4.33- Geometry of rotor and stator for standard and enlarged shear gap in Silverson L4R inline mixer

Widening the shear gap has two effects on milling performance. First, it reduces the power draw by the mixer due to reduced rotor and stator interactions and the smaller rotor diameter. As a result, particles experience lower intensity of disruptive energy in the mixing zone. Second, a wider shear gap means a larger volume of the dispersion zone and as a result the maximum local energy dissipation rate decreases as will be shown in Chapter 5.

Wet milling experiments were conducted to find the effect of shear gap width on particle size reduction. Sucrose-IPA system was milled in Silverson L4R inline mixer with enlarged shear gap at different rotor speeds of 5000, 6500, and 8000 rpm. The flow rate is held constant at 3.0 lpm. Figure 4.34 to Figure 4.39 show the evolution of particle size distribution from initial size distribution to final distribution. It is important to note that the mixer with enlarged shear gap is not able to draw and concentrate enough power to break down particles to a unimodal and narrow size distribution, and therefore the final distribution (Figure 4.39) is bimodal.

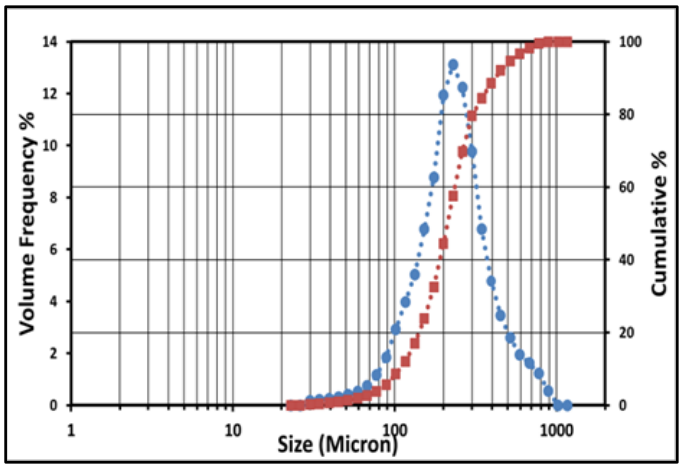

Figure 4.34 - Initial size distribution (obtained by sieving) measured with the laser diffraction method - wet milling of sucrose in IPA at 8000 rpm and 3.0 lpm – Silverson L4R inline mixer with enlarged shear gap

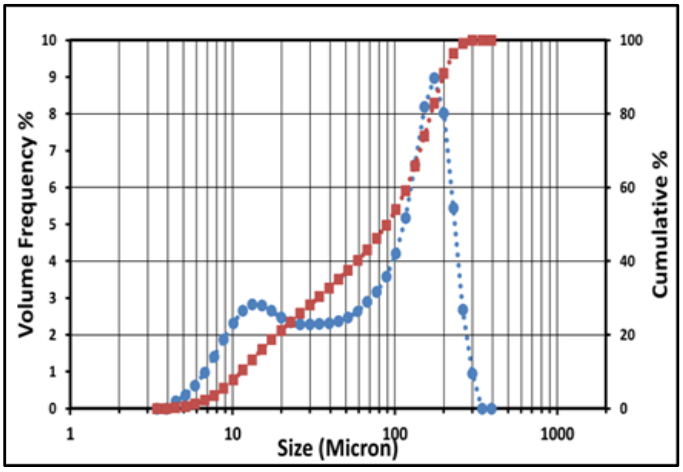

Figure 4.35 - Particle size distribution measured with laser diffraction method resulted from wet milling of sucrose in IPA at 8000 rpm and 3.0 lpm after 15 tank turnovers – Silverson L4R inline mixer with enlarged shear gap

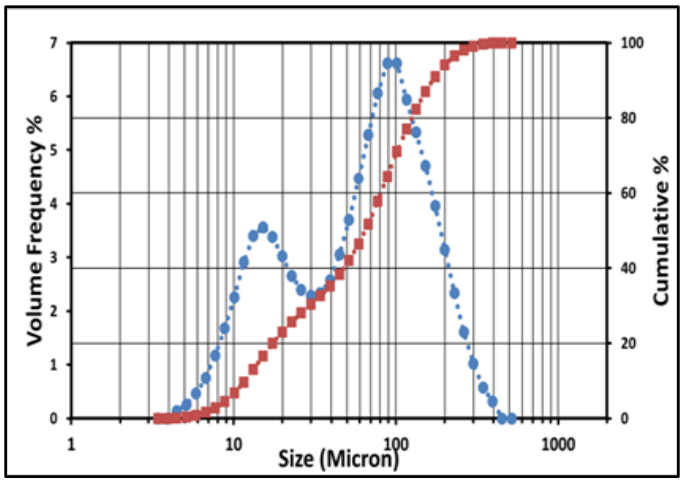

Figure 4.36 - Particle size distribution resulted from wet milling of sucrose in IPA at 8000 rpm and 3.0 lpm after 30 tank turnovers – Silverson L4R inline mixer with enlarged shear gap

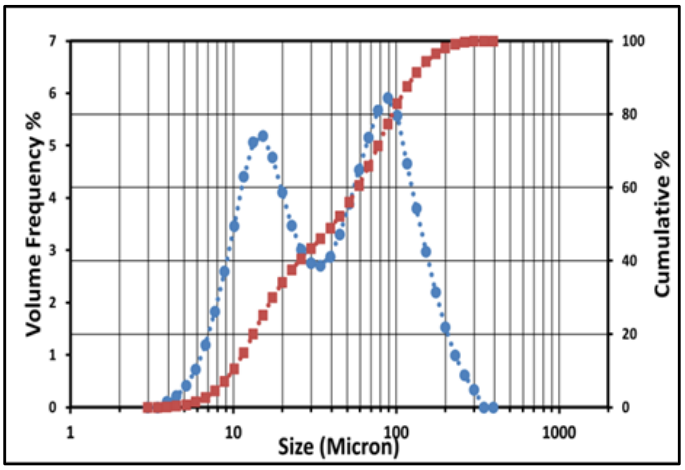

Figure 4.37 - Particle size distribution resulted from wet milling of sucrose in IPA at 8000 rpm and 3.0 lpm after 45 tank turnovers – Silverson L4R inline mixer with enlarged shear gap

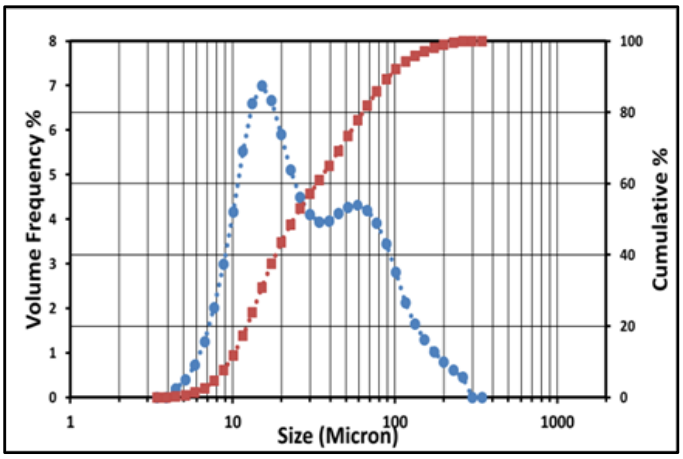

Figure 4.38 - Particle size distribution resulted from wet milling of sucrose in IPA at 8000 rpm and 3.0 lpm after 90 tank turnovers – Silverson L4R inline mixer with enlarged shear gap

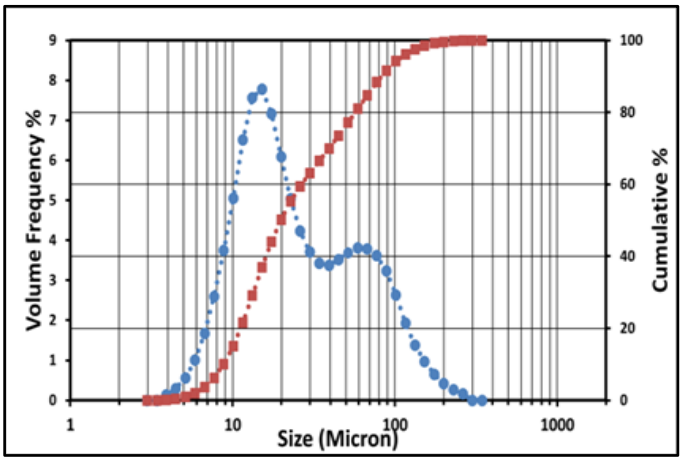

Figure 4.39 - Final size distribution resulted from wet milling of sucrose in IPA at 8000 rpm and 3.0 lpm – Silverson L4R inline mixer with enlarged shear gap

Figure 4.40 shows the effect of rotor speed on the rate of size reduction in the Silverson L4R inline mixer with the enlarged shear gap. Similar to wet milling results in the mixer with the standard shear gap, the rotor speed has a strong effect on the rate of size reduction as well as the ultimate equilibrium size. The sharp size reduction rate at the beginning is due to fracture mechanism in which the particles break into fragments of comparable size. The following slow breakage part is due to attrition mechanism by which small fragments are chipped off from larger particles.

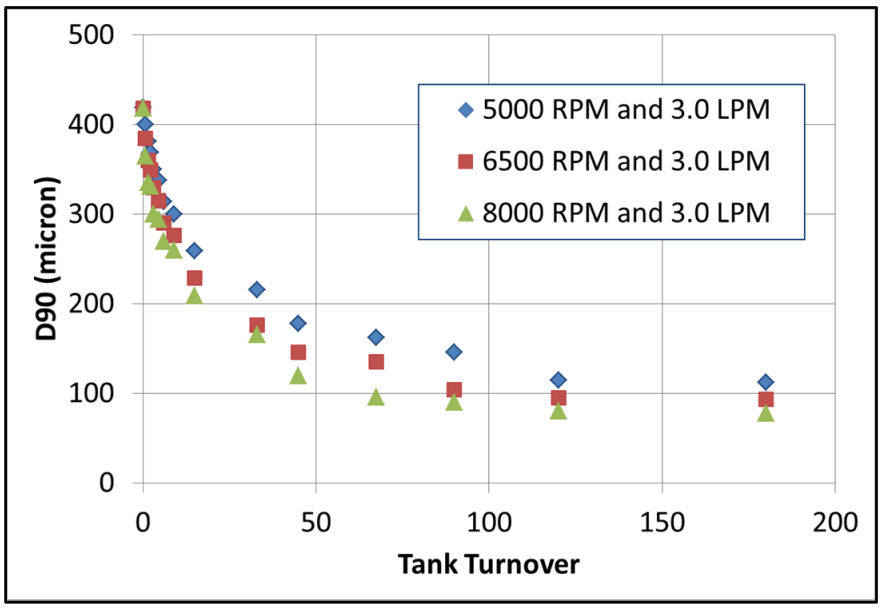

Figure 4.40 - Silverson L4R inline mixer with enlarged shear gap; rotor speed effect on sucrose breakage (laser diffraction measurement) – Flow rate is fixed at 3.0 lpm

Figure 4.41 to Figure 4.43 compare the wet milling performance of the enlarged shear gap, 1.7 mm, with the standard shear gap, 0.2 mm, at 5000, 6500, and 8000 rpm respectively. There is apparently a much higher initial breakage rate and smaller ultimate particle size associated with standard shear gap in all cases.

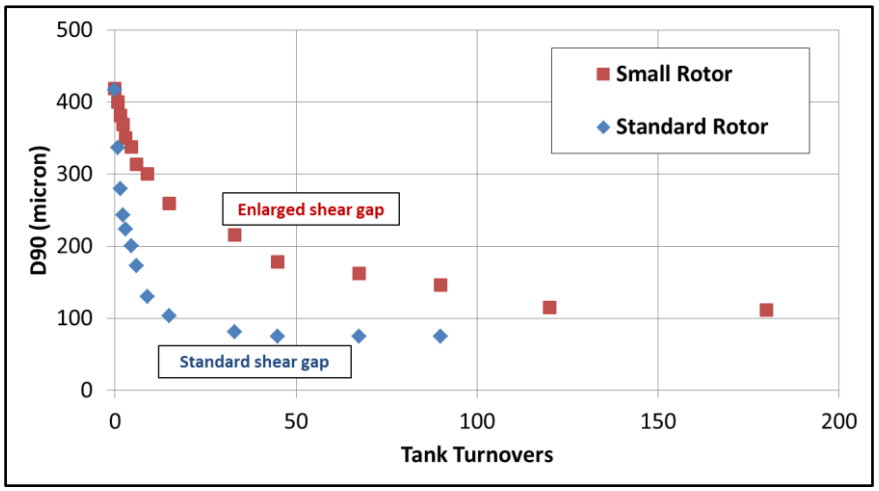

Figure 4.41 - Shear gap effect on milling performance of inline rotor-stator device – wet milling of sucrose in IPA at 5000 rpm and 3.0 lpm

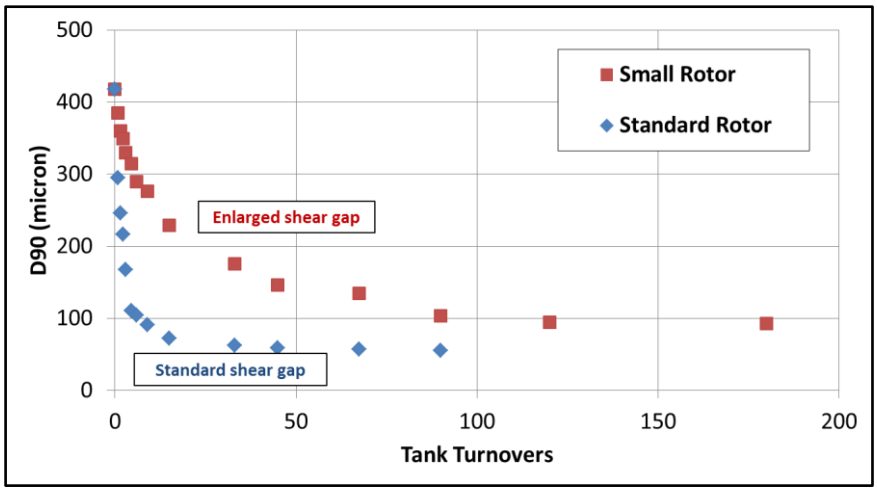

Figure 4.42 - Shear gap effect on milling performance of inline rotor-stator device – wet milling of sucrose in IPA at 6500 rpm and 3.0 lpm

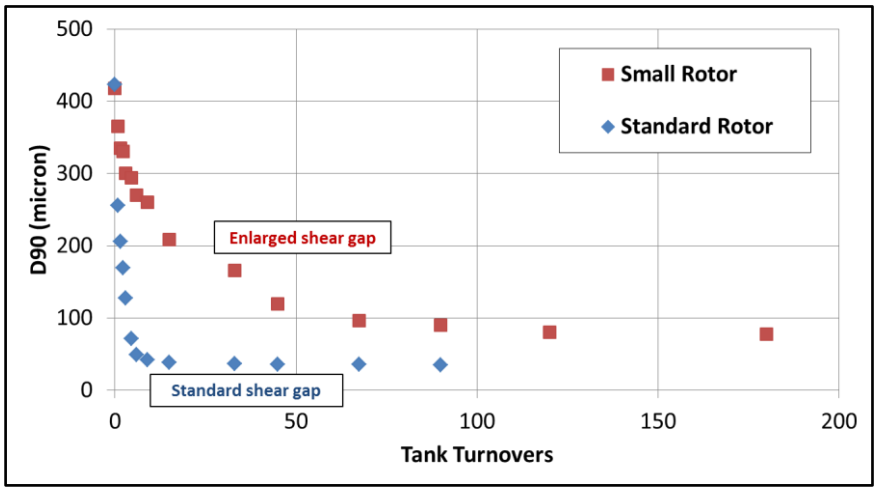

Figure 4.43 - Shear gap effect on milling performance of inline rotor-stator device – wet milling of sucrose in IPA at 8000 rpm and 3.0 lpm

In the case of the standard shear gap (0.2 mm), the initial D90 (420 µm) is larger than the shear gap and it mills down to D90s smaller than the shear gap. Whereas, in the case of the enlarged shear gap (1.7 mm), the initial D90 is smaller than shear gap and it still mills down to much smaller D90s. This observation implies that the breakage of particles is not due to compression or tearing (Figure 4.44.a) and single particle-wall impacts (Figure 4.44.b) are the dominant breakage mode. The significance of particle-particle collision (Figure 4.44.c) is discussed in previous section.

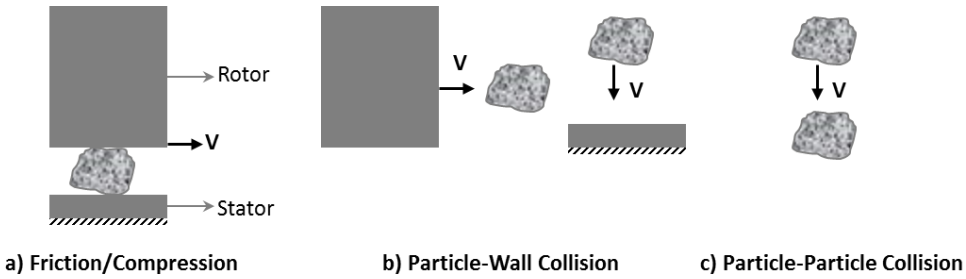

Figure 4.44- Different loading modes in a rotor-stator mixer, a) Friction or compression, b) Particle-wall collision, c) Particle-particle collision

4.8.3 –Silverson L4R Batch Mixer

The performance of a rotor–stator mixer can be related to the Reynolds number and the power number with rotor diameter as a characteristic dimension. The power curves of rotor–stator mixers have similar shape to that of stirred tank with the power number inversely proportional to the Reynolds number in the laminar flow regime and practically constant in the turbulent flow regime. The laminar flow regime, indicated by the constant slope of 1/Re of the power curve, extends to Re = 100 instead of Re = 10 as in the case of stirred tank [63, 64]. In the turbulent flow regime, which is the case in this study, (Re >10,000), the power number is independent of Re number and varies from 0.8 to 3 depending on the geometry of the rotor and stator mixer.

In spite of smaller rotor and stator dimensions compared to inline mixer (dimensions are given in Table 4.1), L4R batch mixer draws more power and has a higher power number (power draw and power number calculations are given in Chapter 5). Furthermore, due to the flow condition inside the holding tank, and its smaller dispersion zone, the batch mixer develops a higher local energy dissipation rates compared with the inline mixer. Consequently, it achieves higher milling rates and delivers a smaller ultimate (equilibrium) particle size.

Figure 4.45 to Figure 4.50 show the evolution of particle size distribution from initial to final distribution for wet milling of sucrose-IPA in Silverson L4R batch mixer at 8000 rpm. The effect of rotor speed on milling performance of sucrose is shown in Figure 4.51. The rotor speed has a strong effect on the rate of size reduction as well as the ultimate equilibrium size. Furthermore, sharp breakage rate at the beginning following by slow changes is observed in particle breakage data.

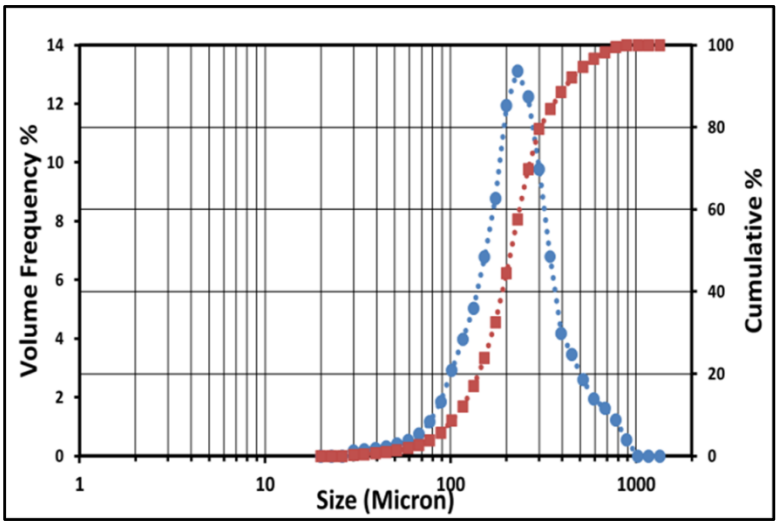

Figure 4.45 - Initial size distribution (obtained by sieving) measured with the laser diffraction method - wet milling of sucrose in IPA at 8000 rpm – Silverson L4R batch mixer

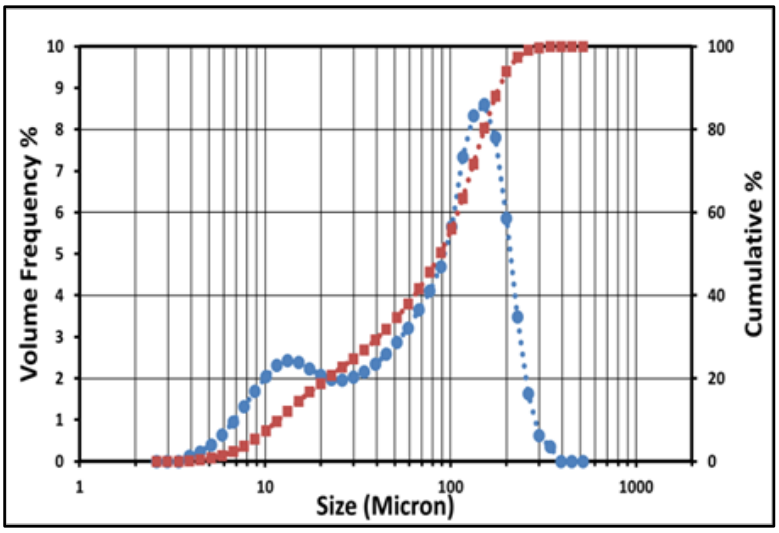

Figure 4.46 - Particle size distribution measured with the laser diffraction method resulted from wet milling of sucrose in IPA at 8000 rpm after 1 min – Silverson L4R batch mixer

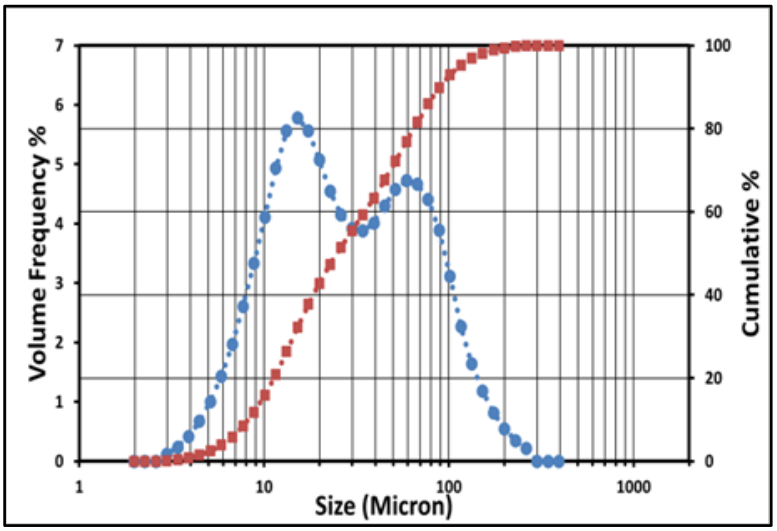

Figure 4.47 - Particle size distribution resulted from wet milling of sucrose in IPA at 8000 rpm after 2 mins – Silverson L4R batch mixer

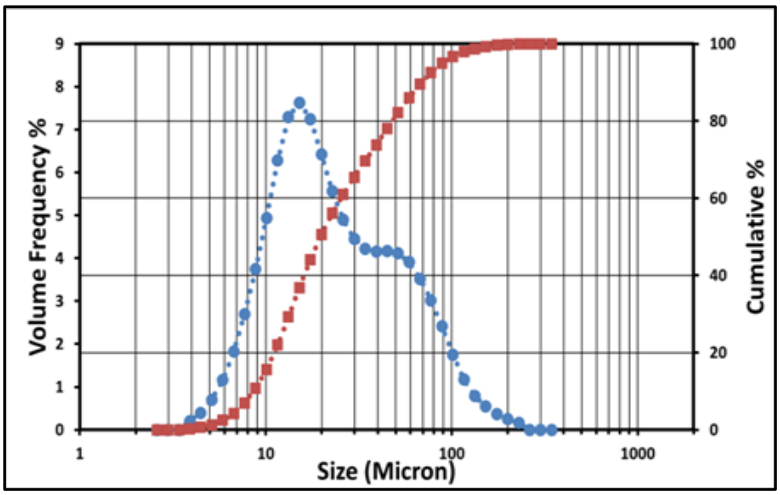

Figure 4.48 - Particle size distribution resulted from wet milling of sucrose in IPA at 8000 rpm after 3 mins – Silverson L4R batch mixer

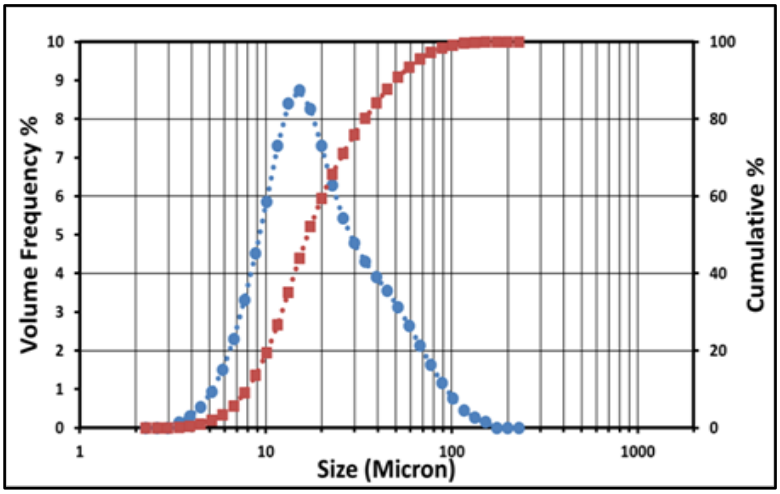

Figure 4.49 - Particle size distribution resulted from wet milling of sucrose in IPA at 8000 rpm after 10 mins – Silverson L4R batch mixer

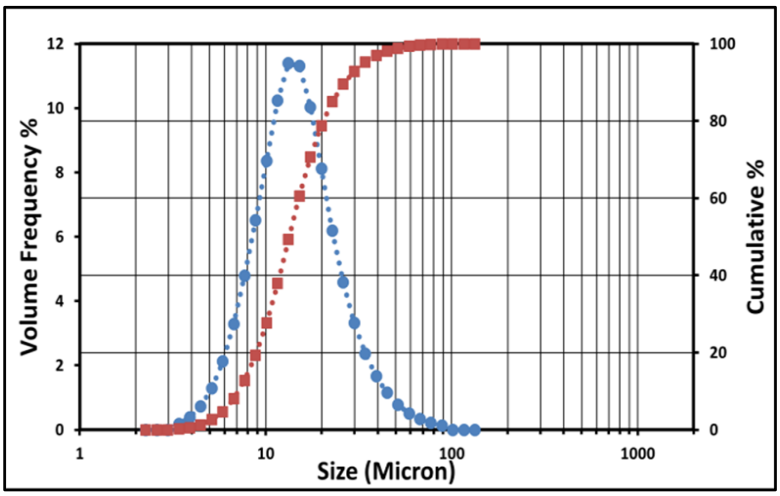

Figure 4.50 – Final (t= 90 mins) particle size distribution resulted from wet milling of sucrose in IPA at 8000 rpm – Silverson L4R batch mixer

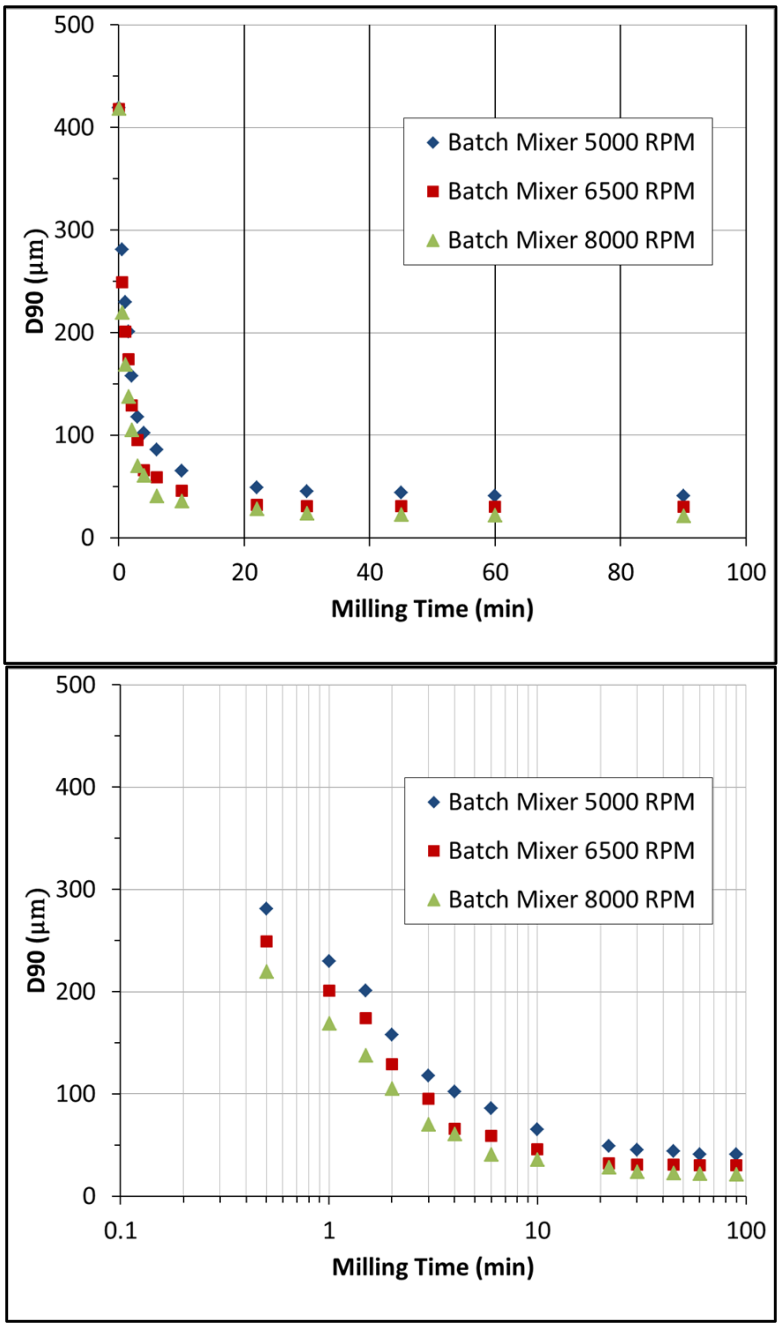

Figure 4.51 - Silverson L4R batch mixer; rotor speed effect on sucrose breakage (laser diffraction measurement) – lower graph is log-normal representation of the data in upper graph

4.9 –Summary

A series of wet milling experiments with different crystal-antisolvent systems has been developed and performed in the Silverson L4R rotor-stator mixers, to investigate the effect of milling conditions, mixer geometry, and particle physical

properties on ultimate particle size and particle breakage kinetics. Three test materials, i.e., sucrose, glycine, and ascorbic acid, were used in the experiments to provide a range of material properties and explore their influence on the wet milling behavior. Different rotor speeds were used to explore the effect of energy input and operational conditions on milling performance. Three different mixer geometries were used, i.e. a Silverson L4R inline mixer with standard and enlarged shear gap, and a Silverson L4R batch mixer, to examine the effect of mixer geometry on particle breakage behavior. Long milling times were provided to ensure that all particles experienced the regions with maximum local energy dissipation rate multiple times and the size distribution no longer changes from one tank turnover to the next. It was shown that:

- Increasing rotor speed/power input at constant throughput, intensify the milling process and leads to a smaller ultimate particle size. Furthermore, the rate of milling increases with increasing the rotor speed.

- Increasing throughput (flowrate) at constant rotor speed, decreases the milling rate however it does not have significant effect on the ultimate particle size. Lower throughput gives more residence time for particles in the mixing head leading to more collision and the higher breakage rate.

- Particle physical properties determine their resistance against the fracture and their mode of deformation. Generally, Particles with higher hardness and lower fracture toughness are more liable to break.

- The Silverson L4R batch mixer is a better mixer compared to the inline unit because it delivers higher size reduction rates and smaller ultimate particle size.

- The clearance between rotor and stator (shear gap width) in inline mixer has a significant effect on the milling rate and ultimate particle size.

Chapter 5: Model Validation and Mechanistic Correlations

In this chapter, the suitability of mechanistic models developed in Chapter 3 to predict the wet milling experimental data for the different rotor-stator mixer geometries presented in Chapter 4 investigated.

5.1 –Suitability of Different Mechanistic Models to Predict the Wet Milling Behavior

The mechanistic correlation in Table 3.4 are given in the form of maximum stable particle size over the rotor diameter (x/D) as a function of reciprocal of rotor tip speed ($1/u_{tip}$). Here, as discussed in Chapter 4, D90 is used as a representative of maximum stable particle size, i.e., x = D90.

In Figure 5.1, D90/D for the wet milling equilibrium data for sucrose, glycine, and ascorbic acid at different rotor speeds (the ultimate particle size is independent of the mill head throughput rate) are plotted against the corresponding $1/u_{tip}$ for the Silverson L4R inline mixer with standard shear gap. The wet milling data for the inline mixer with enlarged shear gap and the batch mixer were not used here because they do not have geometrical similarity with the inline mixer with the standard shear gap. They will be used in next section where the mechanistic correlations for the devices without geometric similarity are introduced.

It is shown that the ultimate particle size data, for different crystal-antisolvent systems in the inline mixer with the standard shear gap, are well fit by a line with slope of 1.6 on a logarithmic plot. This slope suggests that the inertial subrange models better fit the experimental data than the macroscale models, which predicted

much larger slopes. Furthermore, this slope is in agreement with models based on elastic mechanism of Gahn and Mersmann [33] which predicts the slope of $\frac{24}{17} = 1.4$ and elastic-plastic mechanism of this study which predicts slope of $\frac{12}{7} = 1.7$.

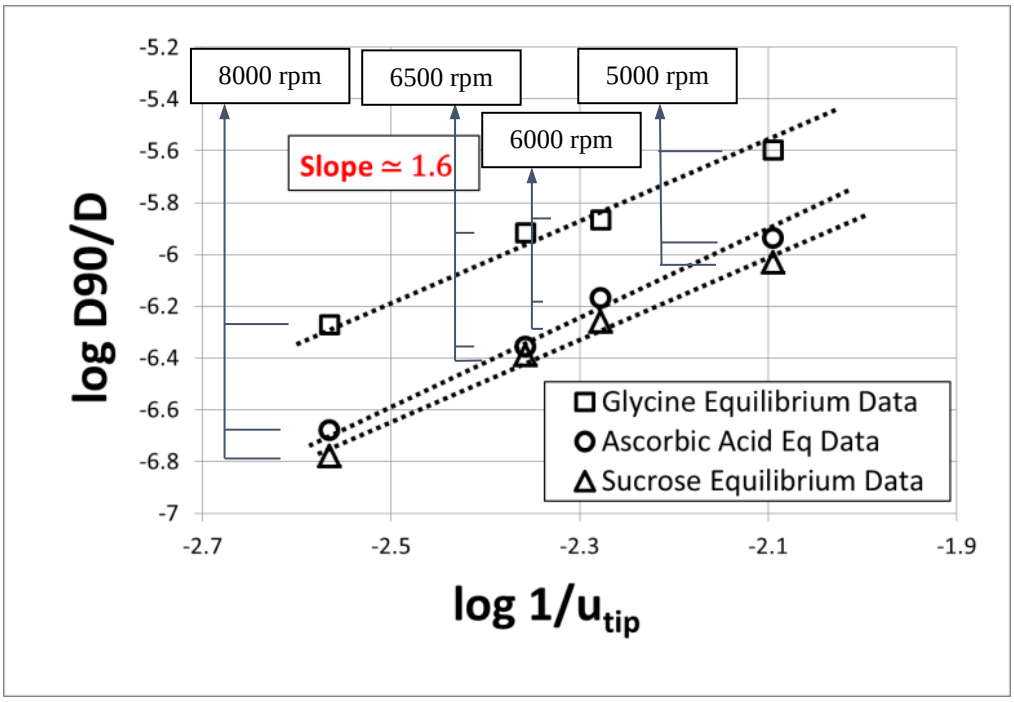

Figure 5.1- Suitability of different models to fit the wet milling equilibrium data for different crystals in Silverson L4R inline mixer with standard shear gap (trend line comparison)

It is important to note that the model based on the indentation mechanism (predicting a power law dependency of -3 with the u_{tip}) underestimates the energy required for size reduction whereas, the plastic mechanism model (predicting slope of $\frac{6}{5} = 1.2$) overestimates the energy requirement. This conclusion is in agreement with classical theories where: 1) kick's law (similar to indentation mechanism) does not account for the particle size and consequently underestimates the energy requirement, 2) Rittinger's law (similar to plastic mechanism) overestimates the energy requirement by assuming that surface energy of the material controls the particle

fracture, 3) Bond's law (similar to elastic-plastic mechanism) describes the energy requirements properly.

In Figure 5.2 to Figure 5.5, wet milling data for sucrose, glycine, and ascorbic acid in the Silverson L4R inline mixer with the standard shear gap is plotted along with a best fit line for breakage models (based on turbulent inertial subrange theory for disruptive stress as given in Table 3.5). The degree of success of each model to collapse the data is assessed based on the goodness of the fit as summarized in Table 5.1. Other than predicting the trend, the model based on elastic-plastic mechanism for cohesive stress and turbulent inertial subrange theory for disruptive stress is able to collapse the data of different materials on a single curve with reasonable goodness of fit (Figure 5.5). The final expression is given by:

$$\frac{\mathrm{D90}}{\mathrm{D}} = 2.6 \times 10^{-5}\ \mathrm{Co_{EP}}^{-6/7} \qquad (5.1)$$

Table 5.1 - Goodness of fit of different models to collapse the experimental data for milling of different materials in the inline mixer with the standard shear gap (IST=Inertial subrange of turbulence)

Cohesive stress	**Disruptive stress**	**Breakage model**	**Goodness of fit**
Indentation approach	IST	$\frac{x}{D} \sim Co_I^{-3/2}$	R-square= -8.5
Plastic mechanism	IST	$\frac{x}{D} \sim Co_P^{-3/5}$	R-square= 0.63 RMSE= 4.6e-4
Elastic mechanism	IST	$\frac{x}{D} \sim Co_E^{-12/17}$	R-square= 0.60 RMSE= 5.0e-4
Elastic-plastic mechanism	IST	$\frac{x}{D} \sim Co_{EP}^{-6/7}$	R-square= 0.91 RMSE= 1.7e-7

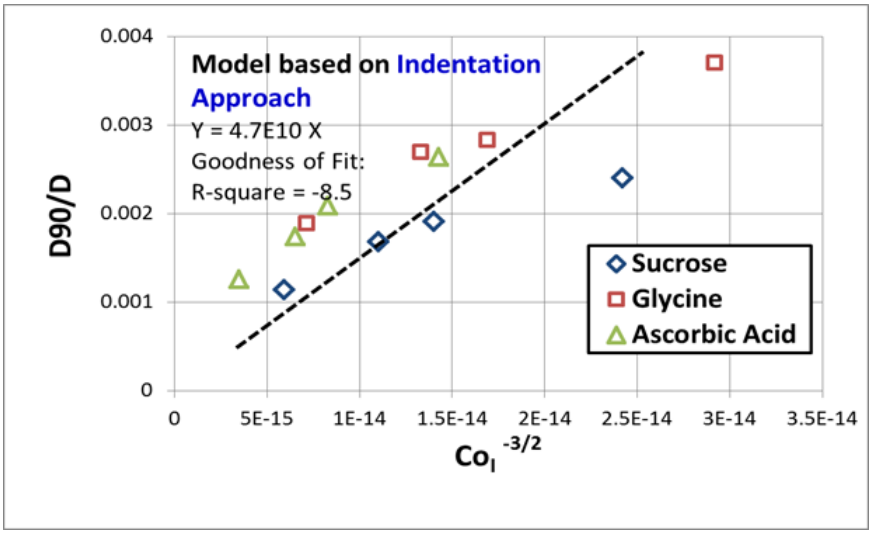

Figure 5.2 - Suitability of the model based on indentation approach (Lawn and Marshal model) to predict the wet milling behavior of different crystals in Silverson L4R inline rotor-stator mixer with standard shear gap at different rotor speeds

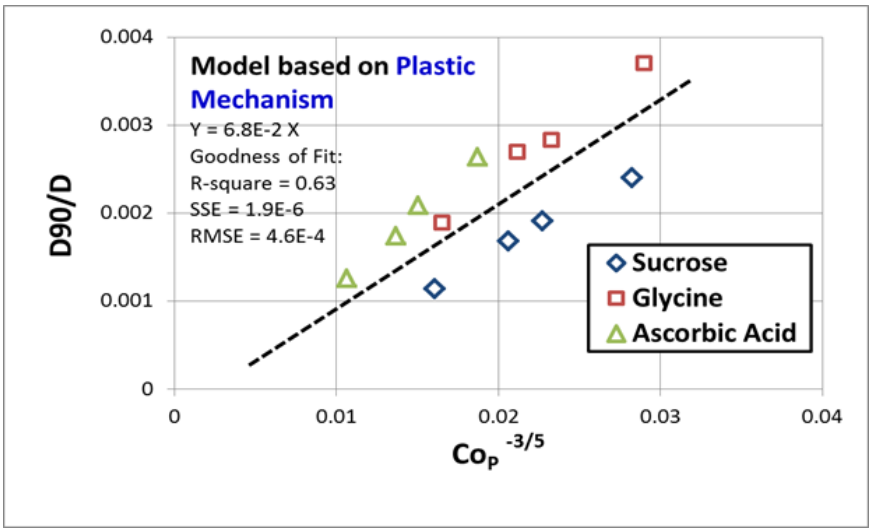

Figure 5.3 - Suitability of the model based on plastic mechanism (Ghadiri and Zhang model) to predict the wet milling behavior of different crystals in Silverson L4R inline rotor-stator mixer with standard shear gap at different rotor speeds

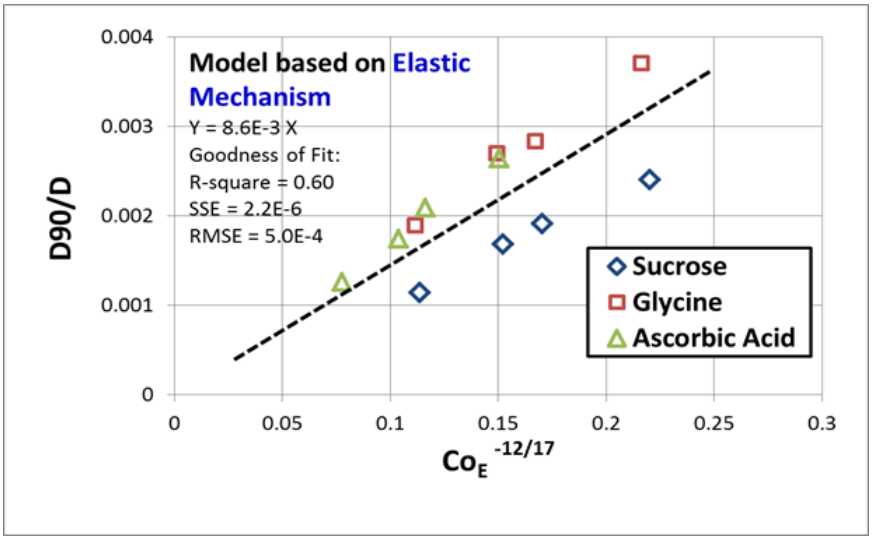

Figure 5.4 - Suitability of the model based on elastic mechanism (Gahn and Mersmann model) to predict the wet milling behavior of different crystals in Silverson L4R inline rotor-stator mixer with standard shear gap at different rotor speeds

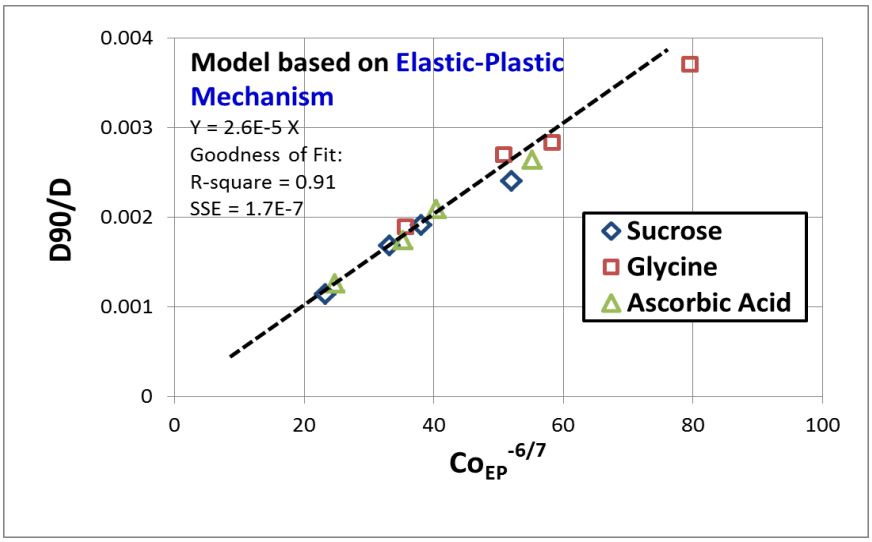

Figure 5.5 - Suitability of the model based on elastic-plastic mechanism (current study) to predict the wet milling behavior of different crystals in Silverson L4R inline rotor-stator mixer with standard shear gap at different rotor speeds

Here, a geometrically similar analysis is performed to investigate the suitability of breakage models to predict the wet milling experimental data in the inline mixer with the standard shear gap. Although we don't have enough experimental data for the inline mixer with the enlarged shear gap and in the batch mixer to perform the geometrically similar analysis, but these data along with the data from the inline

mixer with the standard shear gap are used in next section for analysis of devices without geometrical similarity.

5.2 –Scale Up strategy based on Local Energy Dissipation Rate

Several investigators have studied the importance of turbulent energy dissipation rate and power draw in predicting the drop size in liquid-liquid dispersions at high Reynolds number [65–67]. It is possible to facilitate the scale up/down efforts, and compare the data from different geometries using the concept of local energy dissipation rate. Average energy dissipation rate is simply the available power per fluid mass. However, the maximum particle size obtained at equilibrium is determined by the maximum or local energy dissipation rate rather than the average energy dissipation rate in the mixing head. For example, Davies [67] showed that the local energy dissipation rate for agitated tanks can be estimated by considering the power generated by the stirrer in the swept volume of the impeller. Here for rotor-stator mixers, local energy dissipation rate is defined as:

$$\varepsilon = \frac{P}{\rho_f V_{DZ}} \tag{5.2}$$

where P is power draw of the mixer, ρ_f is fluid density, and V_{DZ} is volume of dispersion zone (volume with highest dissipation rates). The dispersion zone of different geometries and scales are different. Knowledge of velocity field in the mixer, based on experiments or simulations, aid the proper evaluation of this zone. It is reasonable to define the dispersion zone for rotor stator mixers as:

$$V_{DZ} = \text{Volume of Stator Holes} + \text{Shear Gap Volume} \tag{5.3}$$

Most of the energy that is supplied to a rotor-stator mixer is dissipated in this region, i.e., the density of energy dissipation rate is much higher in this region when compared with other regions in the mixer. Table 5.2 summarizes the volume of dispersion zone of the mixers that are used in this study.

Table 5.2 - Volume of dissipersion zone for inline mixer with standard and enlarged shear gaps and batch mixer

Mixer Type	Stator Hole Volume	Shear Gap Volume	Dispersion Zone Volume V_{DZ}
Inline Mixer with Standard Shear Gap	1.2 ml	0.4 ml	1.6 ml
Inline Mixer with Enlarged Shear Gap	1.2 ml	2.8 ml	4.0 ml
Batch Mixer	0.9 ml	0.2 ml	1.1 ml

The power draw of different mixers is obtained using experimental and computational methods. For inline mixers with standard and enlarged shear gap, a CFD simulation is conducted and the power draw of the mixer is calculated based on the torque on the shaft and rotor blades at different rotor speeds as shown in Table 5.3 and Table 5.4. The simulation details are given in Chapter 6. For the Silverson L4R batch mixer, experimental data as well as CFD simulations for power draw were available in literature [63,68] and presented in Table 5.5. It is important to note that the experimental data supports the computational results for power calculations. The power numbers of different mixers were calculated as:

$$N_P = \frac{Power}{\rho_f N^3 D^5} \tag{5.4}$$

Where ρ_f is fluid density, N is rotational speed (rpm), and D is rotor diameter. It is important to note that despite the fact that the power number of inline mixer with standard shear gap is smaller than that of enlarged shear gap, it draws more power and as a result higher energy dissipation rates are present in this mixer. Since power number goes as D^5, small changes in rotor diameter, D, have a large effect on the magnitude of N_P.

Table 5.3- Tip speed, Reynolds number, power, and power number of Silverson L4R inline mixer with standadr shear gap at different rotor speeds – CFD investigation (see Chapter 6 for details)

Rotor Speed	Inline Mixer Standard Shear Gap, D = 31.1 mm				
N (RPM)	u_{tip} (m/s)	Re	Power (W)	N_P	Local ε
5000	8.12	80,000	13.9	0.9	11,052
6500	10.56	104,000	30.6	0.9	24,332
8000	12.99	129,000	57.1	0.9	45,403

Table 5.4- Tip speed, Reynolds number, power, and power number of Silverson L4R inline mixer with enlarged shear gap at different rotor speeds – CFD investigation (see Chapter 6 for details)

Rotor Speed	Inline Mixer Enlarged Shear Gap, D = 28.2 mm				
N (RPM)	u_{tip} (m/s)	Re	Power (W)	N_P	Local ε
5000	7.36	66,000	9.5	1.0	3,321
6500	9.57	86,000	20.9	1.0	7,347
8000	11.78	106,000	39.0	1.0	13,404

Table 5.5- Tip speed, Reynolds number, power, and power number of Silverson LR batch mixer at different rotor speeds based on data of Padron [63]

Rotor Speed	Batch Mixer, Standard Shear Gap, D = 28.1 mm				
N (RPM)	u_{tip} (m/s)	Re	Power (W)	N_P	Local ε
5000	7.31	66,000	23.0	2.3	26,601
6500	9.51	86,000	50.5	2.3	58,408
8000	11.70	106,000	94.2	2.3	108,952

To this point it was reasoned that the concept of local energy dissipation rate provides a better measure of disruptive stresses present in the mixer and by taking into account the power draw and geometry of the mixer, it can be used to scale up/down the wet milling processes in different milling devices. Figure 5.6 shows the equilibrium data for wet milling of sucrose, glycine, and ascorbic acid in different mixers that are plotted against local energy dissipation rate in a logarithmic scale. This graph shows that maximum stable particle size is a function of dissipation rate raised to a power of 0.5. This relationship was predicted by the elastic-plastic model as given in Table 3.5.

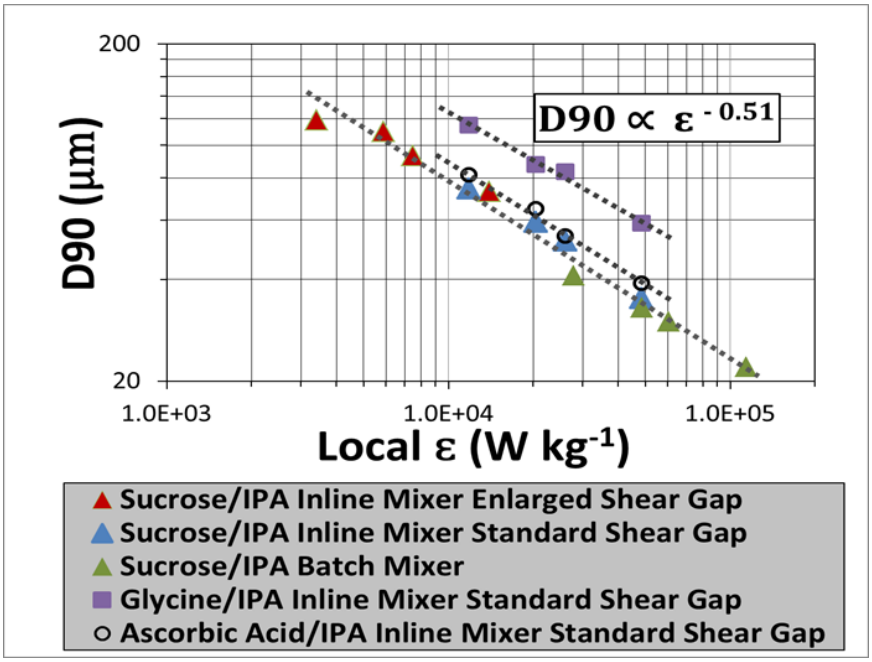

Figure 5.6 - Maximum stable particle size plotted against local maximum energy dissipation rate for wet milling of sucrose, glycine, and ascorbic acid in Silverson L4R inline mixer with standard and enlarged shear gap, and Silverson L4R batch mixer at 5000, 6000, 6500, and 8000 rpm

In Figure 5.7 to Figure 5.10, wet milling data of different crystals obtained in different mixers with different geometries is plotted along with breakage models based on energy dissipation rate from Table 3.5 in Chapter 3. The degree of success of each model to collapse the data is assessed based on the goodness of the fit summarized in Table 5.6. In addition to predicting the trend, the elastic-plastic model is able to collapse the data of different materials on a single curve with acceptable goodness of fit. The final expression is given by:

$$D90 = 13.6 \left(\frac{EK_c}{\rho_P H} \right)^{6/7} \frac{1}{\varepsilon^{4/7}} \qquad (5.5)$$

Table 5.6 - Goodness of fit of different models to collapse the experimental data for milling of different materials in the inline mixer with the standard and enlarged shear gap and in the batch mixer

Mechanism	Breakage model	Goodness of fit
Indentation approach	$x \sim (\frac{cK_c}{\rho_P H})^{3/2} \frac{1}{\varepsilon}$	R-square= -4.3
Plastic mechanism	$x \sim (\frac{{K_c}^2}{\rho_P H})^{3/5} \frac{1}{\varepsilon^{2/5}}$	R-square= 0.69 RMSE= 2.1e-2
Elastic mechanism	$x \sim (\frac{K_c^{\frac{3}{2}}}{\rho_P H^{\frac{1}{2}}})^{12/17} \frac{1}{\varepsilon^{8/17}}$	R-square= 0.78 RMSE= 3.7e-2
Elastic-plastic mechanism	$x \sim (\frac{EK_c}{\rho_P H})^{6/7} \frac{1}{\varepsilon^{4/7}}$	R-square= 0.92 RMSE= 2.9e-3

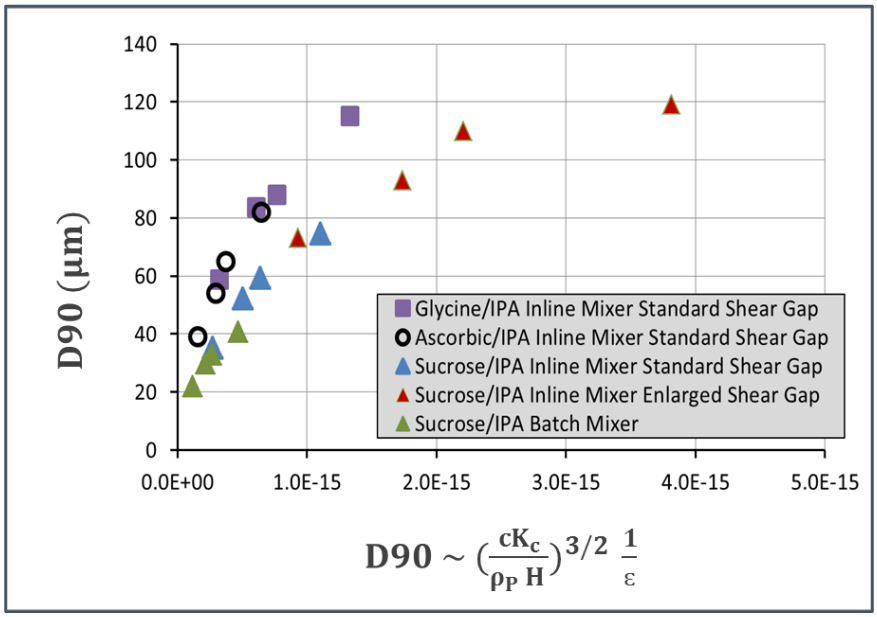

Figure 5.7 - Suitability of the model based on indentation approach to collapse the wet milling equilibrium data for different crystals in Silverson L4R inline rotor-stator mixer with standard and enlarged shear gap, and batch mixer at different rotor speeds

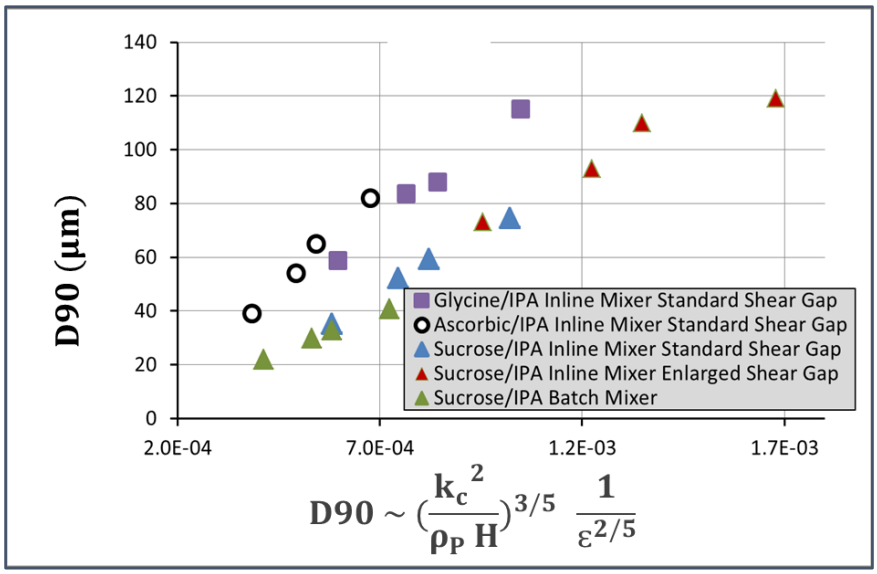

Figure 5.8 - Suitability of the model based on plastic mechanism to collapse the wet milling equilibrium data for different crystals in Silverson L4R inline rotor-stator mixer with standard and enlarged shear gap, and batch mixer at different rotor speeds

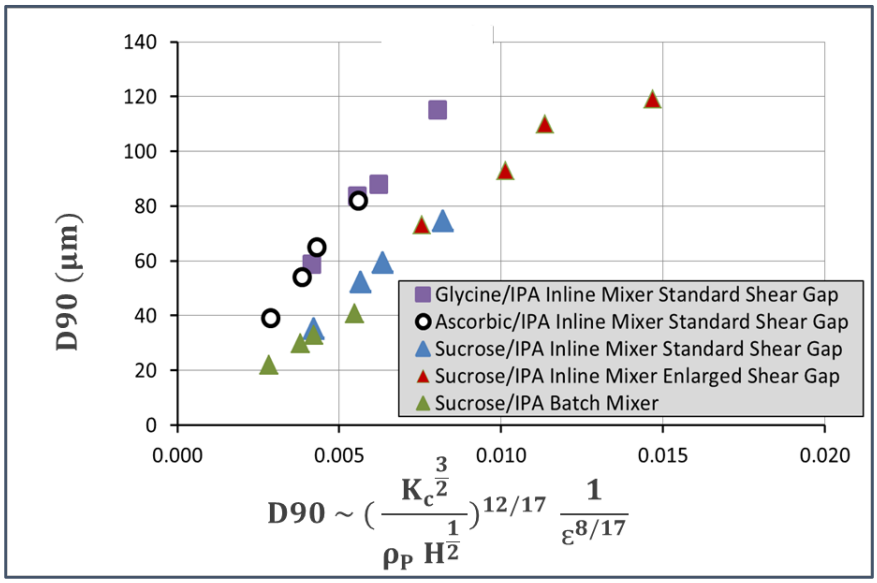

Figure 5.9 - Suitability of the model based on elastic mechanism to collapse the wet milling equilibrium data for different crystals in Silverson L4R inline rotor-stator mixer with standard and enlarged shear gap, and batch mixer at different rotor speeds

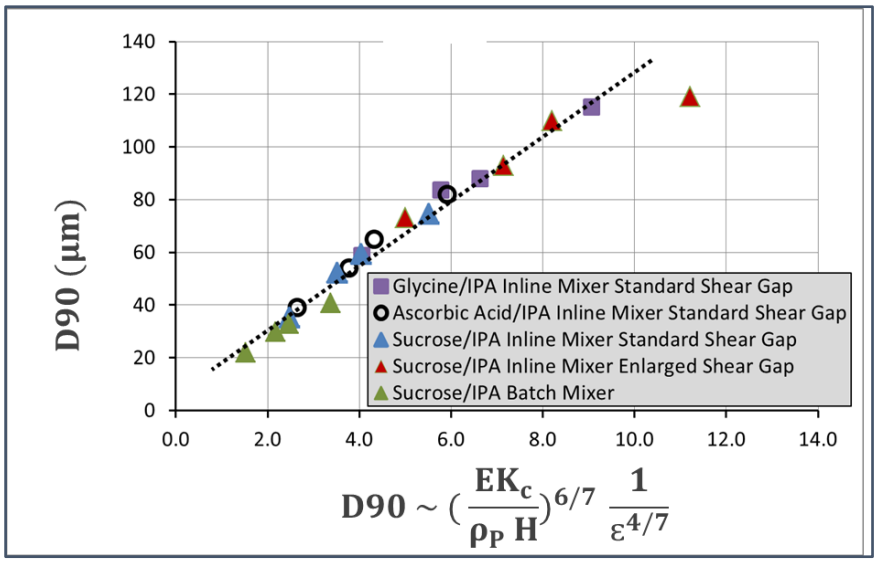

Figure 5.10 - Suitability of the model based on elastic-plastic mechanism to collapse the wet milling equilibrium data for different crystals in Silverson L4R inline mixer with standard and enlarged shear gap, and batch mixer at different rotor speeds

5.3 –The Rate of Size Reduction and Mechanistic Correlations for Breakage Kernel

There are two common methods to define a breakage kernel: the power law kernel and the exponential kernel. They can be written in general form as:

$$g(x) = \frac{1}{\text{breakage time}} \times \text{probability of breakage} \qquad (5.6)$$

There are different methods to define the breakage time. It can be defined based on time constant of the process, i.e., rotational rate of rotor in rotor-stator mixers. In slurries with turbulent condition, particles in the scale of turbulent inertial subrange have a breakage time proportional to the lifetime of eddies and can be written as (Batchelor):

$$t_b \sim x^{2/3} \varepsilon^{-1/3} \qquad (5.7)$$

where t_b is breakage time, x is particle size, and ε is energy dissipation rate. Different kernels have different breakage probabilities. The breakage probability in the power law kernel is simply defined based on the ratio of cohesive stress to disruptive stress raised to a power as:

$$\text{probability of breakage} = c_1 \left(\frac{\tau_c}{\tau_D}\right)^{c_2} \tag{5.8}$$

Whereas, the exponential kernel is based on the reaction rate analogy and is defined as [69]:

$$\text{probability of breakage} = e^{-\frac{\tau_c}{\tau_D}} \tag{5.9}$$

Using the cohesive stresses, τ_c, and disruptive stresses, τ_D, developed in Chapter 3 and given in Table 3.2 and Table 3.3 , each kernel will result in 8 different expressions for probability of breakage based on different cohesive and disruptive mechanisms. Here, the disruptive stress based on inertial subrange model of turbulence and macroscale velocity is used to construct the Table 5.7 and Table 5.8 respectively.

Table 5.7- Power law and exponential breakage kernels with inertial subrange turbulence model as the disruptive stress

	Power law kernel	Exponential kernel
Mechanism	$g(x) = \left(\begin{matrix}\text{Frequency of Passage}\\ \text{through Impeller Region}\end{matrix}\right) \times \left(\begin{matrix}\text{Probabiliy of Breakage}\\ \text{while in Impeller Region}\end{matrix}\right)$ Impeller Passage Frequency $\sim N$ Probability of Breakage $\sim a\left(\frac{\tau_c}{\tau_D}\right)^b$	$g(d) = \frac{1}{\text{Breakage Time}} \times \text{Probability of Breakage}$ Breakage Time $\sim d^{2/3}\ \epsilon^{-1/3}$ Probability of Breakage $\sim e^{-\frac{\tau_c}{\tau_D}}$
Indentation	$g(x) = c_1 N\left(\frac{c K_c}{\rho_p H \epsilon^{2/3} x^{2/3}}\right)^{c_2}$	$g(x) = c_1\ x^{-2/3}\ \epsilon^{1/3}\ e^{-\frac{c_2 c K_c}{\rho_p H \epsilon^{2/3} x^{2/3}}}$
Plastic	$g(x) = c_1 N\left(\frac{K_c}{\rho_p H \epsilon^{2/3} x^{5/3}}\right)^{c_2}$	$g(x) = c_1\ x^{-2/3}\ \epsilon^{1/3}\ e^{-\frac{c_2 K_c}{\rho_p H \epsilon^{2/3} x^{5/3}}}$
Elastic	$g(x) = c_1 N\left(\frac{K_c^{3/2}}{\rho_p H^{1/2} \epsilon^{2/3} x^{17/12}}\right)^{c_2}$	$g(x) = c_1\ x^{-2/3}\ \epsilon^{1/3}\ e^{-\frac{c_2 K_c^{3/2}}{\rho_p H^{1/2} \epsilon^{2/3} x^{17/12}}}$
Elastic-Plastic	$g(x) = c_1 N\left(\frac{E K_c}{\rho_p H \epsilon^{2/3} x^{7/6}}\right)^{c_2}$	$g(x) = c_1\ x^{-2/3}\ \epsilon^{1/3}\ e^{-\frac{c_2 E K_c}{\rho_p H \epsilon^{2/3} x^{7/6}}}$

Table 5.8-Power law and exponential breakage kernels with macroscale model as the disruptive stress

	Power law kernel	Exponential kernel
Mechanism	$g(x) = \left(\begin{matrix}\text{Frequency of Passage}\\ \text{through Impeller Region}\end{matrix}\right) \times \left(\begin{matrix}\text{Probabiliy of Breakage}\\ \text{while in Impeller Region}\end{matrix}\right)$ Impeller Passage Frequency $\sim N$ Probability of Breakage $\sim a\left(\frac{\tau_c}{\tau_D}\right)^b$	$g(d) = \frac{1}{\text{Breakage Time}} \times \text{Probability of Breakage}$ Breakage Time $\sim d^{2/3}\ \epsilon^{-1/3}$ Probability of Breakage $\sim e^{-\frac{\tau_c}{\tau_D}}$
Indentation	$g(x) = c_1 N\left(\frac{c K_c}{\rho_p H u^2}\right)^{c_2}$	$g(x) = c_1\ x^{-2/3}\ \epsilon^{1/3}\ e^{-\frac{c_2 c K_c}{\rho_p H u^2}}$
Plastic	$g(x) = c_1 N\left(\frac{K_c}{\rho_p H u^2 x}\right)^{c_2}$	$g(x) = c_1\ x^{-2/3}\ \epsilon^{1/3}\ e^{-\frac{c_2 K_c}{\rho_p H u^2 x}}$
Elastic	$g(x) = c_1 N\left(\frac{K_c^{3/2}}{\rho_p H^{1/2} u^2 x^{3/4}}\right)^{c_2}$	$g(x) = c_1\ x^{-2/3}\ \epsilon^{1/3}\ e^{-\frac{c_2 K_c^{3/2}}{\rho_p H^{1/2} u^2 x^{3/4}}}$
Elastic-Plastic	$g(x) = c_1 N\left(\frac{E K_c}{\rho_p H u^2 x^{1/2}}\right)^{c_2}$	$g(x) = c_1\ x^{-2/3}\ \epsilon^{1/3}\ e^{-\frac{c_2 E K_c}{\rho_p H u^2 x^{1/2}}}$

A population balance equation is used to model the milling kinetics which can be expressed as:

$$\frac{\partial f(x,t)}{\partial t} = \int_x^{\infty} f(x',t)\, g(x')\, \beta(x',x)\, dx' - g(x)\, f(x,t) \qquad (5.10)$$

where $f(x,t)$ is cumulative fraction of particle with size *x* at time *t*, $g(x)$ is breakage kernel, and $\beta(x',x)$ is breakage distribution function (accounts for the size distribution of daughter particles after the fracture of the parent particle). The left hand side is the accumulation term, and the right hand side includes birth (production due to breakage of larger particles) and death terms (due breakage). It is possible to apply this equation to the largest size interval where the birth term is zero, and assume first order kinetics as:

$$\frac{\partial f(D90(t))}{\partial t} = - g(D90)\, f(D90(t)) \qquad (5.11)$$

By substituting the breakage function, $g(D90)$, with those given in Table 5.7 and Table 5.8, Equation 5.11 can be solved analytically or numerically to obtain the D90 as a function of milling time. The suitability of the different breakage kernels to fit the wet milling experimental data investigated and it is found that the power law kernels cannot adequately fit data. Here, the suitability of exponential kernels based on inertial subrange turbulence and different deformation mechanisms are discussed.

By substituting the breakage kernel based on elastic-plastic mechanism, plastic mechanism, and elastic mechanism (Table 5.7), the Equation 5.11 can be written as:

$$\frac{\partial D90}{\partial t} = - c_1\, \varepsilon^{\frac{1}{3}}\, e^{-\frac{c_2\, E\, K_c}{\rho_p\, H\, \varepsilon^{\frac{2}{3}}\, D90^{\frac{7}{6}}}}\, D90^{1/3} \qquad (5.12)$$

$$\frac{\partial D90}{\partial t} = -\, c_1\, \epsilon^{1/3}\, e^{-\frac{c_2\, K_c}{\rho_p\, H\, \epsilon^{2/3}\, D90^{5/3}}} D90^{1/3} \qquad (5.13)$$

$$\frac{\partial D90}{\partial t} = -\, c_1\, \epsilon^{1/3}\, e^{-\frac{c_2\, K_c{}^{3/2}}{\rho_p\, H^{1/2}\, \epsilon^{2/3}\, D90^{17/12}}} D90^{1/3} \qquad (5.14)$$

The degree of success of different breakage kernels given in Equations 5.12-14 is assessed based on the milling rate data obtained in wet milling of sucrose in IPA at the Silverson L4R inline mixer with the standard and enlarged shear gap. Figure 5.11 illustrates the result of applying elastic-plastic exponential breakage kernel to model the data from the inline mixer. Figure 5.12 and Figure 5.13 show the result of breakage kernels based on plastic deformation mechanism and elastic deformation mechanism respectively. Figure 5.14 to Figure 5.16 illustrates the data fit based on elastic-plastic kernel for different crystals, sucrose, glycine, and ascorbic acid in inline mixer with the standard shear gap at different milling conditions. It is found that the breakage kernel based on elastic-plastic model is more successful in predicting the rate of milling in the inline mixer with different shear gaps.

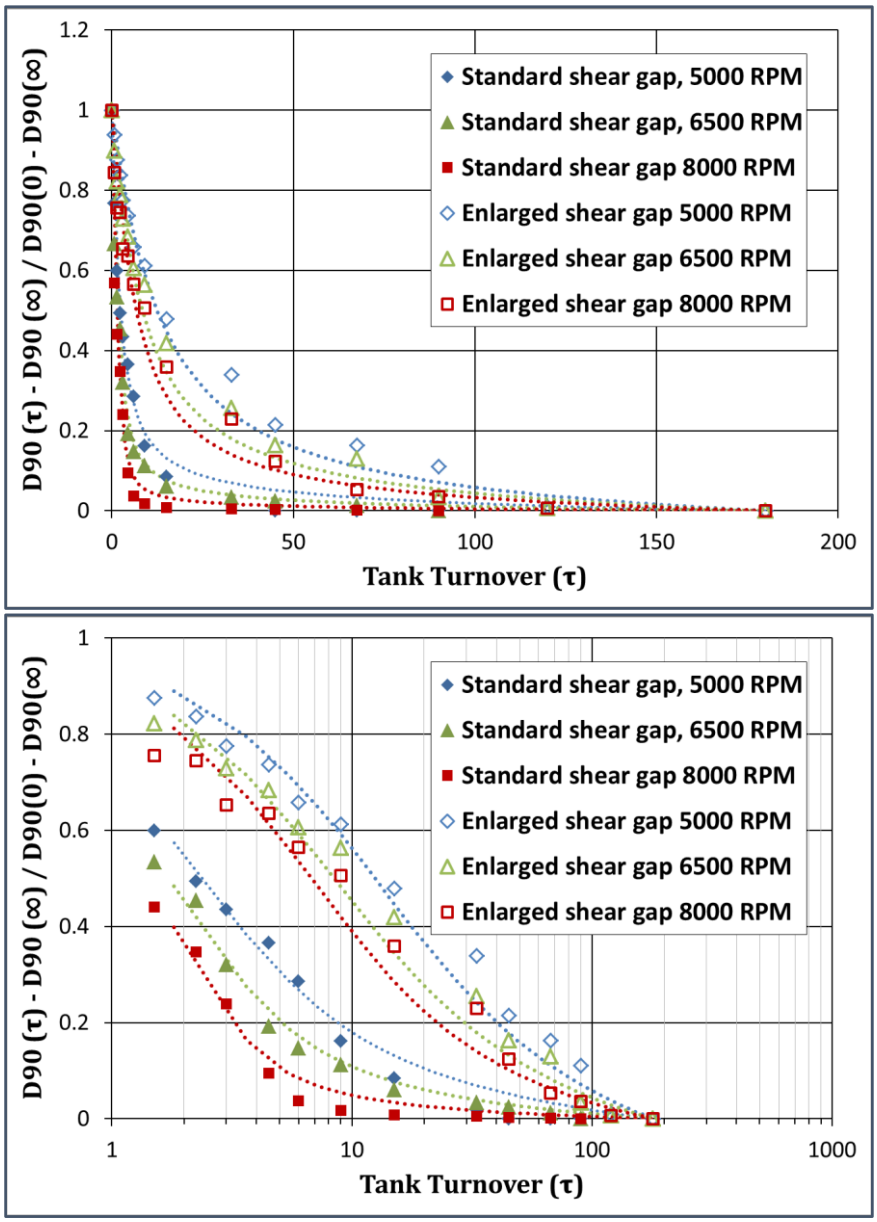

Figure 5.11 - Suitability of breakage kernel based on elastic-plastic model in predicting the milling rate of sucrose in inline mixer with standard and enlarged shear gaps at different rotor speeds and constant flow rate of 3.0 lpm, dotted lines are the model fits; lower graph is log-normal representation of the data in upper graph

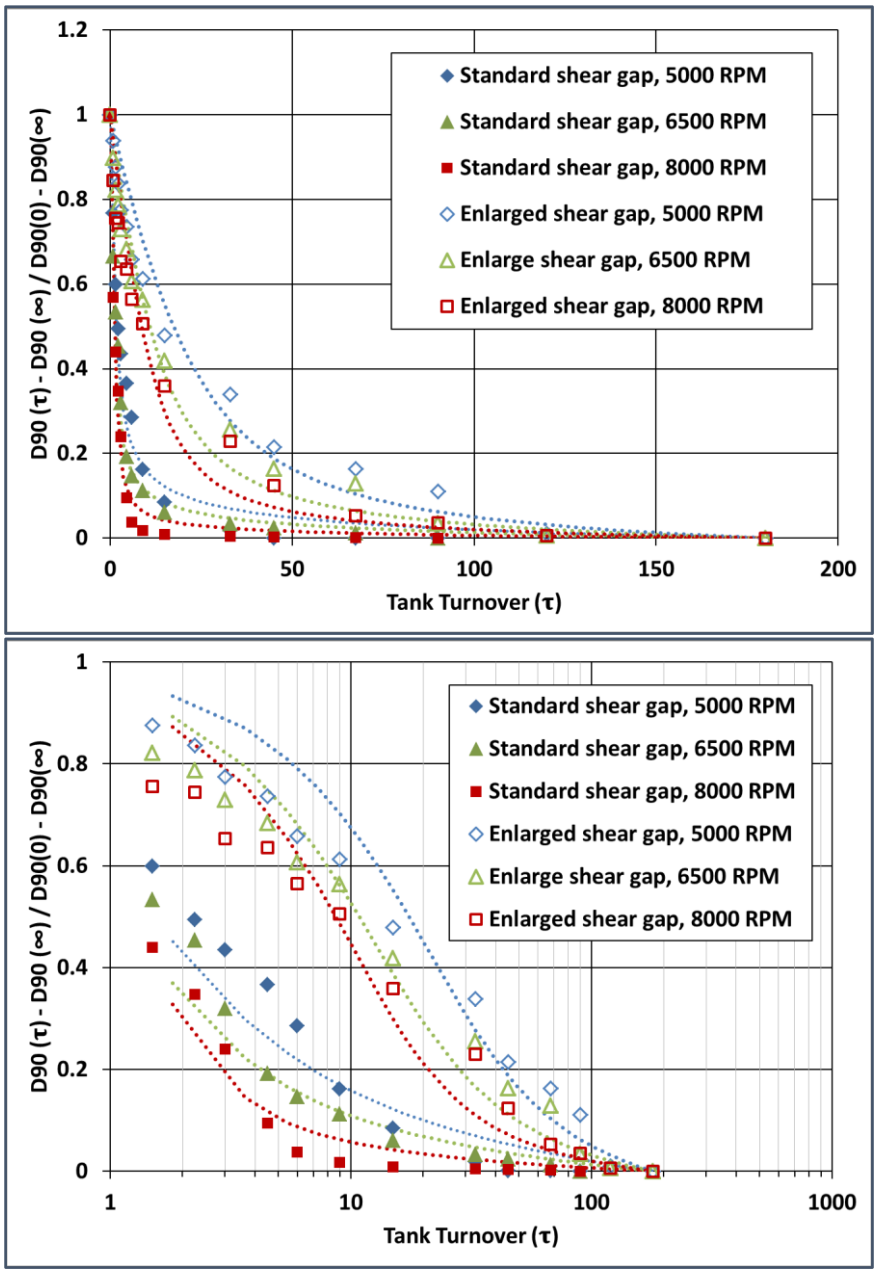

Figure 5.12 - Suitability of breakage kernel based on plastic model in predicting the milling rate of sucrose in inline mixer with standard and enlarged shear gaps at different rotor speeds and constant flow rate of 3.0 lpm, dotted lines are the model fits; lower graph is log-normal representation of the data in upper graph

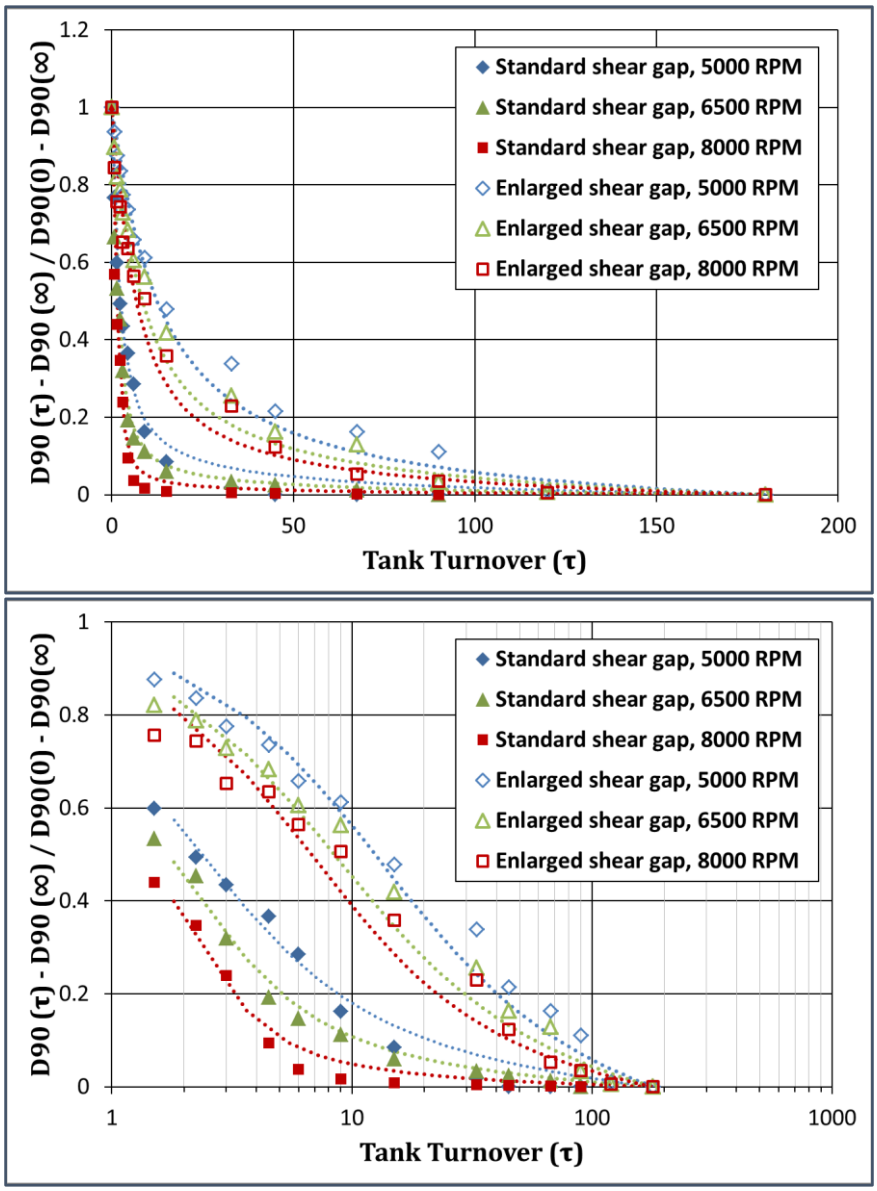

Figure 5.13 - Suitability of breakage kernel based on elastic model in predicting the milling rate of sucrose in inline mixer with standard and enlarged shear gaps at different rotor speeds and constant flow rate of 3.0 lpm, dotted lines are the model fits; lower graph is log-normal representation of the data in upper graph

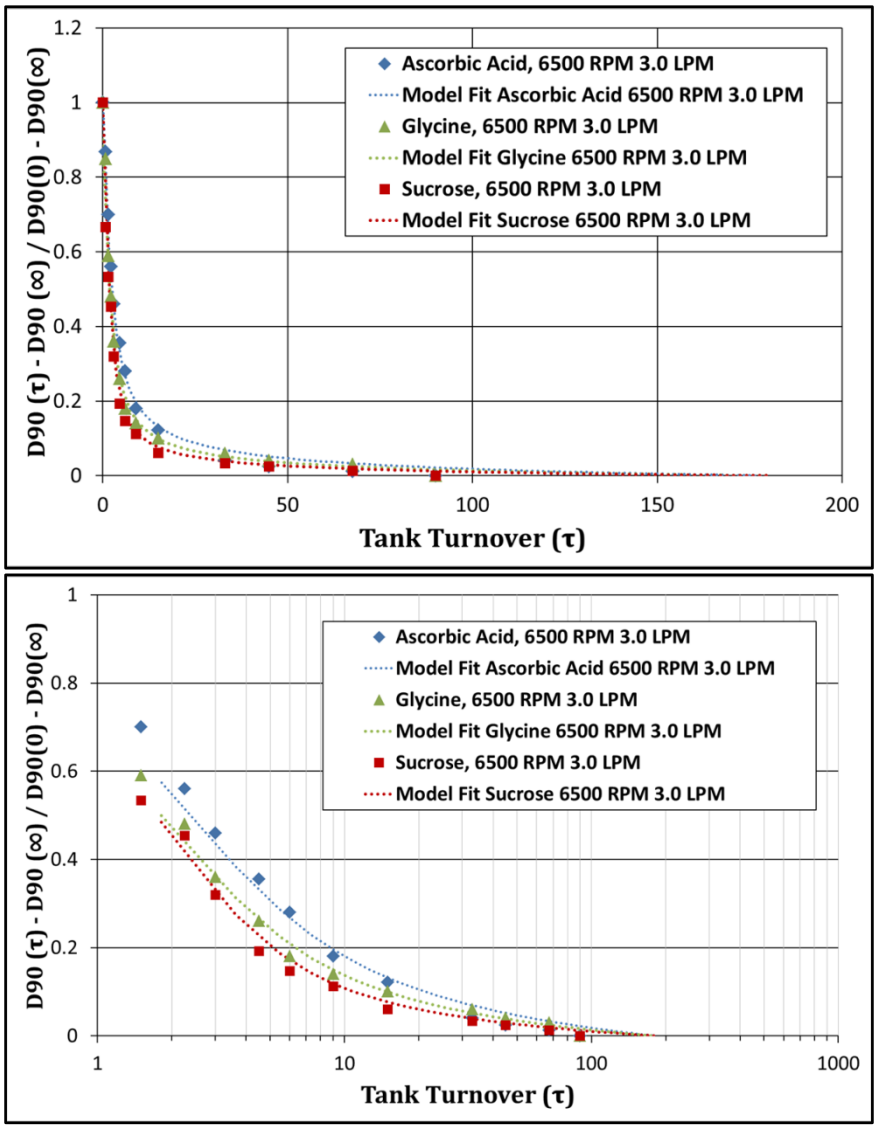

Figure 5.14 - Suitability of breakage kernel based on elastic-plastic model in predicting the milling rate of sucrose, glycine, and ascorbic acid in inline mixer with standard shear gap at 6500 rpm and 3.0 lpm, dotted lines are the model fits; lower graph is log-normal representation of the data on upper graph

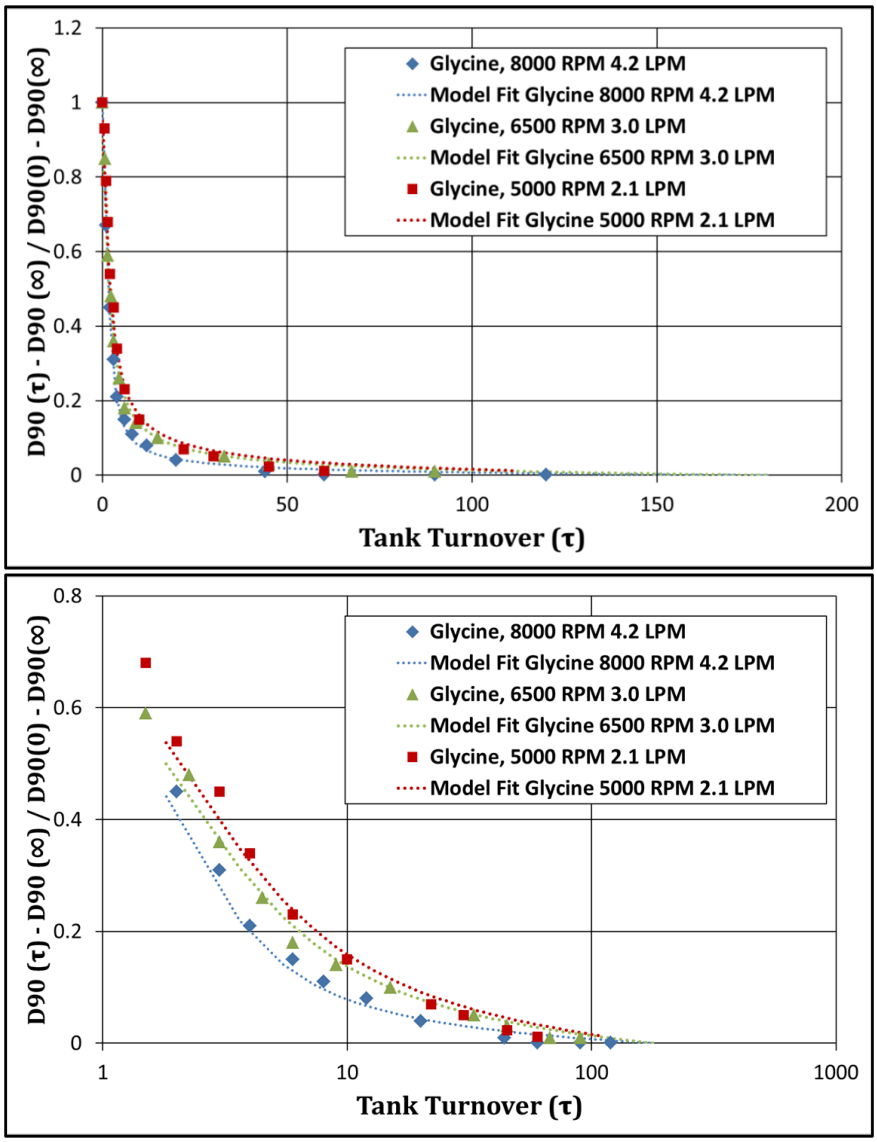

Figure 5.15 - Suitability of breakage kernel based on elastic-plastic model in predicting the milling rate of glycine in inline mixer with standard shear gap at different milling conditions, dotted lines are the model fits; lower graph is log-normal representation of the data on upper graph

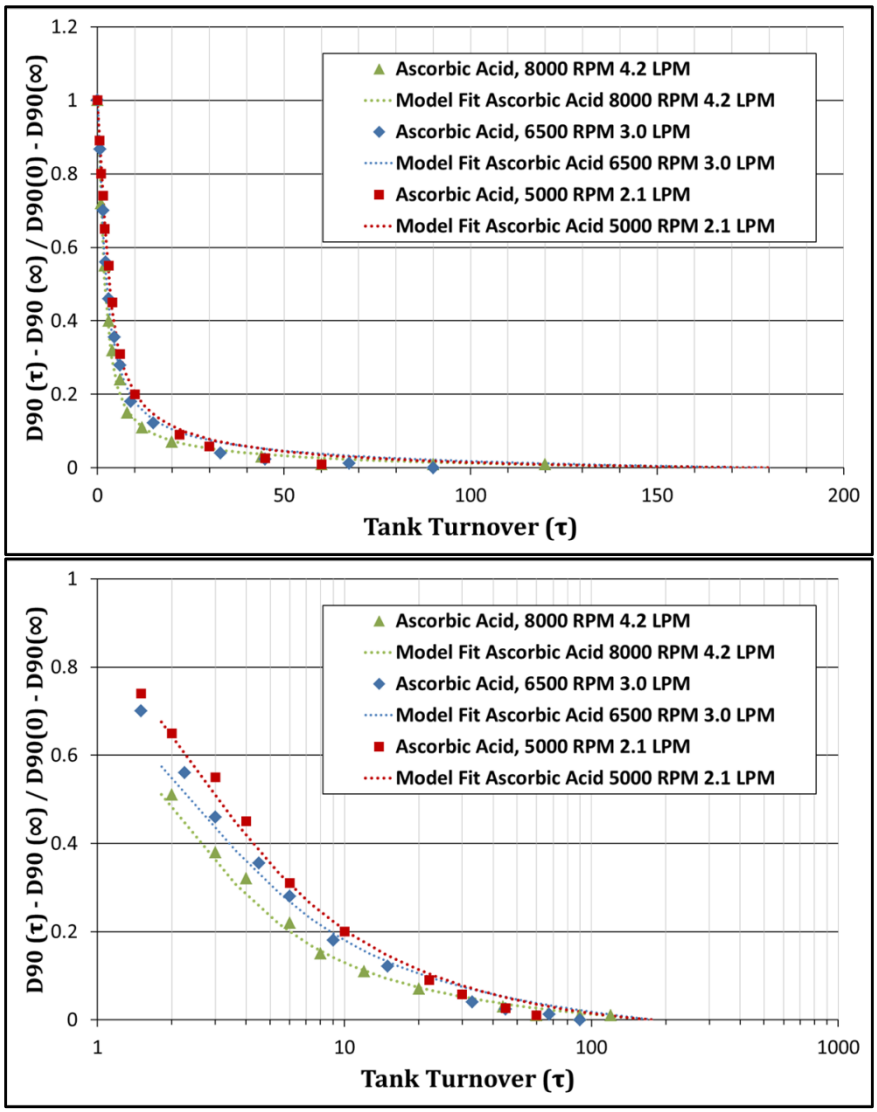

Figure 5.16 - Suitability of breakage kernel based on elastic-plastic model in predicting the milling rate of ascorbic acid in inline mixer with standard shear gap at different milling conditions, dotted lines are the model fits; lower graph is log-normal representation of the data on upper graph

5.4 –Summary

The potential of mechanistic models to predict the crystal breakage behavior in rotor-stator mixers was investigated. Based upon the wet milling experimental data it was demonstrated that:

- Because the size scale of the particles and the operating condition of the rotor-stator mixers, an inertial subrange model for disruptive forces and an elastic-

plastic deformation mechanism for cohesive forces adequately describes the crystal breakage behavior in these mixers.

- It was shown that the Comminution number is useful to correlate the data for geometrically similar mixers. It provides a useful approach to predict the effect of different operating condition as well as crystal physical properties on size reduction.

- The concept of local energy dissipation rate calculated as the power input to the mixer divided by the dispersion zone (volume between rotor and stator plus the volume of stator slots) is developed to correlate the data for devices without geometric similarity. This approach was successful in correlating the maximum stable particle size from mixers with different geometries.

- The mechanistic theory is further utilized to provide breakage kernels based on probability of collision and collision rate theories. Different breakage kernels based on power law approach and exponential approach are developed. The suitability of different kernels to fit the wet milling experimental data are investigated. It was found that an exponential breakage kernel based on elastic-plastic deformation mechanism and inertial subrange turbulence disruptive model is more successful to fit the experimental data.

Chapter 6: CFD Simulations of the Silverson L4R Inline Mixer

In previous chapters, the Silverson L4R inline mixer with the standard shear gap (SSG) and the enlarged shear gap (ESG) was used to investigate the effect of mixer geometry on wet milling performance of different crystal-antisolvent systems. It was shown that the local energy dissipation rate can be utilized to predict the milling behavior of crystals in different mixers with different geometries. To obtain the local energy dissipation rates, knowledge of the power draw of different mixers is required. Here, CFD simulations are employed to find the power draw of the Silverson L4R inline mixer with the standard and the enlarged shear gap.

6.1 –Power Draw and Power Number in Rotor-Stator Mixers

High shear rotor-stator mixers are employed in many processes that include wet milling, homogenization, dispersion, dissolving, and chemical reaction [70]. High turbulence, high deformation rate, and high-speed jet impingement are believed to be the reasons that rotor-stator mixers are efficient as process intensification devices [58,71]. Owing to their widespread use, the body of knowledge for rotor-stator mixers is evolving rapidly. The major advancements are in the areas of flow characterization and fluid dynamics [68,71–77], power draw measurement [63,64,78–82], liquid-liquid dispersion [57–59,83–92], deagglomeration of nanoparticle clusters [55,56,93], and wet milling [50–54].

Power draw specification perhaps is the most crucial measure in a rotor-stator mixer. The costs associated with the power requirements are usually a significant part of the operational costs. Moreover, many scale-up rules and modeling efforts in rotor-stator mixers depend heavily on the specific power input. Power draw is generally a

function of mixer geometry, rotor speed, viscosity, and density of the working fluid (i.e., a fluid with higher density will draw more power from the mixer motor). Based on an energy balance, it is possible to calculate the power input to the system by insulating the mixing system and measuring the rise in temperature. This method is called calorimetric method and requires high sensitivity thermistors and proper insulation. Another method to acquire the power draw of the mixer is to measure the electrical power input to the mixer motor. Based on motor efficiency charts provided by the manufacturer, it is possible to calculate the power output of the motor. In this case it is important to consider the energy loss due to bearings and friction which makes the power exerted to the working fluid lower than the motor's power output. Another common practice is to measure the torque on the mixer shaft. A torque meter is used with a strain gauge transducer and a signal amplifier. When a torque is applied to the shaft, the strain derives a change in the electrical resistance of the gauge, producing an electrical signal that is proportional to the applied torque. This torque can be used to calculate the power draw of the mixer as:

$$P = 2\pi NT \tag{6.1}$$

where P is the power draw, N is rotational speed, and T is the torque.

Padron [63] used a strain gauge load cell to measure the power draw of different mixers with different stator heads. He carefully examined the different available length scales in the rotor stator mixers, such as rotor diameter, shear gap width, and hydraulic diameter of stator holes. He reported that the definitions of the power number (N_P) and Reynolds number (Re) based on rotor diameter, as shown in equations 6.2 and 6.3, can be used satisfactorily to correlate the power draw data for a

rotor-stator mixer. In the equations below, ρ is fluid density, N is rotor speed, D is rotor diameter, μ fluid viscosity, and P is the power draw of the mixer.

$$Re = \frac{\rho N D^2}{\mu} \tag{6.2}$$

$$N_P = \frac{P}{\rho N^3 D^5} \tag{6.3}$$

Padron demonstrated that the power number of rotor stator mixers is inversely proportional to the Reynolds number up to Re = 100 (laminar regime) and remains constant above Re = 10,000 (turbulent regime). For the Silverson L4R batch mixer in the turbulent regime, he reported a power number of 1.7 for the disintegrating head, 2.1 for the slotted head, and 2.3 for the square hole stator head. It is important to note that the instantaneous power draw of the mixer varies as the rotor blades sweep the stator slots in the mixing head and the reported values are an average taken in one full revolution of the rotor.

Recently, with the development of high speed computers and advanced numerical methods it is feasible to compute the flow field characteristics inside a rotor-stator mixer with both Reynolds-Averaged Navier-Stokes (RANS) and large-eddy simulations (LES). This allows predicting the extent of the hydraulic forces and the amount of torque exerted by fluid to the rotor. Extensive research was conducted by Kevala (2001) on two-dimensional sliding-mesh simulations of an inline rotor stator mixer. In this study the flow fields for IKA prototype mixer with two different shear gap widths were simulated and the results were compared to experimental measurements. It was found that the RANS simulation results provided a good

qualitative estimate of the velocity field. However, quantitatively, the three-dimensional flow field was not well-modelled with two-dimensional simulation.

Barailler et al. [72] studied the behaviour of a viscous fluid in a VMI-Rayneri batch rotor-stator mixer with a shear gap of 1.04 mm. A three-dimentional CFD simulation using POLY3D was used to predict the torque, shear stress, flow rate, and velocity field for a number of low rotational speeds. They showed that the simulation result for torque analysis was in good agreement with experimental data. Furthermore, they reported that the maximum stress experienced in shear gap was consistent with the nominal shear stress defined as the tip speed divided by the shear gap width.

Utomo et al. [73,74] studied the flow field in a Silverson L4R batch mixer with different stator heads, i.e. disintegrating, slotted, and square hole. For the CFD simulations, they used a transient sliding mesh technique, standard k–ε model, and enhanced wall function with 60 time steps per rotor revolution and 1.1 to 1.4 million computational cells. The mixing head is positioned at the center of the holding tank as shown in Figure 6.1.a. They calculated the power numbers for different stator geometries and reported that the predicted values are 10 to 20% lower than those measured experimentally by Padron (2001). Their simulation results for power number and Padron's experimental measurements of power number for different stator geometries in the Silverson L4R batch mixer are given in Table 6.1.

Table 6.1- Power number discrepancy between measurement and simulation results of Silverson L4R batch mixer with different stator geometries

Stator geometry	N_P (measurement [63])	N_P (simulation [74])	Discrepancy
Disintegrating head	1.7	1.53	10%
Slotted head	2.1	1.66	20.9%
Square hole head	2.3	2.05	10.9%

Yang [68] conducted RANS simulations for the Silverson L4R batch mixer (lab scale) at constant tip speed to study the scale up strategies. In particular, the Silverson L4R batch mixer with a slotted head stator was investigated. The mixing head was positioned in an off-center configuration (Figure 6.1.b) as suggested by the manufacturer to enable higher speed operations without vortexing to promote top to bottom mixing. A transient sliding mesh technique, realizable k–ε model, and enhanced wall functions with 720 time steps per rotor revolution was used to simulate the flow field. Several mesh with different number of computational cells, 1.6, 4.2, and 5.6 million, was used for simulation. A significant change in the flow field characteristics with the increase of the mesh size from 1.6 to 4.2 million cells was reported, whereas the differences in the mean and turbulent flow field between 4.2 and 5.6 million cell simulations were not significant. The power number obtained from 1.6 million cell simulations was 1.7 whereas the power number obtained from 4.2 and 5.6 million cells simulations was 2.1 which is in agreement with Padron's experimental power draw measurements for the slotted head stator.

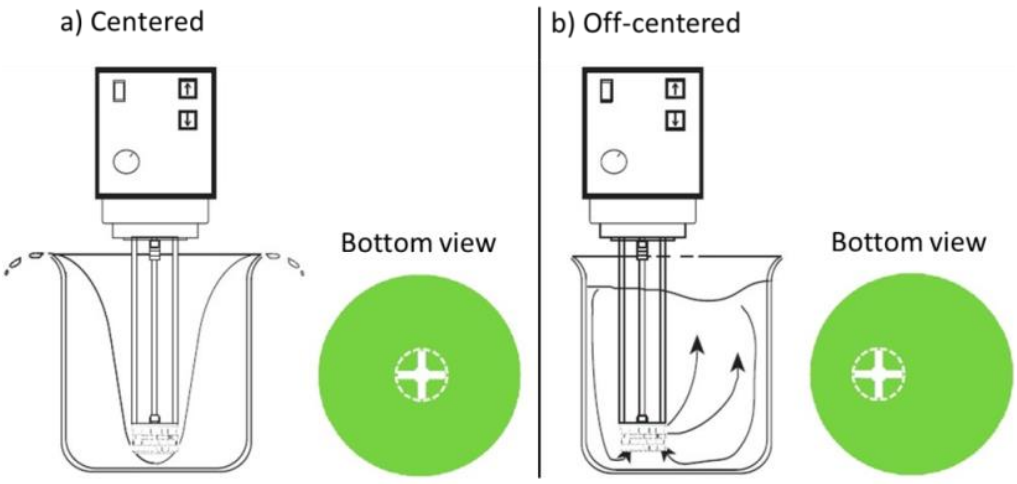

Figure 6.1- (a) centered and (b) off-centered configurations of Silverson L4R batch mixer inside a holding tank

Ko [76] conducted a three-dimensional simulations of an IKA inline rotor stator mixer for different rotor speeds and flow conditions. He refined the number of computational cells in the shear gap to resolve the high shear stresses and the velocity field in this region. An increase in mesh size from 2.8 to 10 million cells (increasing the number of cells across the shear gap) was necessary for a mesh independent simulation of low-speed low-flow condition.

The investigations summarized above indicate the necessity for a high density of computational cells to resolve the large velocity gradient in shear gap, stator slot, and slot jet regions of a rotor stator mixer. It is important to note that the size of the cells in the smallest scale of the geometry has a repercussion on the total number of cells because the size of adjacent cells must be in the same order to produce a consistent mesh. As a result, when a high density mesh is used in the shear gap region, this concentration propagates into the rest of the domain.

6.2 –Geometry Details and Grid Generation Strategy

The Silverson L4R inline rotor-stator mixer assembly consists of an inlet pipe, outlet pipe, and the mixing head where the rotor and stator are located as shown in Figure 6.2. The rotor is a radial 4-blade impeller that rotates inside a stator with square-hole slots with clearance or shear gap of 0.2 mm. The stator head has 104 slots with the opening of 2.4 mm * 2.4 mm * 2 mm. The thickness of the stator wall is 2 mm and the height and inner diameter are 18.9 mm and 31.5 mm, respectively. The geometry details are summarized in Table 6.2.

Figure 6.2- Silverson L4R inline mixer. The image at the left is the entire assembly with attached inlet and outlet pipes. The right image show the high-shear mill head with the rotor surrounded by the stator.

Table 6.2- Geometry details of Silverson L4R inline and batch mixers

Mixer Dimensions	Silverson L4R Inline Mixer	
	Standard Shear Gap	Enlarged Shear Gap
Rotor Diameter	31.1 mm	28.2 mm
Shear Gap Width	0.2 mm	1.7 mm
Square Hole Stator	104 Square Hole Slots	
Size of Stator Slots	2.4 mm × 2.4 mm × 2.0 mm	
Thickness of stator	2.0 mm	
Height of stator ring	18.9 mm	
Inner Diameter of stator	31.5 mm	

The standard rotor diameter is 31.1 mm. This diameter was modified to provide a range of shear gap widths. In this study, different shear gap widths of 0.2, 0.23, 0.85, 1.65, and 1.70 mm were simulated. The goal was to investigate the effect of clearance width on power draw of the mixer. The SSG has 0.2 mm and the ESG has 1.70 mm clearance between rotor and stator. Figure 4.33 shows a simplified schematic of the SSG and ESG labelled with characteristic dimensions.

ANSYS Workbench was used to develop the computational grid. The model volume was divided to two primary zones: rotating zone and stationary zone as shown in Figure 6.3. This is needed to model flow around the rotor and establish regions with different frames of reference. Different methods exist to solve the flow field around a rotating body such as the single reference frame (SRF), multiple reference frame (MRF), and sliding mesh techniques. For rotor-stator mixers, the sliding mesh technique is most successful for evaluating the time-periodic features of the flow, and was thus applied to the Silverson inline mixer in this work. In this technique, the model volume must be separated into rotating and stationary zones. At each time step, the cells in the rotating zone rotate with a given velocity and hence, the relationship between cells at the interface of stationary and rotating zones must be re-evaluated similar to a non-conformal surface.

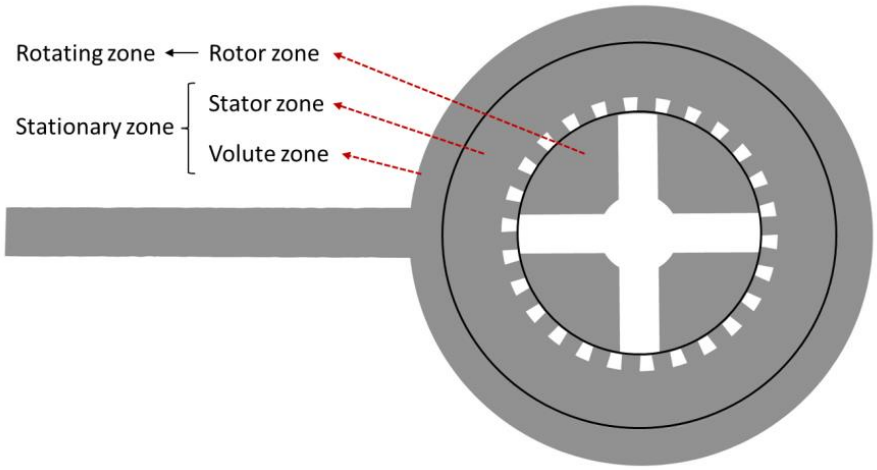

Figure 6.3- Illustration of rotating and stationary zones – the stationary zone is further divided into stator and volute zones for better control of meshing strategy

The stator slots have cubic geometry that is connected to a cylindrical wall. This geometry makes it difficult to obtain hexagonal cells in this region. Therefore, the stationary zone is divided to two zones: stator and volute. This strategy helped to get a symmetric stator zone that can be divided to 13 identical pieces. The grid generation

was performed on one piece; it was then rotated to give the complete stator volume. This in turn gave more control on grid generation process and resulted in consistent hexagonal cells in this region. The zone definitions are illustrated in Figure 6.3. The rotor zone includes the volume between the rotor blades and half of the shear gap. Hexahedral meshing was used exclusively in this zone. Using the sliding mesh technique, the rotor zone was set to rotate with the speed of 0.5° per time step. The volute volume is comprised of the inlet and outlet pipes as well as the volume between the face of the stator zone and the volute cover. The stator zone includes half the volume of the shear gap, stator slots, and the volume behind the stator. This fluid zone was also meshed using hexahedrons only and is in a stationary reference frame. The interface between each zone is non-conformal, meaning that a direct one-to-one relationship between interface cells of the adjacent zones does not exist. This requires Fluent to use an interpolation algorithm to calculate flow across the interface. Because of the rotation of the rotor zone, the relationship between rotor cells and stator cells at the interface must be re-evaluated at each time step.

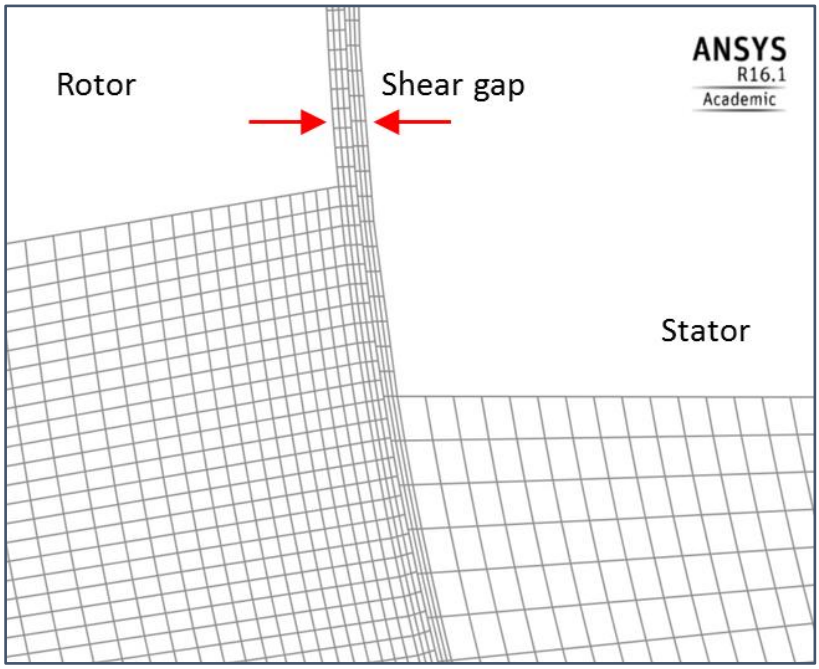

Figure 6.4 - Grid refinement in standard shear gap, Silverson L4R inline mixer

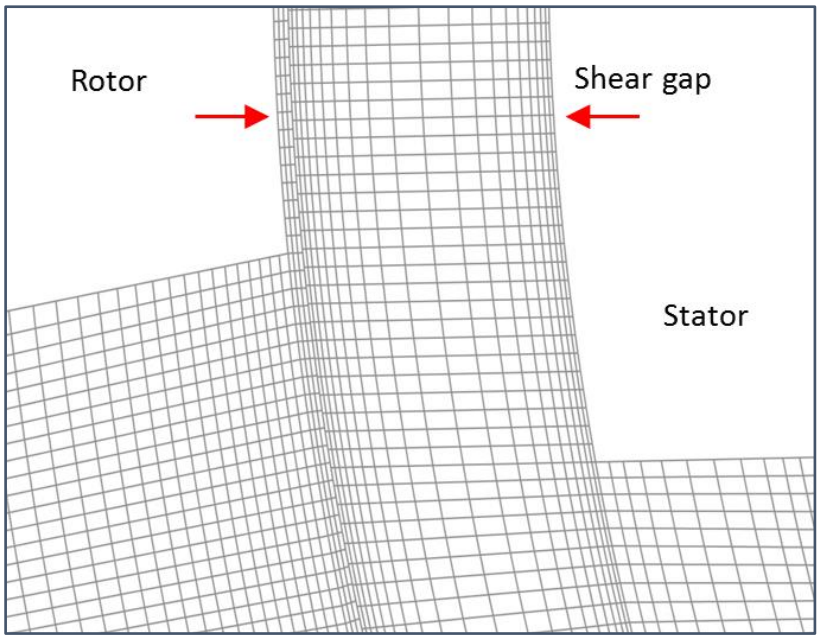

Figure 6.5 - Grid refinement in enlarged shear gap, Silverson L4R inline mixer

The smallest length scale in rotor-stator mixers is the shear gap width, and therefore the grid was characterized primarily by the number of cells across the shear gap. This in turn has a significant influence on the total number of cells in the model because it is generally desired that the aspect ratio of cells (i.e., the ratio between the length of the longest side and the length of the shortest side) not exceed 10:1. Initially, a coarse mesh with 2 million cells was produced and simulated. The output from this preliminary mesh was read into the fine mesh to initialize the flow field. The fine grid consists of 8 million cells with 6 cells across the shear gap for the standard shear gap and 20 cells for the enlarged shear gap as shown in Figure 6.4 and Figure 6.5.

6.3 –Solution Methods

The RANS equations were used to model the flow field in full 3D geometry. The Boussinesq approximation was applied to approximate the Reynolds stresses in RANS equations, requiring additional equations to model the turbulent viscosity. The realizable k-ε turbulent model was used to calculate turbulent viscosity, where k is

turbulent kinetic energy and ε is the turbulence energy dissipation rate. To solve these transport equations, a pressure-based solver within the commercial software package, ANSYS Fluent was used. Fluent converts the continuous transport equations into discretized forms around each computational cell. Balance of the transport equations in each cell implies overall conservation within the model. A second order discretization for pressure, a second order upwind discretization for momentum, turbulent kinetic energy, and turbulence energy dissipation rate, and a second order implicit scheme for time stepping were used in this study. For boundary conditions, pressure inlet and pressure outlet with zero-gauge pressure were used.

The finite volume equations at each time step essentially represent a boundary value problem, so the treatment of fluid boundary layers at model surfaces is critically important in CFD simulations. This is particularly important in the current work because the shear gap, one of the primary regions of interest, is strongly affected by boundary conditions. There are different models to approximate the flow near the walls. Kim [77] reported that both non-equilibrium wall functions (NEWF) and enhanced wall treatment (EWT) produce similar results in comparison between particle image velocimetry data and CFD simulations for an inline rotor-stator mixer, but EWT is computationally more efficient. Therefore, a EWT model was employed here to model the near wall velocities.

In this study, the rotor was set to rotate in clockwise direction (from the top view), and the rotation rates were 4000 and 8000 rpm. Water was used as the working fluid with density and viscosity of 998.2 Kg/m3 and 0.001003 Pa·s respectively. The y-axis coincided with the vertical axis of the shaft. The origin of the coordinate system was located on the mid-plane of the rotor and the positive y direction was

upward. The convergence criterion on each time step was evaluated based on the residuals. They must reach a value smaller than 10^{-5} before proceeding to the next time step. Here, the residual was calculated as the imbalance in the algebraic equations summed overall the computational cells.

6.4 –Simulation Results and Discussion

The coordinate system used in the Silverson inline L4R mixer is shown in Figure 6.6. The XZ plane at y=-130 mm is shown where θ is the angle between the centerline of the rotor blade and the x axis. The rotor rotates in the clockwise direction.

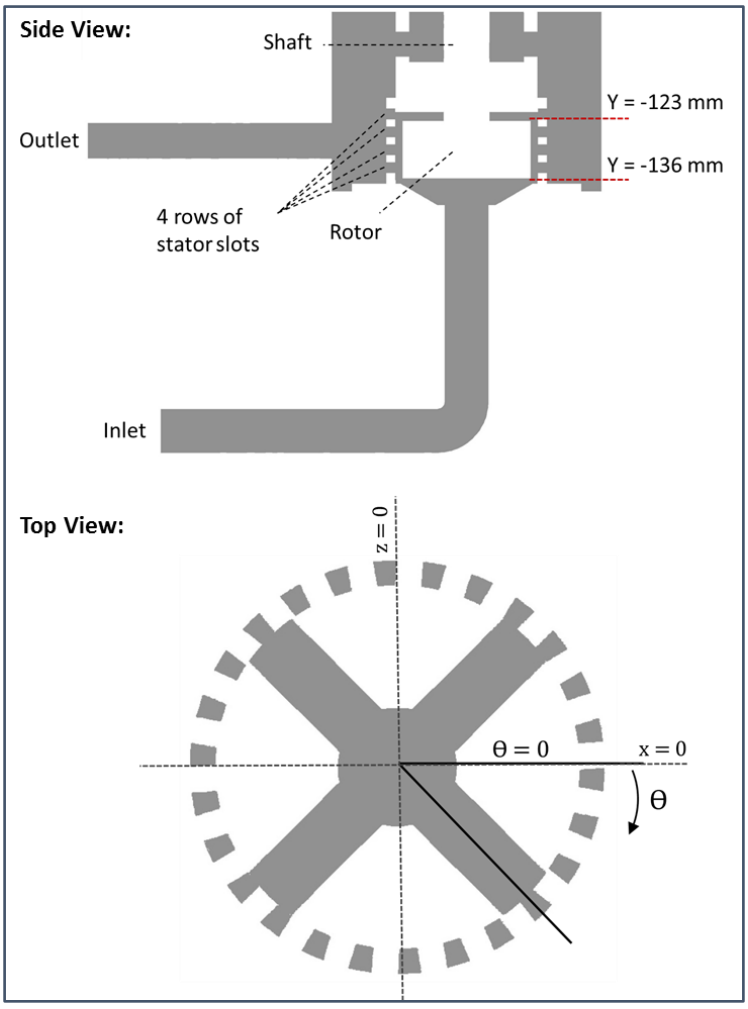

Figure 6.6 - The coordinate system shown on the mid-plane of Silverson L4R inline mixer

6.4.1 –Velocities within the Rotor and Stator Zones

The high-speed rotation of blades in the clockwise direction generates a tangential flow in the rotor zone and shear gap region. This high speed tangential flow, in shear gap region collide with the downstream edge of the stator slot, and hence, the flow direction changes to tangential-radial and eventually to the radial direction and forms strong jets. These strong jets emerging from the downstream edge of the slots develop a counterclockwise flow in the volute region behind the stator, ultimately discharging the fluid through the outlet pipe. Figure 6.7 to Figure 6.11 illustrate the velocity patterns on the XZ plane at y = -130 mm for both the standard and enlarged shear gap at blade positions of θ = -23, -13, 0, 13, and 23 degrees respectively. The different positions of the blade as well as the magnification used in this figure are intended to give a clear picture of the flow field in shear gap and stator region. Different flow patterns are observed as the jets emerge through the stator holes. There is a significant amount of flow impinging on the downstream edge of the stator creating a recirculation region (vortex), where there is a strong jet on one side and low speed recirculation flow on the other side of the stator slots.

For the case of the SSG, the jets dissipate close to the stator head and therefore the vortices are bounded inside the stator sloth. The center of these vortices moves in a circular path as a function of the rotor blade position. A different flow pattern is observed for the case of the ESG where two distinct regions of flow exist: a region of high speed tangential velocity that impinges on the downstream edge of stator and escapes further into the volute extending to the volute wall, and a low velocity region that re-enters the stator slot from the volute and gets entrained into the outward flowing stator jet. The resulting flow pattern has larger recirculation loops which

extend into the volute area. This can be explained by considering the narrower jet structure and lower intensity of counter clockwise tangential flow in the volute area for the ESG. Furthermore, for the case of the SSG with narrow clearance, the higher intensity of the impingement on the stator edge causes the jet pattern to change direction to radial and then tangential in the direction opposite to the rotation. This in turn creates a higher pressure resistance and hence shorter jet length. It is important to note that for both cases, when the blade moves towards the downstream edge, the jet speed decreases and the recirculation region widens as the blade blocks the fluid in the rotor region from passing through the stator square hole. The flow field animations are given in Appendix E.

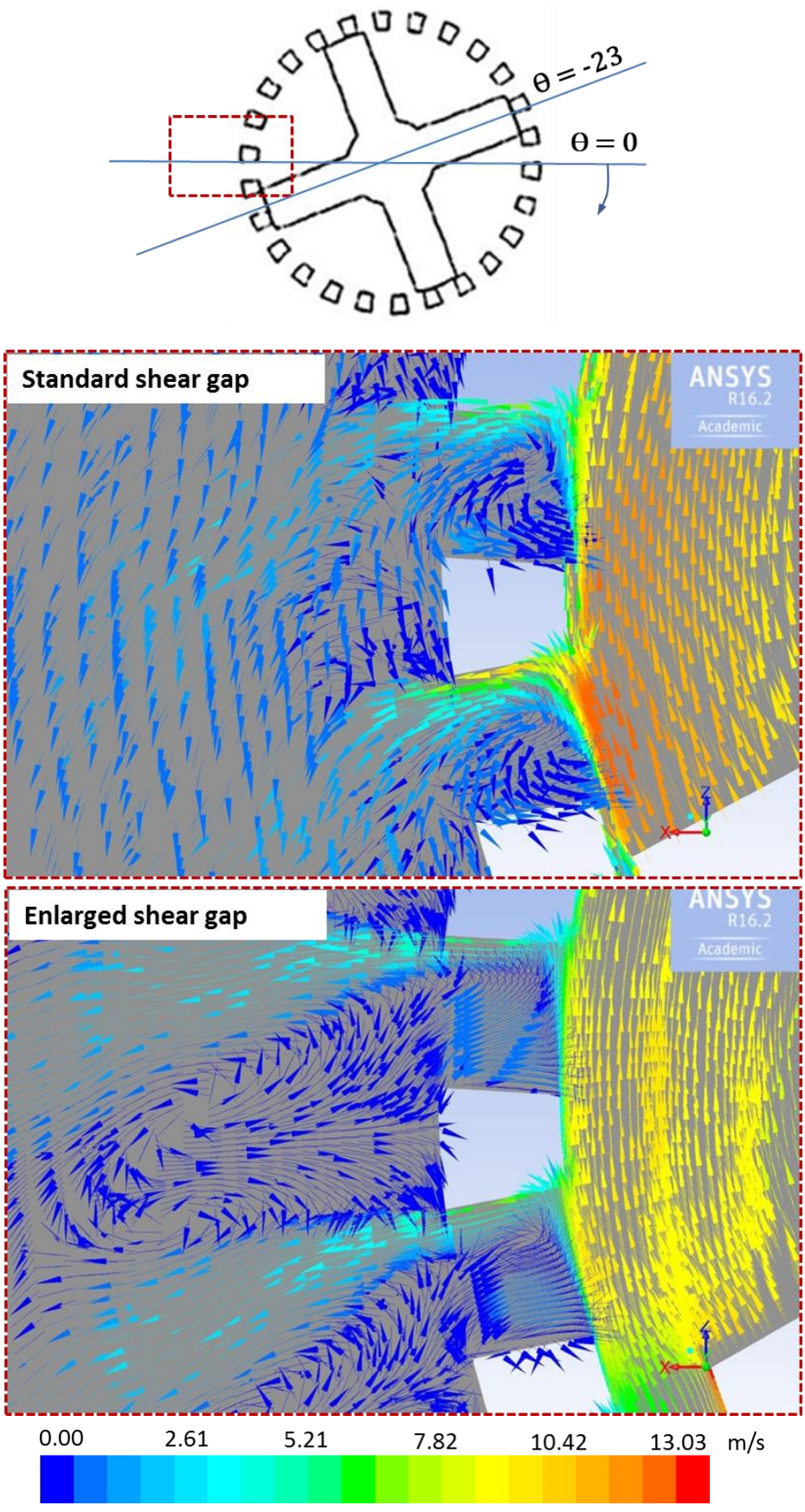

Figure 6.7 - Velocity vector flow field for Silverson L4R inline mixer with standard and enlarged shear gap at 8000 rpm and rotor position of θ = -23°

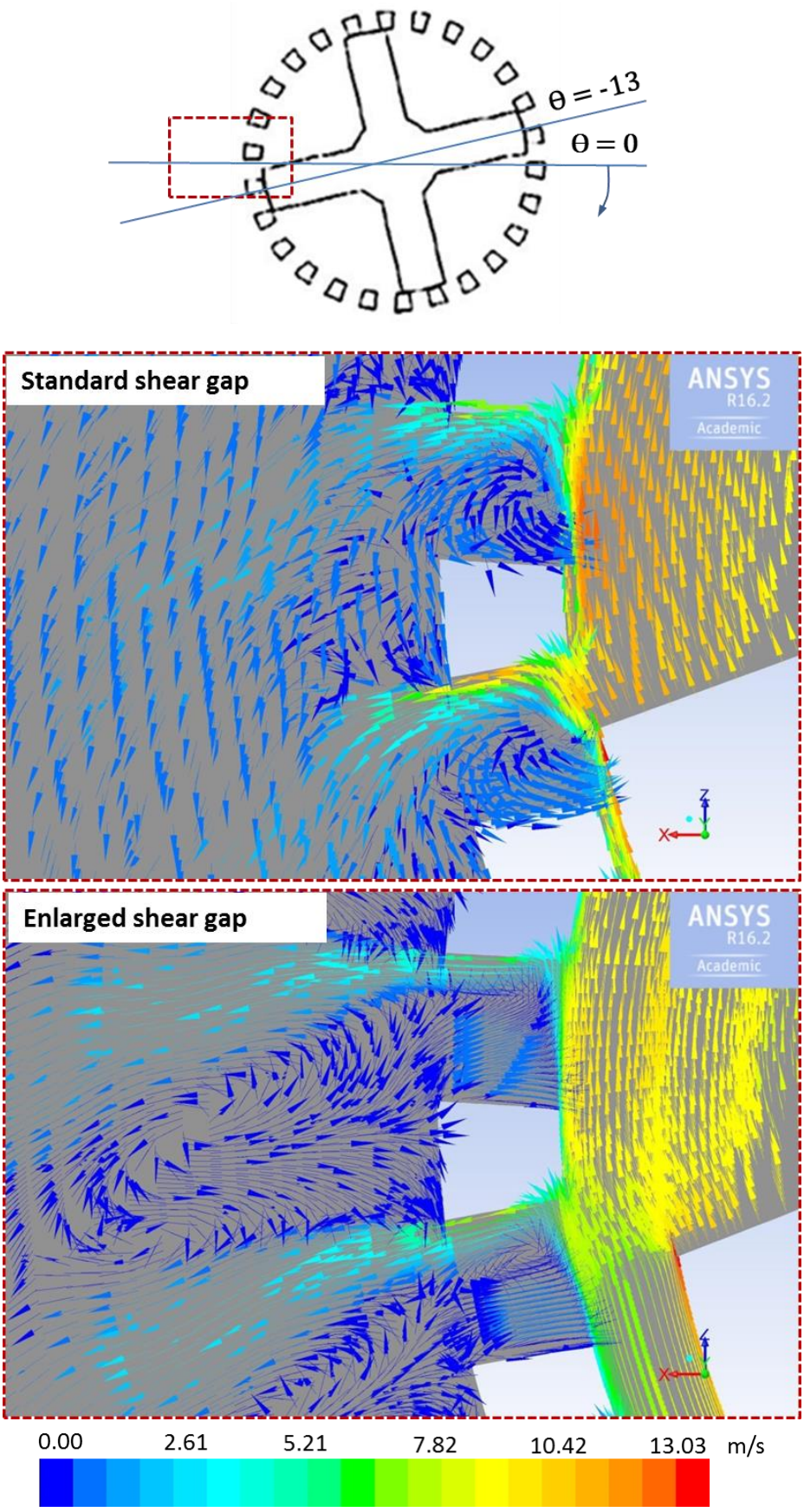

Figure 6.8 - Velocity vector flow field for Silverson L4R inline mixer with standard and enlarged shear gap at 8000 rpm and rotor position of Θ = -13°

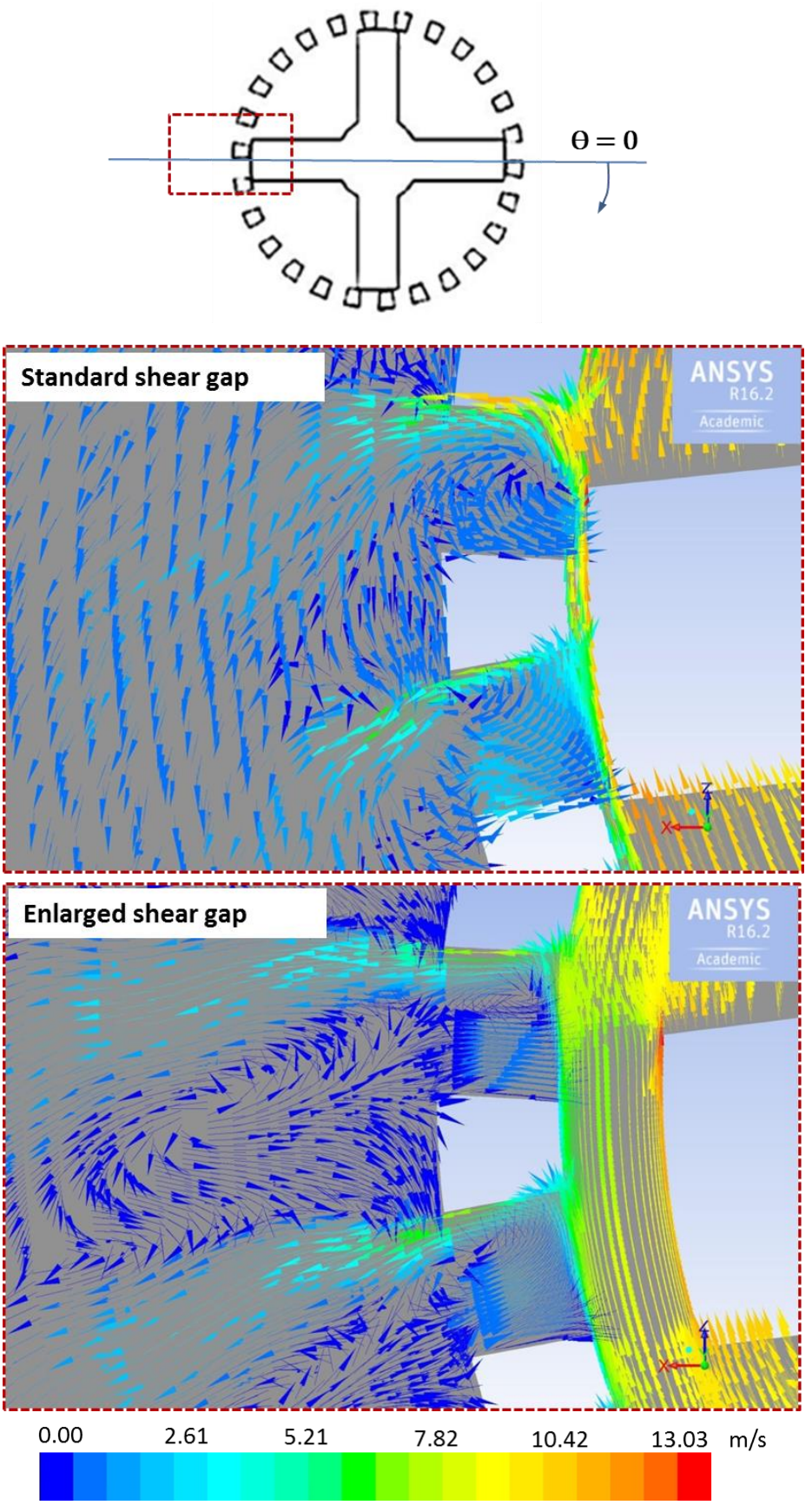

Figure 6.9 - Velocity vector flow field for Silverson L4R inline mixer with standard and enlarged shear gap at 8000 rpm and rotor position of Θ = 0

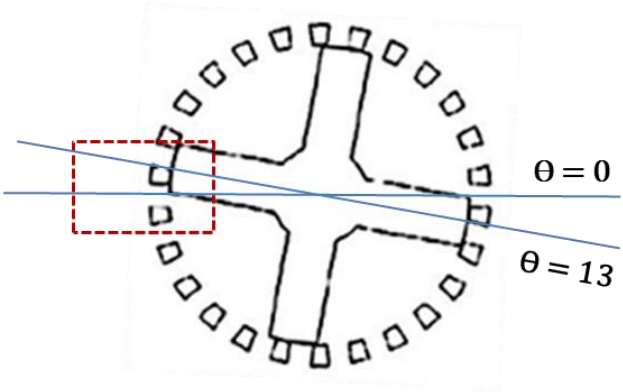

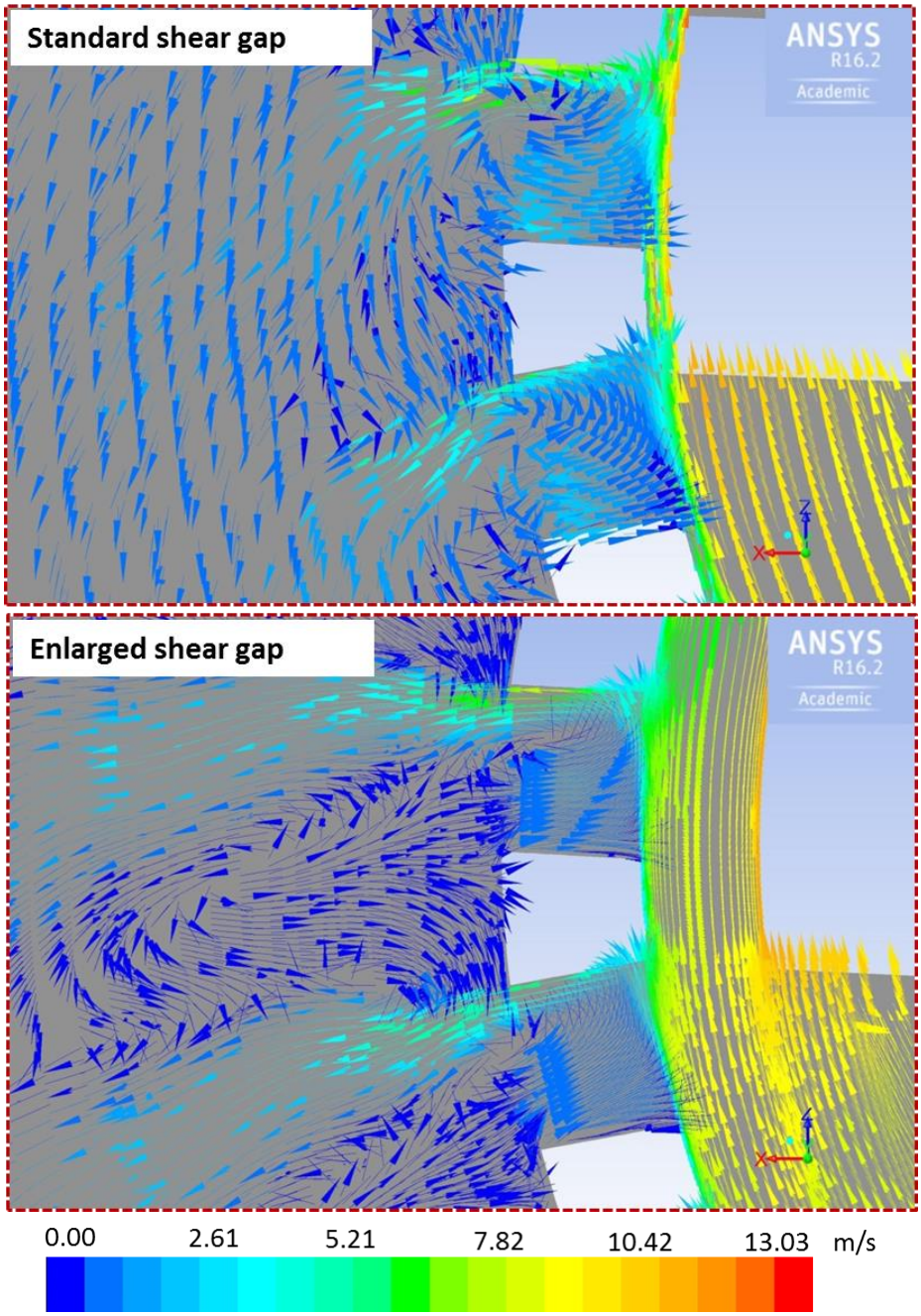

Figure 6.10 - Velocity vector flow field for Silverson L4R inline mixer with standard and enlarged shear gap at 8000 rpm and rotor position of Θ = 13°

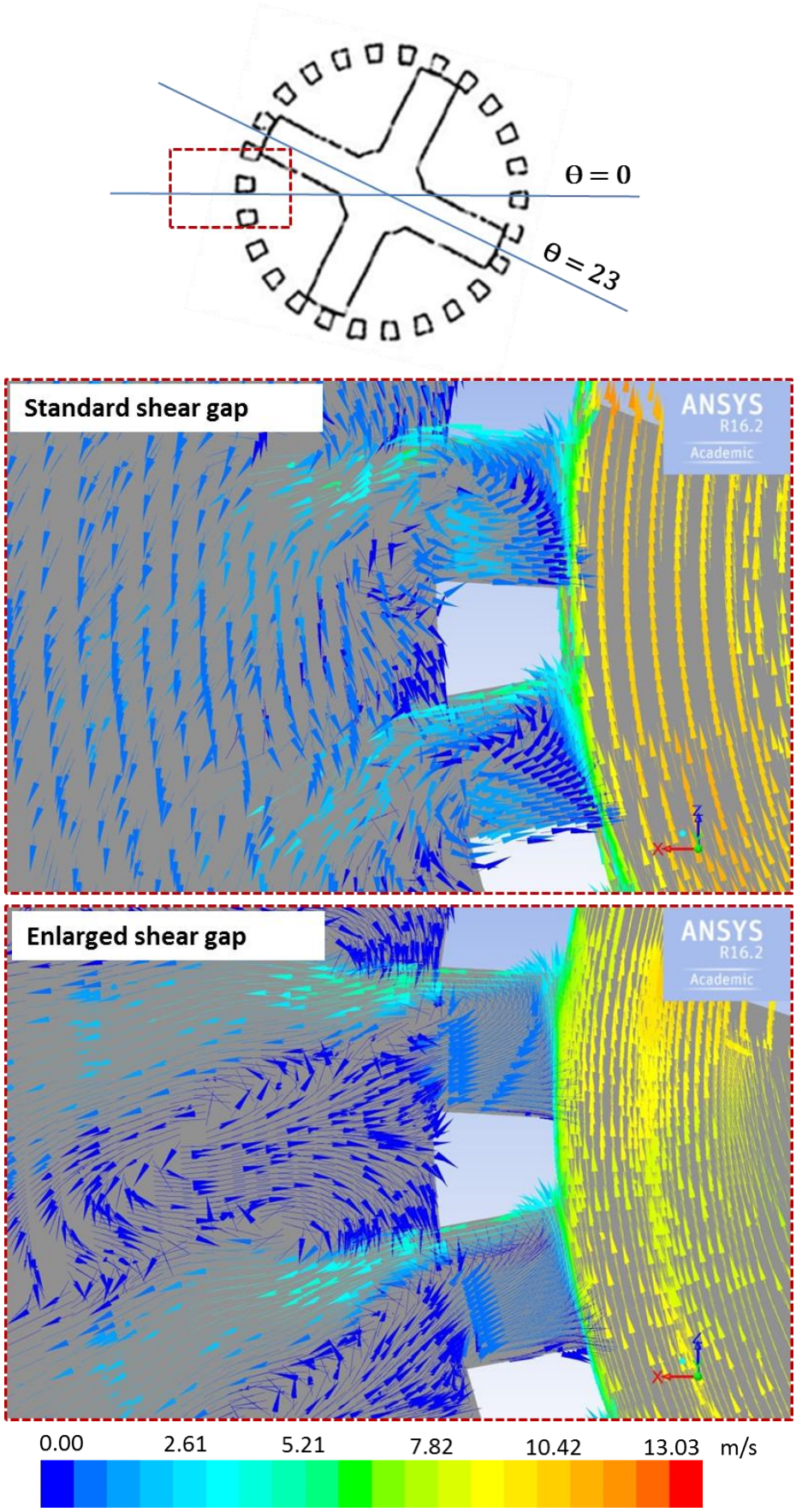

Figure 6.11 - Velocity vector flow field for Silverson L4R inline mixer with standard and enlarged shear gap at 8000 rpm and rotor position of Θ = 23°

6.4.2 –Total Energy Dissipation Rate and Turbulent Kinetic Energy

The contours of normalized turbulent energy dissipation rate on XZ plane of the mixer with y = -130 mm are provided in Figure 6.12 to Figure 6.16 for both the SSG and ESG configurations at different rotor positions and at a rotational speed of 8000 rpm. The dissipation rate values are normalized by N^3D^2 where D is always the standard rotor diameter to facilitate the comparison. The simulation results show a non-uniform distribution of energy dissipation rate in different regions of the mixer; the intensity of dissipation rate is at least one order of magnitude larger in the shear gap and jet region compared to other regions in the mixer. Furthermore, the mixer with SSG is more successful in focusing energy dissipation in the shear gap and jet region and creating larger volumes of high energy dissipation rates compared to the mixer with the ESG. It is important to note that for both cases, the blade position with respect to the stator sloth affects the intensity and volume of the high energy dissipation region in the jet zone. This effect is more pronounced for the case of the SSG.

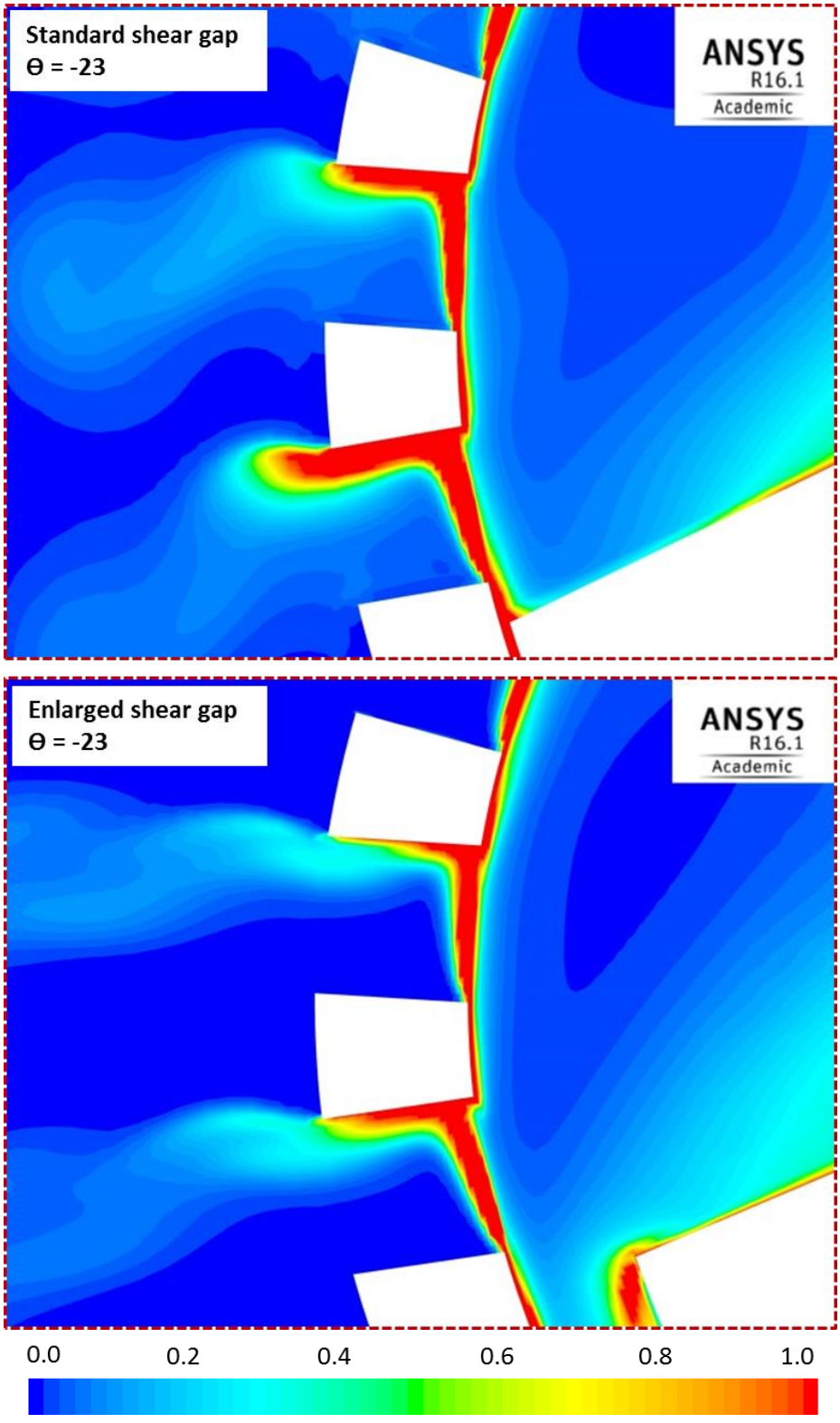

Figure 6.12 - Contours of normalized turbulent energy dissipation rate for Silverson L4R inline mixer with standard and enlarged shear gap at 8000 rpm and Θ = -23° (normalized by N^3D^2 of SSG)

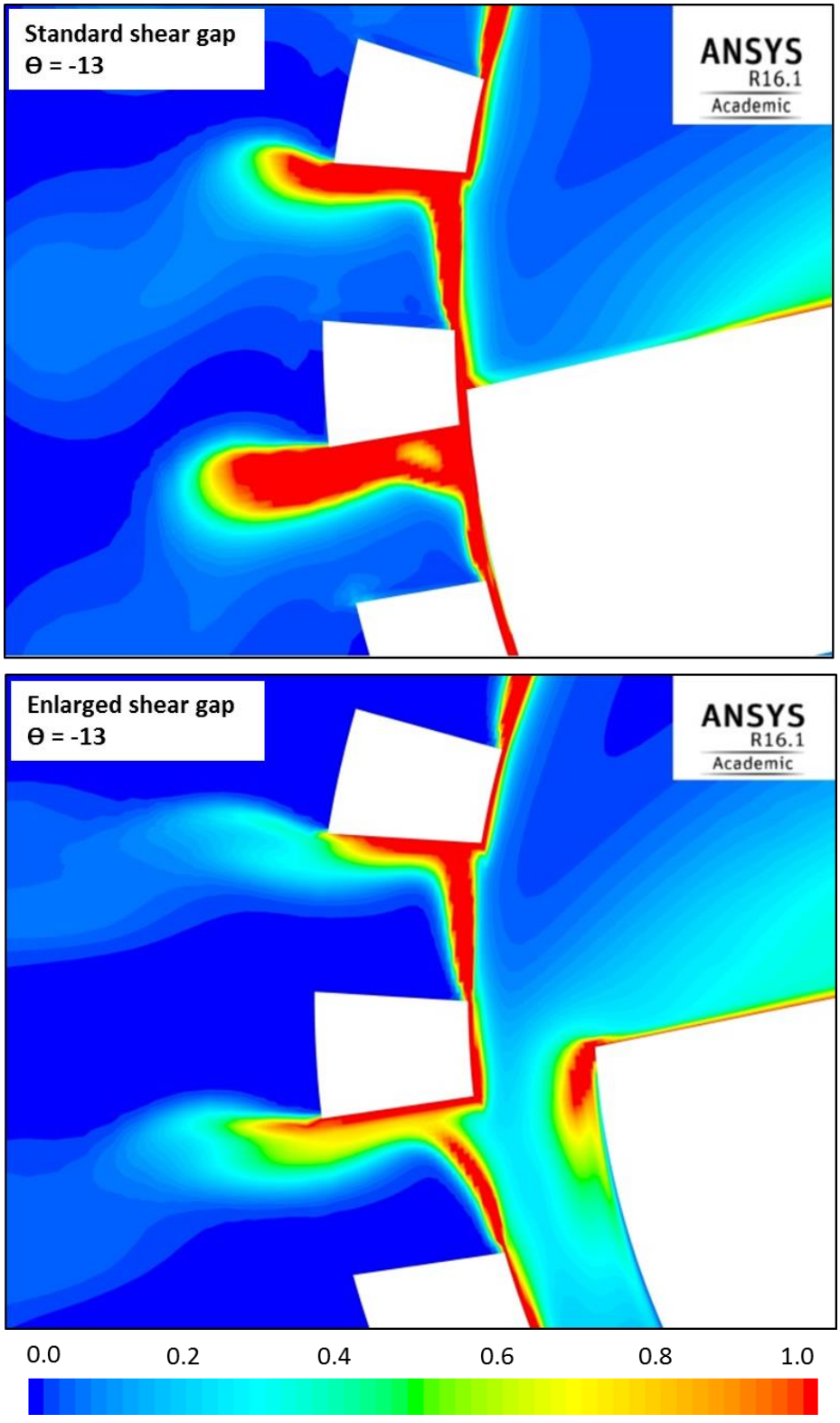

Figure 6.13 - Contours of normalized turbulent energy dissipation rate for Silverson L4R inline mixer with standard and enlarged shear gap at 8000 rpm and Θ = -13° (normalized by N^3D^2 of SSG)

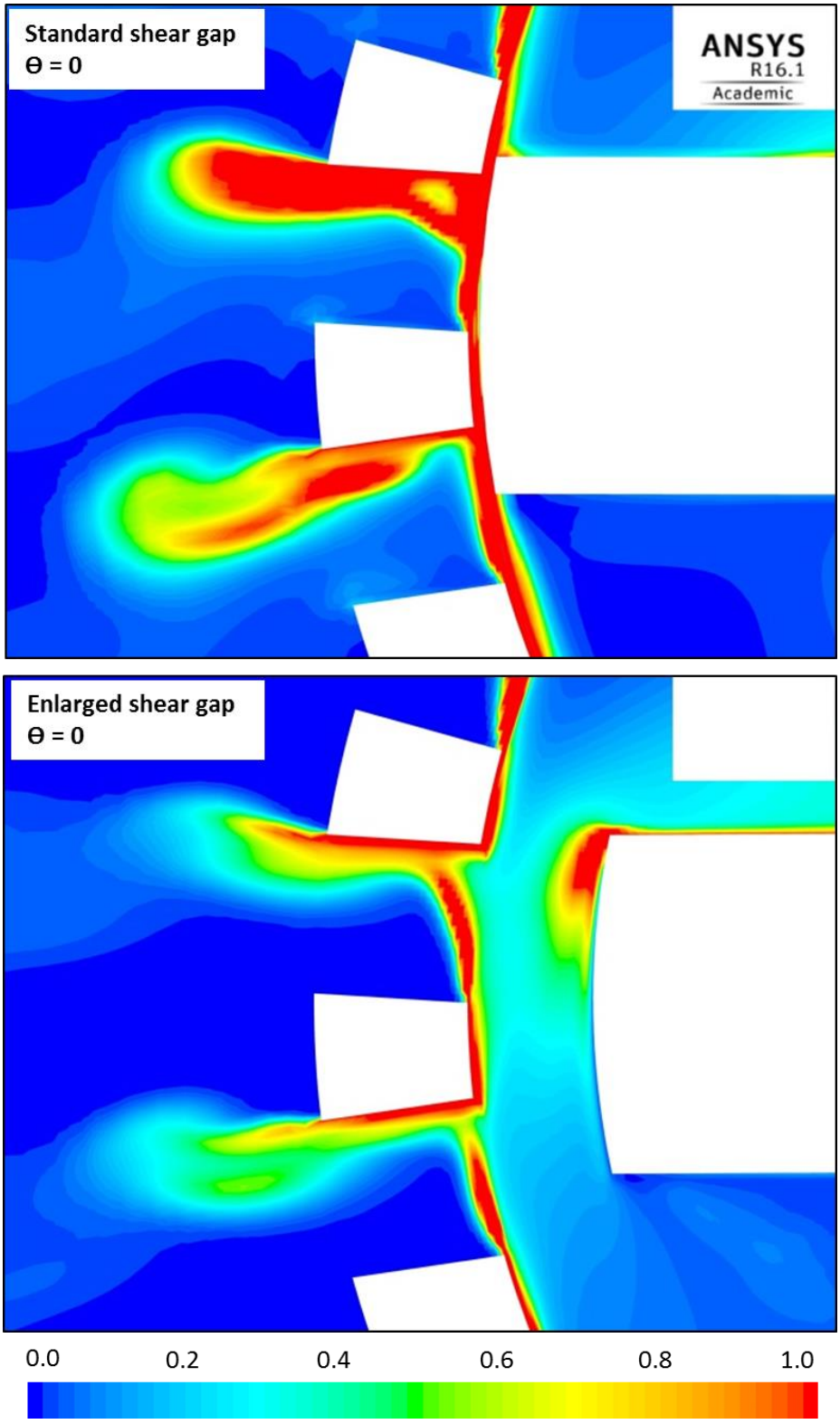

Figure 6.14 - Contours of normalized turbulent energy dissipation rate for Silverson L4R inline mixer with standard and enlarged shear gap at 8000 rpm and Θ = 0 (normalized by N^3D^2 of SSG)

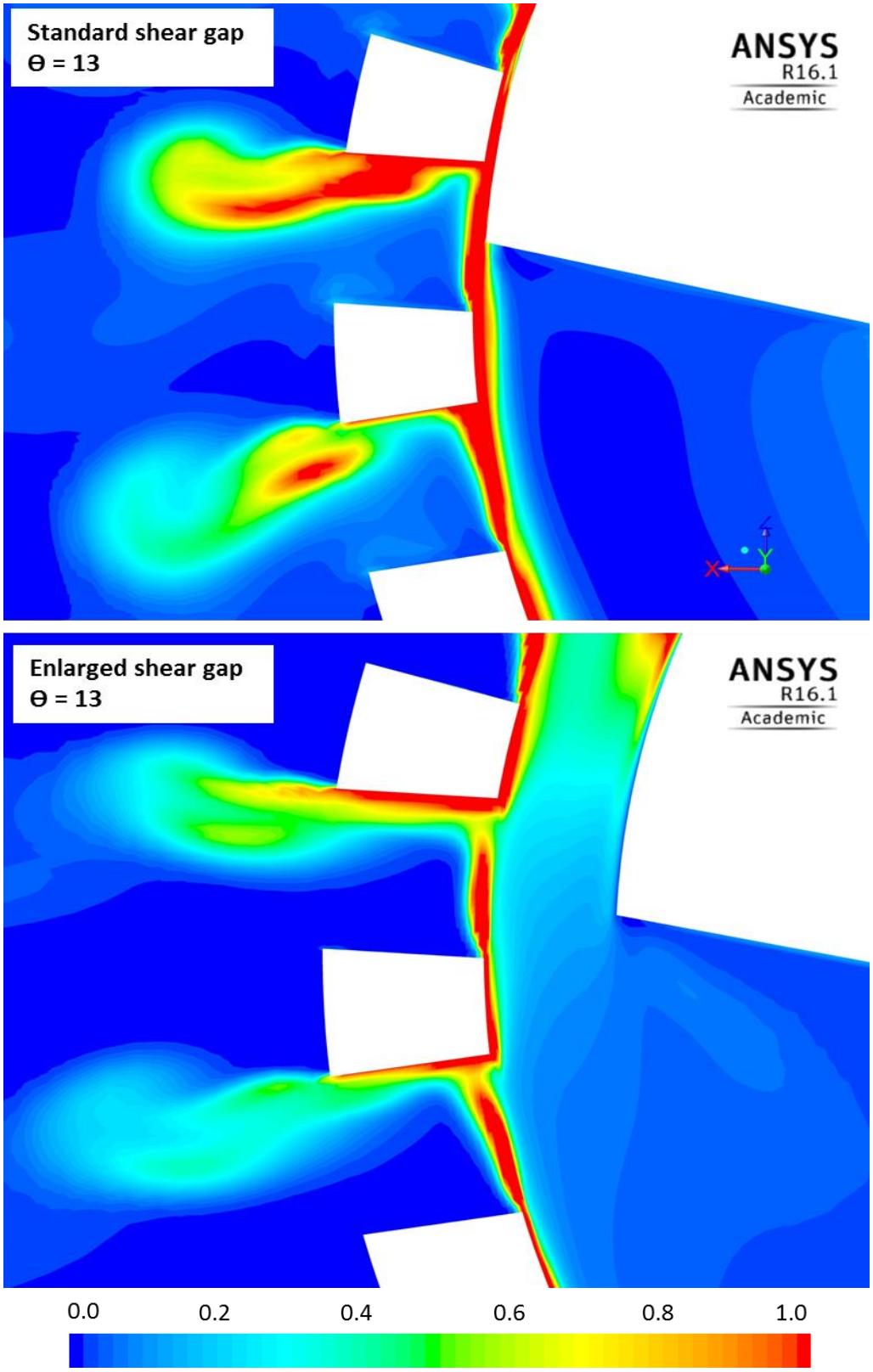

Figure 6.15 - Contours of normalized turbulent energy dissipation rate for Silverson L4R inline mixer with standard and enlarged shear gap at 8000 rpm and Θ = 13 (normalized by N3D2 of SSG)

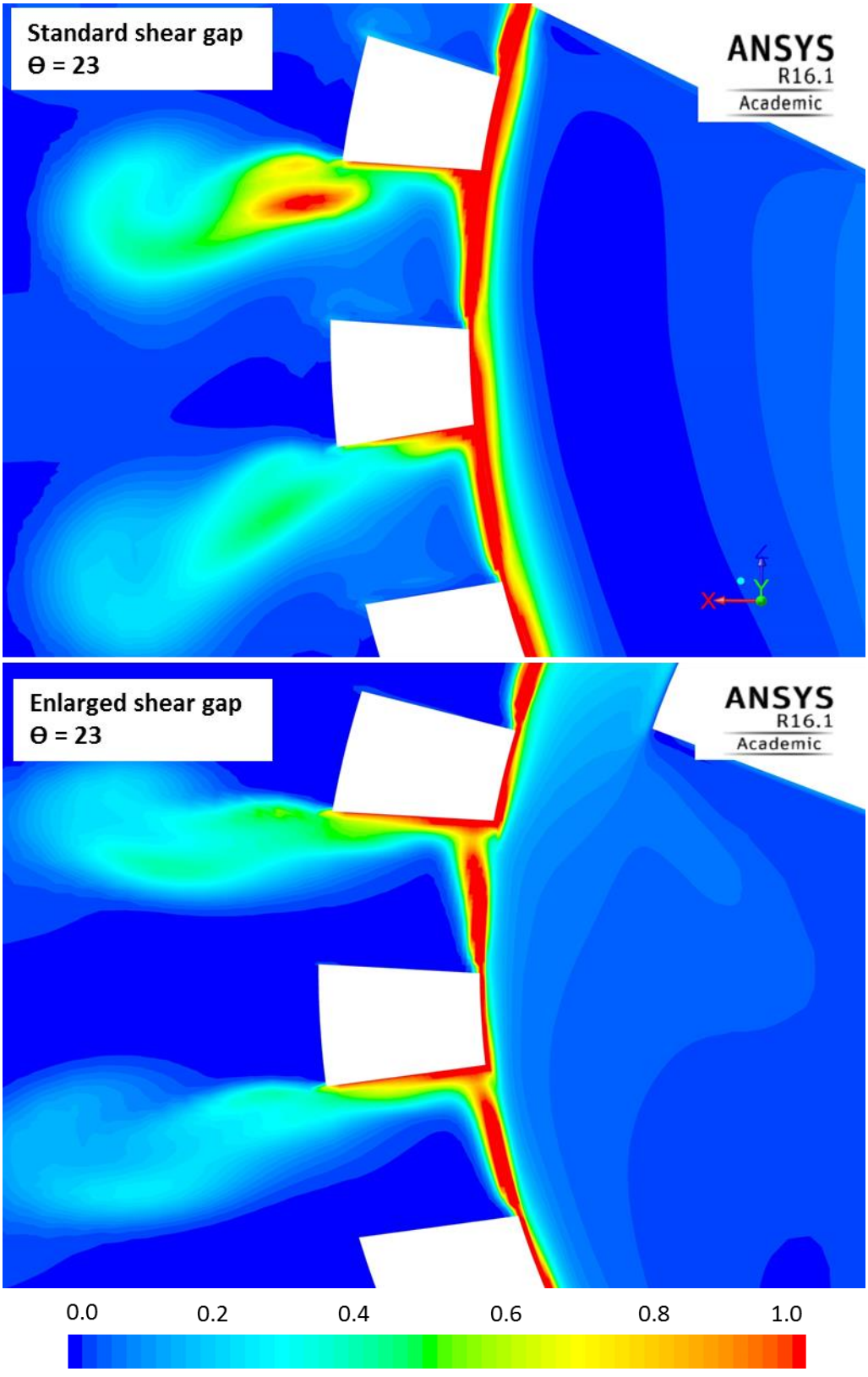

Figure 6.16 - Contours of normalized turbulent energy dissipation rate for Silverson L4R inline mixer with standard and enlarged shear gap at 8000 rpm and Θ = 23 (normalized by N3D2 of SSG)

The contours of turbulent kinetic energy (TKE) are provided in Figure 6.17 to Figure 6.21 for both the SSG and ESG configurations at different rotor positions. TKE is a measure of macroscale eddy fluctuating velocities in turbulent flow. This energy produced at the macroscale level with large eddies is transferred down to smaller and smaller eddies as an energy cascade and finally dissipates by viscous forces at or below the Kolmogorov scale. The simulation results show a higher intensity of TKE in the rotor swept volume and jet regions compared to other regions in the mixer. In the case of SSG, the velocity of impingement on the downstream edge of stator sloth is higher resulting in higher intensity of TKE compared to ESG configuration.

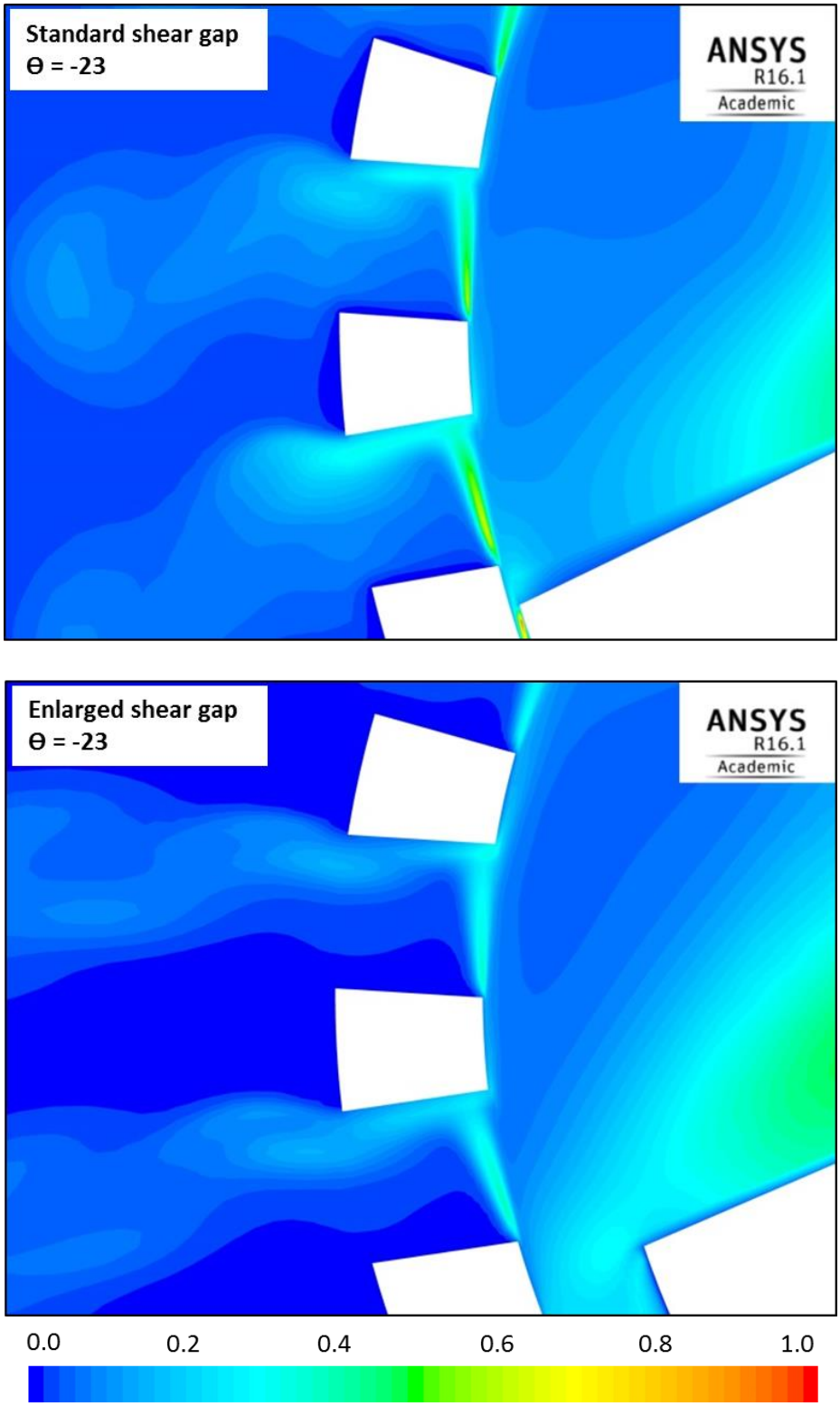

Figure 6.17 - Contours of normalized turbulent kinetic energy for Silverson L4R inline mixer with standard and enlarged shear gap at 8000 rpm and Θ = -23° (normalized by N^2D^2 of SSG)

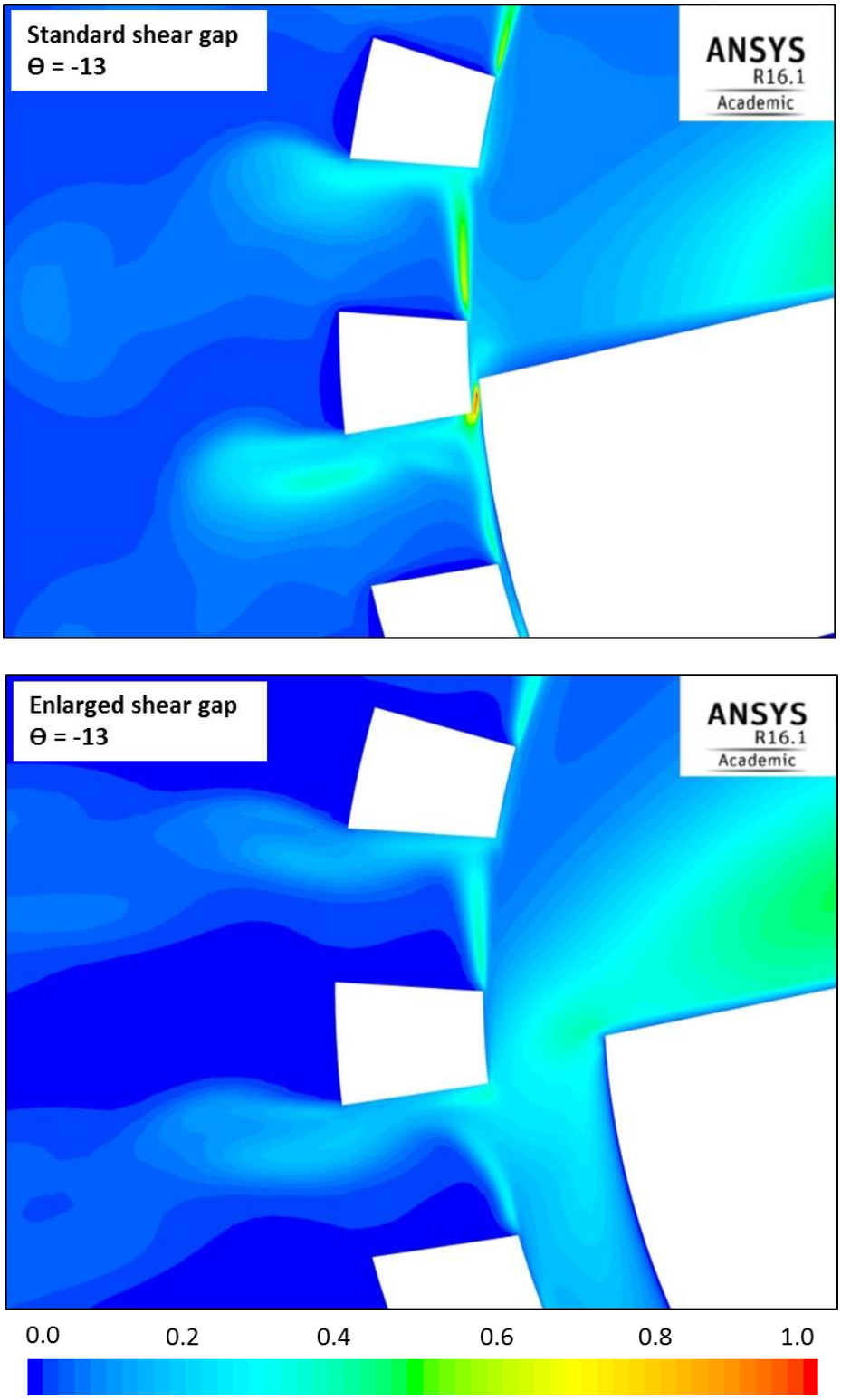

Figure 6.18 - Contours of normalized turbulent kinetic energy for Silverson L4R inline mixer with standard and enlarged shear gap at 8000 rpm and Θ = -13° (normalized by N^2D^2 of SSG)

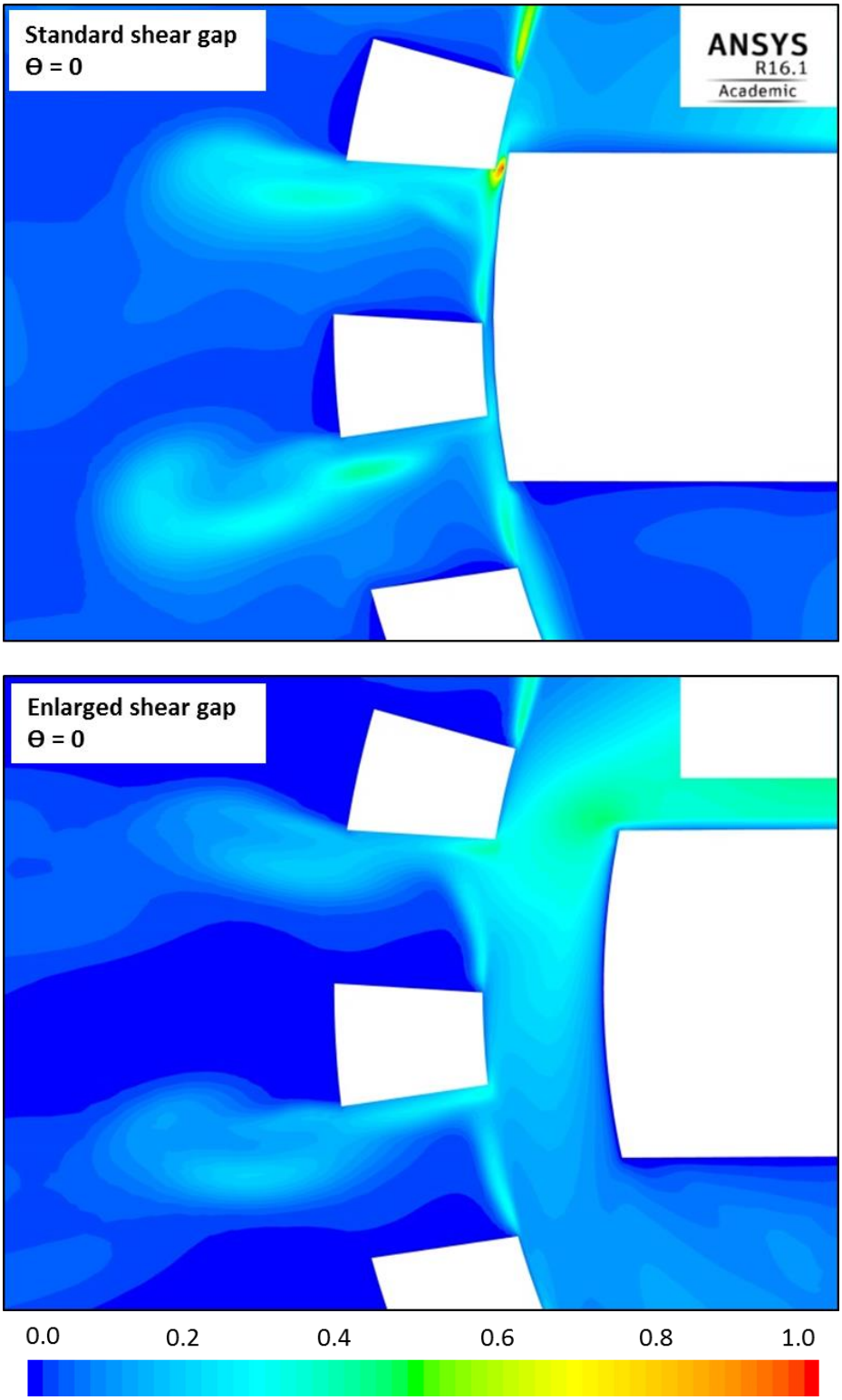

Figure 6.19 - Contours of normalized turbulent kinetic energy for Silverson L4R inline mixer with standard and enlarged shear gap at 8000 rpm and Θ = 0 (normalized by N^2D^2 of SSG)

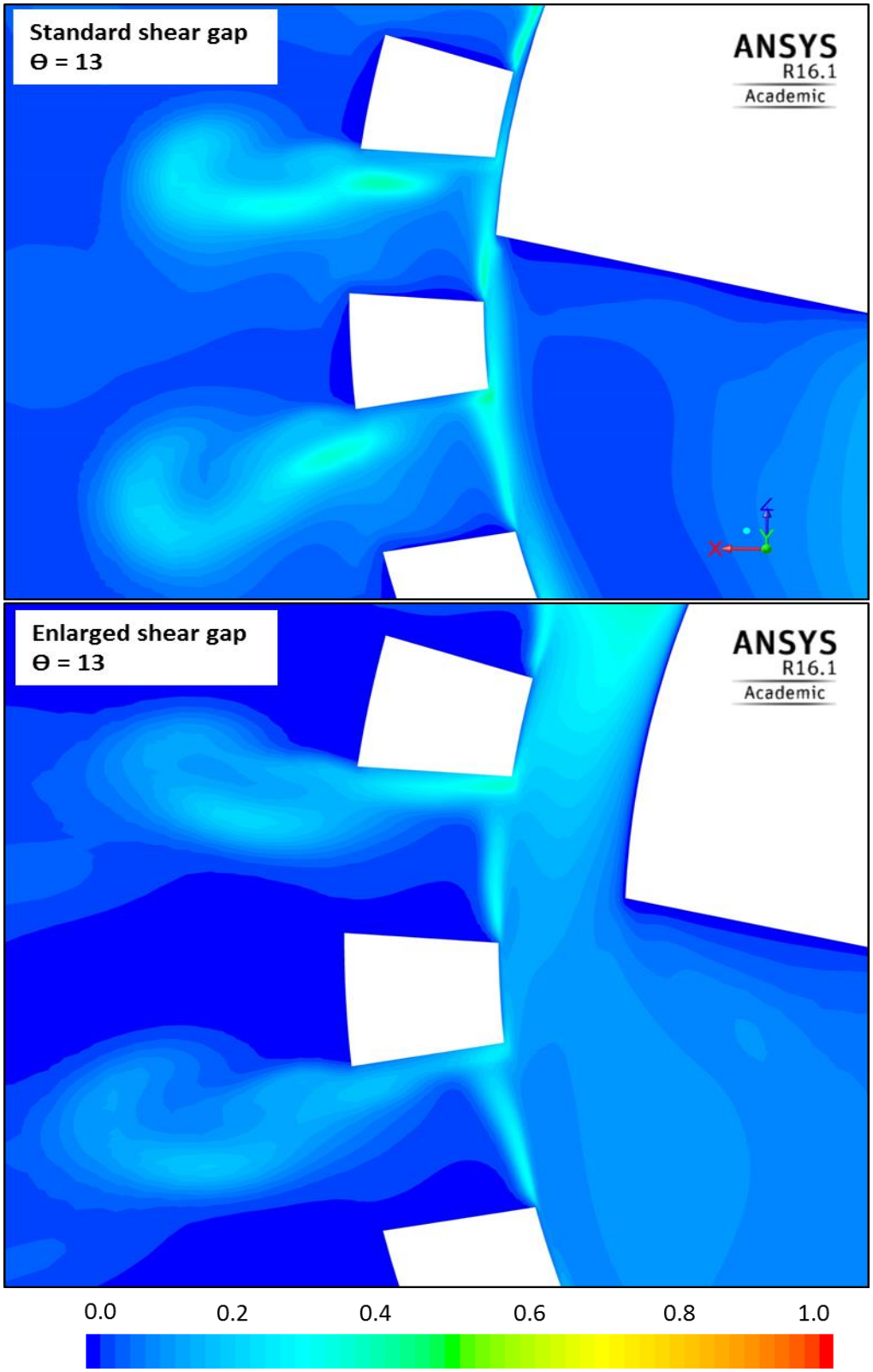

Figure 6.20 - Contours of normalized turbulent kinetic energy for Silverson L4R inline mixer with standard and enlarged shear gap at 8000 rpm and Θ = 13 (normalized by N2D2 of SSG)

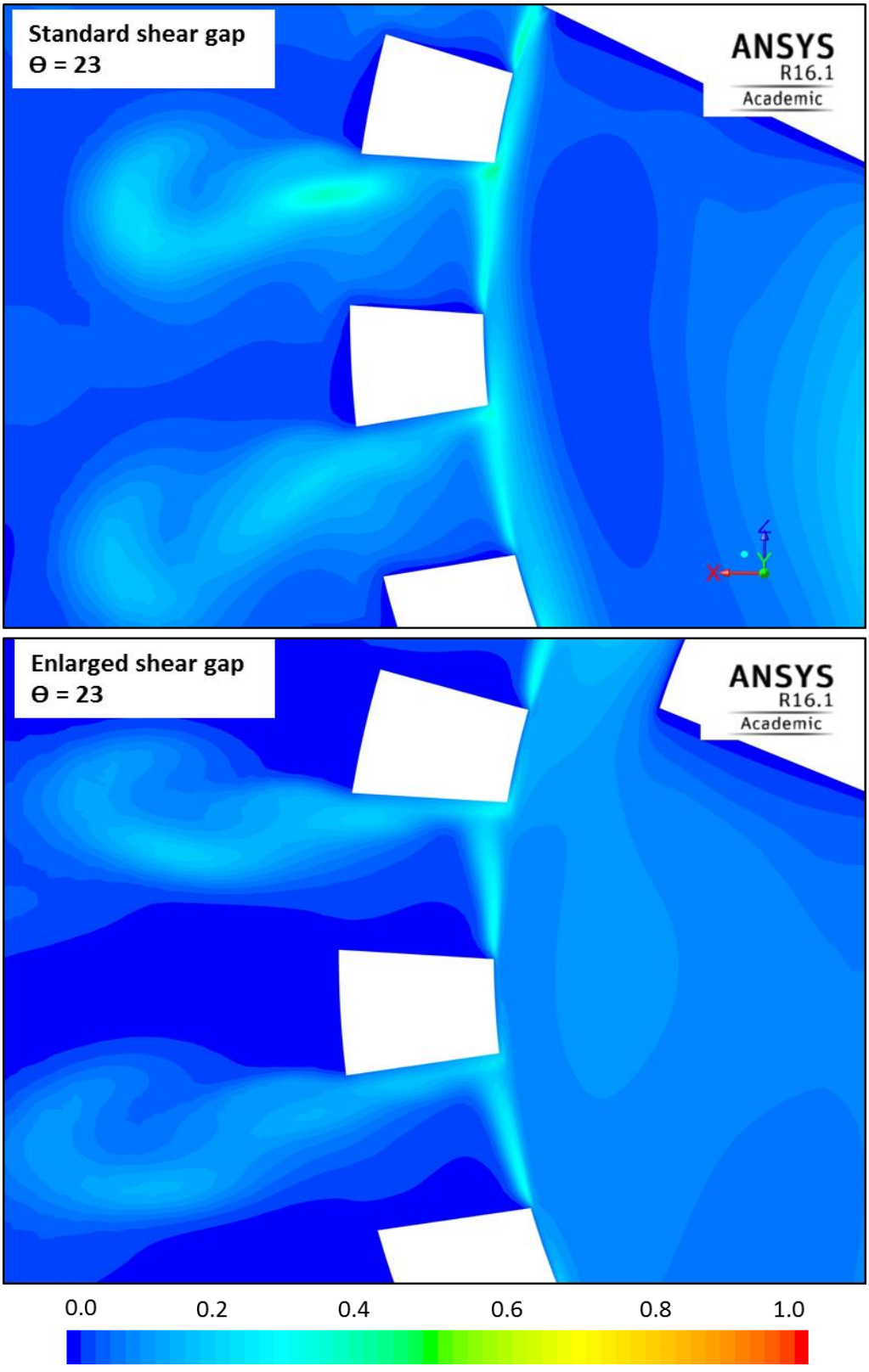

Figure 6.21 - Contours of normalized turbulent kinetic energy for Silverson L4R inline mixer with standard and enlarged shear gap at 8000 rpm and Θ = 23 (normalized by N2D2 of SSG)

6.4.3 –Power Draw and Power Number Calculations

The macroscale energy input to the mixer is produced by the drag force acting on the rotor blades. The resulting force is proportional to the rotor tip speed, which is proportional to the rotational rate, and rotor diameter as:

$$F \propto \rho U^2 D^2 \tag{6.4}$$

where F is drag force, ρ is fluid density, U is tip speed, and D is rotor diameter. The power can be defined as the intensity of force acting at certain velocity. By adopting Equation 6.4 and substituting the tip speed in terms of rotational velocity, πND, and using the relationship between force and power, $F = P/U$, an expression for power scale is obtained as:

$$P \propto \rho N^3 D^5 \tag{6.5}$$

This expression gives a power scale for turbulent flows that can be used in non-dimensionalizing the power input and defining a power number as indicated in Equation 6.3. The above analysis shows that power draw is related to the drag experienced by the rotor and, thus, the power number behaves in the same way as a drag coefficient and reduces to a constant value under fully turbulent flow conditions (Padron 2001). In rotor stator mixers under turbulent condition, the power draw fluctuates with a certain frequency because of the interactions between rotor blades and stator slots, related to their relative position. Figure 6.22 and Figure 6.23 show the deviations of torque from its time averaged values as a function of rotor position, Θ, for SSG and ESG configurations respectively. The torque fluctuations due to rotor and slot interactions is very pronounced in the case of the SSG compared to ESG. The

frequency of these fluctuations can be determined by considering the arrangement of stator slots and the number of rotor blades. There are 26 square holes at each row of the stator. The holes on each row overlap with those on the row above and below. This overlap causes 26×2=52 identical geometry configurations on the stator head. On the other hand, the rotor consists of 4 blades positioned at right angles on the rotor shaft. The number of distinct interactions between the rotor and stator can be calculated by the least common multiple of 52 and 4. This calculation leads to 52 value and is in agreement with simulation results shown in Figure 6.22; in one revolution (360°) of the rotor, there are 52 fluctuations in torque data.

Moreover, there is a low frequency fluctuation with a larger period in the power draw data as shown in Figure 6.22 and Figure 6.23. This fluctuation can be explained by the asymmetry in flow field in the volute where the position of the outlet pipe creates local asymmetric velocity field. To further analyse the power draw data, the amount of torque on the front and back surfaces of rotor blades as well as on the top, bottom, and outer edge surfaces of the rotor were investigated. Figure 6.22 shows the total torque on the rotor of the Silverson L4R inline mixer with the SSG. The torque imparted to the front and back surfaces of one blade of the rotor as well as the torque on top, bottom, and outer edge surfaces are shown. Figure 6.23 shows the total torque on the rotor of the Silverson L4R inline mixer with the ESG. The torque on the front and back surfaces of all 4 blades are given as well. It can be seen that the fluid interactions with the front and back surfaces of the blades are the main contributors to total torque and the effect of drag on top, bottom, and outer edge surfaces of the rotor is not significant.

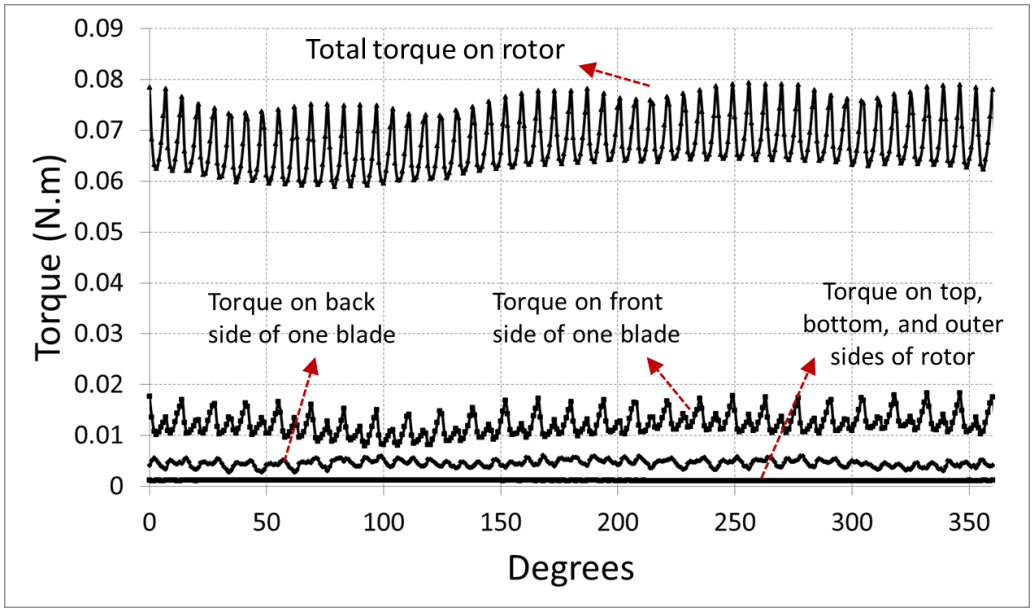

Figure 6.22- Torque on front and back surfaces of one blade, torque on bottom, top, and outer edge surfaces of all 4 blades, and total torque on all 4 blades of Silverson L4R inline mixer with SSG at 8000 rpm

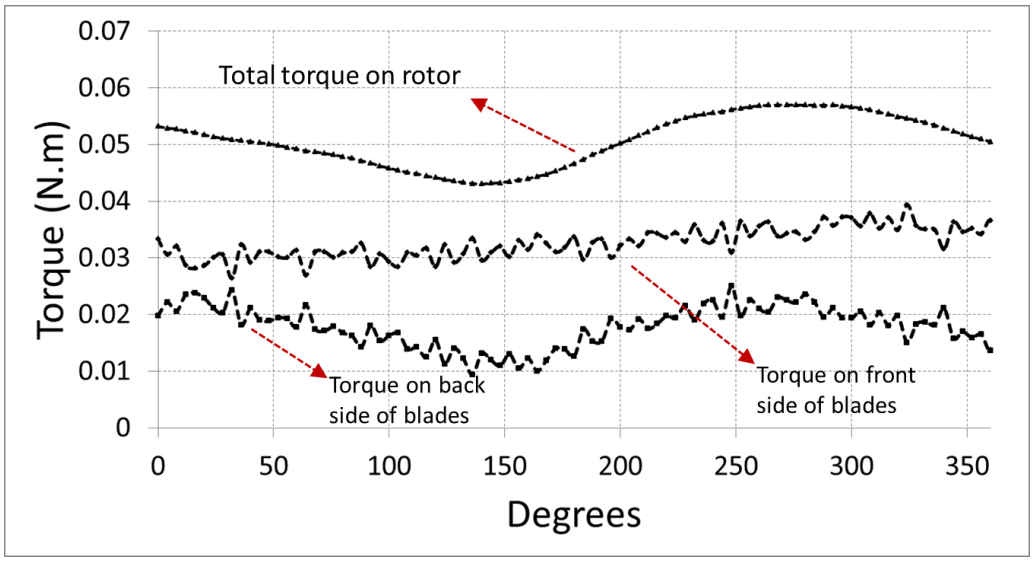

Figure 6.23- Torque on front and back surfaces of the blades (4 blades) and total torque on rotor for Silverson L4R inline mixer with ESG at 8000 rpm

Table 6.3 gives the power draw of the mixers with SSG and ESG calculated using equation 6.1. The mean value of the fluctuations in torque data was used as the torque input. The results show a significant increase in power draw by decreasing the clearance width between rotor and stator (shear gap width). It is important to note that the shear gap width is increased 8.5 times and the rotor diameter is shortened by 10%;

this resulted in a 30% power draw reduction by the mixer with the ESG compared to the mixer with the SSG. Given the differences in energy dissipation rate and power draw data, the mixer with the narrow shear gap draws more power and produces large high-intensity energy dissipation regions which in turn enhances the mixing. Figure 6.24 gives the power draw of the Silverson L4R inline mixer as a function of shear gap width. Deviations from the mean values as a result of asymmetry in flow field and rotor and stator interaction is given by the error bars. The simulation data show an inverse proportionality between power draw and the clearance width between rotor and stator. It is important to note that the power number is related to rotor diameter with a power of -5 and as a result even though power draw of mixer with standard shear gap is larger compared to the power draw of mixer with the enlarged shear gap, its power number is smaller.

Table 6.3- Reynolds number, power number, and pumping number for Silverson L4R inline mixer with SSG and ESG at different rotor speeds

Silverson L4R Inline Mixer	Standard Shear Gap (0.2 mm)		Enlarged Shear Gap (1.7 mm)	
Rotational Speed (rpm)	4000	8000	4000	8000
Tip Speed, u_{tip} (m/s)	6.5	13.0	5.9	11.8
Reynolds Number	65×10^3	130×10^3	52×10^3	105×10^3
Power (W)	7.2	57.1	4.9	39.0
Power Number	0.9	0.9	1.0	1.0
Flow Rate (L/s)	0.14	0.29	0.13	0.27
Pumping Number	0.07	0.07	0.09	0.09

Finally, the effect of shear gap width on the pumping capacity of the mixer was investigated. The volumetric flow rate, Q, was calculated by integration of the

velocity field at the inlet and outlet of the mixer. Pumping number can be calculated as:

$$N_Q = \frac{Q}{ND^3} \tag{6.6}$$

As it is summarized in Table 6.3, the mixer with ESG has a higher pumping number compared with the SSG. The change in flow rate was 7% when the shear gap width is increased from 0.2 to 1.7 mm.

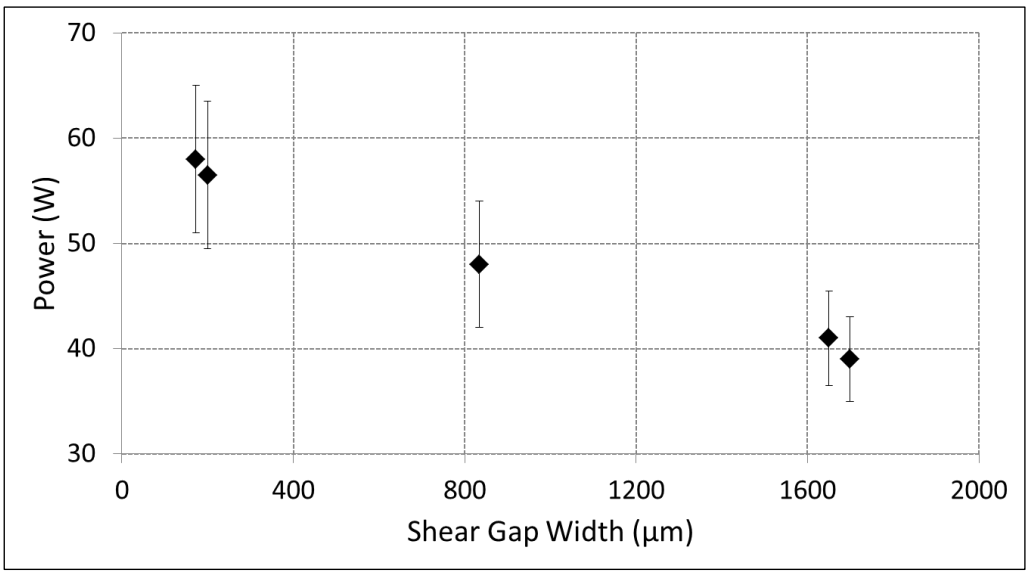

Figure 6.24- Power draw as a function of shear gap width- Silverson L4R inline mixer at 8000 rpm

6.5 –Summary

RANS simulations for the Silverson L4R inline mixer with different shear gap widths were conducted. The effect of shear gap width on the velocity field, turbulent kinetic energy, energy dissipation rate, power draw, and flow number was investigated. It was shown that:

- The velocity field and flow pattern is different in different shear gap width configurations. In particular, the stator jets are wider in the case of standard shear gap which creates higher intensity tangential flow in the volute area. The mixer with enlarged shear gap creates larger recirculation loops behind the stator which extend into the volute area.

- The mixer with narrow shear gap was more successful in focusing the power input in shear gap and stator slots regions. As a result, higher energy dissipation rates were observed in this mixer. The power draw of inline mixer with different shear gap widths is calculated via CFD simulations. The loss of the power draw due to enlarging the shear gap/shortening the rotor diameter is quantified.

- The torque exerted from fluid on tangential surfaces of the rotor is negligible compared to front and back side of the rotor that have a direct interaction with the working fluid.

Chapter 7: Summary and Conclusion

This chapter summarizes the important results and conclusions of this study. Potential future work is also discussed for size measurement considerations, mechanistic model development, population balance modelling, experimental studies, and CFD investigation of wet milling in rotor-stator devices. Additional work for wet milling of different crystal-antisolvent systems in industrial scale rotor-stator mixers and other higher power devices, e.g. valve homogenizers, would be particularly useful to further extend the scaling up/down strategies developed in this work.

The most important result of this study is that there are mechanistic relationships between particle size reduction and power input in wet milling processes using rotor-stator mixers. The mechanistic models can describe and predict the milling behaviour of different crystals considering their size and mechanical properties, mill operating conditions, and mixer geometry. This finding is particularly useful in designing and scaling up wet milling processes in rotor-stator mixers. Furthermore, the scaling laws, non-dimensional correlations, and breakage functions developed here can be applied to other processes in which particle breakage occurs according to the same mechanism(s), e.g., by substituting the particle collision velocity with jet velocity in impinging jets or with superficial velocity in valve homogenizers, the equations presented in Table 3.4 can be used to predict the breakage and attrition behaviour of different crystals with different size ranges in these devices.

7.1 –Particle Size and Physical Properties

Milling generates irregular-shaped particles. To avoid the complexity of reporting various sizes for a single irregular-shaped particle, the equivalent diameter of a particle was used as representative of the particle size, e.g. volume equivalent diameter is the diameter of a sphere having the same volume as the particle.

Various size measurement methods that are used in this study were discussed including sieving, microscope-based image analyzing, laser diffraction, FBRM, and PVM. It was shown that a number based measurement technique can be overwhelmed and saturated by the large number of fine particles that are generated via attrition during a milling process. Therefore, to consider the maximum stable particle size, a volume or surface based measurement technique is preferred in size distribution measurement of milling processes. The sampling method was shown to influence the accuracy of a size distribution measurement. A non-representative sample due to inhomogeneous bulk materials and lack of proper dispersion can result in a large discrepancy in size measurement data. The homogeneity of the sampling was enhanced by proper mixing and confirmed by laser diffraction and FBRM measurements of size distributions acquired from different regions in the sampling/holding vessel.

Mechanical properties of crystals that are important during breakage were discussed including, Young's/elastic modulus, hardness, and fracture toughness. The characteristics of particle deformation depend on these physical properties, i.e., Young's modulus is representative of material resistance to elastic deformation, hardness is representative of material resistance to plastic deformation, and fracture toughness characterizes the fracture behaviour of the material under stress. A

nanoindentation technique was used to measure these properties at the scale of the crystals. The small size scale and anisotropic behaviour of some crystals are the challenges of this measurement technique.

7.2 –Mechanistic Models for particle breakage

A class of mechanistic models for breakage and attrition of crystals and particulate solids have been developed based on elastic deformation, plastic deformation, and fracture mechanics concepts. The functional form of these models was shown to be in agreement with classical comminution theories where the size reduction is empirically related to power consumption. It was shown that the model constants describe the influence of particle physical properties on milling performance.

The forces acting on the particle during milling can be divided into two opposing forces: cohesive forces that resist particle fracture, and disruptive forces to break it. It was shown that the cohesive forces are a function of elastic modulus, hardness, fracture toughness, and particle size. Each of the different mechanistic models predicts different relative importance of the material physical properties and particle size in breakage process. Therefore, 4 different classes of cohesive forces were developed dependent on particle deformation and breakage behaviour under the impacts. Disruptive forces, on the other hand, were found to be a function of particle velocity magnitude promoting particle-particle and particle-wall collisions. While previous studies have related the disruptive force to macroscale velocity, particle sizes are such that they should be influenced by eddy encounters in the inertial subrange of turbulence. Therefore, two classes of disruptive forces were developed dependent on

macroscale velocity, based on rotor tip speed, and eddy velocity given by Kolmogorov's inertial subrange model. The later depends upon the local energy dissipation rate. The disruptive and cohesive forces were employed to construct eight different correlations for ultimate crystal size and its rate of approach. Based on these mechanistic models, a dimensionless comminution number is developed (ratio of disruptive to cohesive forces) to aid physical interpretation and scale up/down efforts for geometrically similar devices. Model discrimination was based on comparison to the wet milling experimental data and demonstrated in Chapter 5.

7.3 –Wet Milling Experiments in Rotor-Stator Mixers

An extensive series of wet milling experiments with different crystal-antisolvent systems were performed in three rotor stator mixers: Silverson L4R inline mixer with standard shear gap, Silverson L4R inline mixer with enlarged shear gap, and Silverson L4R batch mixer with standard shear gap. The effect of milling conditions, mixer geometry, and particle physical properties on ultimate particle size and particle breakage kinetics was investigated. Various breakage modes are examined by varying operating conditions, particle concentration, coatings, and small geometric changes to consider the importance of particle-particle, particle-wall, and fluid shear interactions. The data indicate that:

- Increasing the rotor speed has two effects on milling behavior: first, it boosts the breakage rate; and second, it results in a smaller ultimate particle size at the end of the milling process. It was reasoned that a higher rotor speed draws more power from the motor, and thus higher energy intensity is available in the mixing head to enhance the breakage process.

- Decreasing the throughput through the inline mill head increases the breakage rate but otherwise does not have an effect on ultimate particle size. It was reasoned that a lower flow rate gives more residence time for particles in the mixing head leading to more collision events in one pass, and hence, the higher breakage rate.

- Mechanical properties of particles play an important role in their breakage behavior. Particles with higher hardness and lower fracture toughness are more brittle.

- The concentration of particles in the slurry has a limited effect on breakage rate and a negligible effect on the ultimate size distribution.

- Particle-wall collisions are more important in crystal breakage when compared to particle-particle or fluid shear mechanisms.

- At a given rotor speed, the mixer with higher power draw and smaller dispersion zone (shear gap volume plus stator hole volume) is more successful in concentring the dissipated energy, and hence, leads to higher breakage rate and smaller ultimate particle size.

7.4 –Model Validation and Mechanistic Correlations of Wet Milling

The suitability of mechanistic models to predict the crystal breakage behavior in different rotor-stator mixers was investigated. Based upon the experimental data it was shown that an inertial subrange model for crystals undergoing elastic-plastic deformation well describes the crystal breakage behavior in the different rotor-stator

mixer geometries. It was shown that the comminution number, Co, can be successfully apply to describe and predict the effect of operating condition (i.e., rotor speed), and crystal mechanical properties in geometrically similar devices.

The shear gap and stator hole regions experience the highest densities of energy dissipation rate and most of the energy input to the mixer is dissipated in these regions. Therefore, for devices without geometric similarity, the concept of local energy dissipation rate, defined as the power draw of the mixer per mass of fluid in the shear gap and stator slot regions, was introduced and exploited to compare the data from different mixers with different geometries. This approach was successful in correlating the maximum stable particle size.

The mechanistic theory is further utilized to provide breakage kernels based on probability of collision and collision rate theories. Application of the breakage functions to predict the milling rate as well as their implementation within a Population Balance framework is discussed. The mechanistic framework shows promise for application to a broad class of milling devices under different processing conditions.

7.5 –CFD Simulations and Power Draw Calculations

The effect of shear gap width on the velocity field, turbulent kinetic energy, energy dissipation rate, power draw, and flow number in the Silverson L4R inline rotor–stator mixers has been examined. It was found that the velocity field in the swept volume of the rotor was predominantly tangential and the intensity of the velocities was a function of tip speed. In the shear gap region, the velocity field close to rotor blade was tangential. The impingement of this tangential flow on the

downstream surface of the stator slots caused strong radial jets to emerge from the stator slots. The characteristics of the stator jets emerging from the enlarged shear gap were different than that of narrow shear gap.

In the case of enlarged shear gap, the stator jets extended up to the tank wall, while in the case of narrow shear gap, the jets dissipated close to the stator head due to wider jet structure and higher intensity of counter clockwise tangential flow in the volute area. The jets emerging from stator holes created recirculation loops (vortex) behind them. It was found that the structure and center location of these vortices were different for different shear gaps. The mixer with narrow shear gap was more successful in concentrating the power in shear gap and stator slots regions and higher energy dissipation rates were observed in this mixer. The power draw of the mixers was obtained by calculating the torque on the rotor. It was found that the power draw is a function of shear gap and rotor diameter and by increasing the shear gap, shortening the rotor diameter, the power draw decreases. The effect of shear gap width on the pumping capacity of the mixer was investigated. It was shown that the effect of shear gap width on the flow rate was not significant compared to change in power draw.

7.6 –Future Work

There are several areas where future work could be performed to extend the reach of this study such as:

- The mechanistic correlation represented in Figures 5.3 and 5.10 could be further extended to cover larger range of energy input and particle sizes by acquiring milling data from industrial scale rotor-stator mixers and other higher power

devices such as valve homogenizers. This would be particularly useful to further extend the scaling up/down strategies developed in this work.

- Wet milling experiments with different crystal-antisolvent systems can be performed to further evaluate the mechanistic correlations given in Tables 3.5 and 3.6.

- The crystals used in this study are cubic or very close to a cubic shape. It would be useful to study the wet milling behaviour of crystals with different morphology. Special care must be taken for size measurement of needle shape particles.

- Further analysis and comparison with wet and dry milling literature will be useful to build a master curve based on the proposed models. The challenge would be to obtain the appropriate scales of the different devices and can calculate the power input and the highest available stress.

- The transient behavior of the process can be explored in more detail by solving the population balance equations for the entire population. This will allow a more precise evaluation of the breakage kernels that are developed in this study.

- Furthermore, a mathematical algorithm can be developed in order to map the results from different measurement techniques such as FBRM, PVM, and laser diffraction to help better comparison between different data sets.

Appendix A: Wet milling data for sucrose-IPA system in the Silverson L4R inline mixer with standard shear gap

Sucrose crystals with 10% by weight, dispersed in 2 litres IPA, were fed to the Silverson L4R inline mixer with the standard shear gap at a series of flow rates 2.1, 3.0, and 4.2 L/min and rotor speeds 5000, 6500, and 8000 rpm in the inline setup (see Chapter 4 for details). The samples were taken from the sampling point in the glass vessels at predefined time intervals to investigate particle size reduction. Extra milling time was provided to ensure that all particles experienced the regions with maximum local energy dissipation rate multiple times and the equilibrium is achieved. Here, the complete sets of experimental data acquired at different milling time are presented in terms of different cumulative diameters, D95, D90, D80, D50, and D10 as well as mean diameters, D_{43}, D_{32}, and D_{10} versus milling time in tank turnovers. A sharp breakage rate at the beginning followed by slow changes is observed in the all particle breakage data. The sharp breakage slope is due to fracture mode which refers to the breakage of a particle into fragments of comparable size. The slow breakage part is due to an attrition mechanism by which small fragments are chipped off from larger particles.

A.1 –Wet Milling of Sucrose/IPA at 5000 rpm and 2.1 lpm

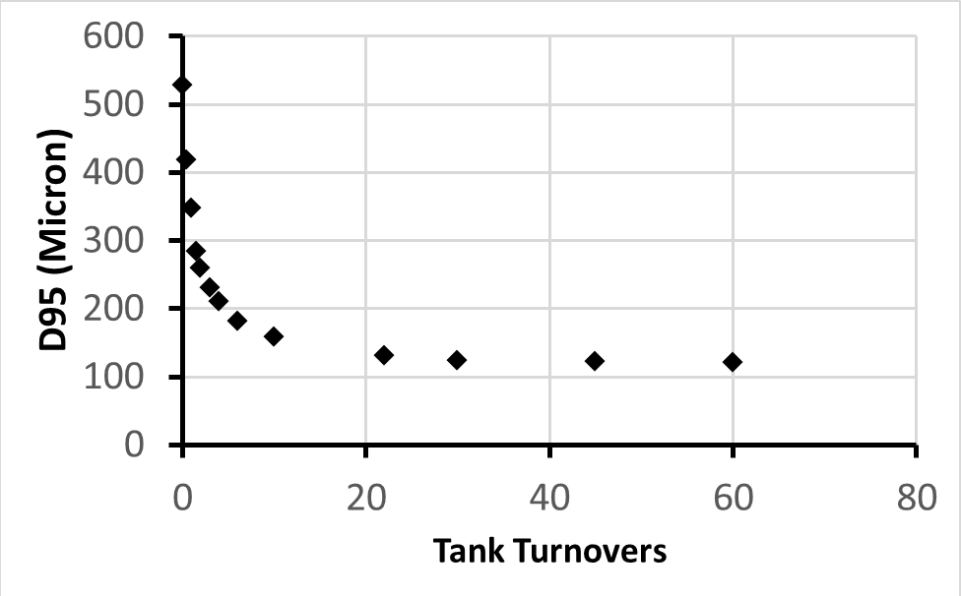

Figure A.1.1 - D95 versus milling time in tank turnovers for sucrose/IPA wet milling at 5000 rpm and 2.1 lpm

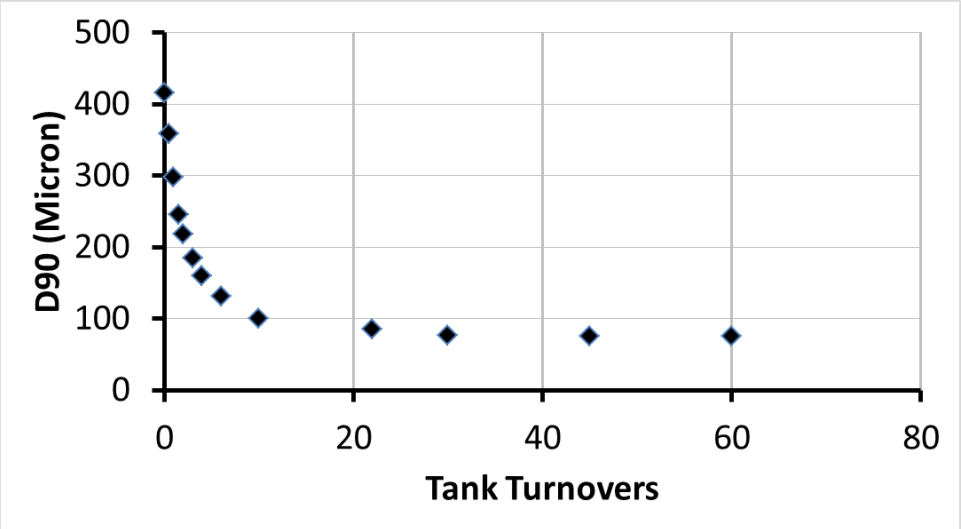

Figure A.1.2 - D90 versus milling time in tank turnovers for sucrose/IPA wet milling at 5000 rpm and 2.1 lpm

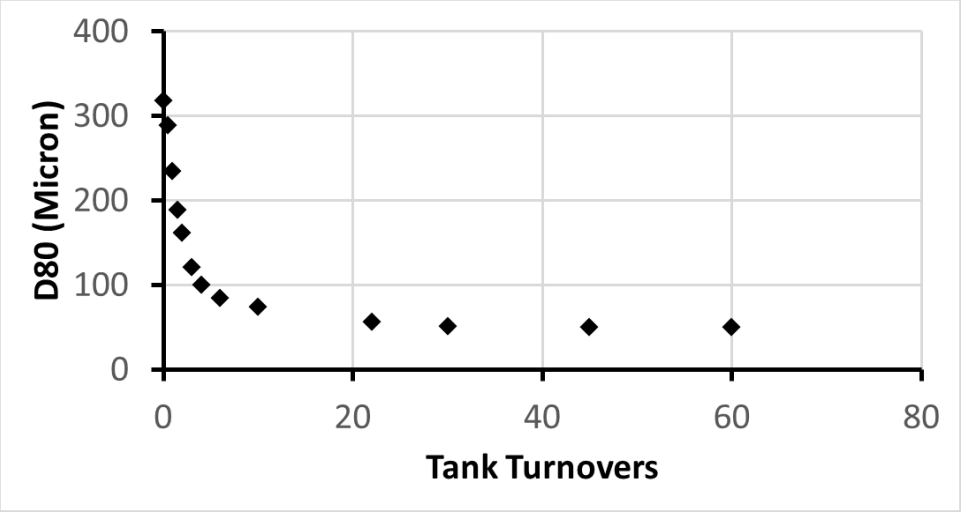

Figure A.1.3 – D80 versus milling time in tank turnovers for sucrose/IPA wet milling at 5000 rpm and 2.1 lpm

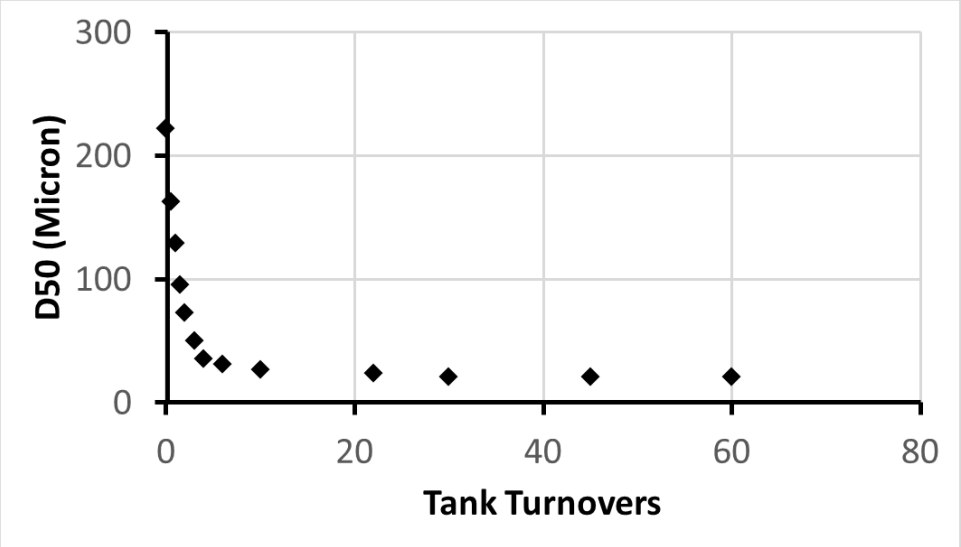

Figure A.1.4 – D50 versus milling time in tank turnovers for sucrose/IPA wet milling at 5000 rpm and 2.1 lpm

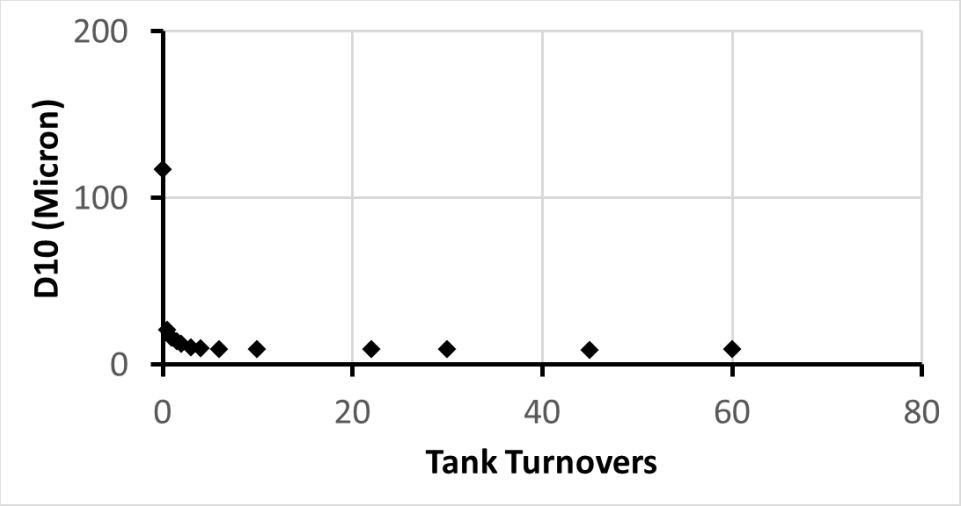

Figure A.1.5 – D10 versus milling time in tank turnovers for sucrose/IPA wet milling at 5000 rpm and 2.1 lpm

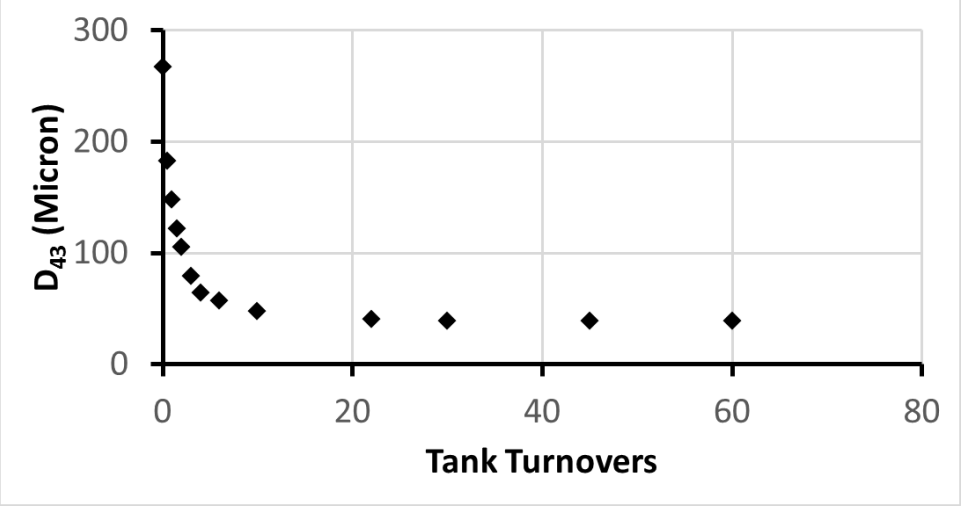

Figure A.1.6 – D_{43} versus milling time in tank turnovers for sucrose/IPA wet milling at 5000 rpm and 2.1 lpm

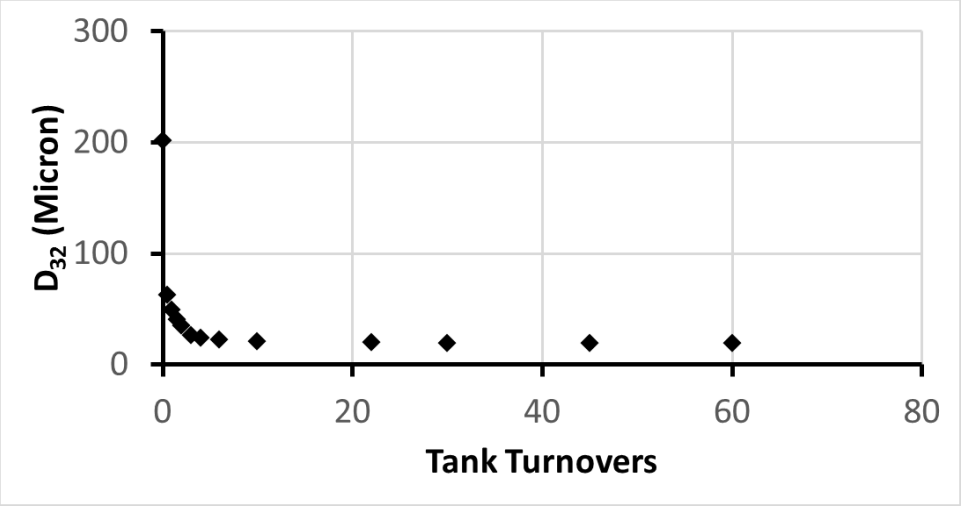

Figure A.1.7 – D_{32} versus milling time in tank turnovers for sucrose/IPA wet milling at 5000 rpm and 2.1 lpm

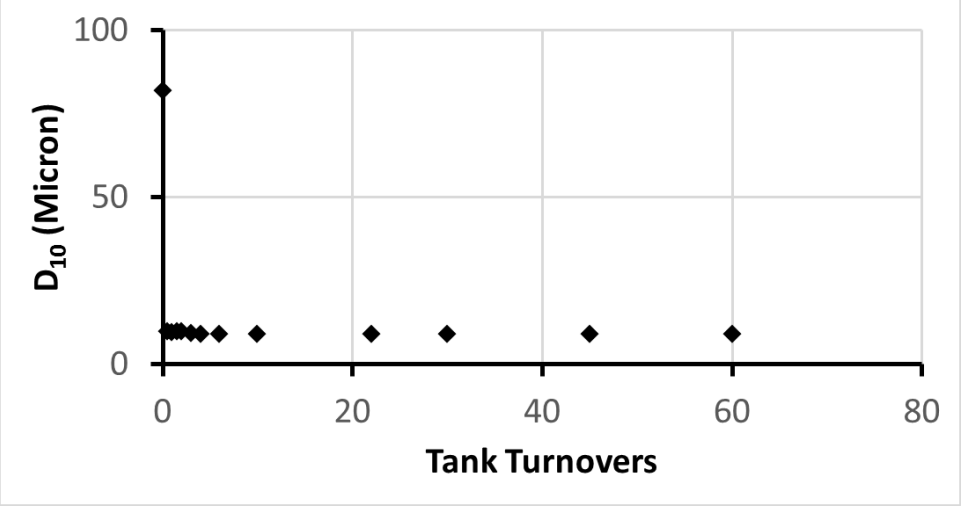

Figure A.1.8 – D_{10} versus milling time in tank turnovers for sucrose/IPA wet milling at 5000 rpm and 2.1 lpm

A.2 –Wet Milling of Sucrose/IPA at 6500 rpm and 2.1 lpm

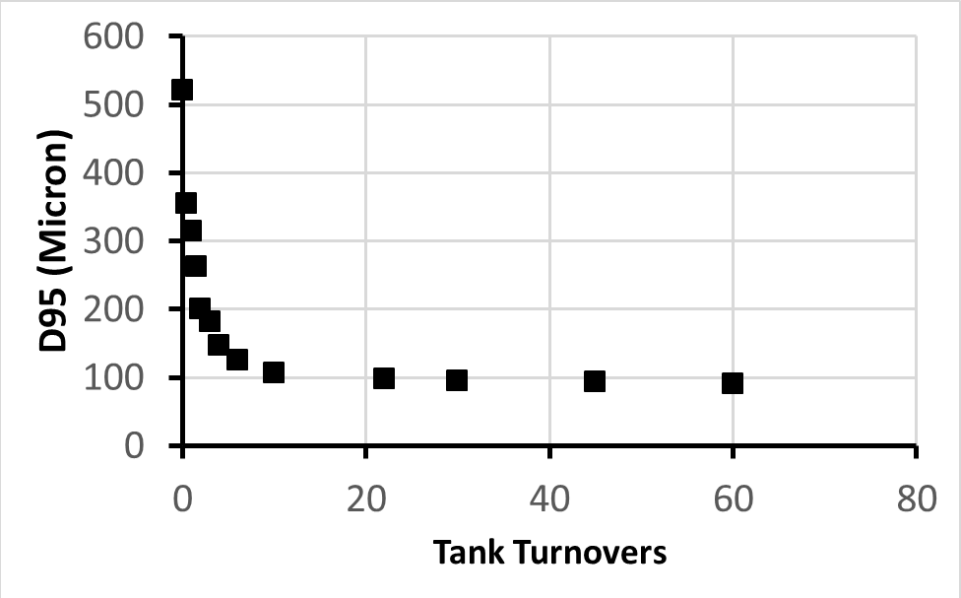

Figure A.2.1 - D95 versus milling time in tank turnovers for sucrose/IPA wet milling at 6500 rpm and 2.1 lpm

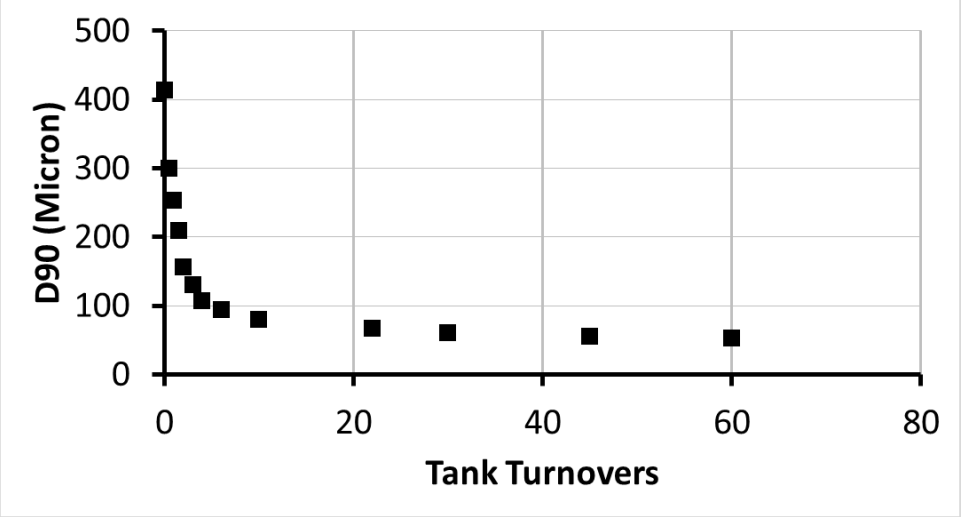

Figure A.2.2 - D90 versus milling time in tank turnovers for sucrose/IPA wet milling at 6500 rpm and 2.1 lpm

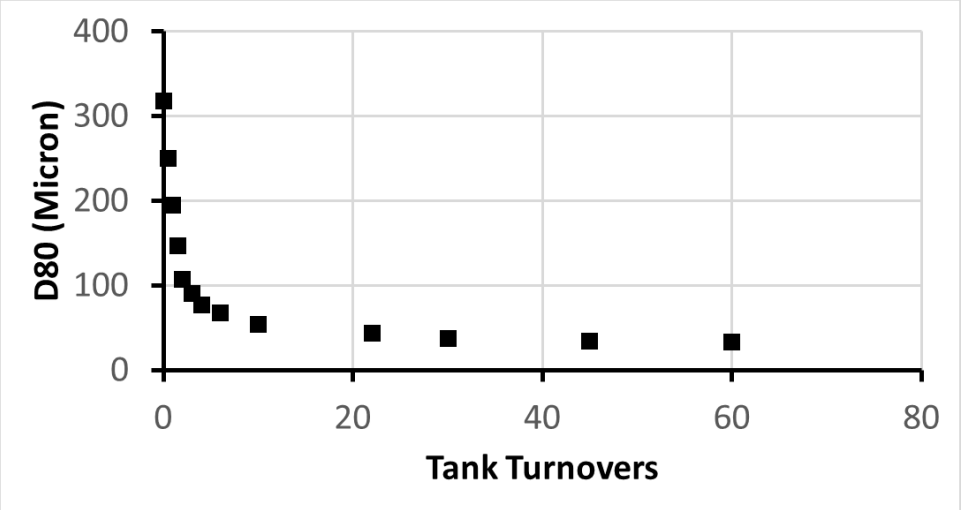

Figure A.2.3 - D80 versus milling time in tank turnovers for sucrose/IPA wet milling at 6500 rpm and 2.1 lpm

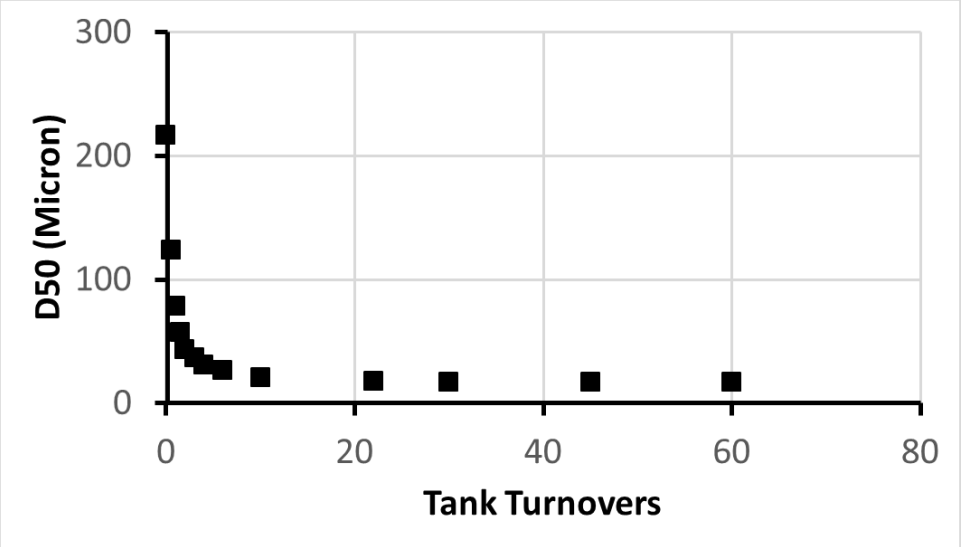

Figure A.2.4 - D50 versus milling time in tank turnovers for sucrose/IPA wet milling at 6500 rpm and 2.1 lpm

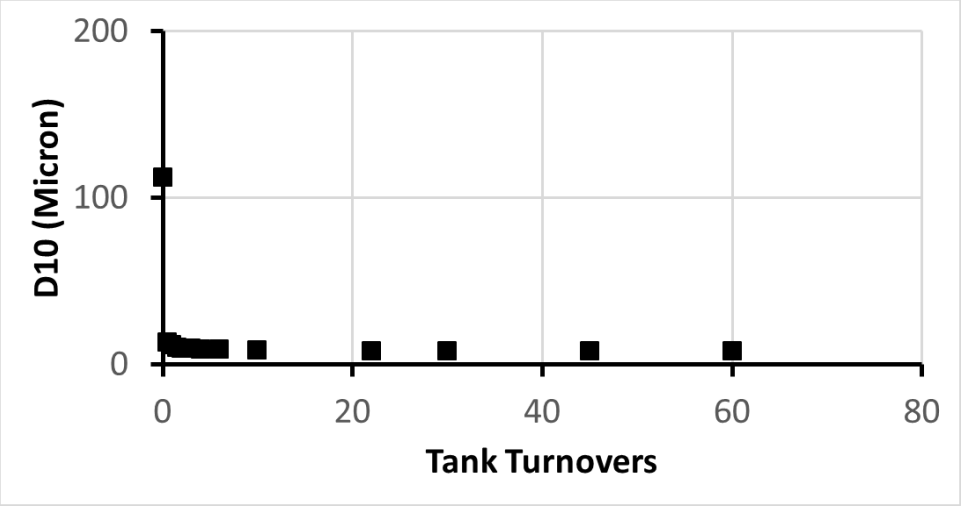

Figure A.2.5 - D10 versus milling time in tank turnovers for sucrose/IPA wet milling at 6500 rpm and 2.1 lpm

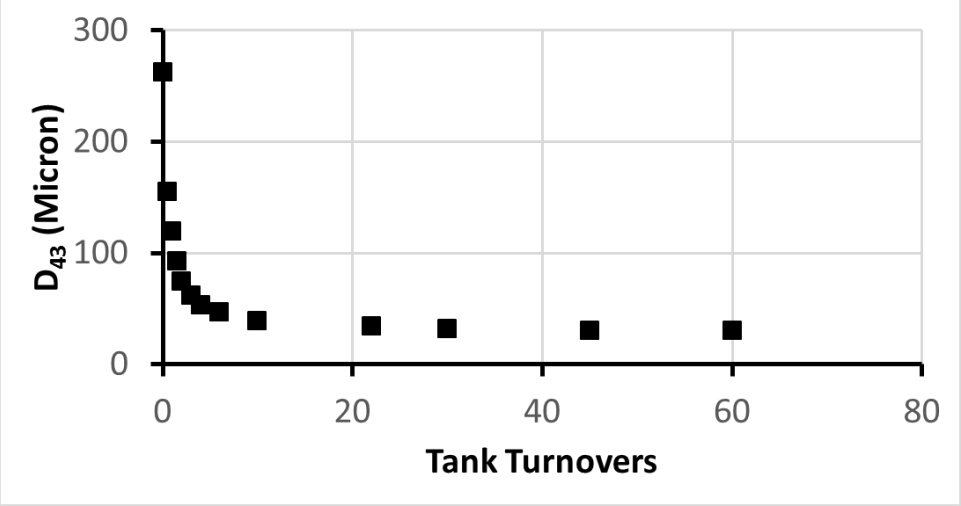

Figure A.2.6 - D_{43} versus milling time in tank turnovers for sucrose/IPA wet milling at 6500 rpm and 2.1 lpm

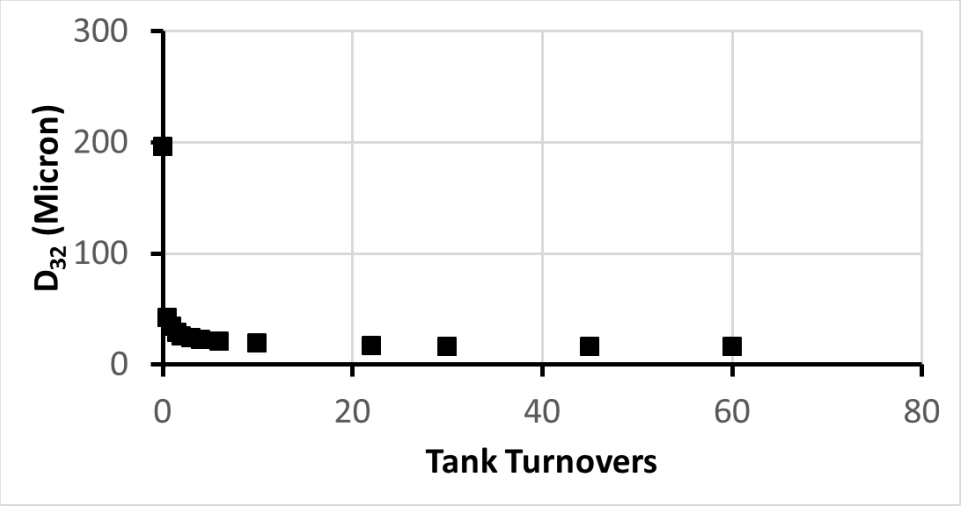

Figure A.2.7 - D_{32} versus milling time in tank turnovers for sucrose/IPA wet milling at 6500 rpm and 2.1 lpm

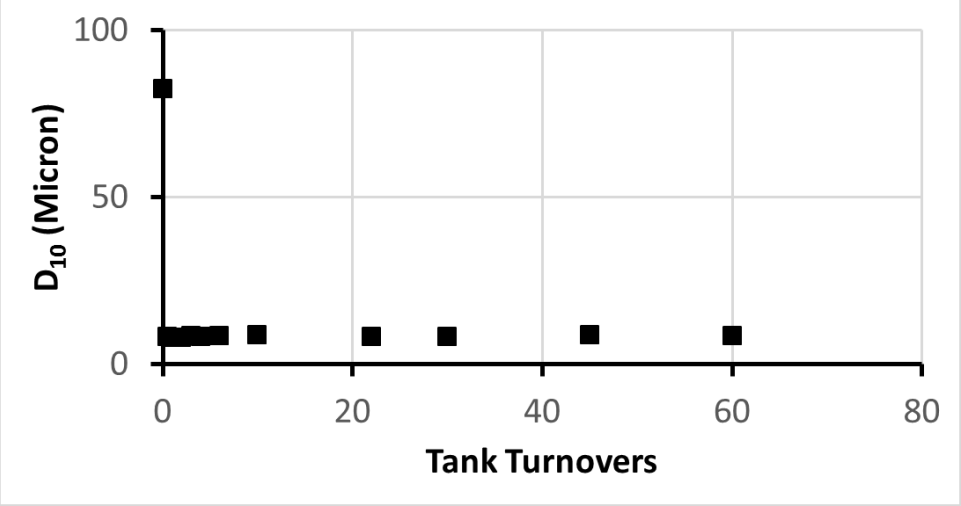

Figure A.2.8 - D_{10} versus milling time in tank turnovers for sucrose/IPA wet milling at 6500 rpm and 2.1 lpm

A.3 –Wet Milling of Sucrose/IPA at 8000 rpm and 2.1 lpm

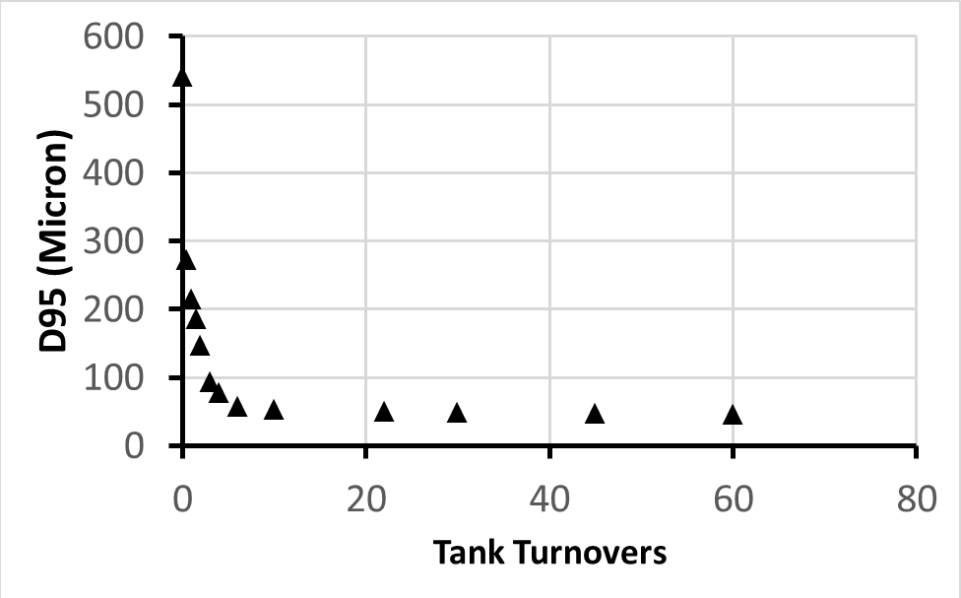

Figure A.3.1 - D95 versus milling time in tank turnovers for sucrose/IPA wet milling at 8000 rpm and 2.1 lpm

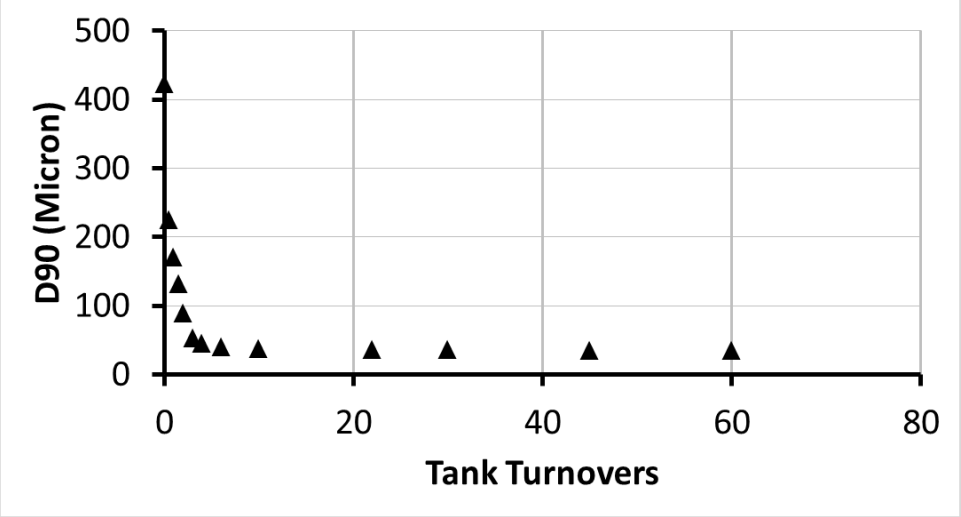

Figure A.3.2 - D90 versus milling time in tank turnovers for sucrose/IPA wet milling at 8000 rpm and 2.1 lpm

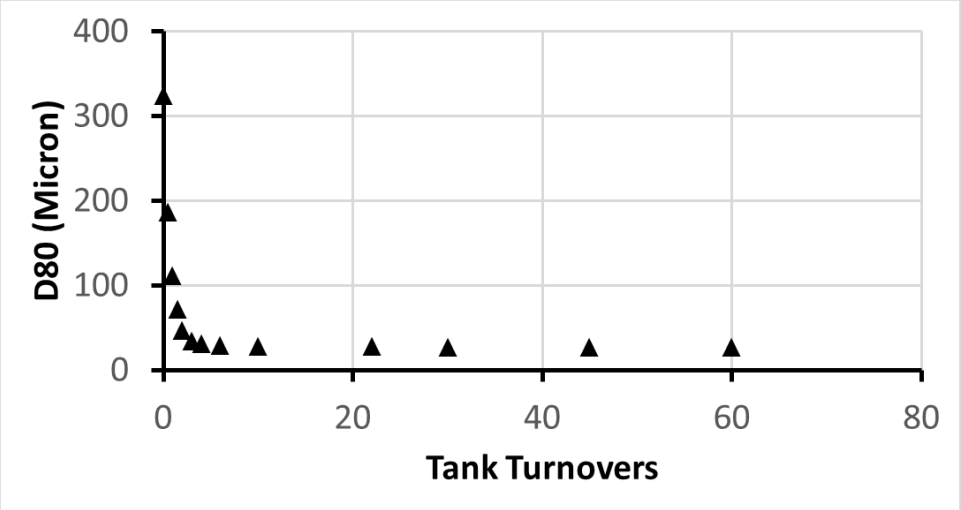

Figure A.3.3 - D80 versus milling time in tank turnovers for sucrose/IPA wet milling at 8000 rpm and 2.1 lpm

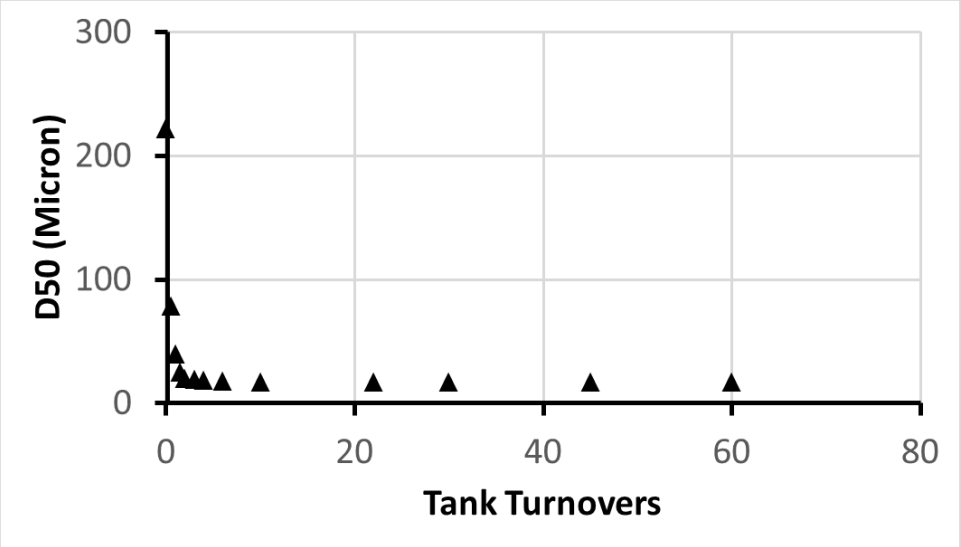

Figure A.3.4 - D50 versus milling time in tank turnovers for sucrose/IPA wet milling at 8000 rpm and 2.1 lpm

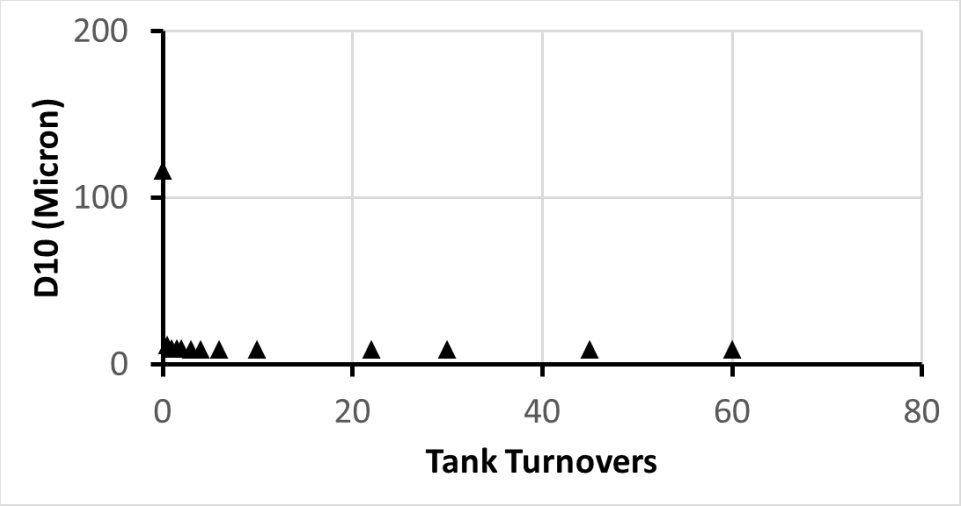

Figure A.3.5 - D10 versus milling time in tank turnovers for sucrose/IPA wet milling at 8000 rpm and 2.1 lpm

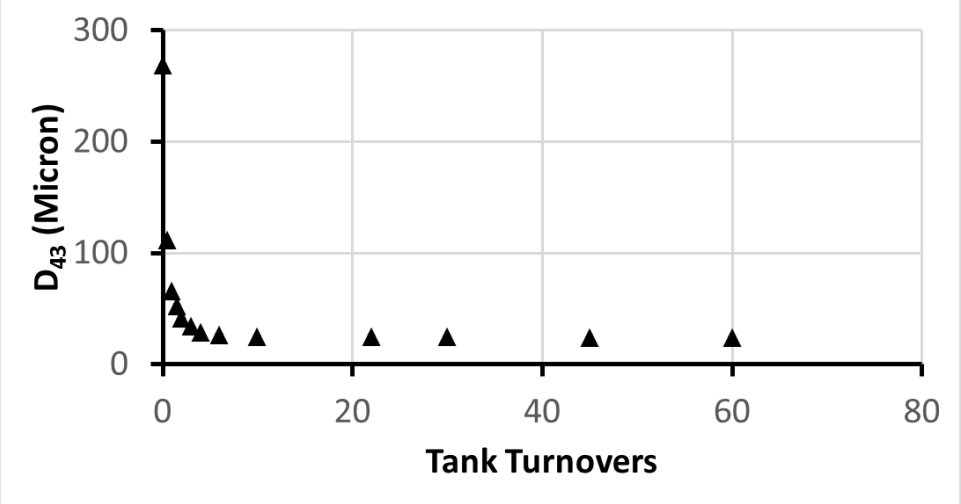

Figure A.3.6 - D_{43} versus milling time in tank turnovers for sucrose/IPA wet milling at 8000 rpm and 2.1 lpm

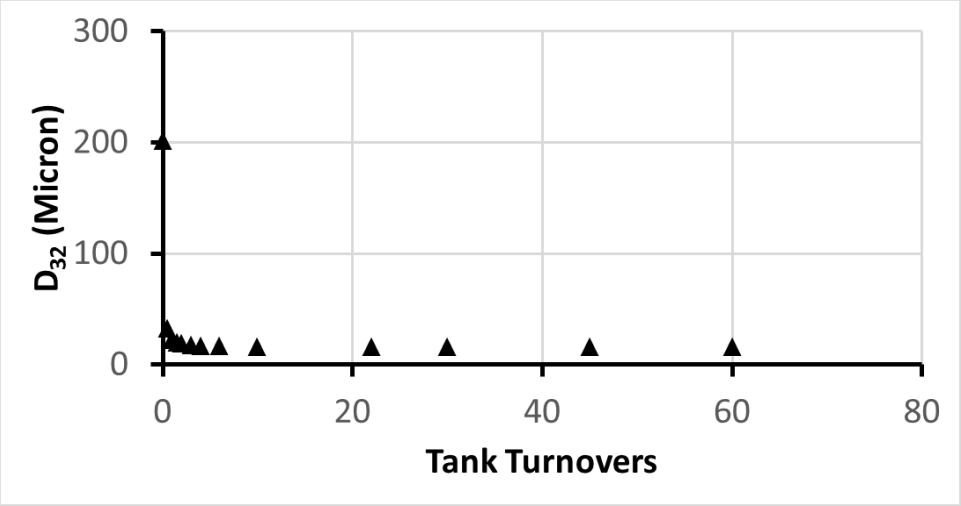

Figure A.3.7 - D_{32} versus milling time in tank turnovers for sucrose/IPA wet milling at 8000 rpm and 2.1 lpm

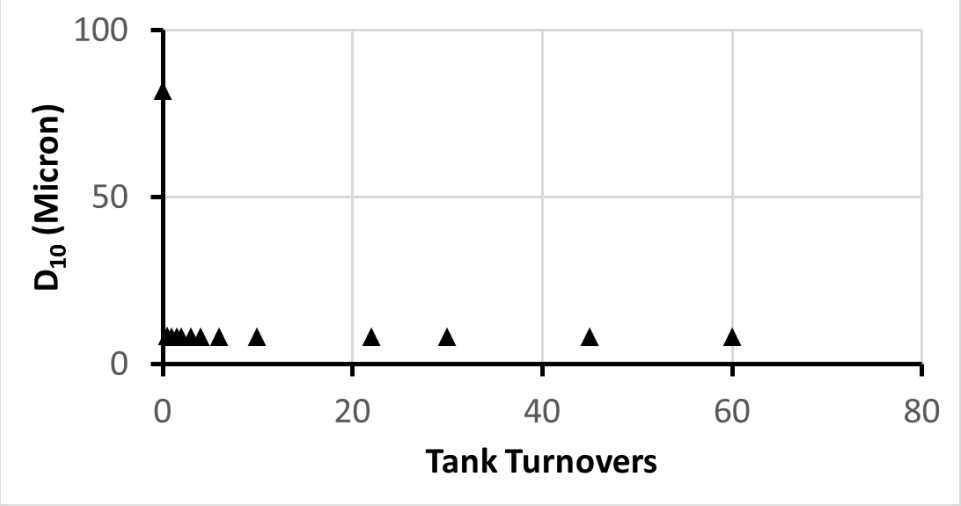

Figure A.3.8 - D_{10} versus milling time in tank turnovers for sucrose/IPA wet milling at 8000 rpm and 2.1 lpm

A.4 –Wet Milling of Sucrose/IPA at 5000 rpm and 3.0 lpm

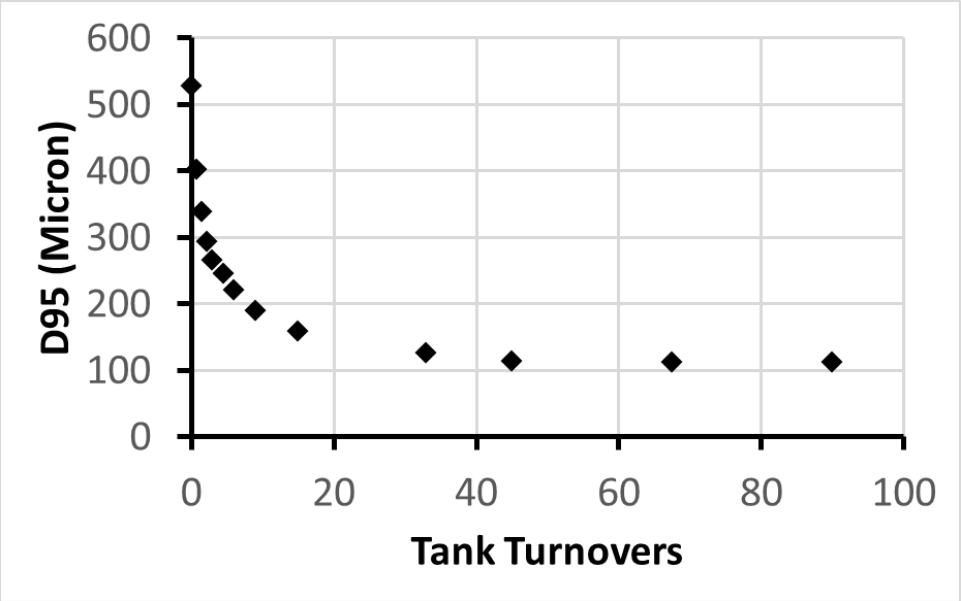

Figure A.4.1 - D95 versus milling time in tank turnovers for sucrose/IPA wet milling at 5000 rpm and 3.0 lpm

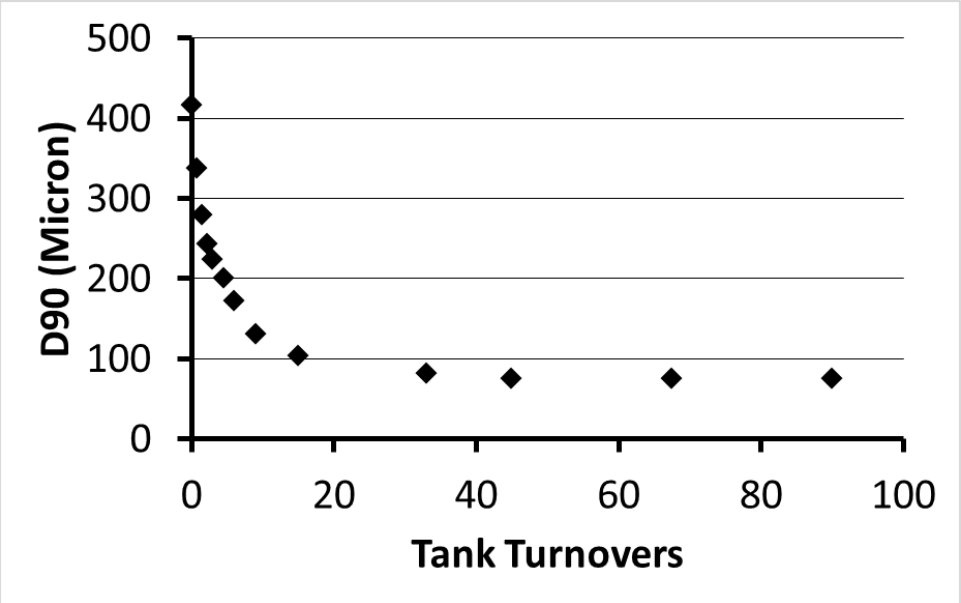

Figure A.4.2 - D90 versus milling time in tank turnovers for sucrose/IPA wet milling at 5000 rpm and 3.0 lpm

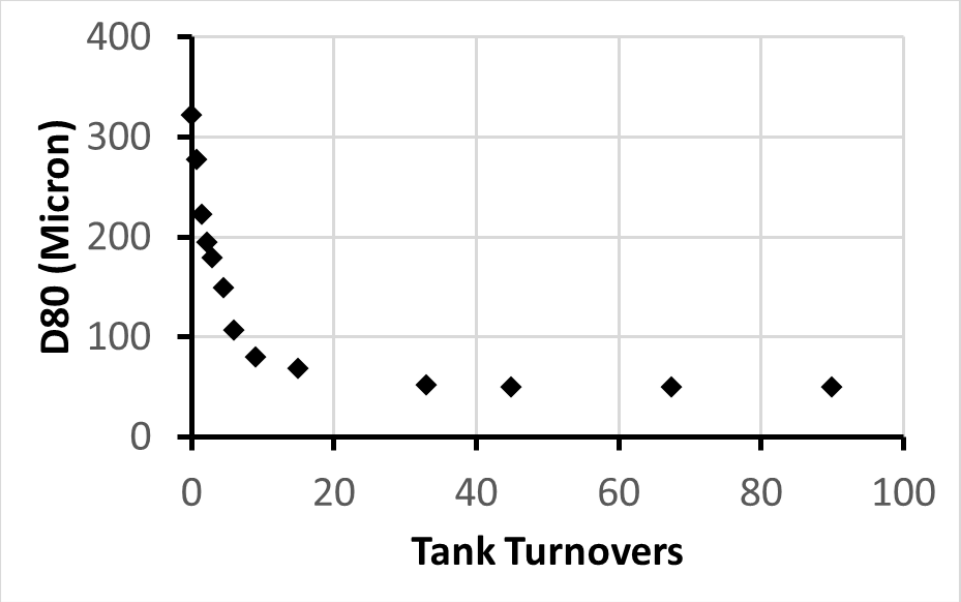

Figure A.4.3 - D80 versus milling time in tank turnovers for sucrose/IPA wet milling at 5000 rpm and 3.0 lpm

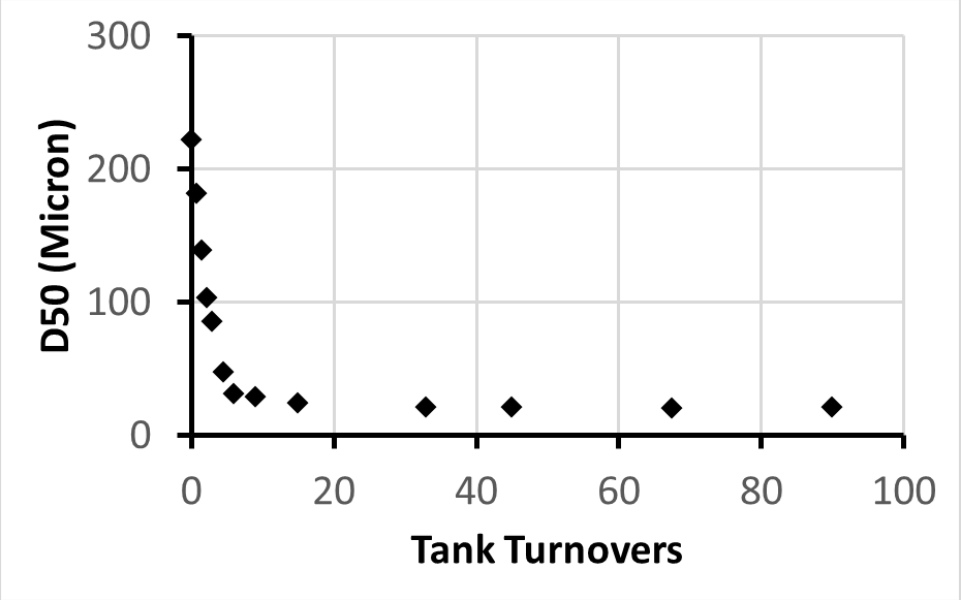

Figure A.4.4 - D50 versus milling time in tank turnovers for sucrose/IPA wet milling at 5000 rpm and 3.0 lpm

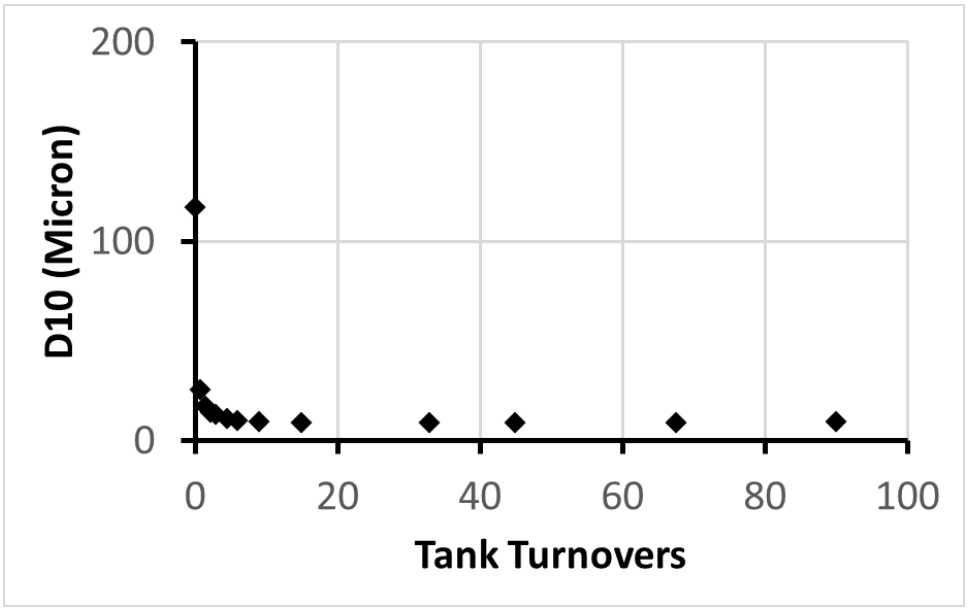

Figure A.4.5 - D10 versus milling time in tank turnovers for sucrose/IPA wet milling at 5000 rpm and 3.0 lpm

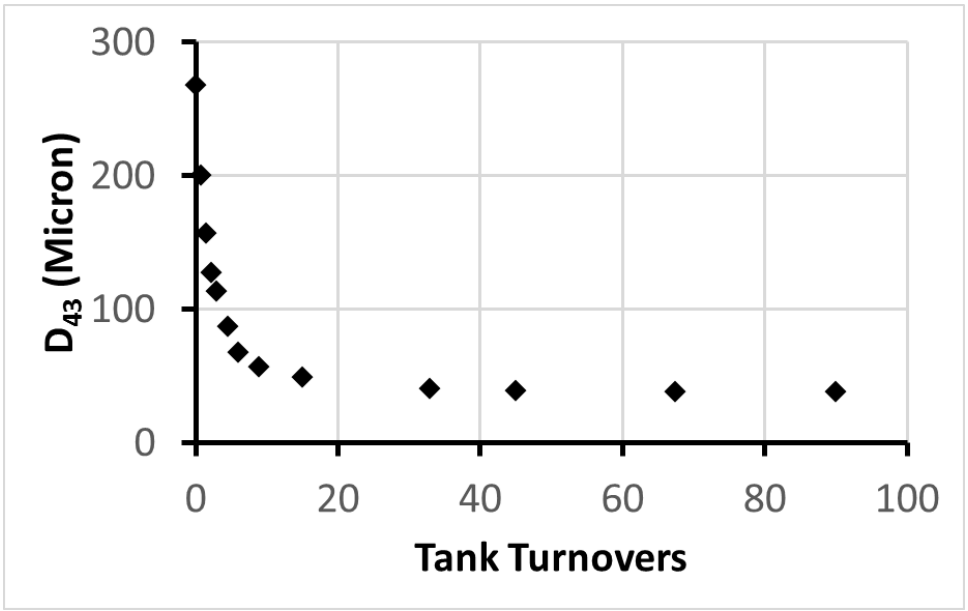

Figure A.4.6 - D_{43} versus milling time in tank turnovers for sucrose/IPA wet milling at 5000 rpm and 3.0 lpm

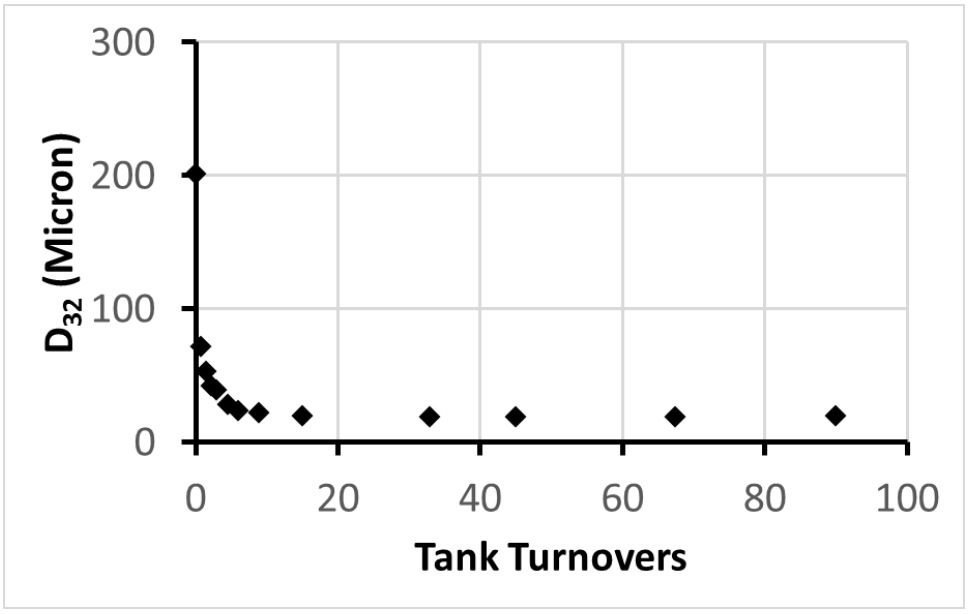

Figure A.4.7 - D_{32} versus milling time in tank turnovers for sucrose/IPA wet milling at 5000 rpm and 3.0 lpm

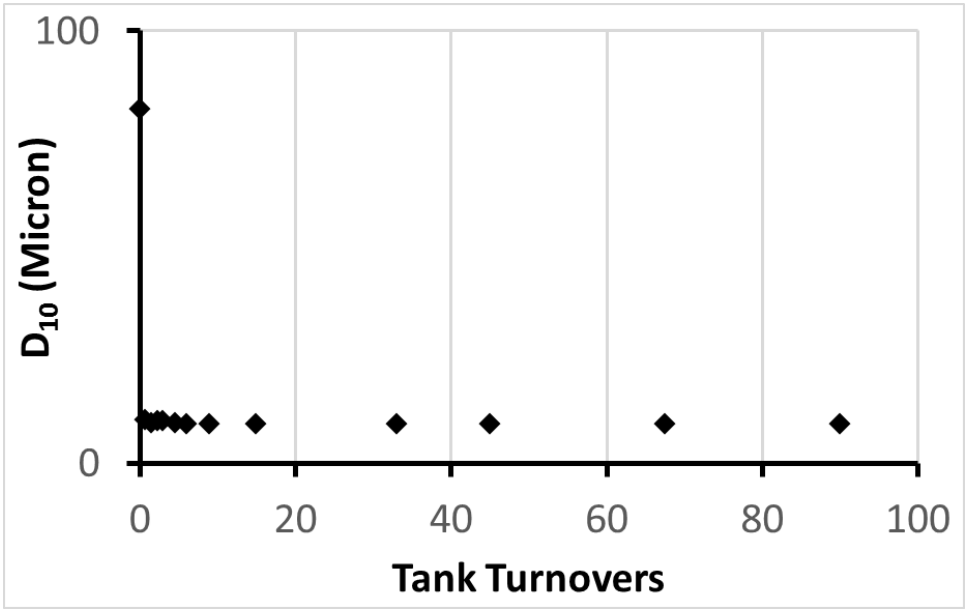

Figure A.4.8 - D_{10} versus milling time in tank turnovers for sucrose/IPA wet milling at 5000 rpm and 3.0 lpm

A.5 –Wet Milling of Sucrose/IPA at 6500 rpm and 3.0 lpm

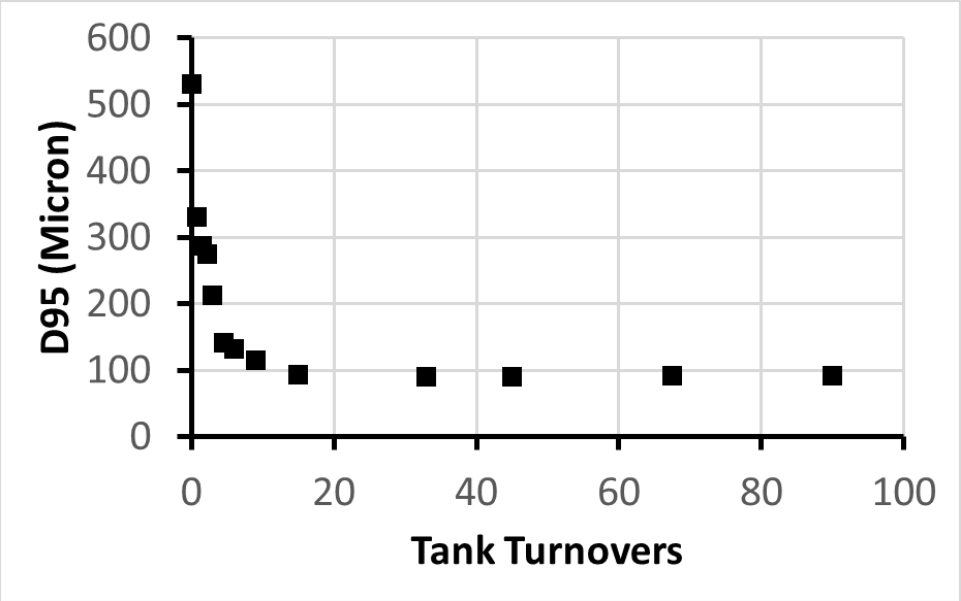

Figure A.5.1 - D95 versus milling time in tank turnovers for sucrose/IPA wet milling at 6500 rpm and 3.0 lpm

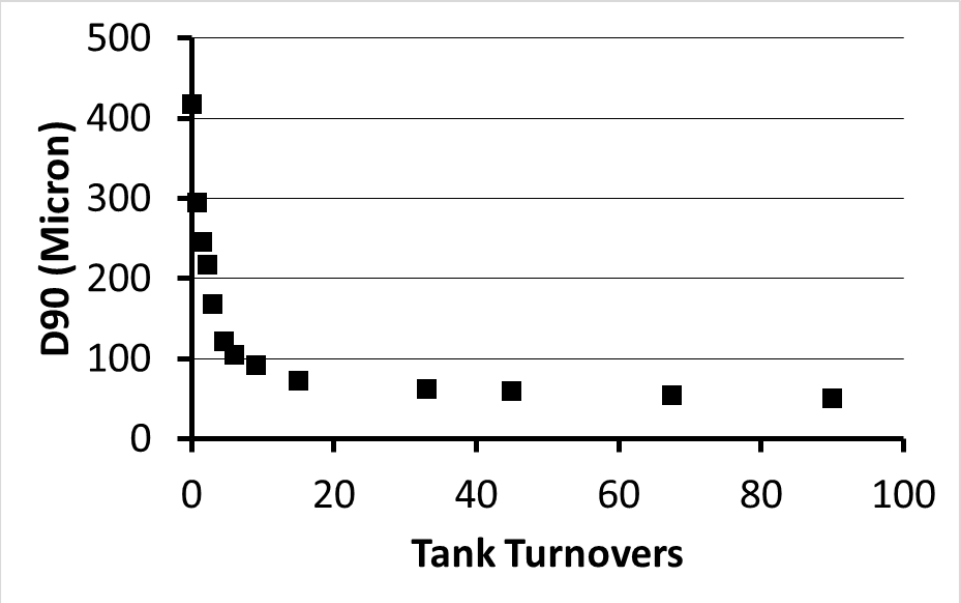

Figure A.5.2 - D90 versus milling time in tank turnovers for sucrose/IPA wet milling at 6500 rpm and 3.0 lpm

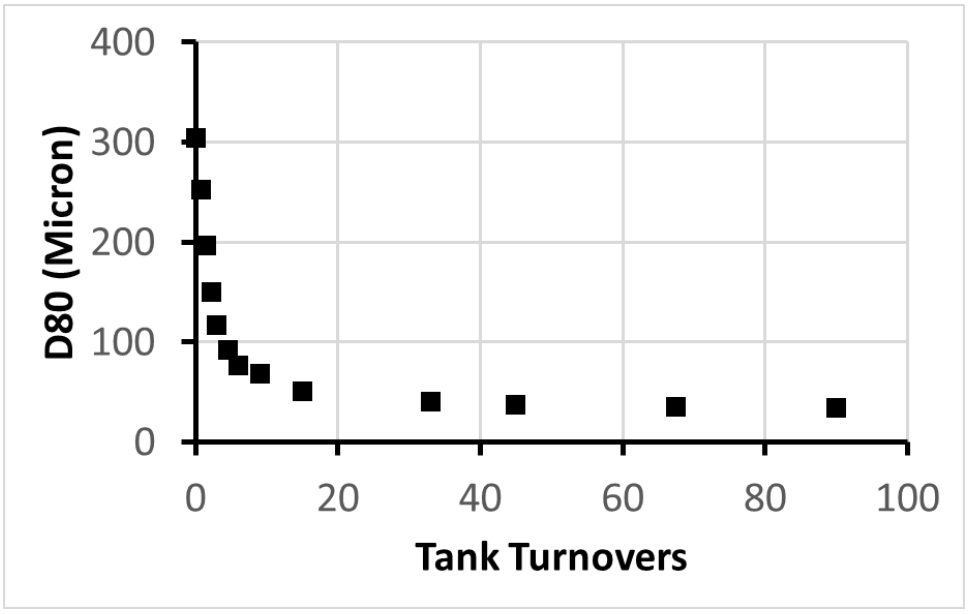

Figure A.5.3 - D80 versus milling time in tank turnovers for sucrose/IPA wet milling at 6500 rpm and 3.0 lpm

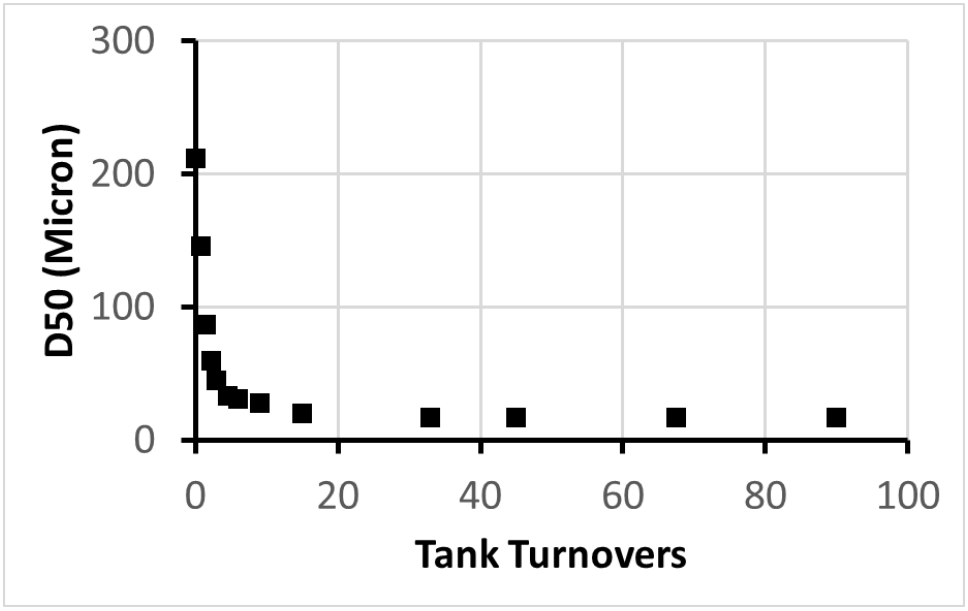

Figure A.5.4 - D50 versus milling time in tank turnovers for sucrose/IPA wet milling at 6500 rpm and 3.0 lpm

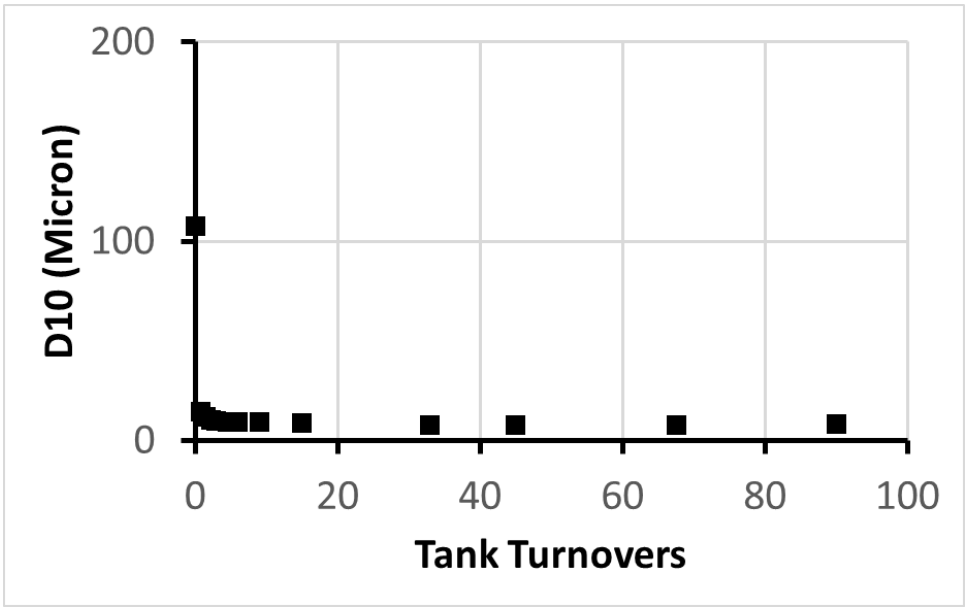

Figure A.5.5 - D10 versus milling time in tank turnovers for sucrose/IPA wet milling at 6500 rpm and 3.0 lpm

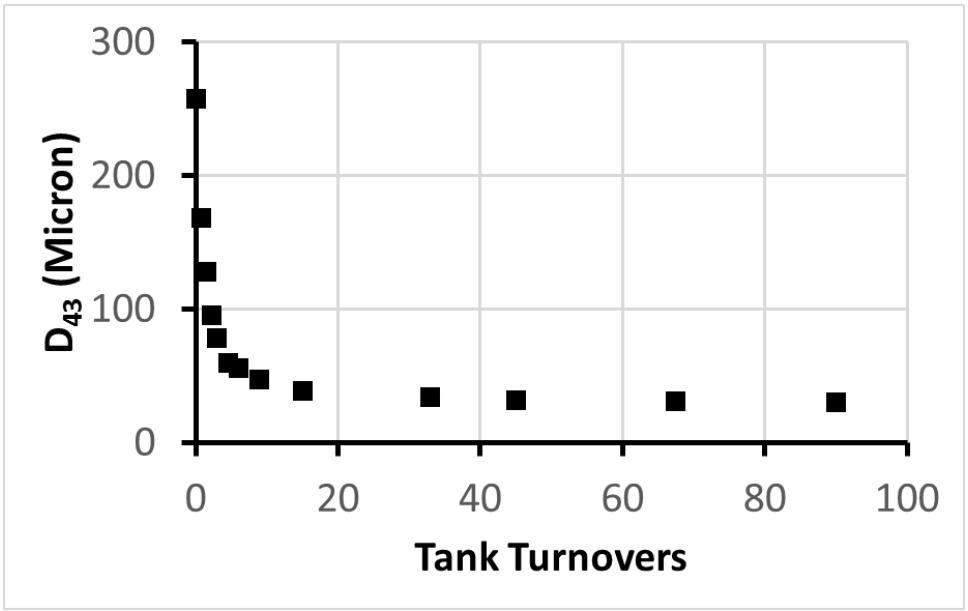

Figure A.5.6 - D_{43} versus milling time in tank turnovers for sucrose/IPA wet milling at 6500 rpm and 3.0 lpm

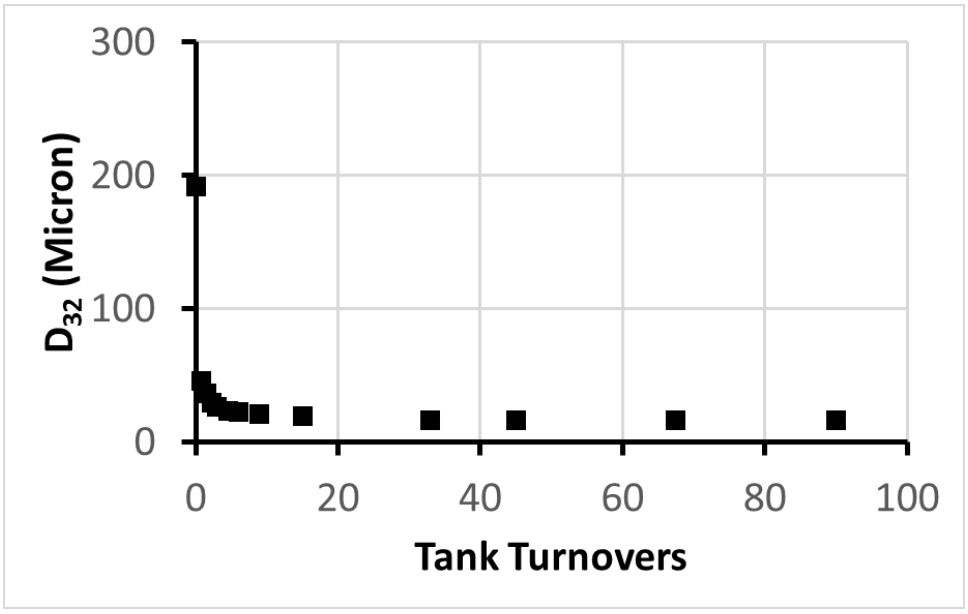

Figure A.5.7 - D_{32} versus milling time in tank turnovers for sucrose/IPA wet milling at 6500 rpm and 3.0 lpm

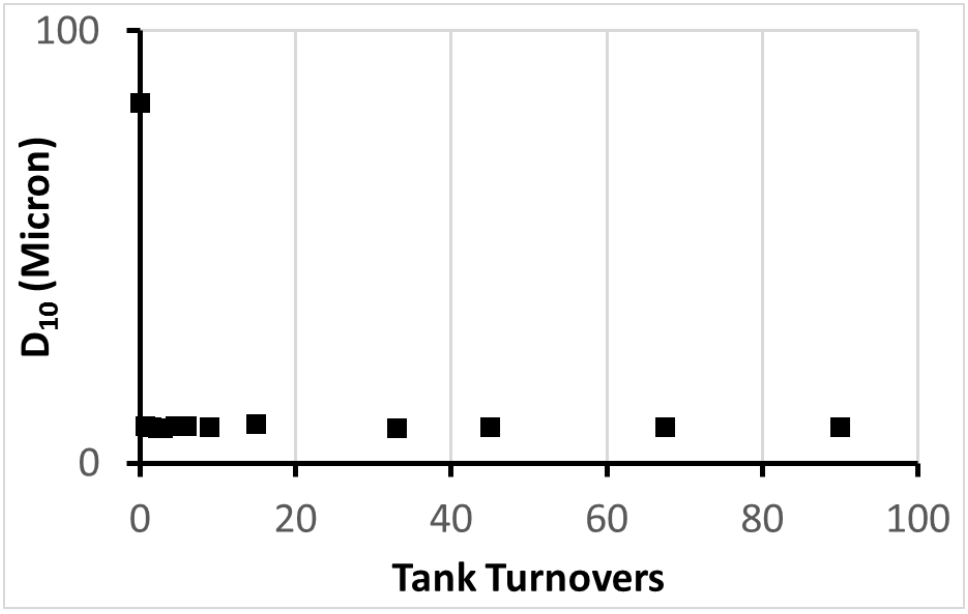

Figure A.5.8 - D_{10} versus milling time in tank turnovers for sucrose/IPA wet milling at 6500 rpm and 3.0 lpm

A.6 –Wet Milling of Sucrose/IPA at 8000 rpm and 3.0 lpm

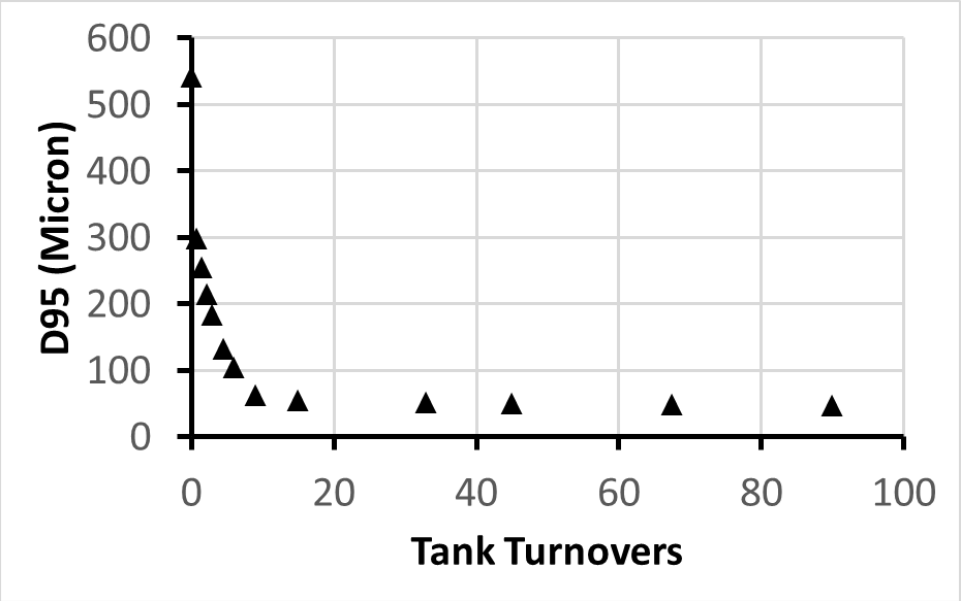

Figure A.6.1 - D95 versus milling time in tank turnovers for sucrose/IPA wet milling at 8000 rpm and 3.0 lpm

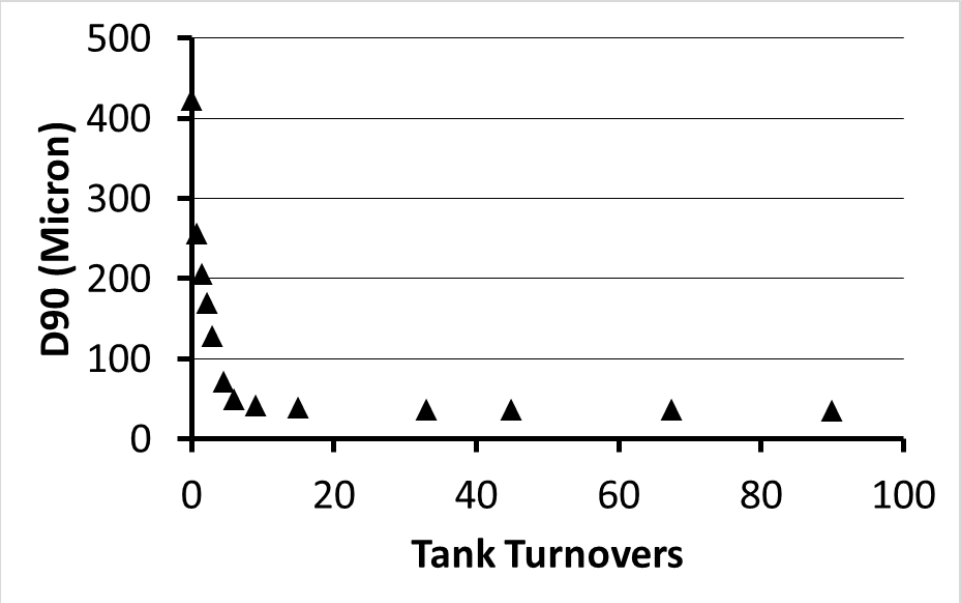

Figure A.6.2 - D90 versus milling time in tank turnovers for sucrose/IPA wet milling at 8000 rpm and 3.0 lpm

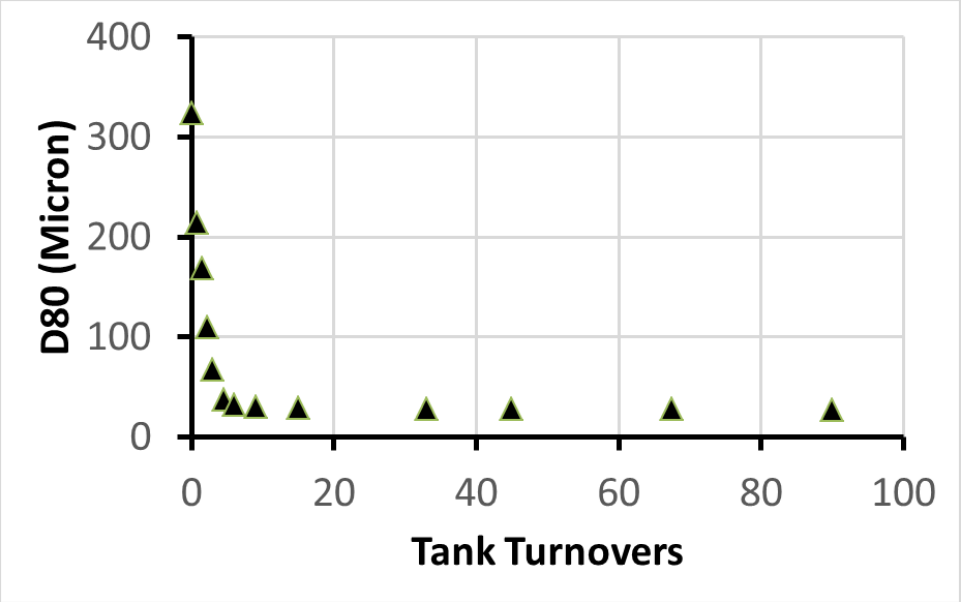

Figure A.6.3 - D80 versus milling time in tank turnovers for sucrose/IPA wet milling at 8000 rpm and 3.0 lpm

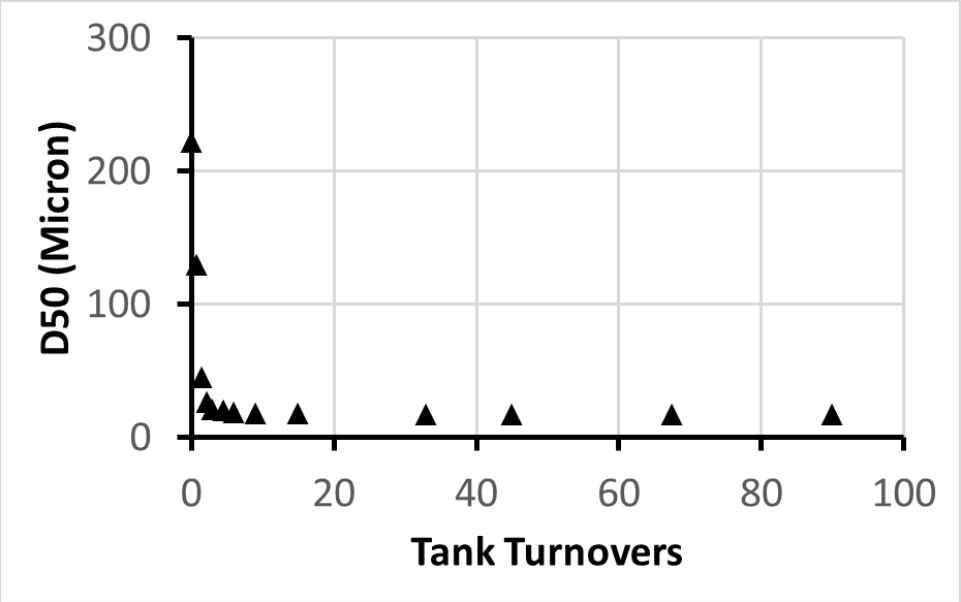

Figure A.6.4 - D50 versus milling time in tank turnovers for sucrose/IPA wet milling at 8000 rpm and 3.0 lpm

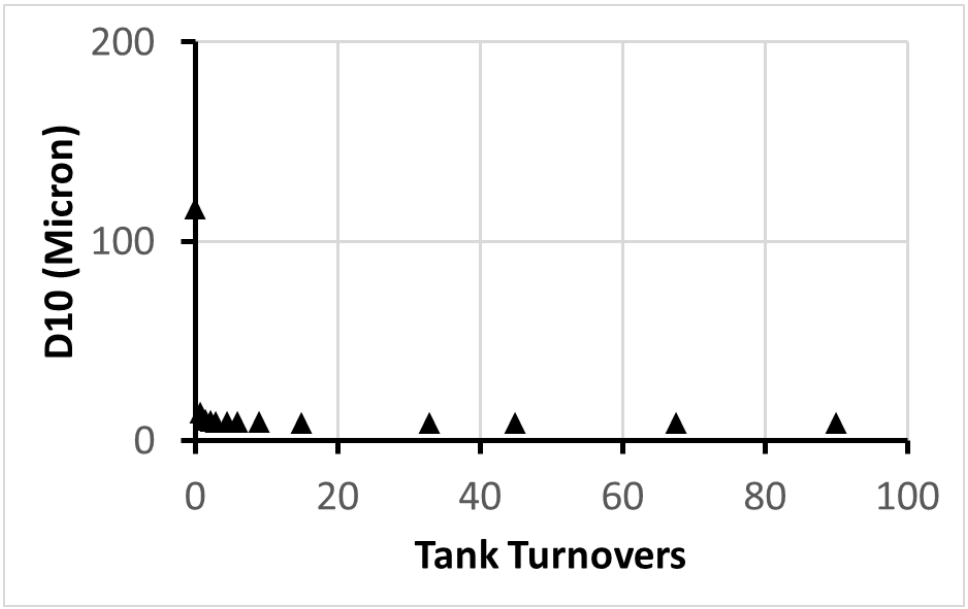

Figure A.6.5 - D10 versus milling time in tank turnovers for sucrose/IPA wet milling at 8000 rpm and 3.0 lpm

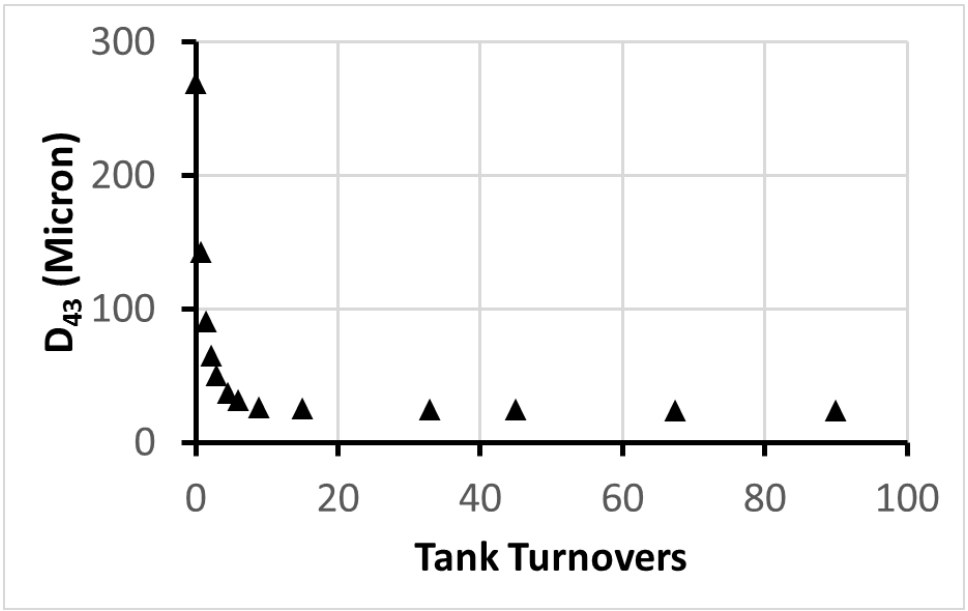

Figure A.6.6 - D_{43} versus milling time in tank turnovers for sucrose/IPA wet milling at 8000 rpm and 3.0 lpm

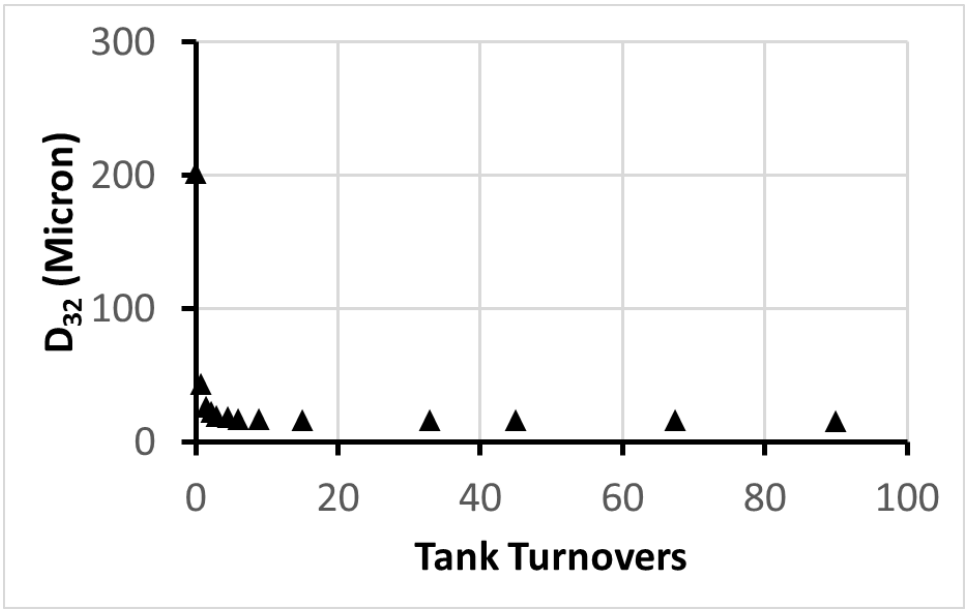

Figure A.6.7 - D_{32} versus milling time in tank turnovers for sucrose/IPA wet milling at 8000 rpm and 3.0 lpm

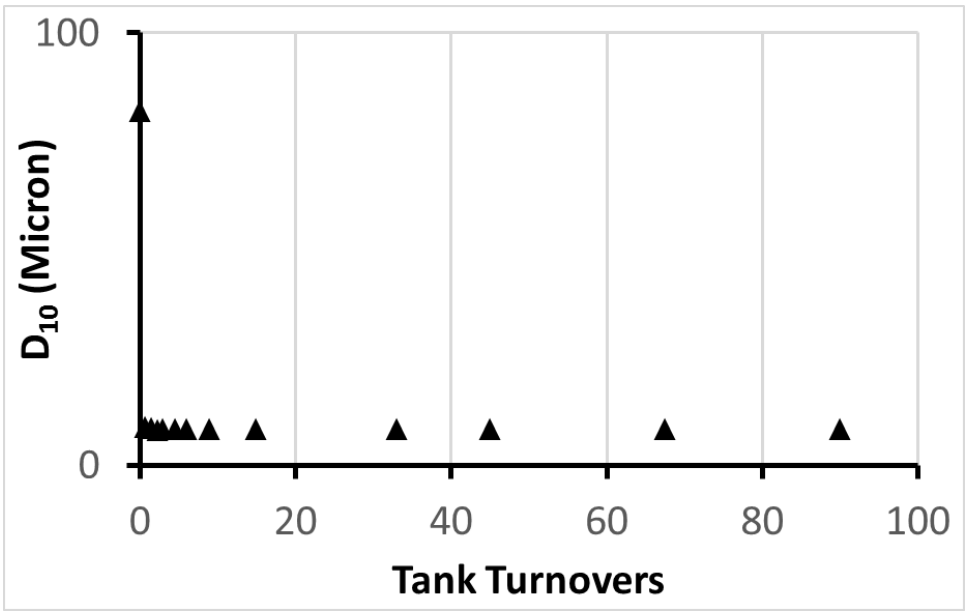

Figure A.6.8 - D_{10} versus milling time in tank turnovers for sucrose/IPA wet milling at 8000 rpm and 3.0 lpm

A.7 –Wet Milling of Sucrose/IPA at 5000 rpm and 4.2 lpm

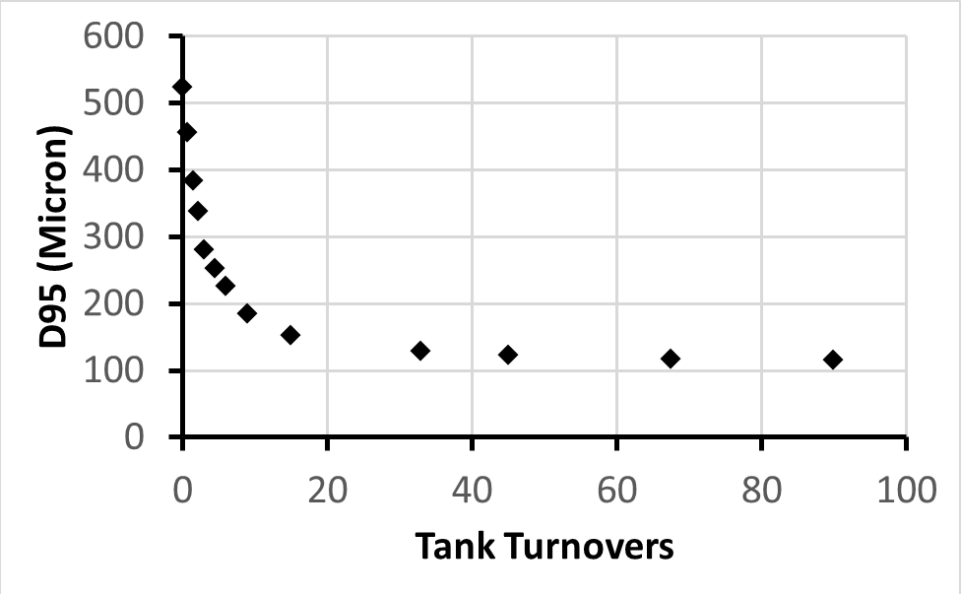

Figure A.7.1 - D95 versus milling time in tank turnovers for sucrose/IPA wet milling at 5000 rpm and 4.2 lpm

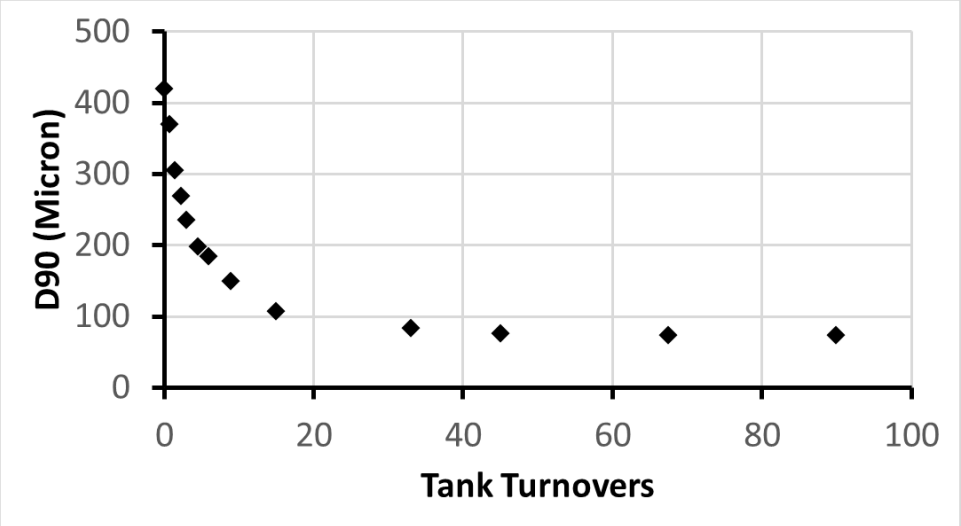

Figure A.7.2 - D90 versus milling time in tank turnovers for sucrose/IPA wet milling at 5000 rpm and 4.2 lpm

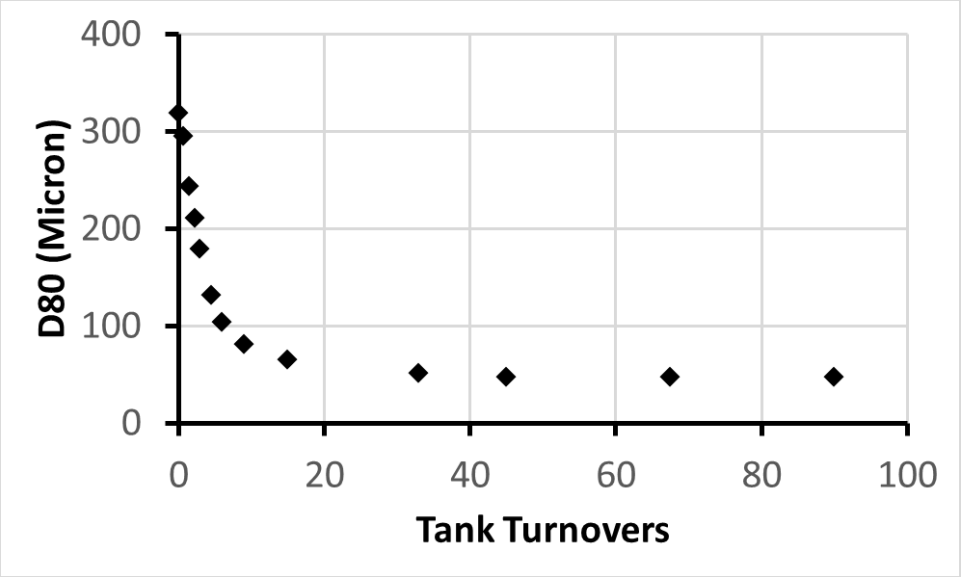

Figure A.7.3 - D80 versus milling time in tank turnovers for sucrose/IPA wet milling at 5000 rpm and 4.2 lpm

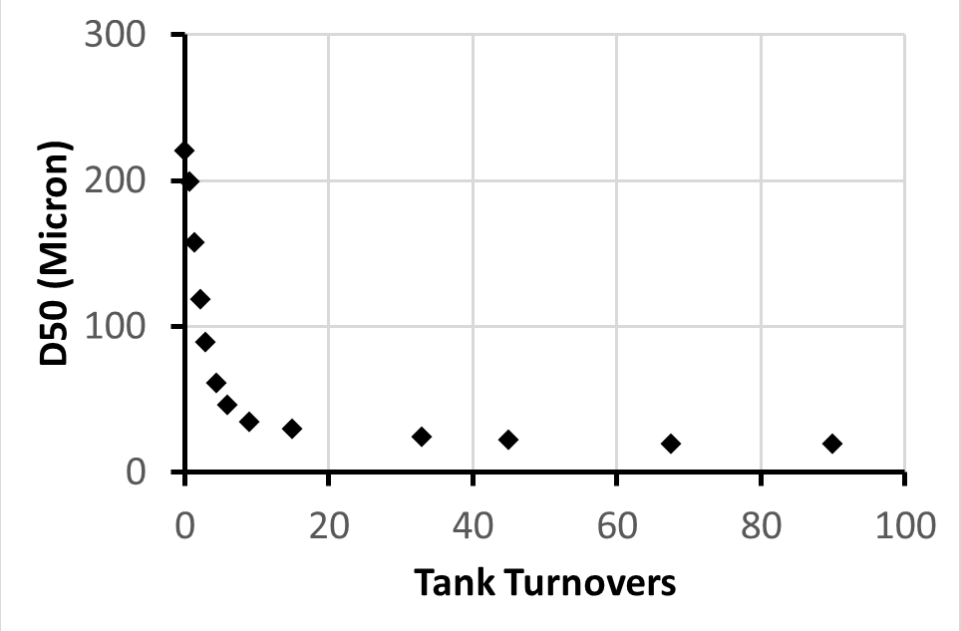

Figure A.7.4 - D50 versus milling time in tank turnovers for sucrose/IPA wet milling at 5000 rpm and 4.2 lpm

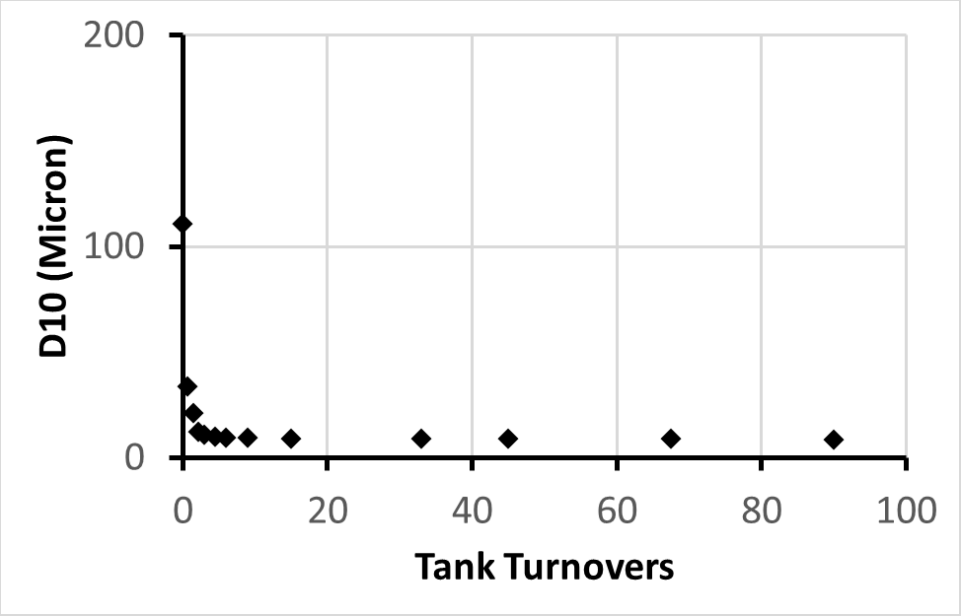

Figure A.7.5 - D10 versus milling time in tank turnovers for sucrose/IPA wet milling at 5000 rpm and 4.2 lpm

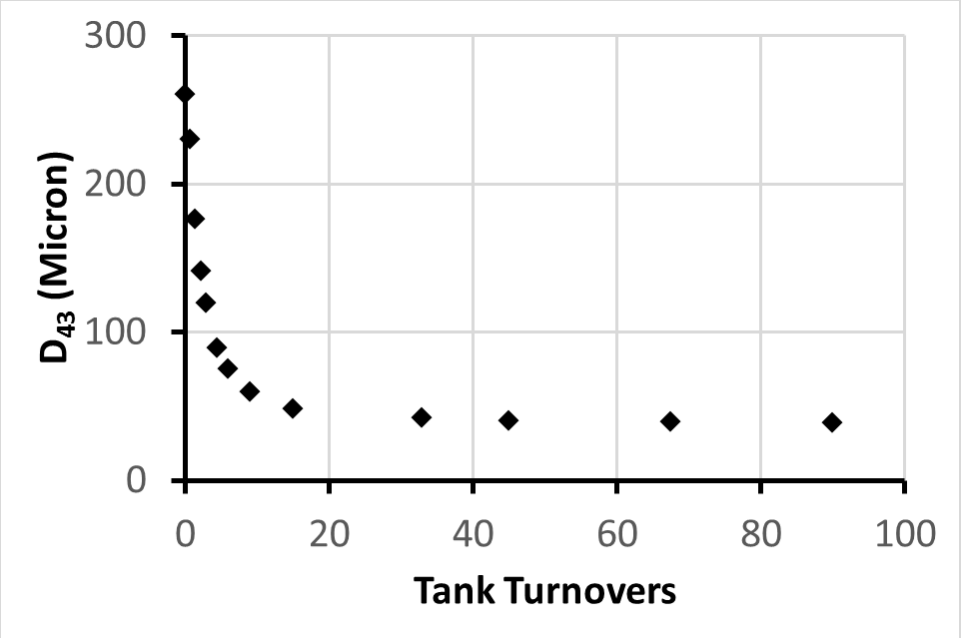

Figure A.7.6 - D_{43} versus milling time in tank turnovers for sucrose/IPA wet milling at 5000 rpm and 4.2 lpm

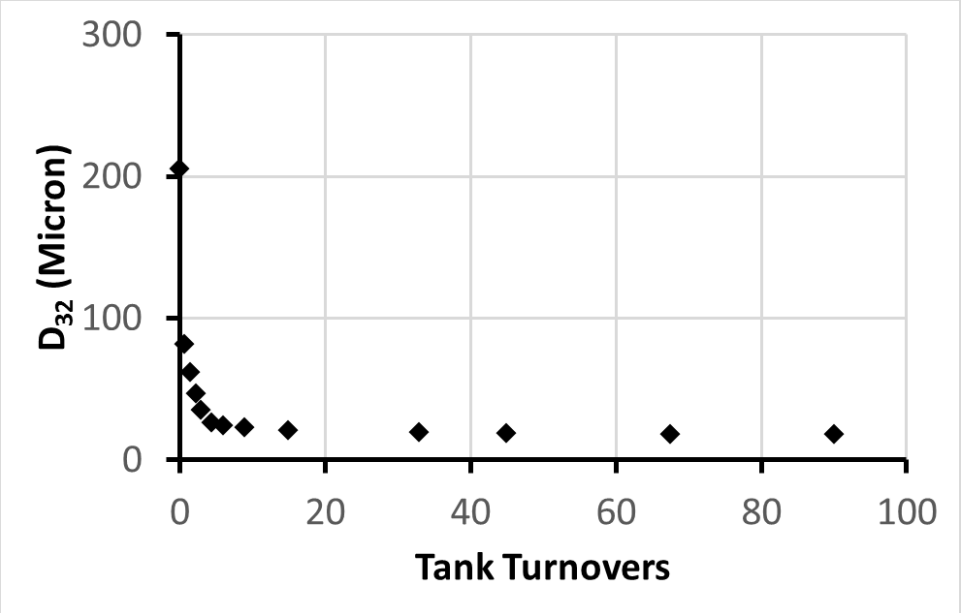

Figure A.7.7 - D_{32} versus milling time in tank turnovers for sucrose/IPA wet milling at 5000 rpm and 4.2 lpm

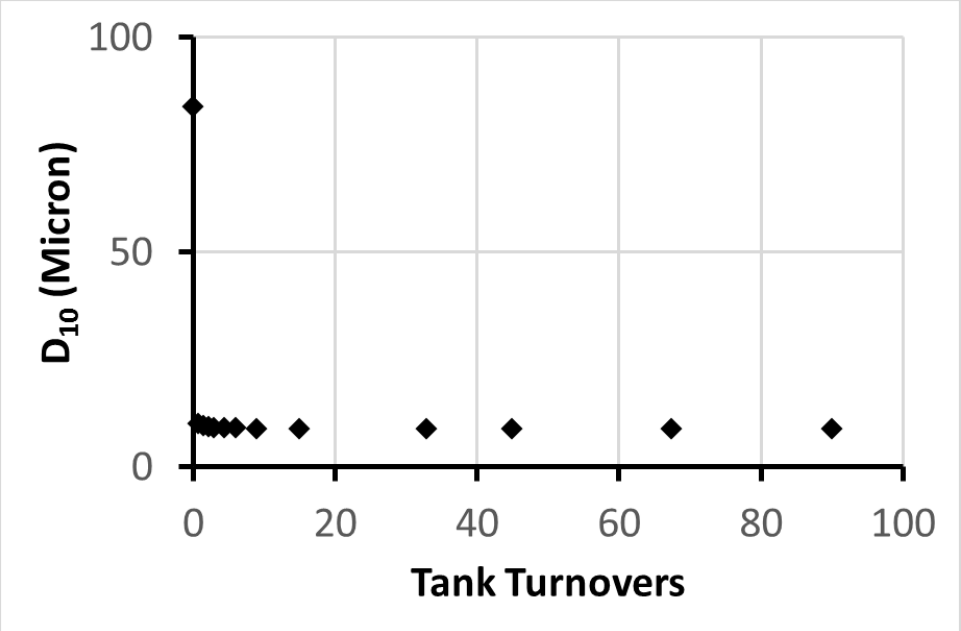

Figure A.7.8 - D_{10} versus milling time in tank turnovers for sucrose/IPA wet milling at 5000 rpm and 4.2 lpm

A.8 –Wet Milling of Sucrose/IPA at 6500 rpm and 4.2 lpm

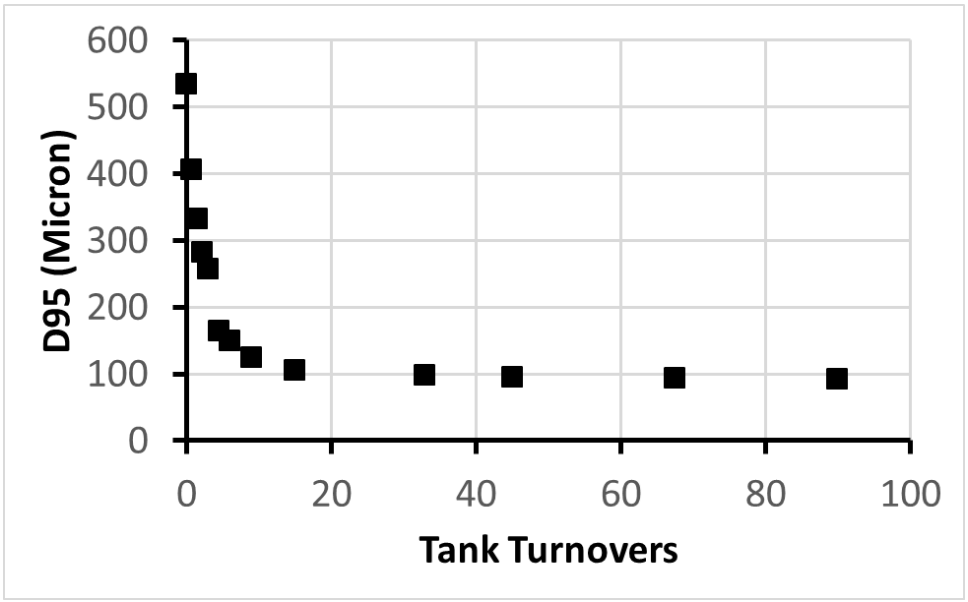

Figure A.8.1 - D95 versus milling time in tank turnovers for sucrose/IPA wet milling at 6500 rpm and 4.2 lpm

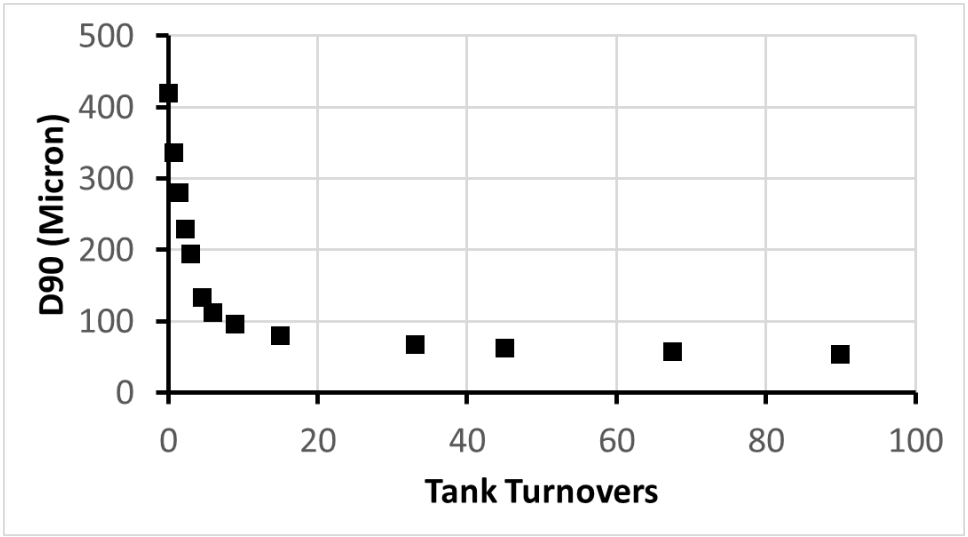

Figure A.8.2 - D90 versus milling time in tank turnovers for sucrose/IPA wet milling at 6500 rpm and 4.2 lpm

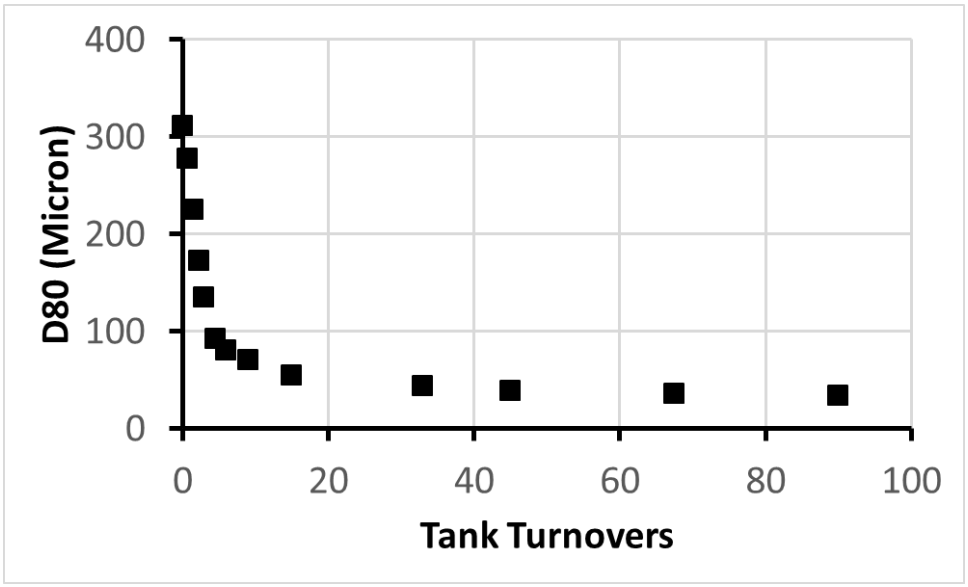

Figure A.8.3 - D80 versus milling time in tank turnovers for sucrose/IPA wet milling at 6500 rpm and 4.2 lpm

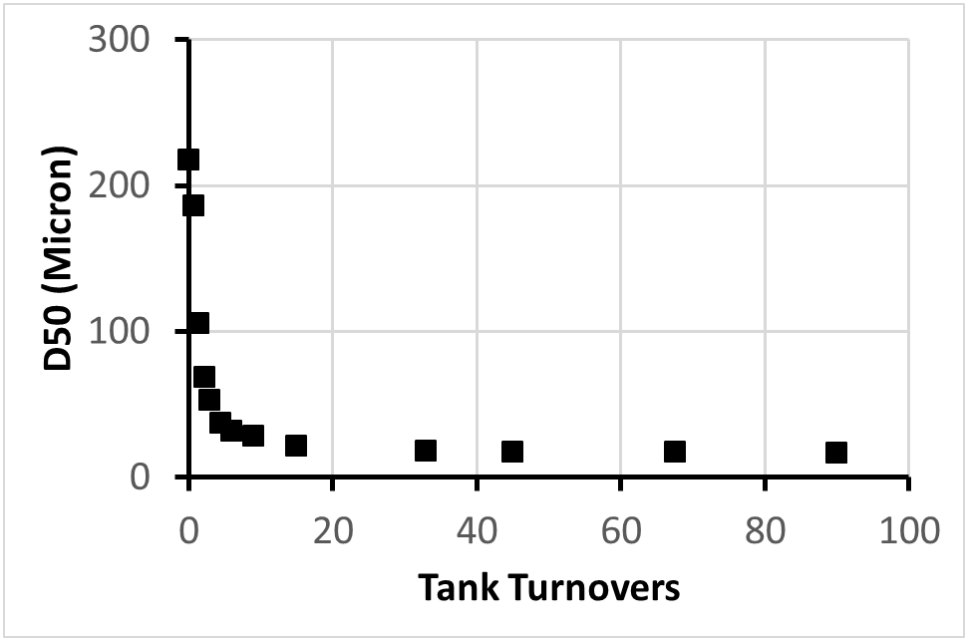

Figure A.8.4 - D50 versus milling time in tank turnovers for sucrose/IPA wet milling at 6500 rpm and 4.2 lpm

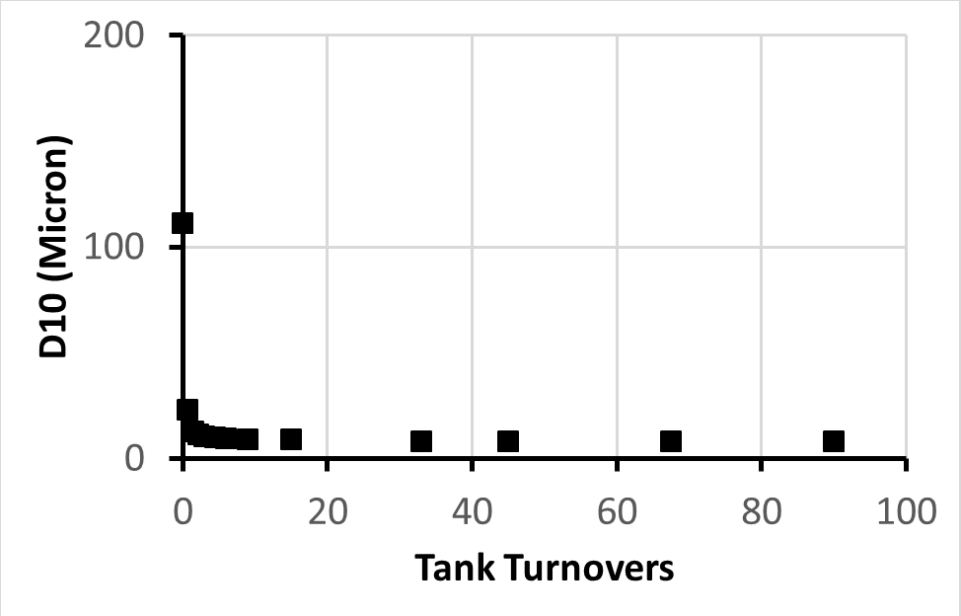

Figure A.8.5 - D10 versus milling time in tank turnovers for sucrose/IPA wet milling at 6500 rpm and 4.2 lpm

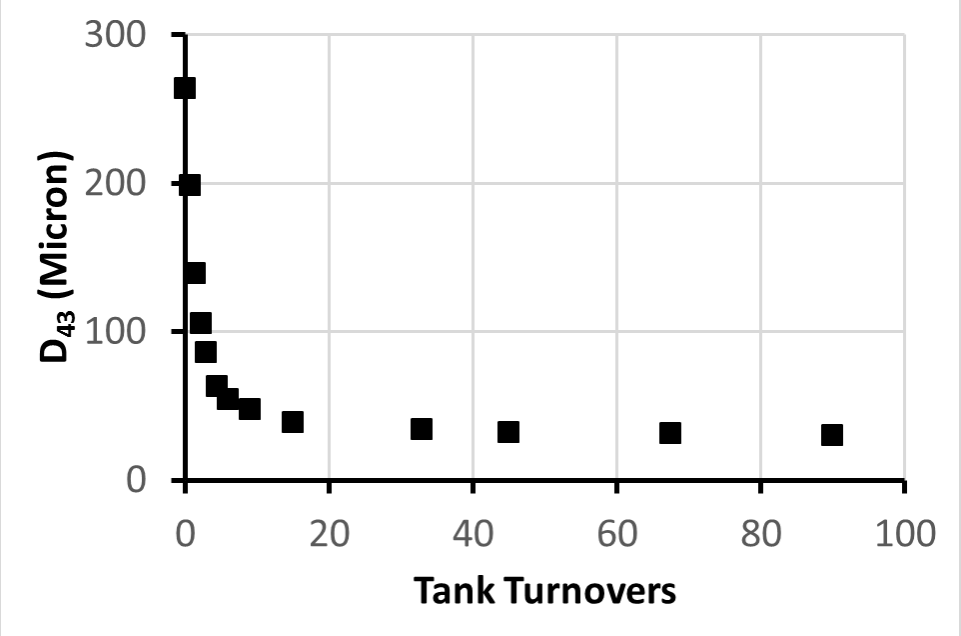

Figure A.8.6 - D_{43} versus milling time in tank turnovers for sucrose/IPA wet milling at 6500 rpm and 4.2 lpm

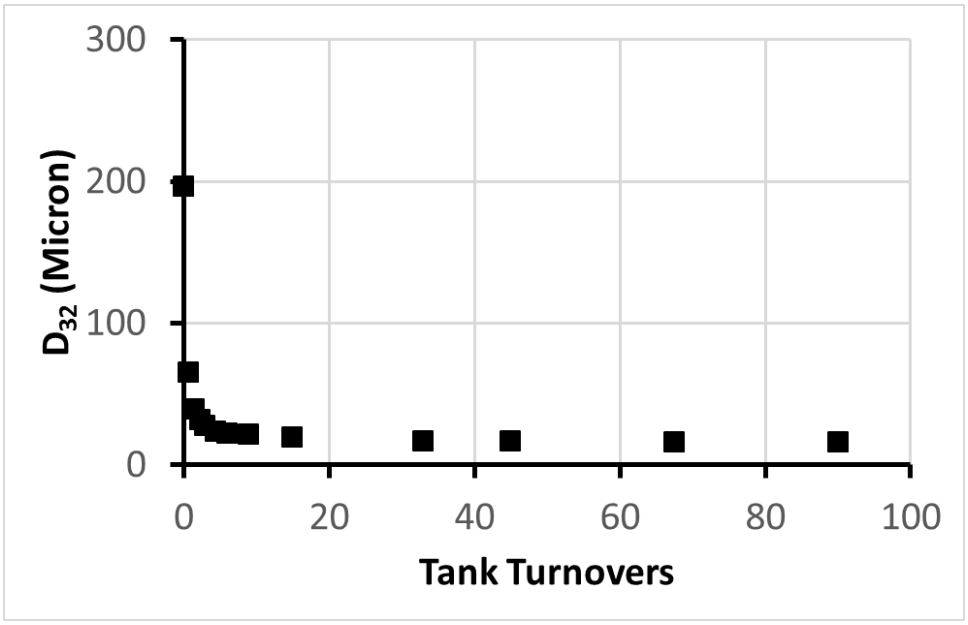

Figure A.8.7 - D_{32} versus milling time in tank turnovers for sucrose/IPA wet milling at 6500 rpm and 4.2 lpm

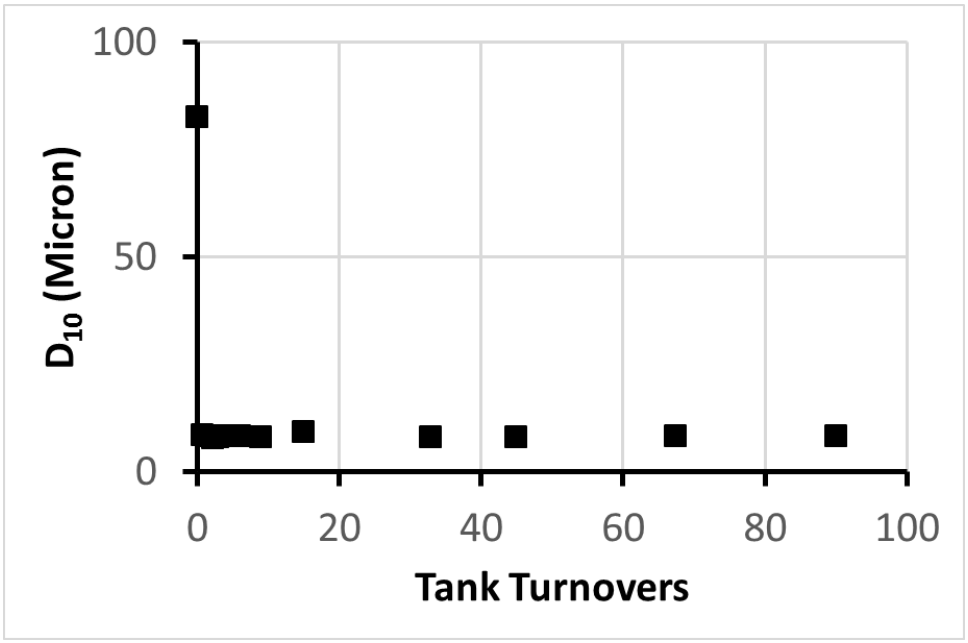

Figure A.8.8 - D_{10} versus milling time in tank turnovers for sucrose/IPA wet milling at 6500 rpm and 4.2 lpm

A.9 –Wet Milling of Sucrose/IPA at 8000 rpm and 4.2 lpm

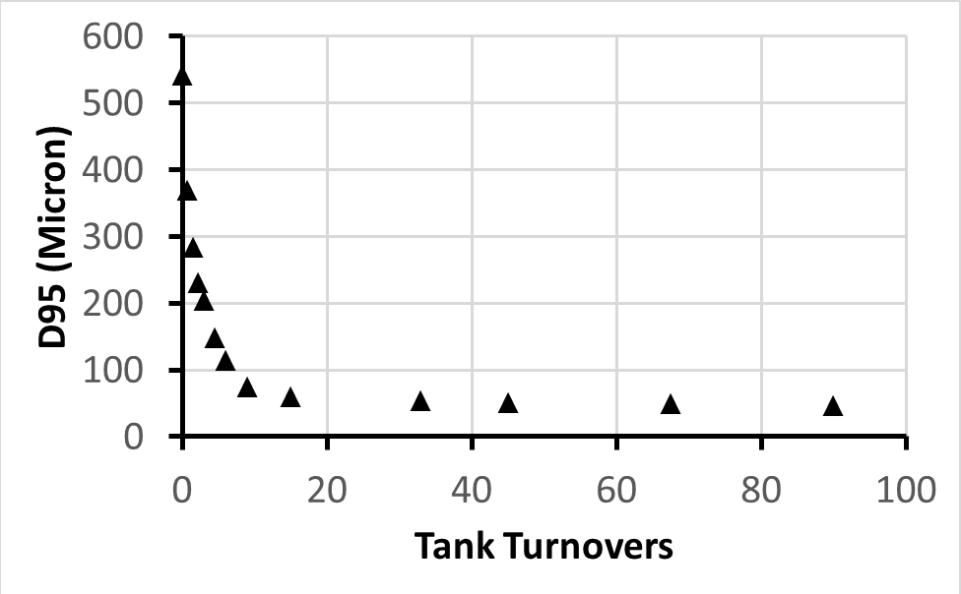

Figure A.9.1 - D95 versus milling time in tank turnovers for sucrose/IPA wet milling at 8000 rpm and 4.2 lpm

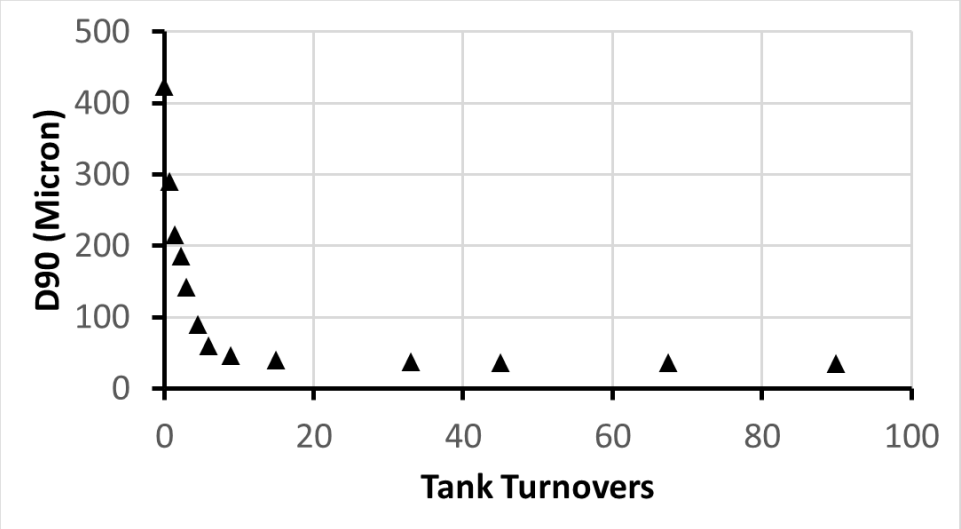

Figure A.9.2 - D90 versus milling time in tank turnovers for sucrose/IPA wet milling at 8000 rpm and 4.2 lpm

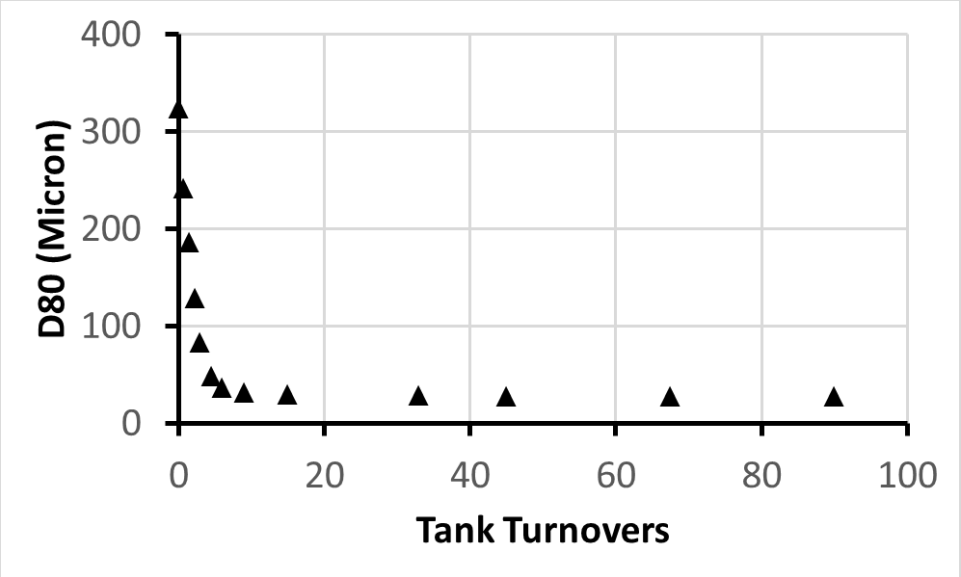

Figure A.9.3 - D80 versus milling time in tank turnovers for sucrose/IPA wet milling at 8000 rpm and 4.2 lpm

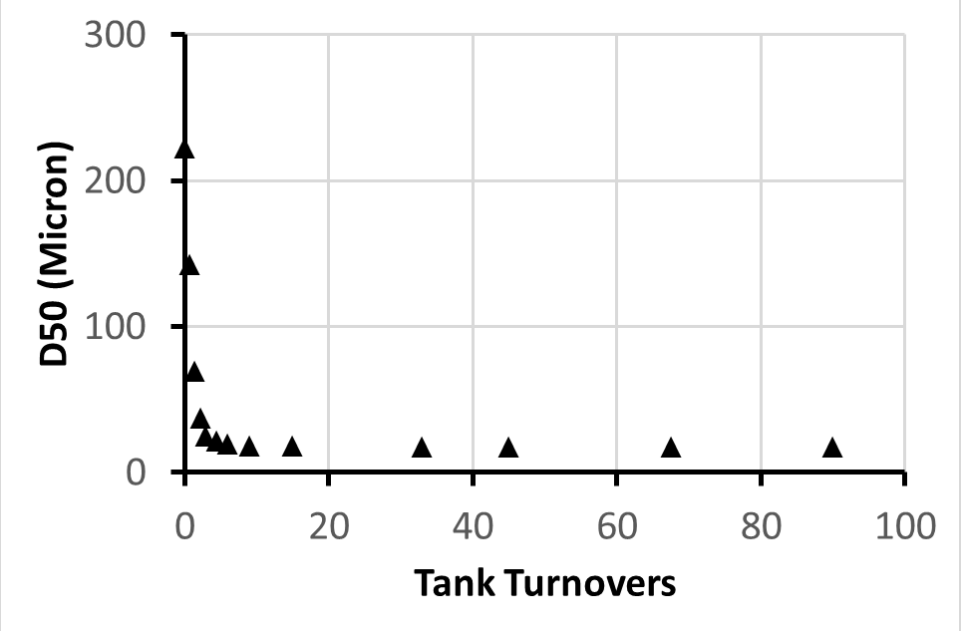

Figure A.9.4 - D50 versus milling time in tank turnovers for sucrose/IPA wet milling at 8000 rpm and 4.2 lpm

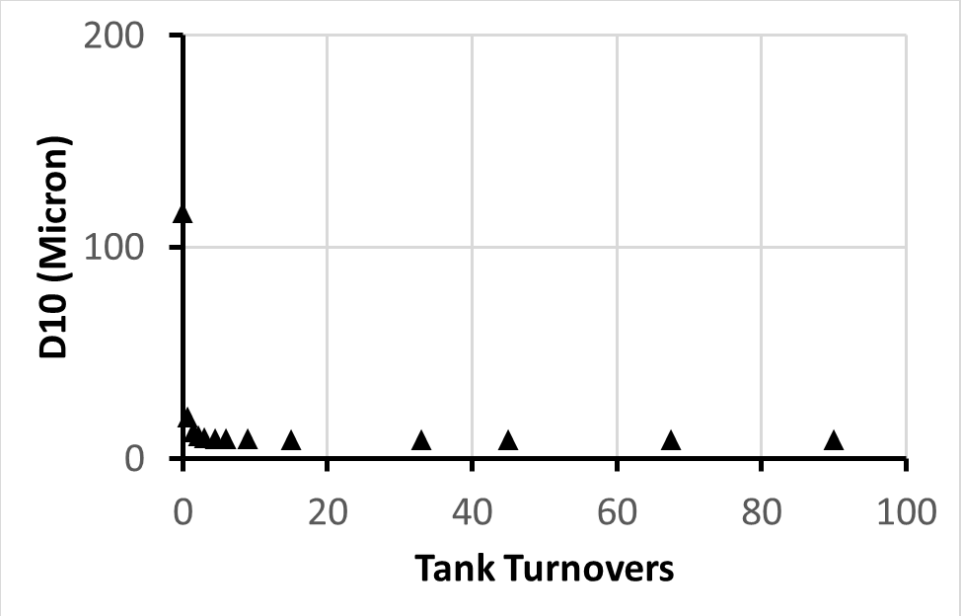

Figure A.9.5 - D10 versus milling time in tank turnovers for sucrose/IPA wet milling at 8000 rpm and 4.2 lpm

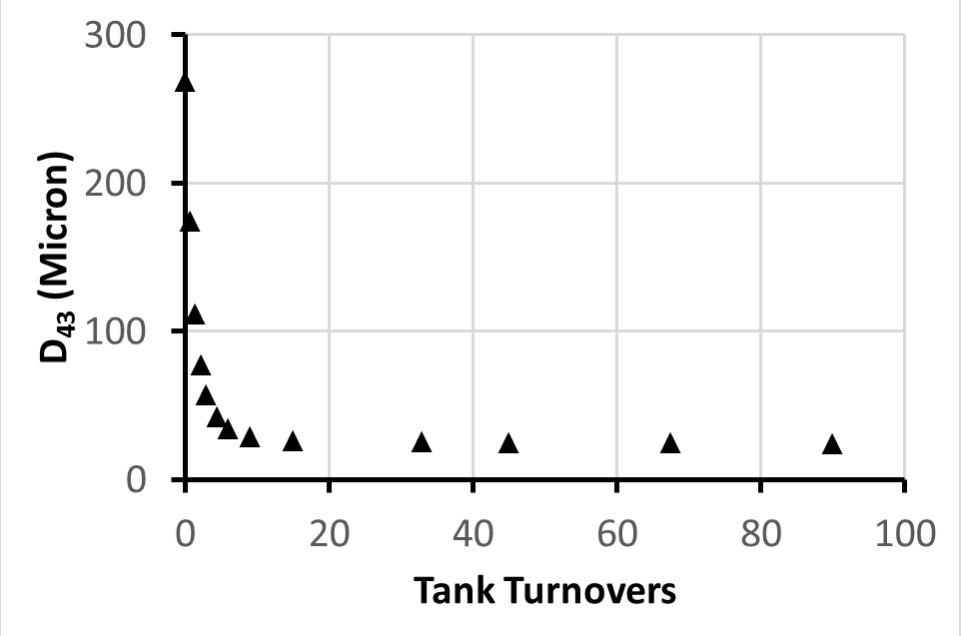

Figure A.9.6 - D_{43} versus milling time in tank turnovers for sucrose/IPA wet milling at 8000 rpm and 4.2 lpm

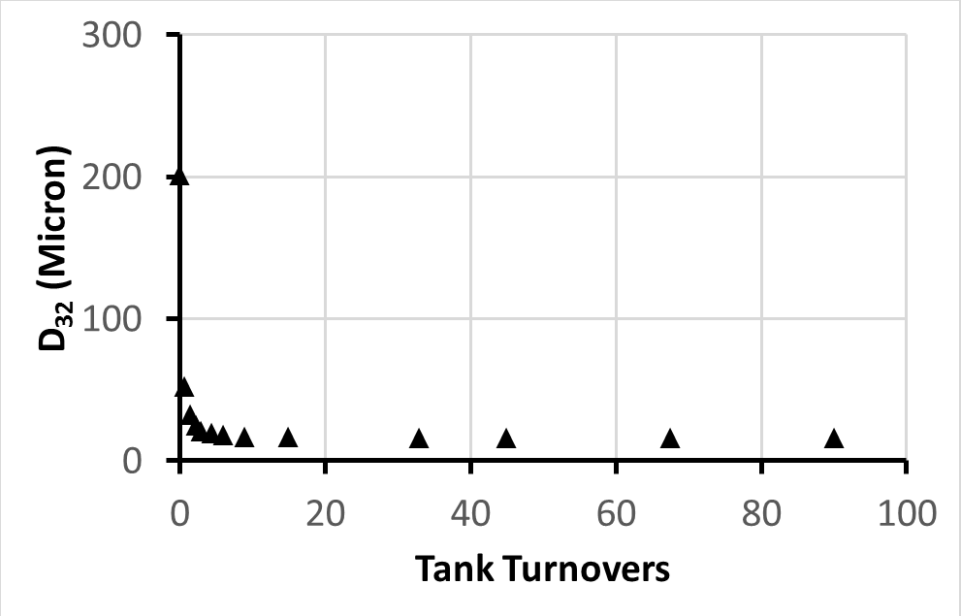

Figure A.9.7 - D_{32} versus milling time in tank turnovers for sucrose/IPA wet milling at 8000 rpm and 4.2 lpm

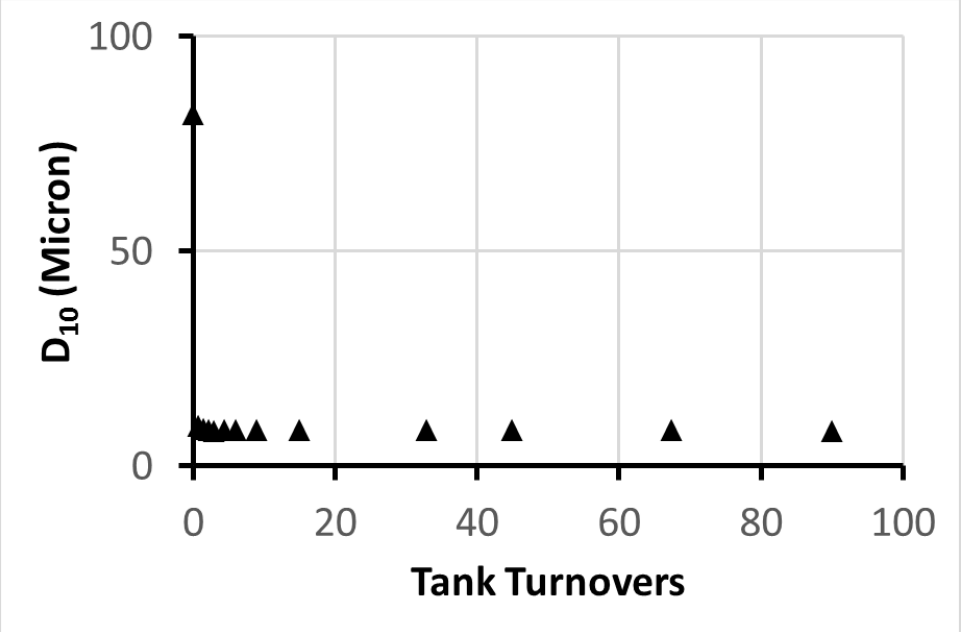

Figure A.9.8 - D_{10} versus milling time in tank turnovers for sucrose/IPA wet milling at 8000 rpm and 4.2 lpm

Appendix B: Wet milling data for glycine-IPA system in the Silverson L4R inline mixer with standard shear gap

Glycine crystals with 10% by weight, dispersed in 2 litres IPA, were fed to the Silverson L4R inline mixer with the standard shear gap at 5000 rpm and 2.1 lpm, 6500 rpm and 3.0 lpm, and 8000 rpm and 4.2 lpm. Extra milling time was provided to ensure that the equilibrium is achieved. Here, the experimental data acquired at different milling time are presented in terms of different cumulative diameters, D95, D90, D80, D50, and D10 versus milling time in tank turnovers.

B.1 –Wet Milling of glycine/IPA at 5000 rpm and 2.1 lpm

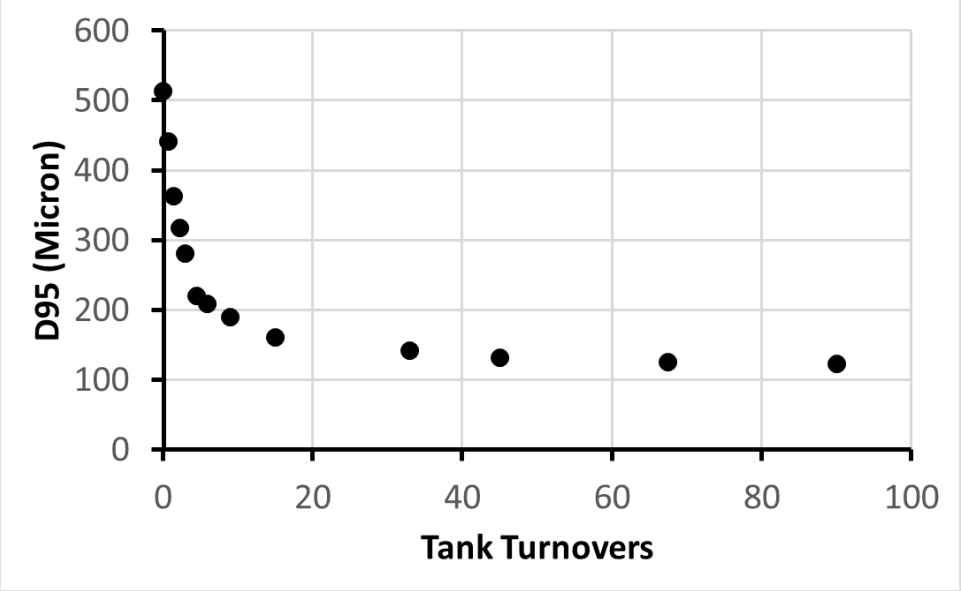

Figure B.1.1 - D95 versus milling time in tank turnovers for glycine/IPA wet milling at 5000 rpm and 2.1 lpm

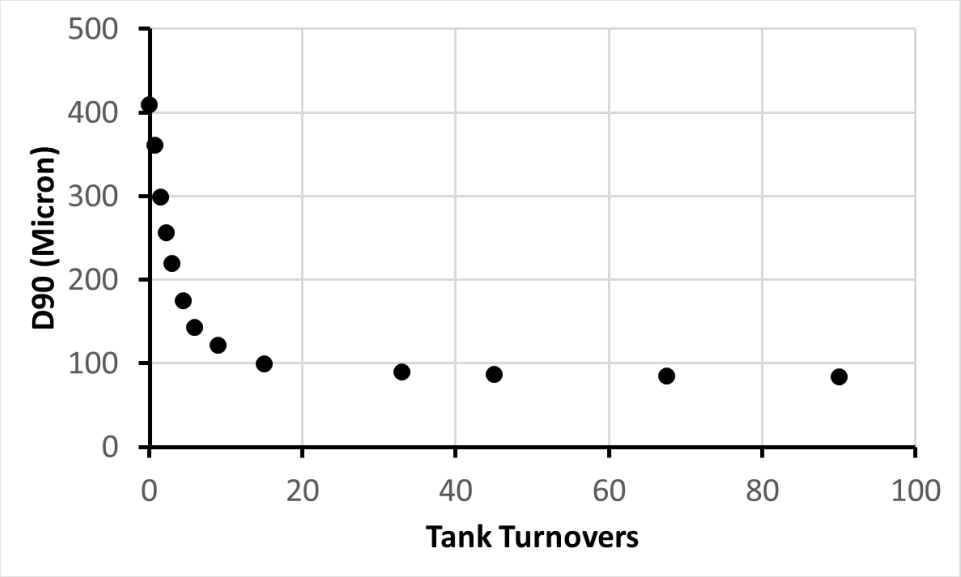

Figure B.1.2 - D90 versus milling time in tank turnovers for glycine/IPA wet milling at 5000 rpm and 2.1 lpm

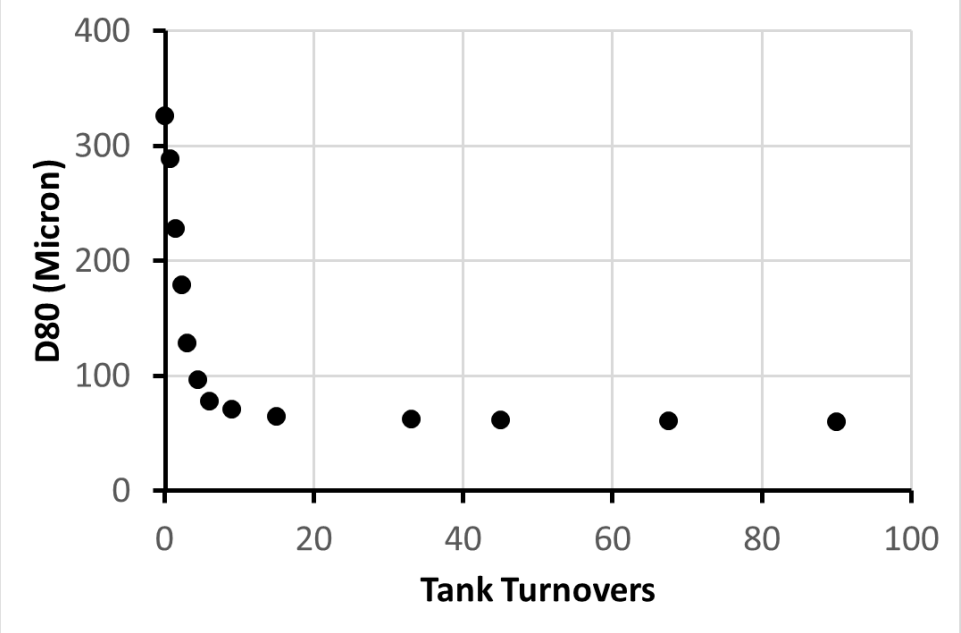

Figure B.1.3 - D80 versus milling time in tank turnovers for glycine/IPA wet milling at 5000 rpm and 2.1 lpm

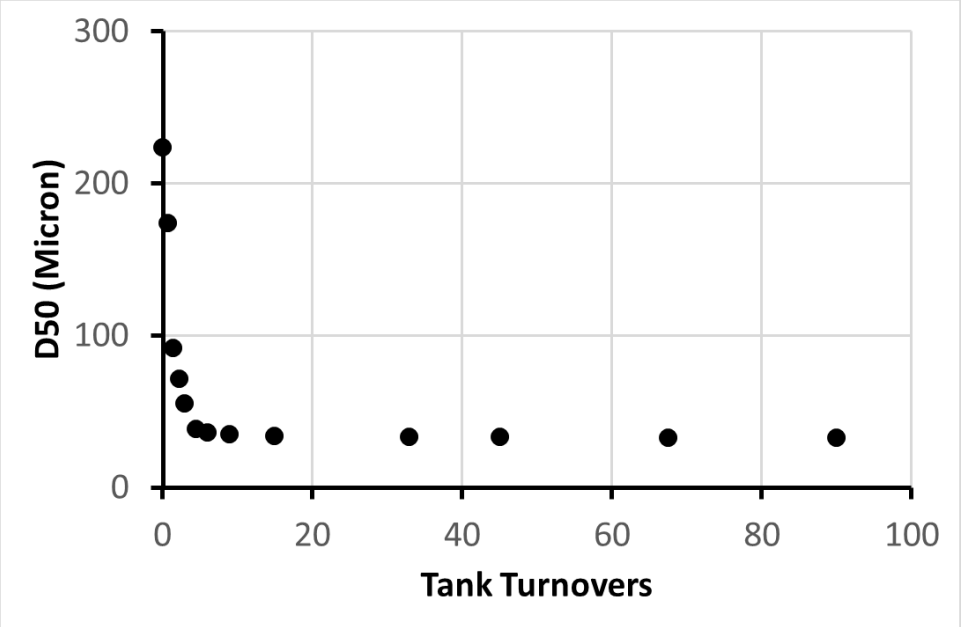

Figure B.1.4 - D50 versus milling time in tank turnovers for glycine/IPA wet milling at 5000 rpm and 2.1 lpm

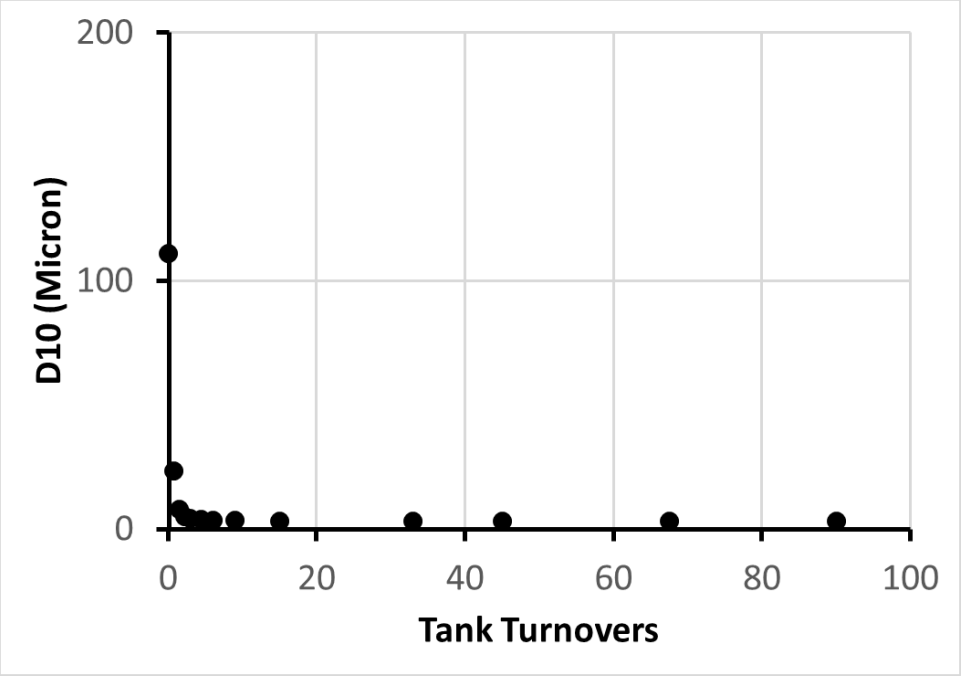

Figure B.1.5 - D10 versus milling time in tank turnovers for glycine/IPA wet milling at 5000 rpm and 2.1 lpm

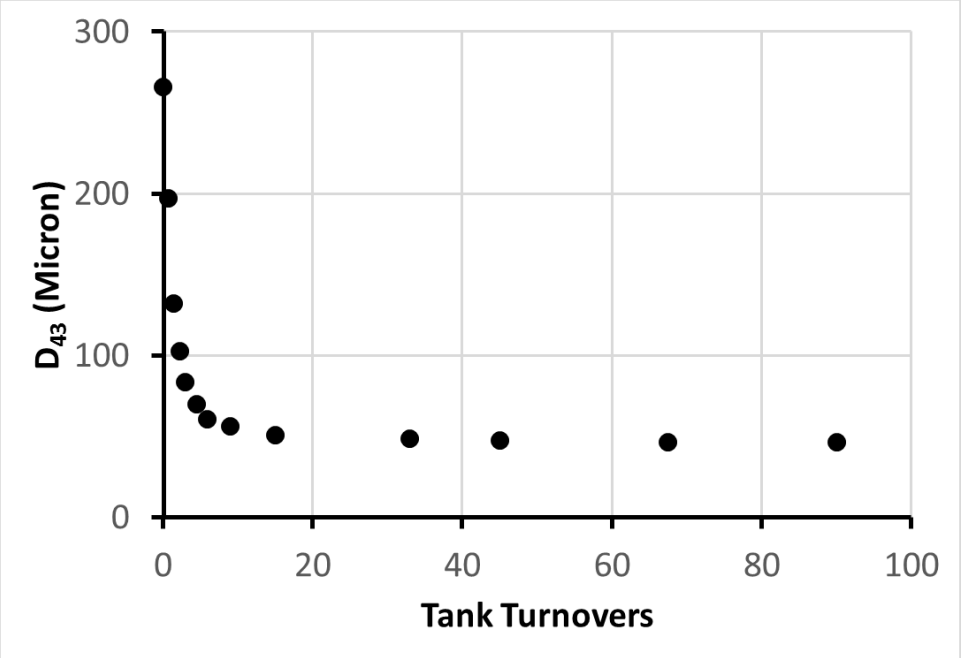

Figure B.1.6 - D_{43} versus milling time in tank turnovers for glycine/IPA wet milling at 5000 rpm and 2.1 lpm

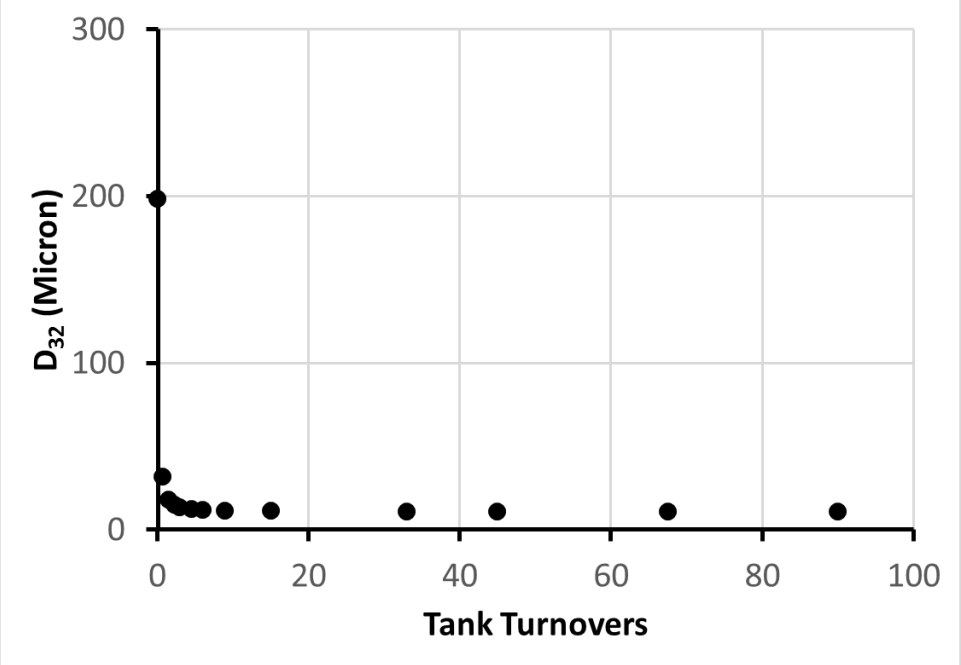

Figure B.1.7 - D_{32} versus milling time in tank turnovers for glycine/IPA wet milling at 5000 rpm and 2.1 lpm

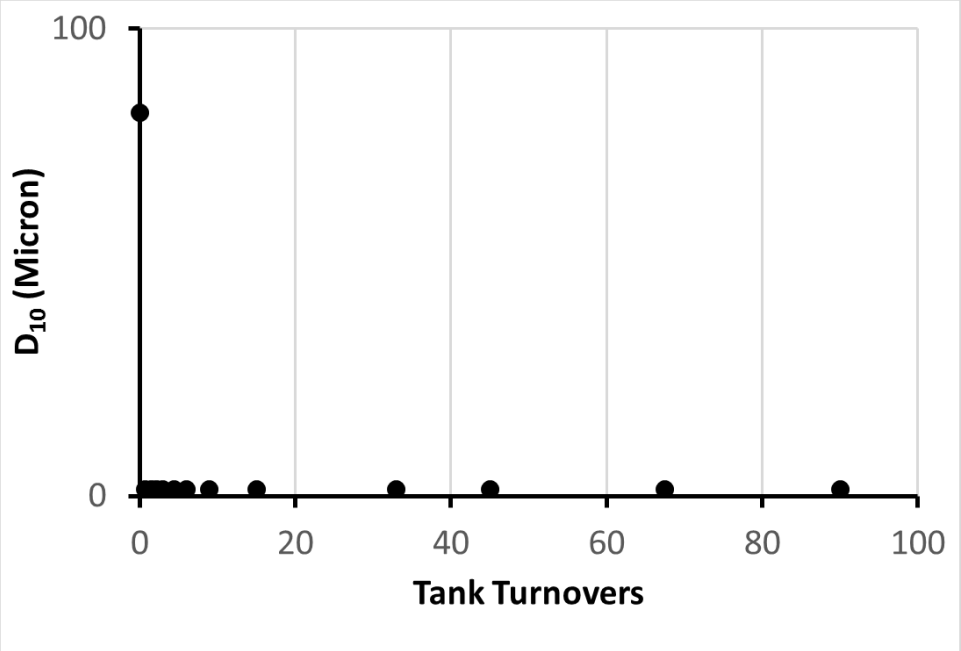

Figure B.1.8 - D_{10} versus milling time in tank turnovers for glycine/IPA wet milling at 5000 rpm and 2.1 lpm

B.2 –Wet Milling of glycine/IPA at 6500 rpm and 3.0 lpm

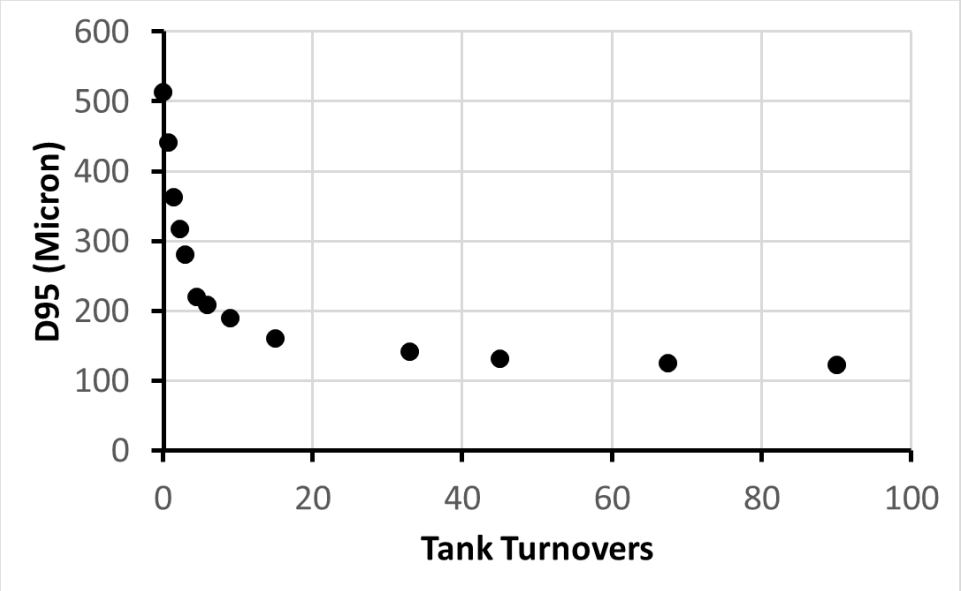

Figure B.2.1 - D95 versus milling time in tank turnovers for glycine/IPA wet milling at 6500 rpm and 3.0 lpm

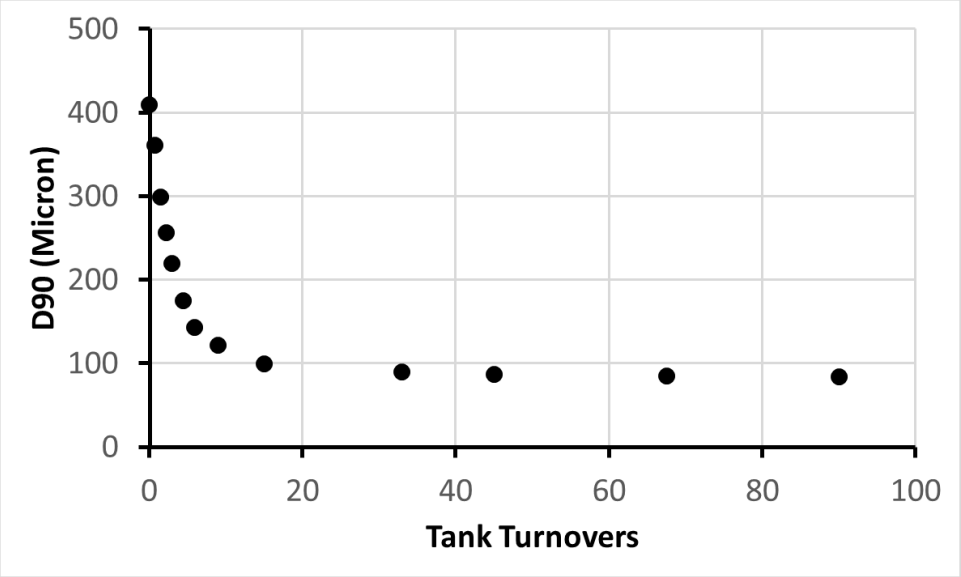

Figure B.2.2 - D90 versus milling time in tank turnovers for glycine/IPA wet milling at 6500 rpm and 3.0 lpm

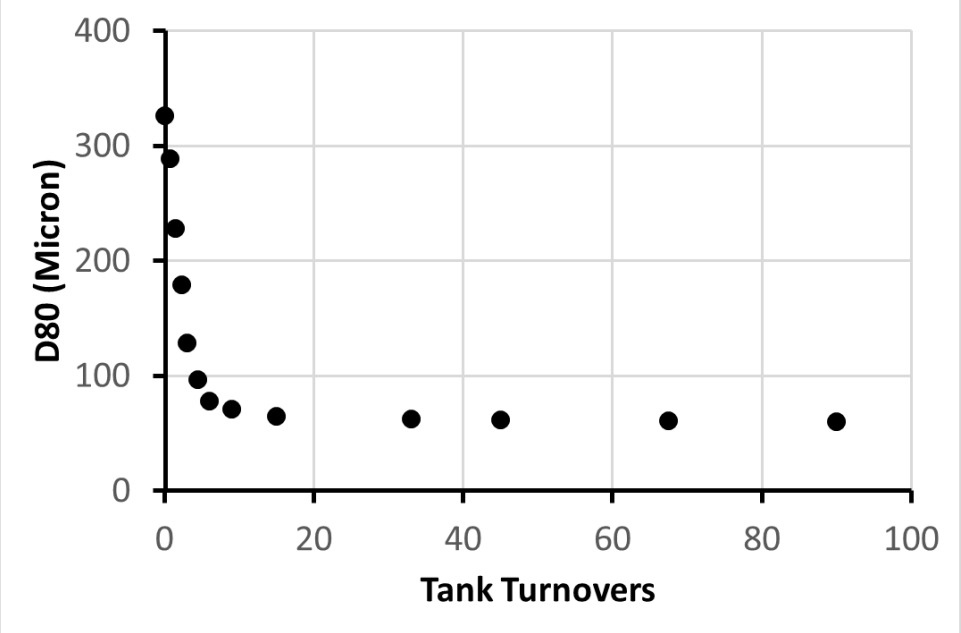

Figure B.2.3 - D80 versus milling time in tank turnovers for glycine/IPA wet milling at 6500 rpm and 3.0 lpm

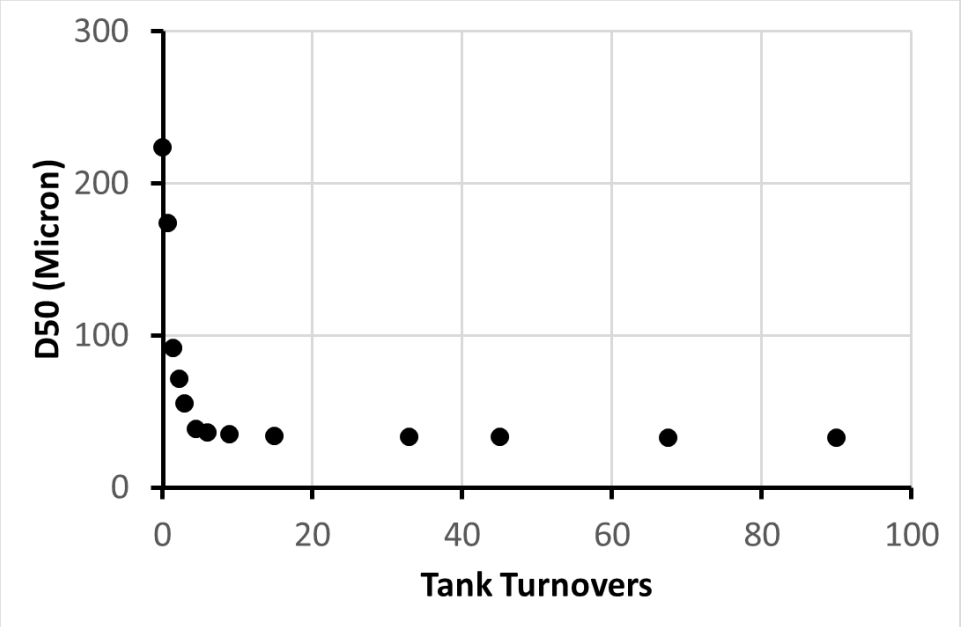

Figure B.2.4 - D50 versus milling time in tank turnovers for glycine/IPA wet milling at 6500 rpm and 3.0 lpm

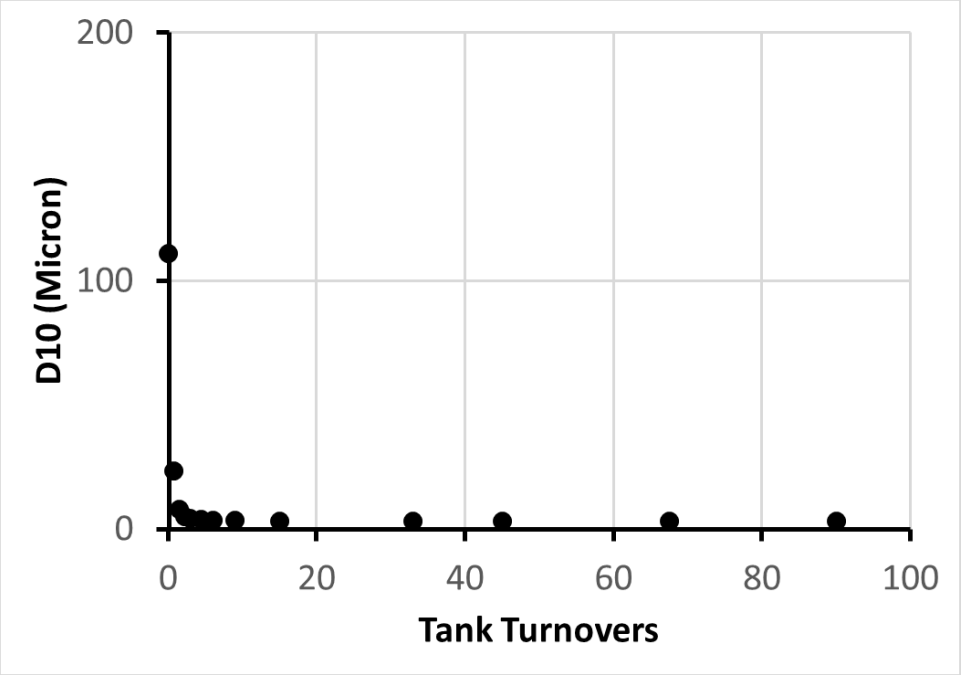

Figure B.2.5 - D10 versus milling time in tank turnovers for glycine/IPA wet milling at 6500 rpm and 3.0 lpm

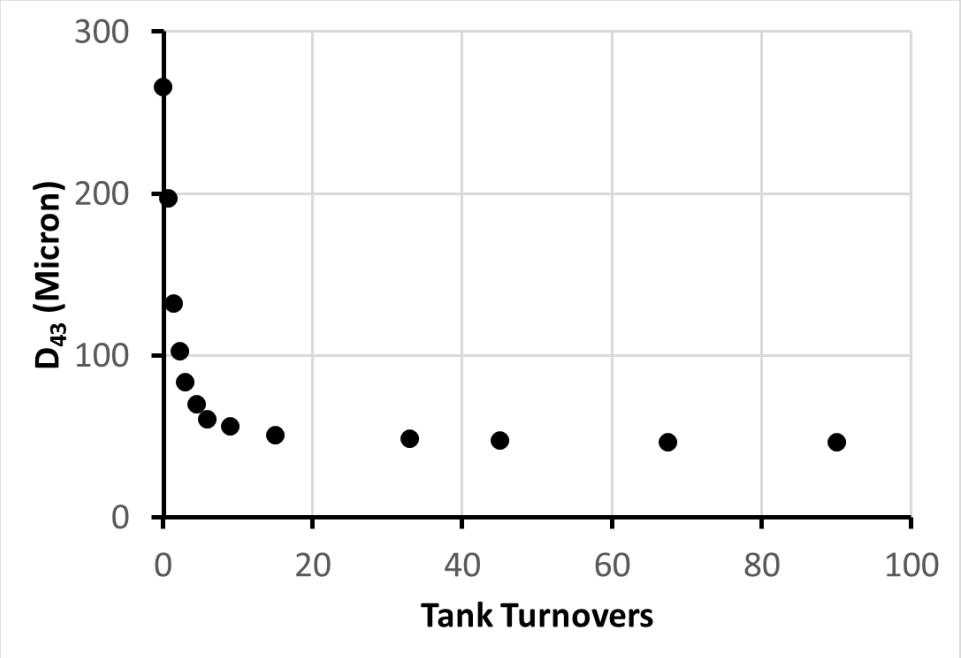

Figure B.2.6 - D_{43} versus milling time in tank turnovers for glycine/IPA wet milling at 6500 rpm and 3.0 lpm

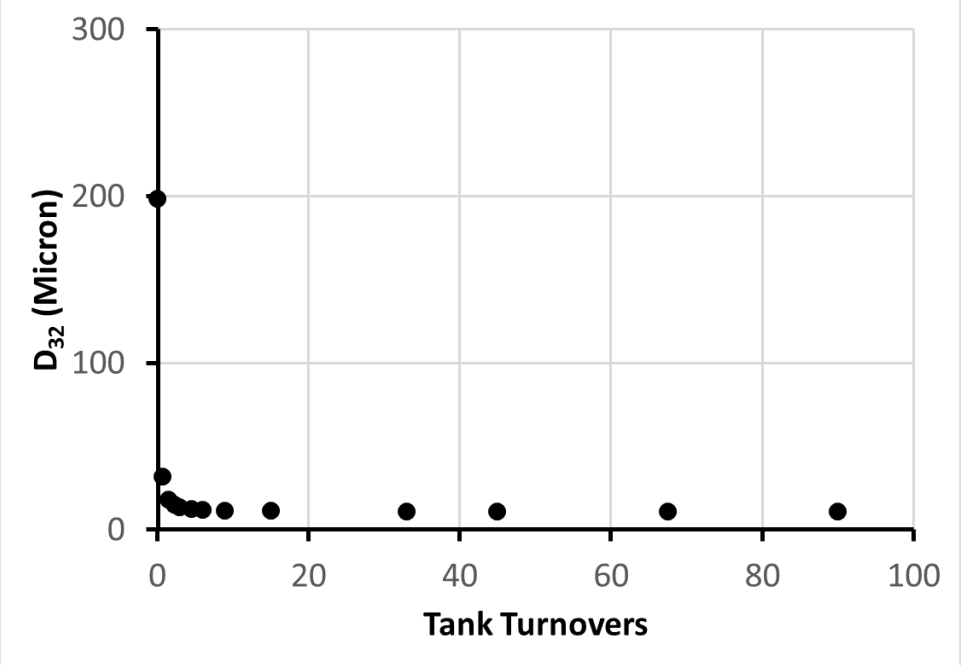

Figure B.2.7 - D_{32} versus milling time in tank turnovers for glycine/IPA wet milling at 6500 rpm and 3.0 lpm

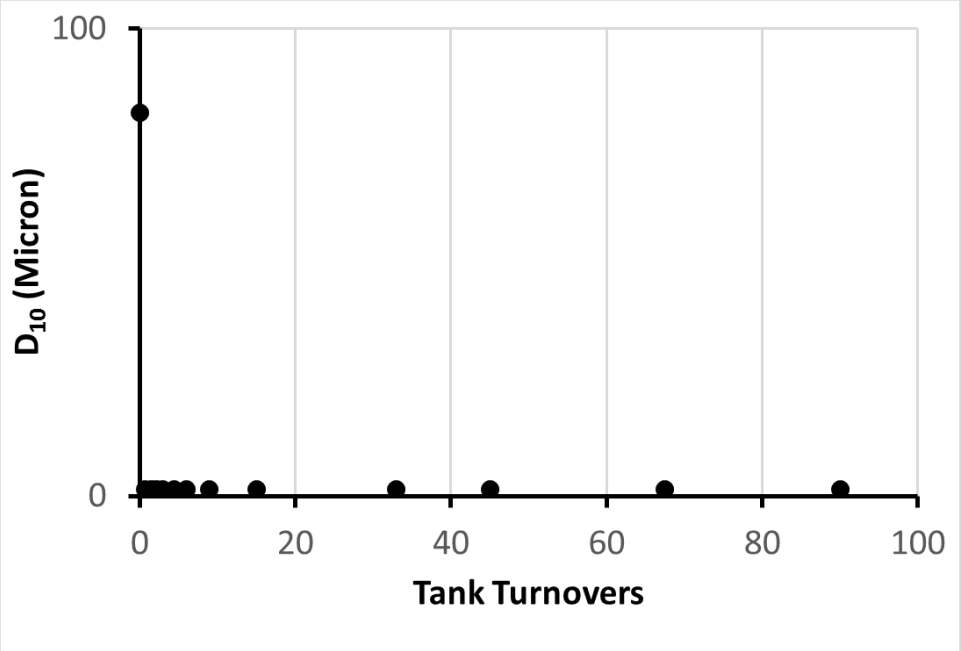

Figure B.2.8 - D_{10} versus milling time in tank turnovers for glycine/IPA wet milling at 6500 rpm and 3.0 lpm

B.3 –Wet Milling of glycine/IPA at 8000 rpm and 4.2 lpm

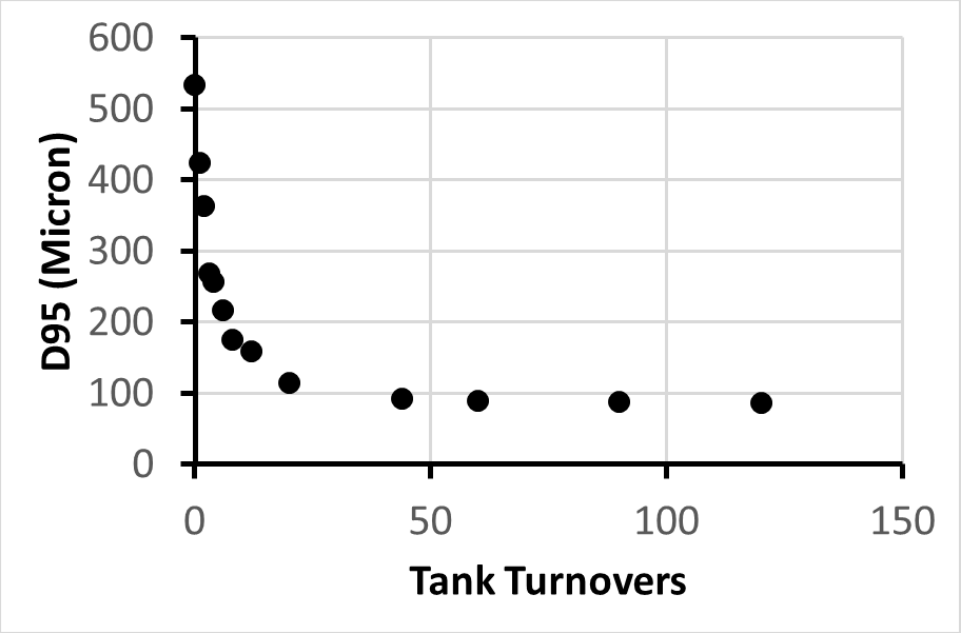

Figure B.3.1 - D95 versus milling time in tank turnovers for glycine/IPA wet milling at 8000 rpm and 4.2 lpm

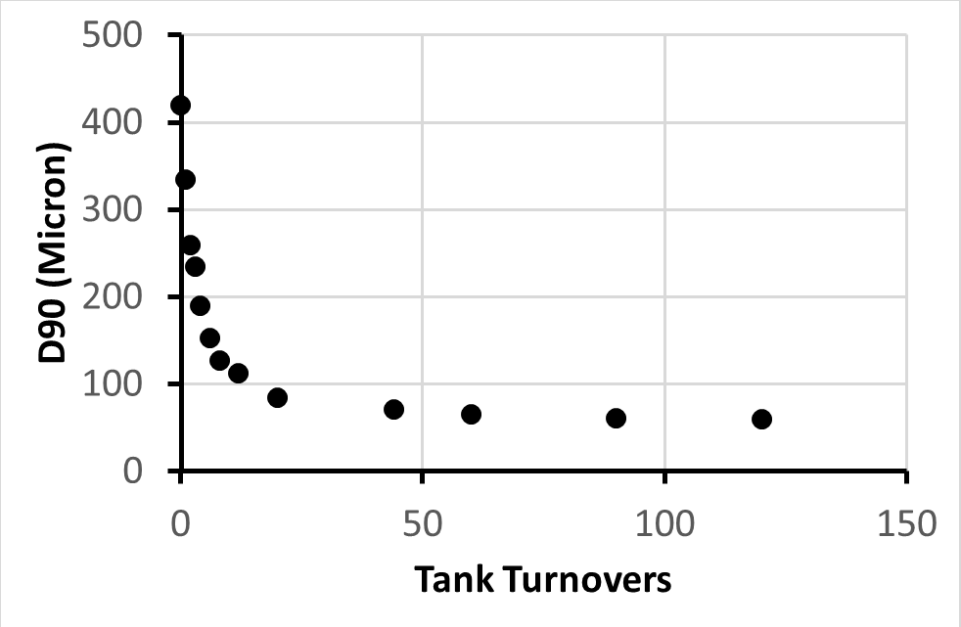

Figure B.3.2 - D90 versus milling time in tank turnovers for glycine/IPA wet milling at 8000 rpm and 4.2 lpm

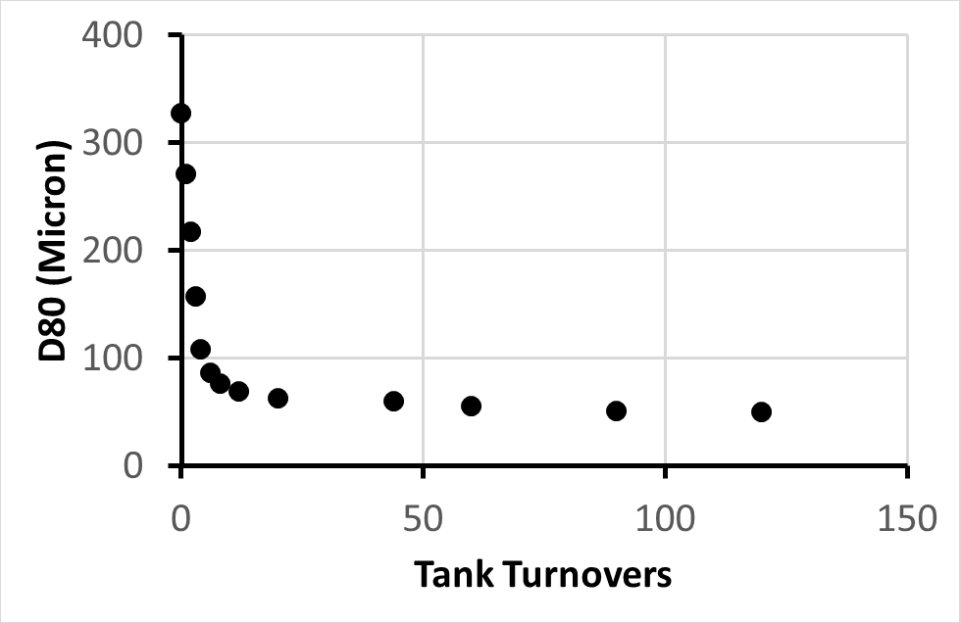

Figure B.3.3 - D80 versus milling time in tank turnovers for glycine/IPA wet milling at 8000 rpm and 4.2 lpm

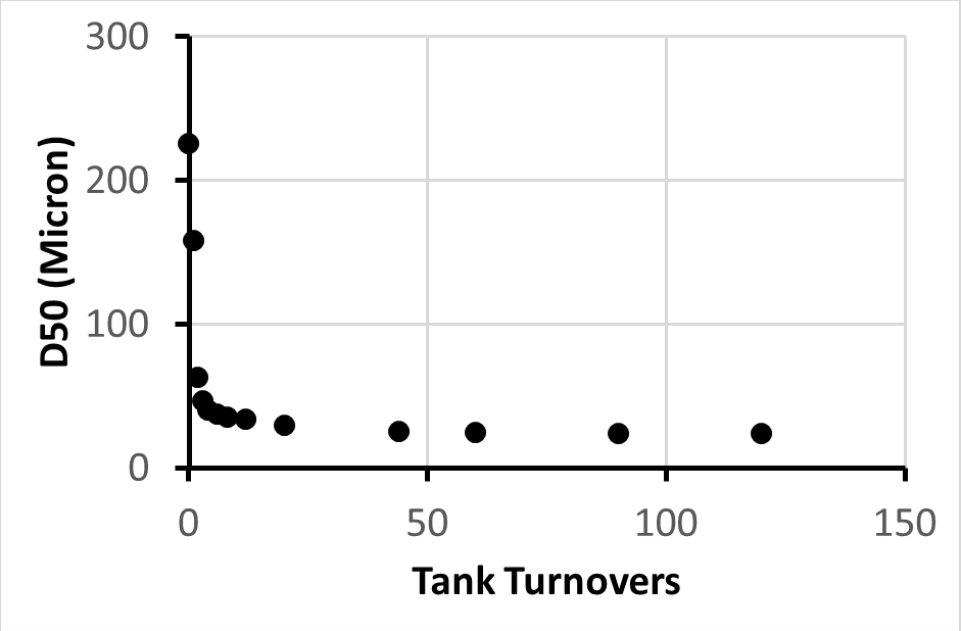

Figure B.3.4 - D50 versus milling time in tank turnovers for glycine/IPA wet milling at 8000 rpm and 4.2 lpm

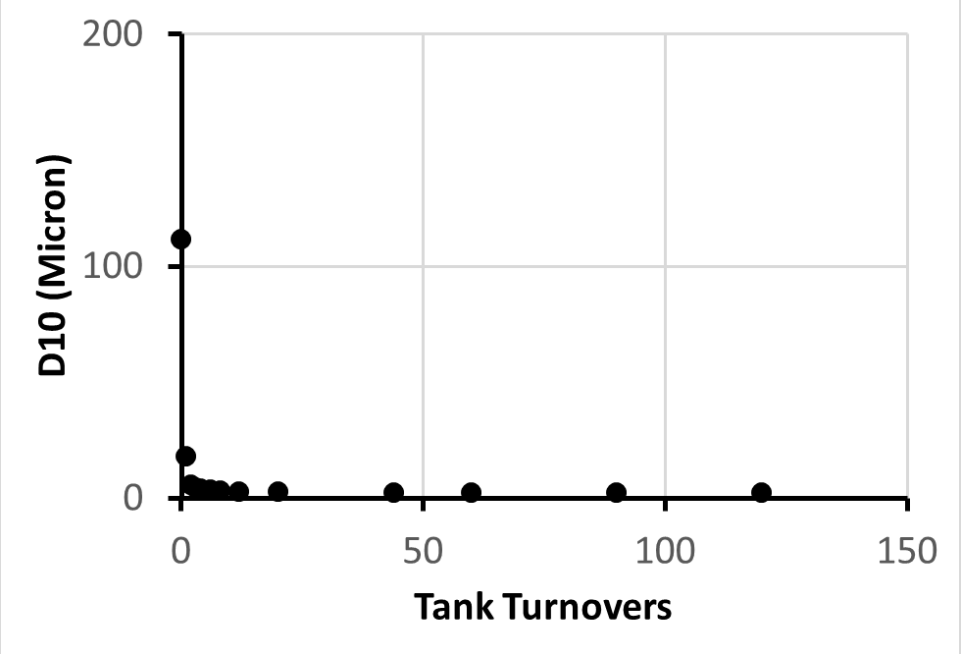

Figure B.3.5 - D10 versus milling time in tank turnovers for glycine/IPA wet milling at 8000 rpm and 4.2 lpm

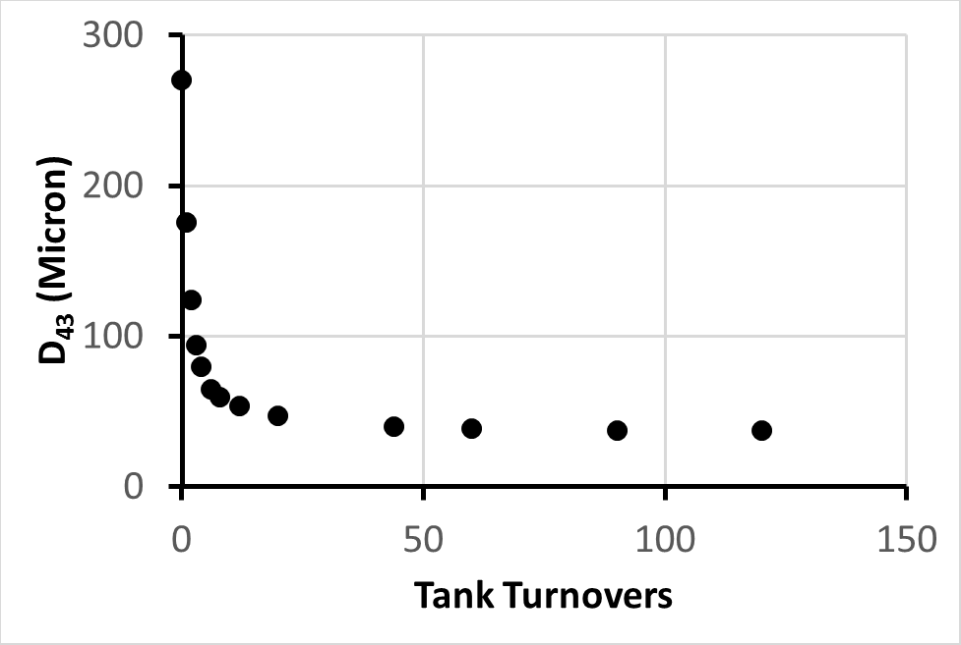

Figure B.3.6 - D_{43} versus milling time in tank turnovers for glycine/IPA wet milling at 8000 rpm and 4.2 lpm

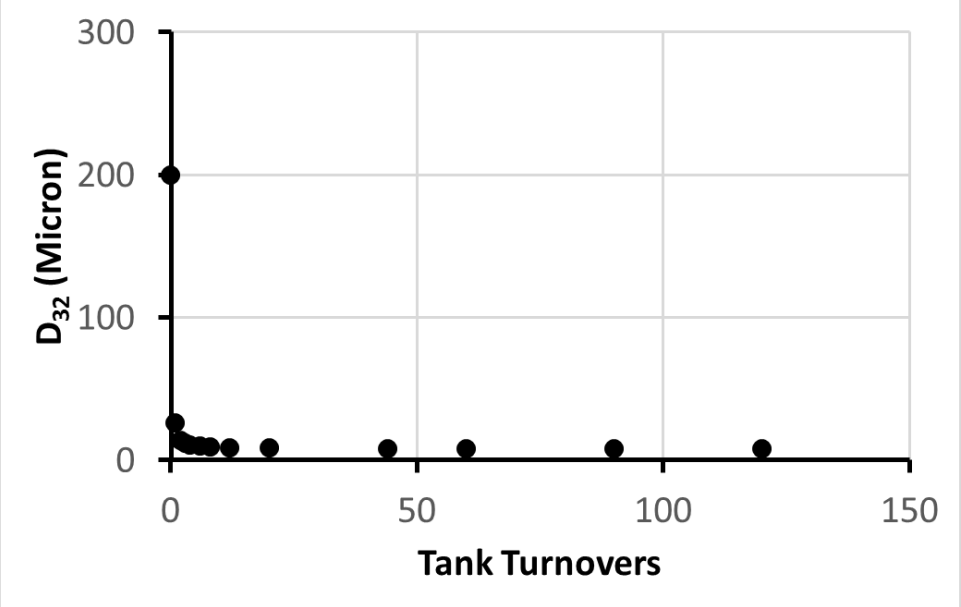

Figure B.3.7 - D_{32} versus milling time in tank turnovers for glycine/IPA wet milling at 8000 rpm and 4.2 lpm

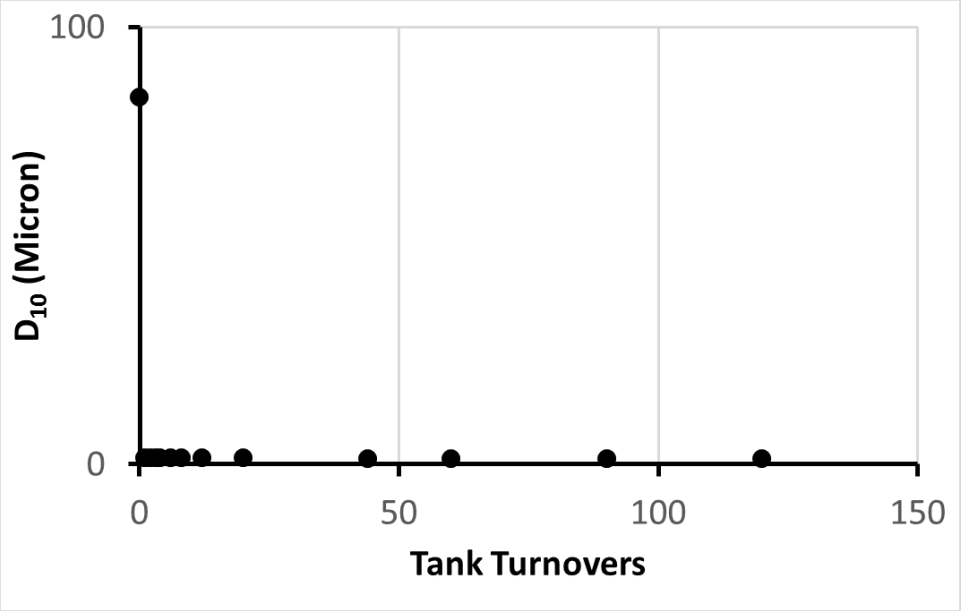

Figure B.3.8 - D_{10} versus milling time in tank turnovers for glycine/IPA wet milling at 8000 rpm and 4.2 lpm

Appendix C: Wet milling data for ascorbic-IPA system in the Silverson L4R inline mixer with standard shear gap

Ascorbic acid crystals with 10% by weight, dispersed in 2 litres IPA, were fed to the Silverson L4R inline mixer with the standard shear gap at 5000 rpm and 2.1 lpm, 6500 rpm and 3.0 lpm, and 8000 rpm and 4.2 lpm. Extra milling time was provided to ensure that the equilibrium is achieved. Here, the experimental data acquired at different milling time are presented in terms of different cumulative diameters, D95, D90, D80, D50, and D10 versus milling time in tank turnovers.

C.1 –Wet Milling of ascorbic acid/IPA at 5000 rpm and 2.1 lpm

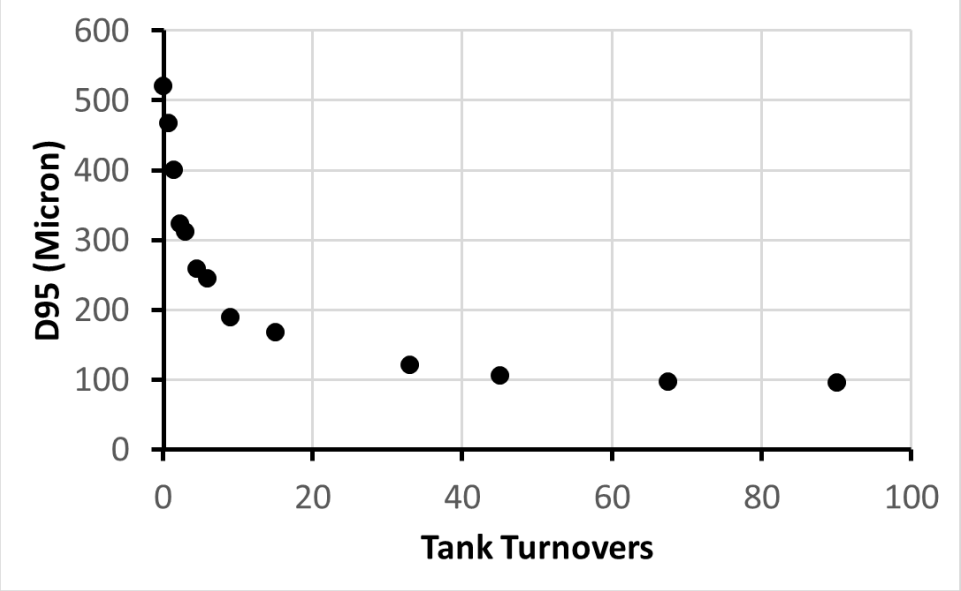

Figure C.1.1 - D95 versus milling time in tank turnovers for ascorbic acid/IPA wet milling at 5000 rpm and 2.1 lpm

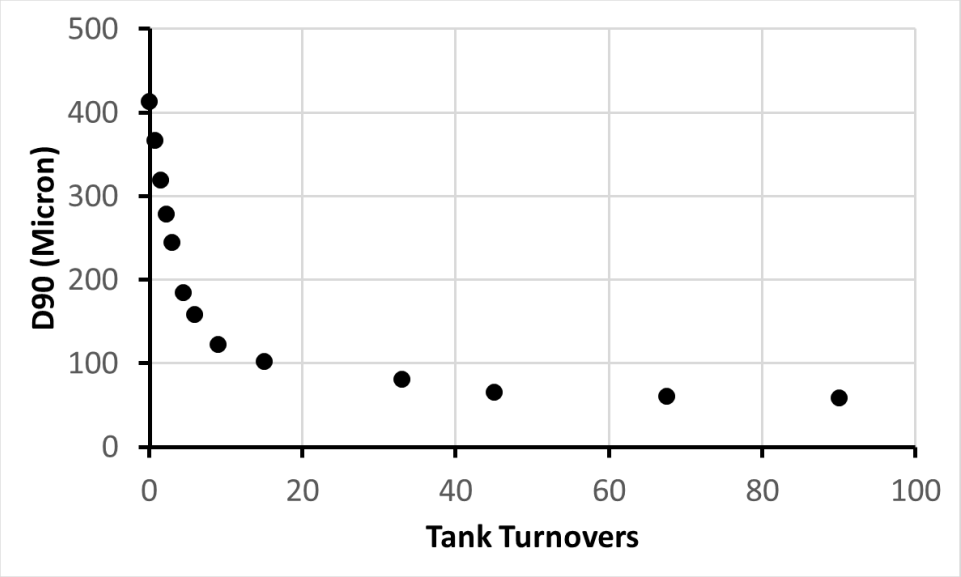

Figure C.1. 2 - D90 versus milling time in tank turnovers for ascorbic acid/IPA wet milling at 5000 rpm and 2.1 lpm

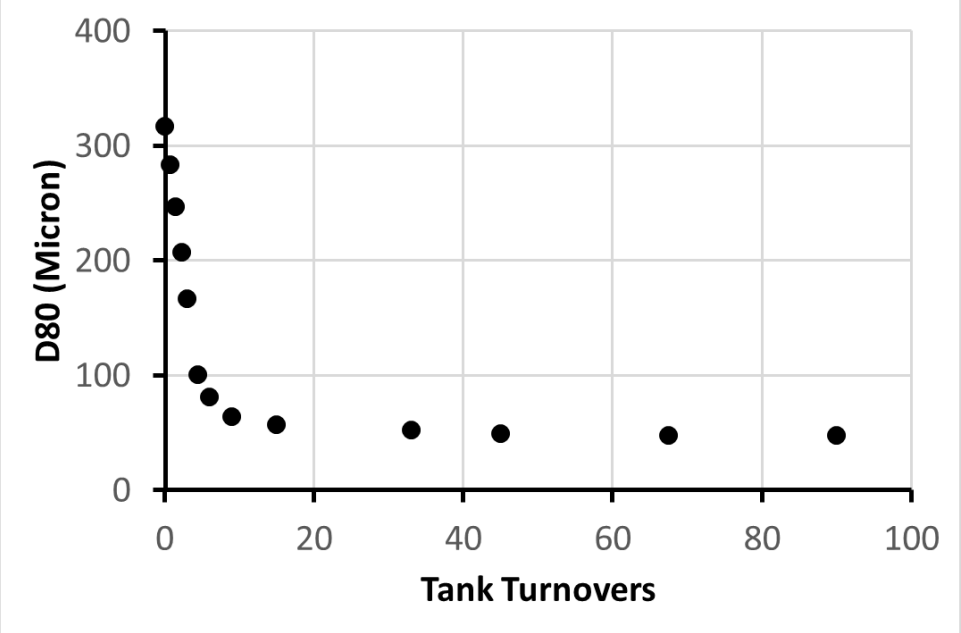

Figure C.1.3 - D80 versus milling time in tank turnovers for ascorbic acid/IPA wet milling at 5000 rpm and 2.1 lpm

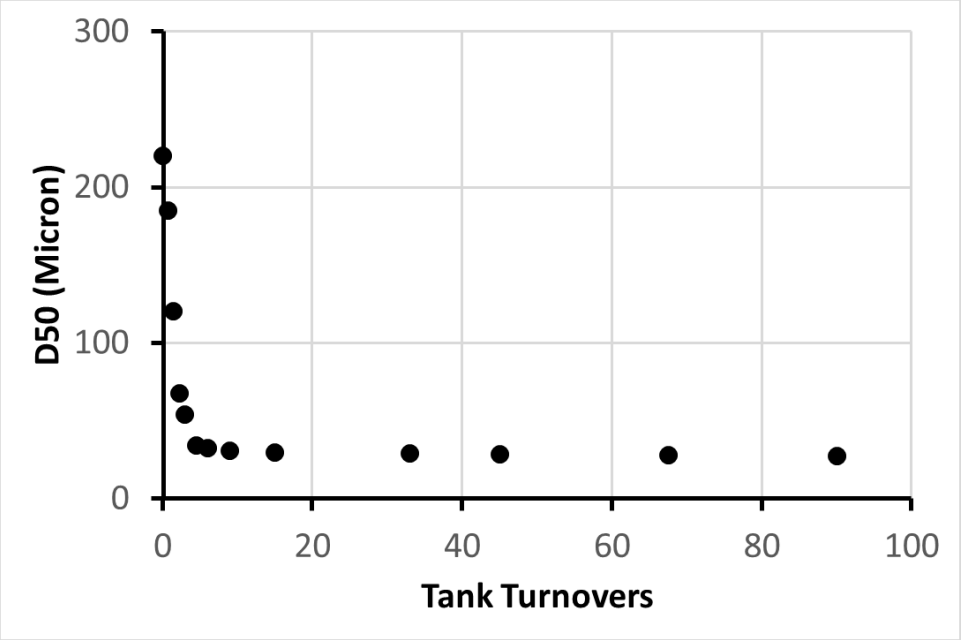

Figure C.1.4 - D50 versus milling time in tank turnovers for ascorbic acid/IPA wet milling at 5000 rpm and 2.1 lpm

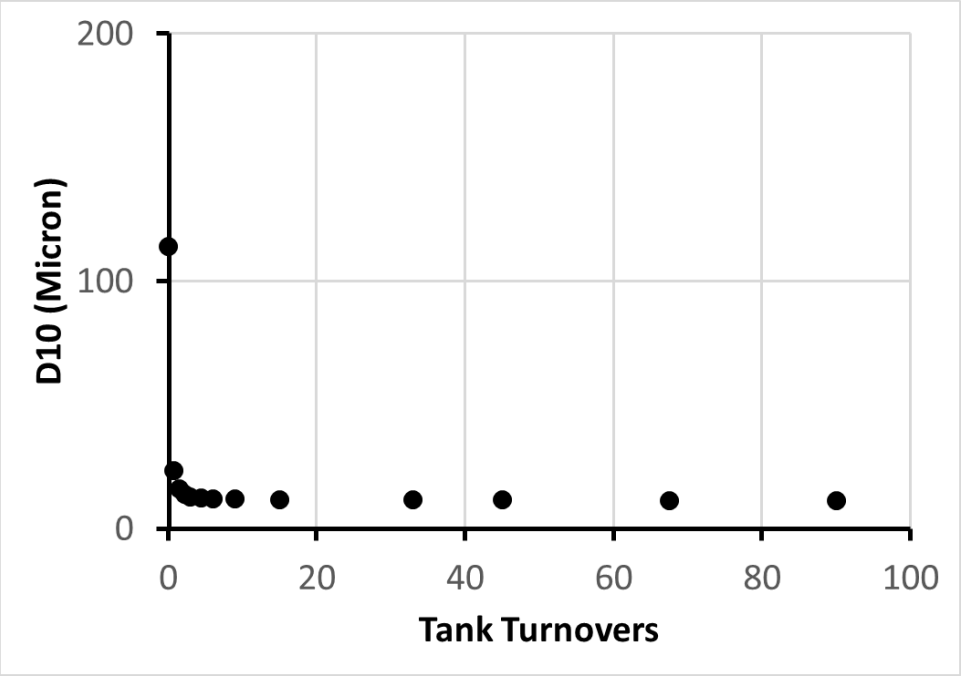

Figure C.1.5 - D10 versus milling time in tank turnovers for ascorbic acid/IPA wet milling at 5000 rpm and 2.1 lpm

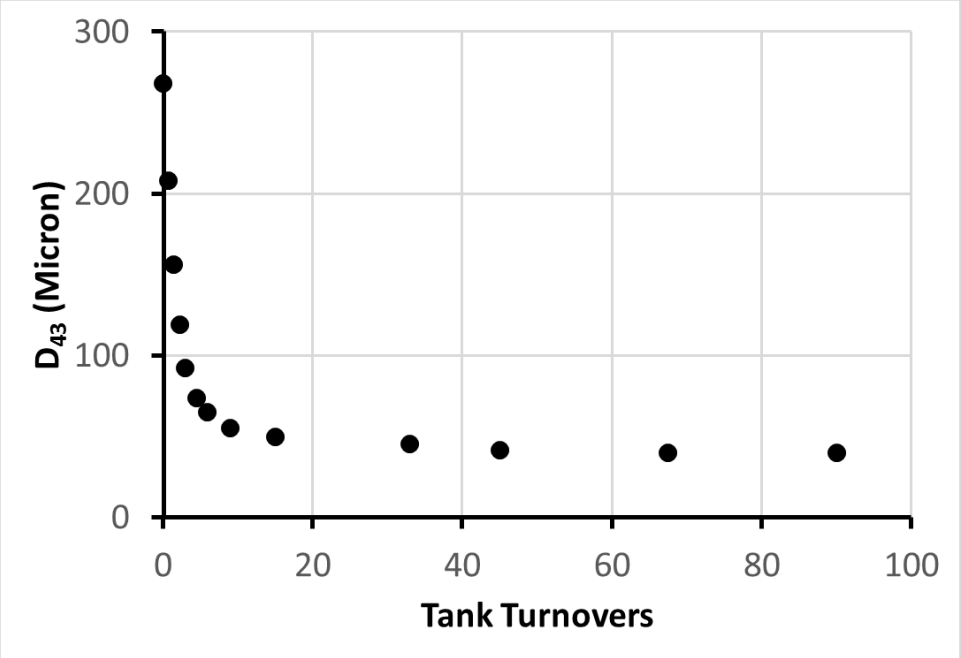

Figure C.1.6 - D_{43} versus milling time in tank turnovers for ascorbic acid/IPA wet milling at 5000 rpm and 2.1 lpm

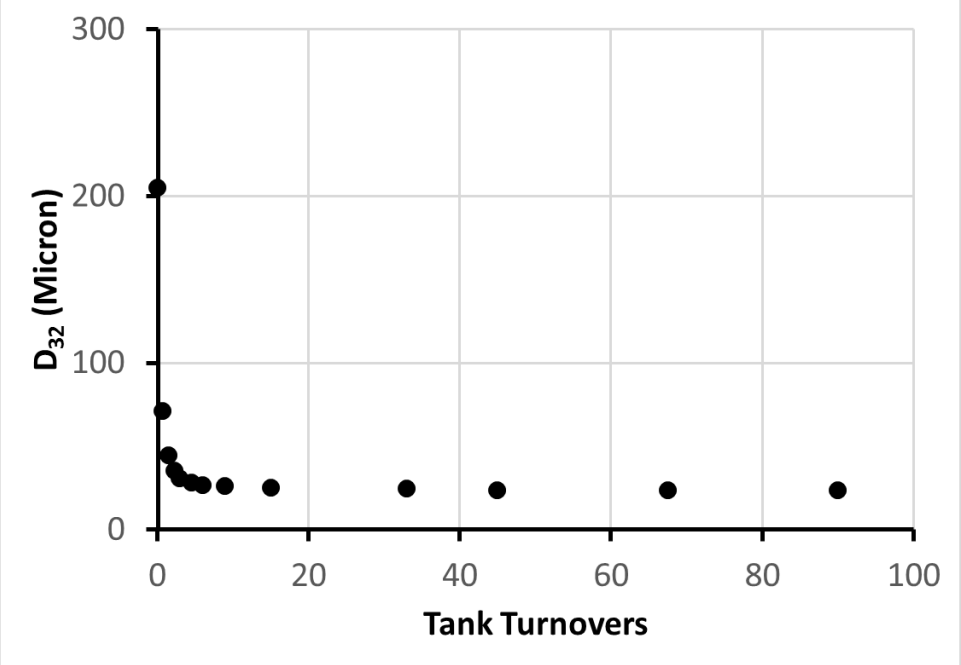

Figure C.1.7 - D_{32} versus milling time in tank turnovers for ascorbic acid/IPA wet milling at 5000 rpm and 2.1 lpm

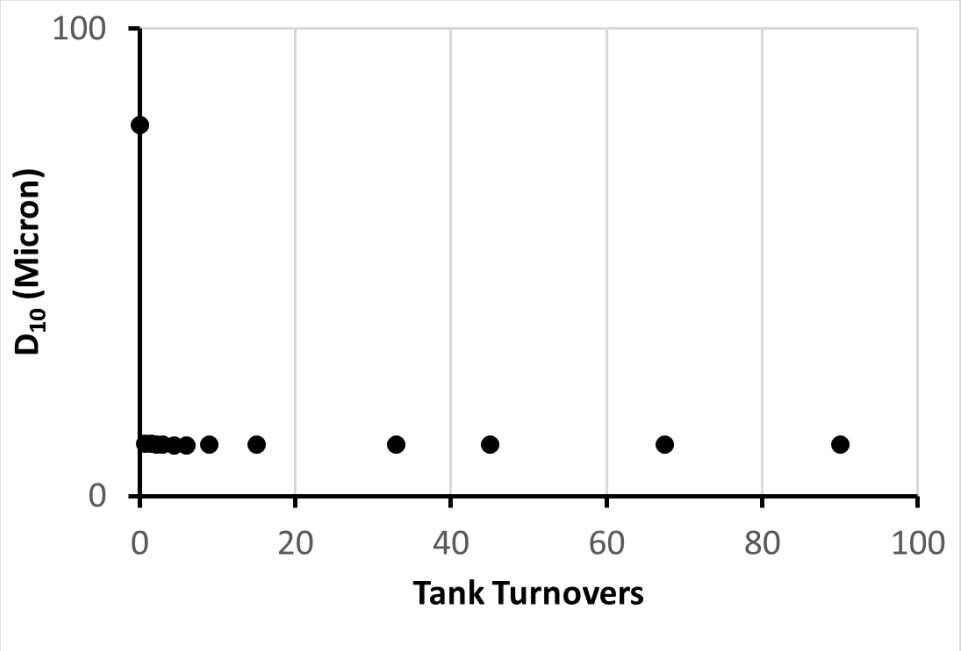

Figure C.1.8 - D_{10} versus milling time in tank turnovers for ascorbic acid/IPA wet milling at 5000 rpm and 2.1 lpm

C.2 –Wet Milling of ascorbic acid/IPA at 6500 rpm and 3.0 lpm

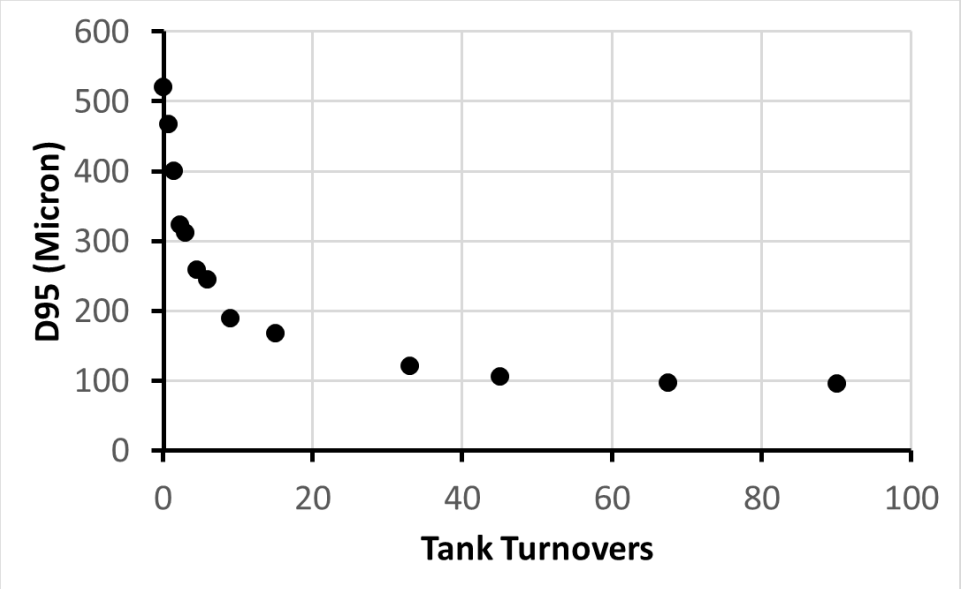

Figure C.2.1 - D95 versus milling time in tank turnovers for ascorbic acid/IPA wet milling at 6500 rpm and 3.0 lpm

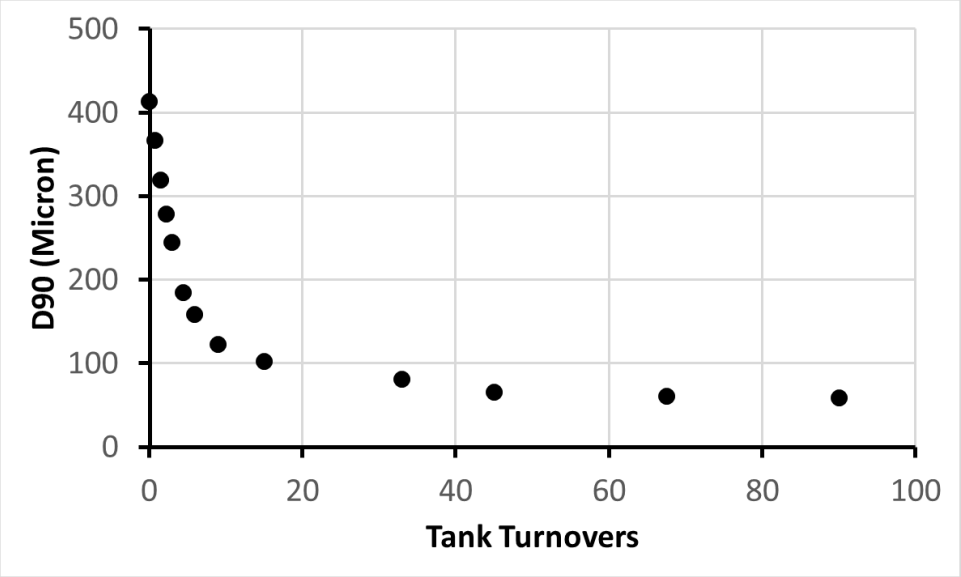

Figure C.2.2 - D90 versus milling time in tank turnovers for ascorbic acid/IPA wet milling at 6500 rpm and 3.0 lpm

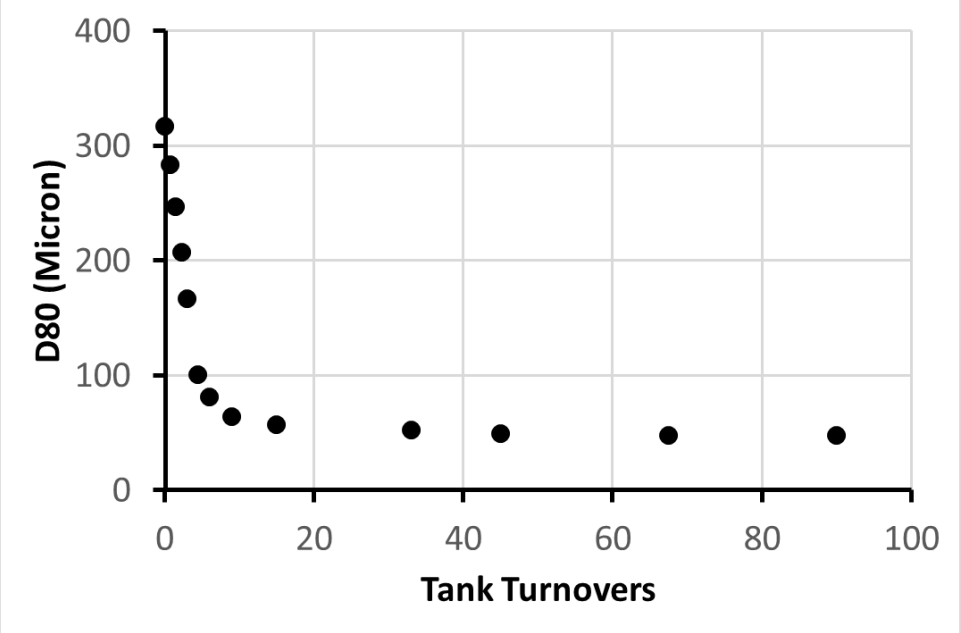

Figure C.2.3 - D80 versus milling time in tank turnovers for ascorbic acid/IPA wet milling at 6500 rpm and 3.0 lpm

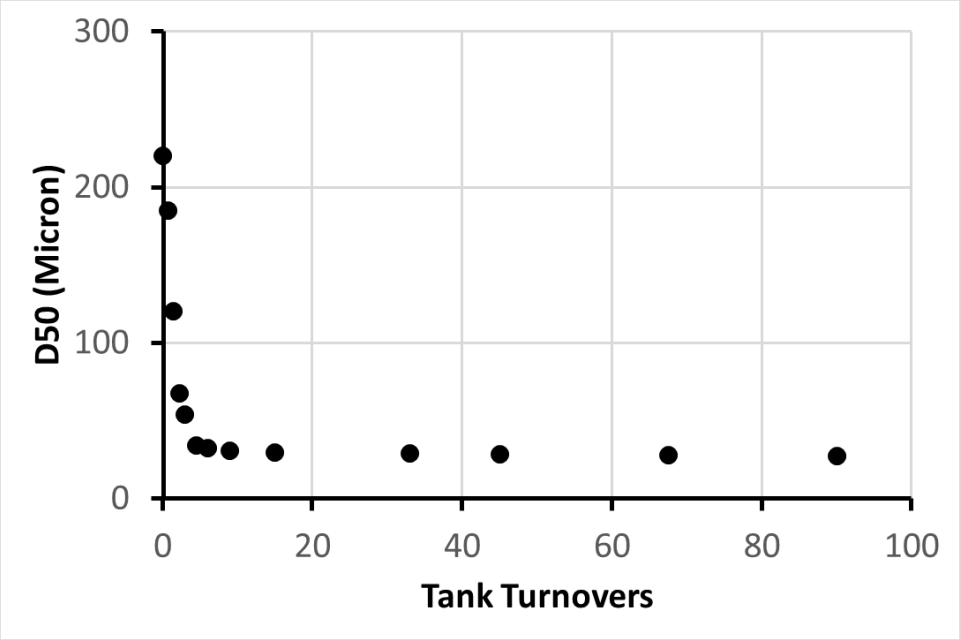

Figure C.2.4 - D50 versus milling time in tank turnovers for ascorbic acid/IPA wet milling at 6500 rpm and 3.0 lpm

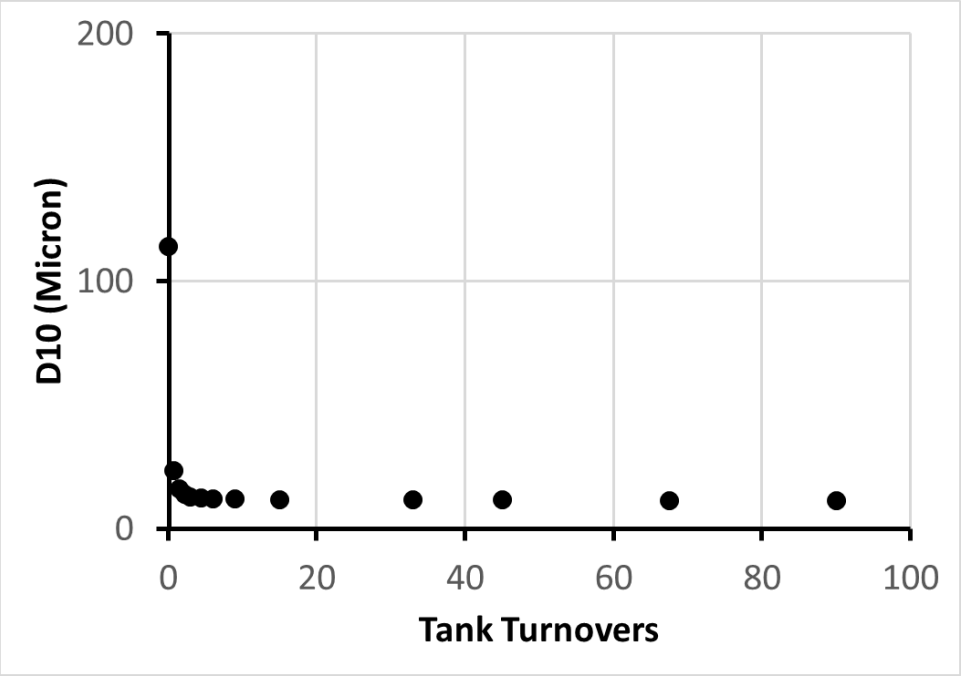

Figure C.2.5 - D10 versus milling time in tank turnovers for ascorbic acid/IPA wet milling at 6500 rpm and 3.0 lpm

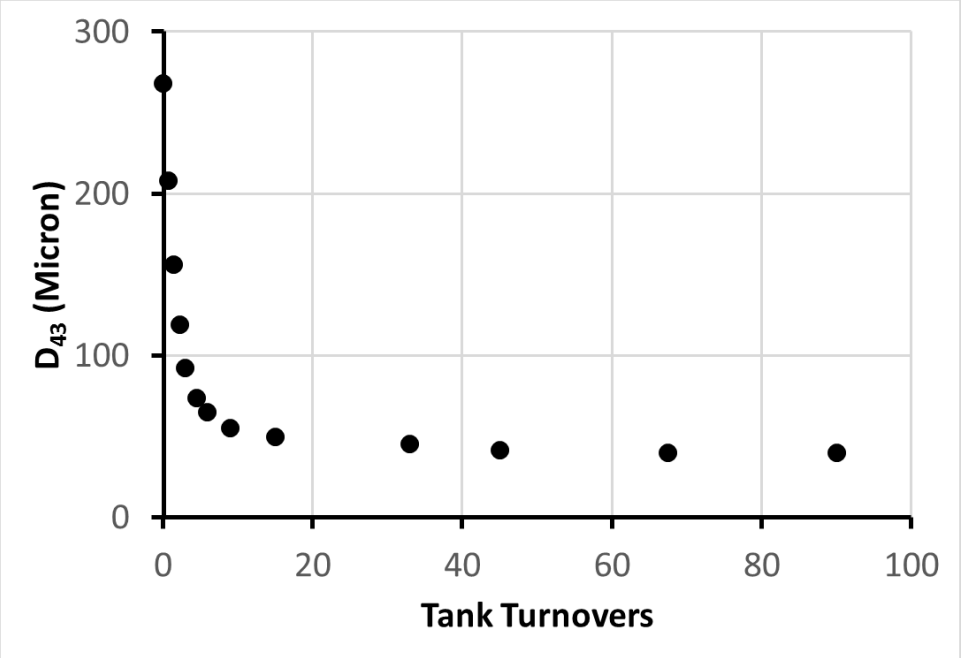

Figure C.2. 6 - D_{43} versus milling time in tank turnovers for ascorbic acid/IPA wet milling at 6500 rpm and 3.0 lpm

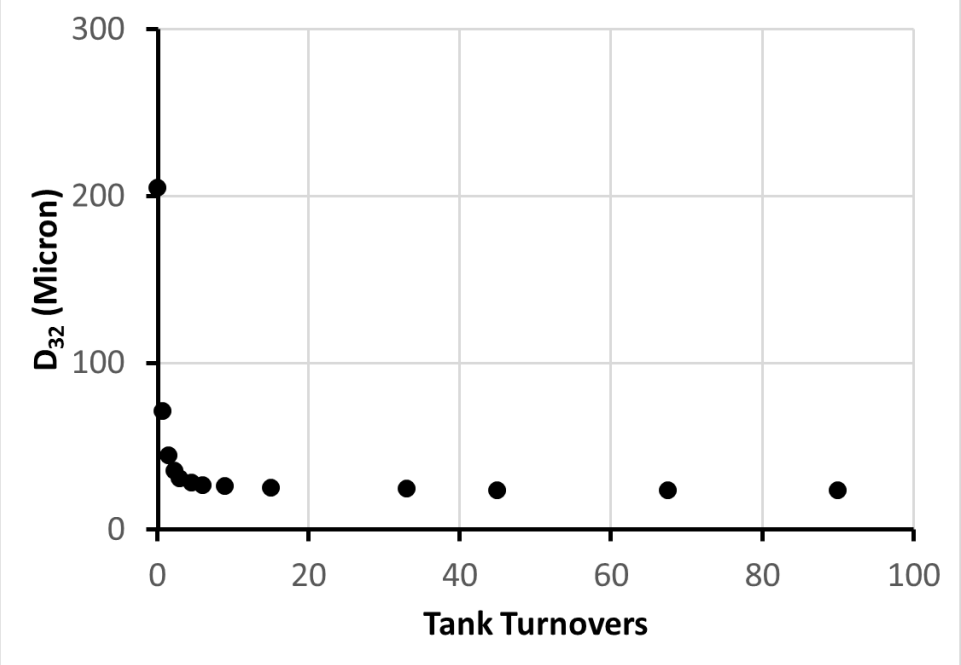

Figure C.2.7 - D_{32} versus milling time in tank turnovers for ascorbic acid/IPA wet milling at 6500 rpm and 3.0 lpm

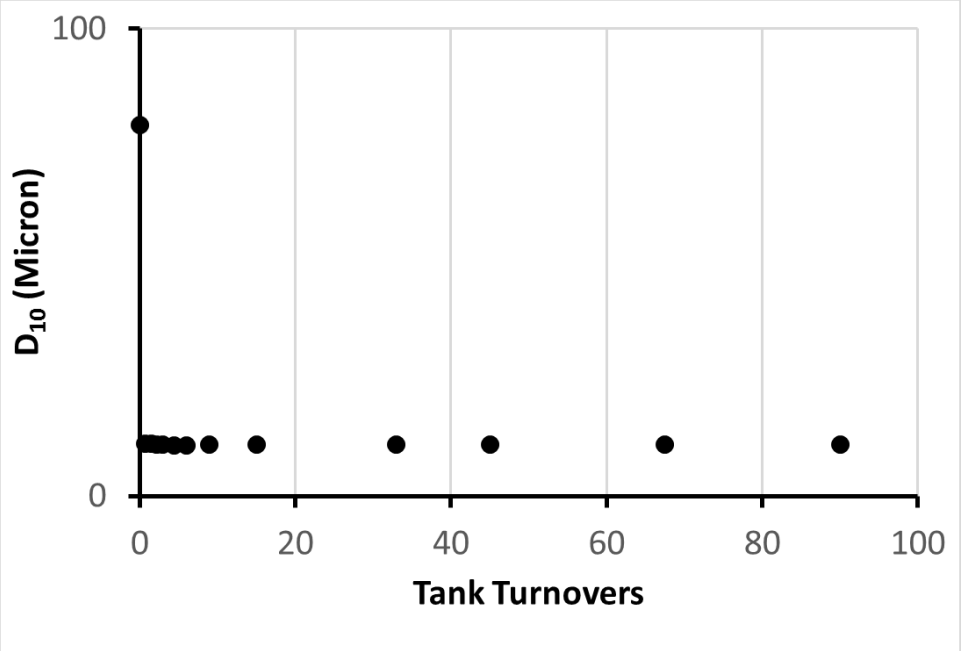

Figure C.2.8 - D_{10} versus milling time in tank turnovers for ascorbic acid/IPA wet milling at 6500 rpm and 3.0 lpm

C.3 –Wet Milling of ascorbic acid/IPA at 8000 rpm and 4.2 lpm

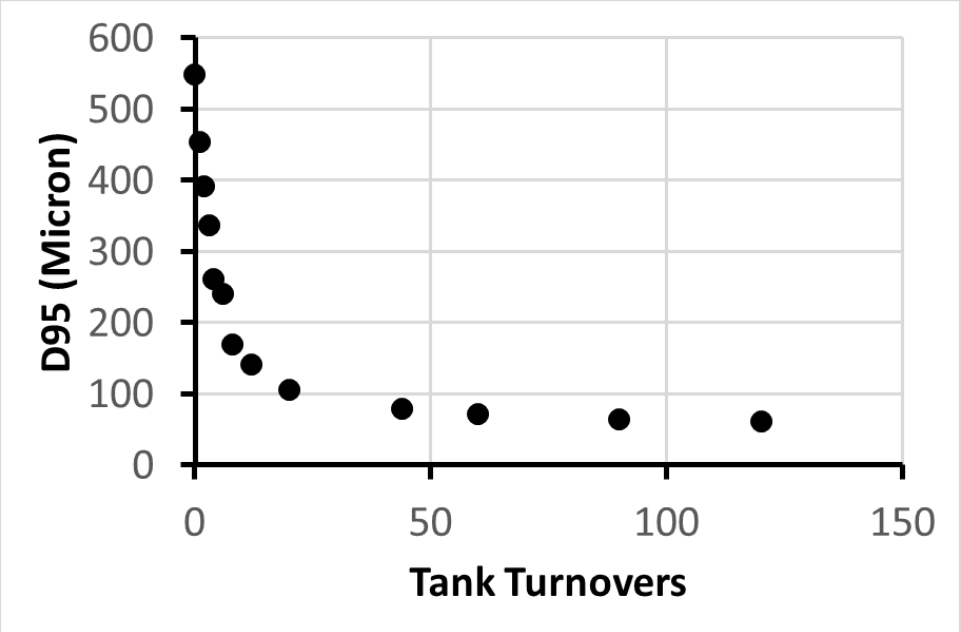

Figure C.3.1 - D95 versus milling time in tank turnovers for ascorbic acid/IPA wet milling at 8000 rpm and 4.2 lpm

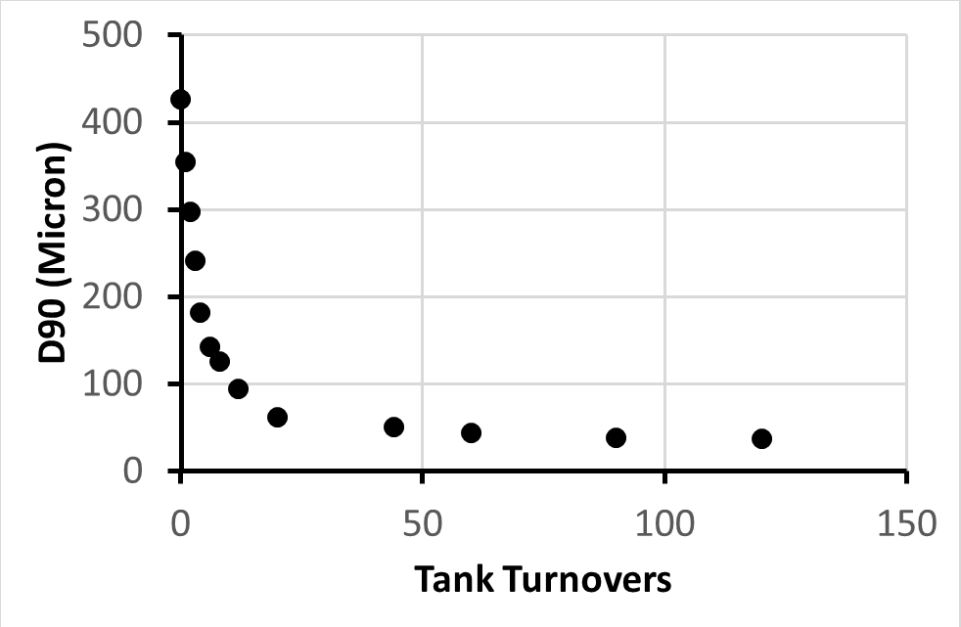

Figure C.3. 2 - D90 versus milling time in tank turnovers for ascorbic acid/IPA wet milling at 8000 rpm and 4.2 lpm

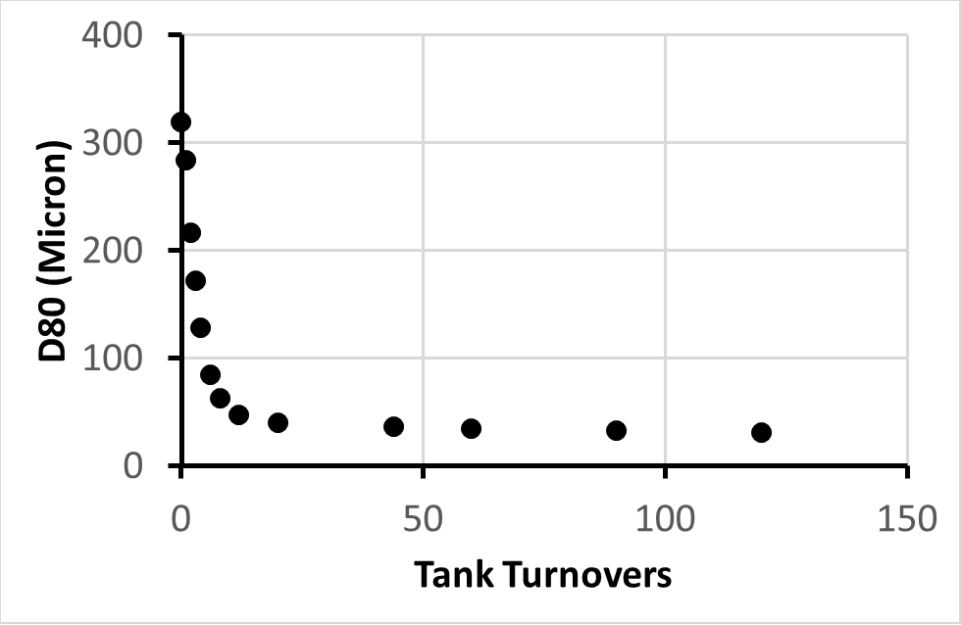

Figure C.3.3 – D80 versus milling time in tank turnovers for ascorbic acid/IPA wet milling at 8000 rpm and 4.2 lpm

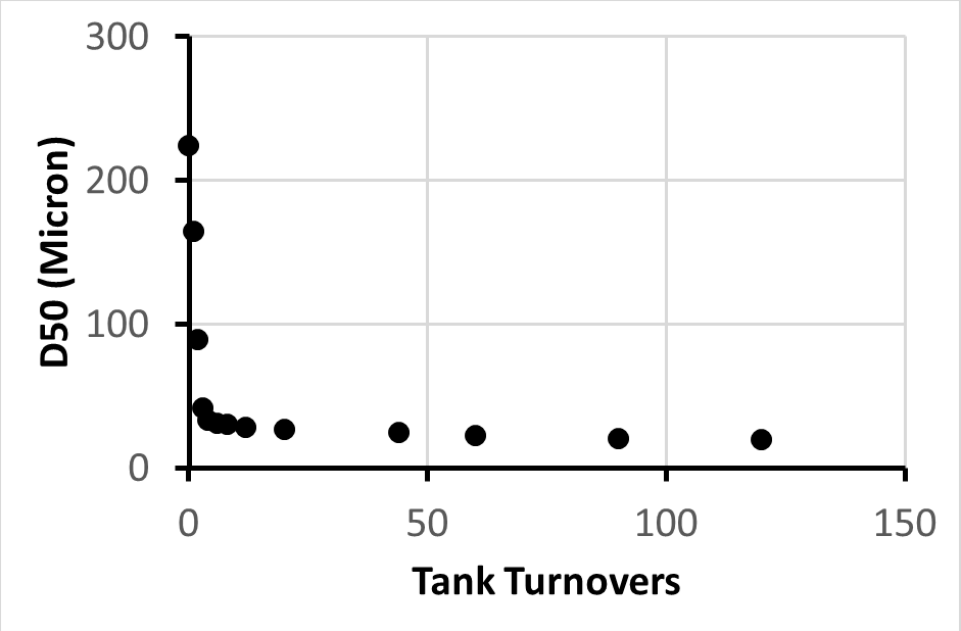

Figure C.3.4 – D50 versus milling time in tank turnovers for ascorbic acid/IPA wet milling at 8000 rpm and 4.2 lpm

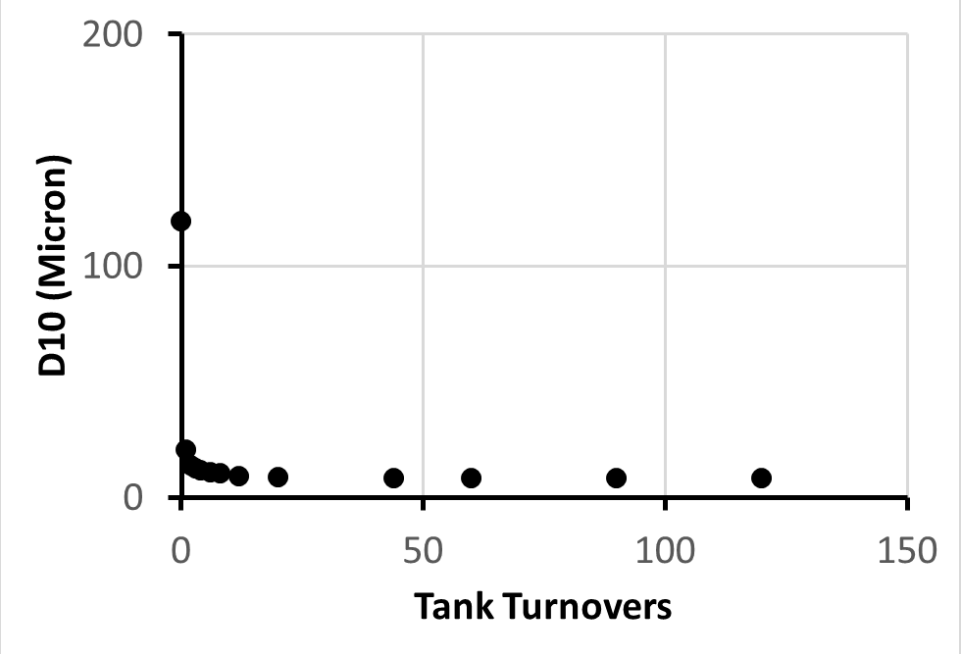

Figure C.3.5 – D10 versus milling time in tank turnovers for ascorbic acid/IPA wet milling at 8000 rpm and 4.2 lpm

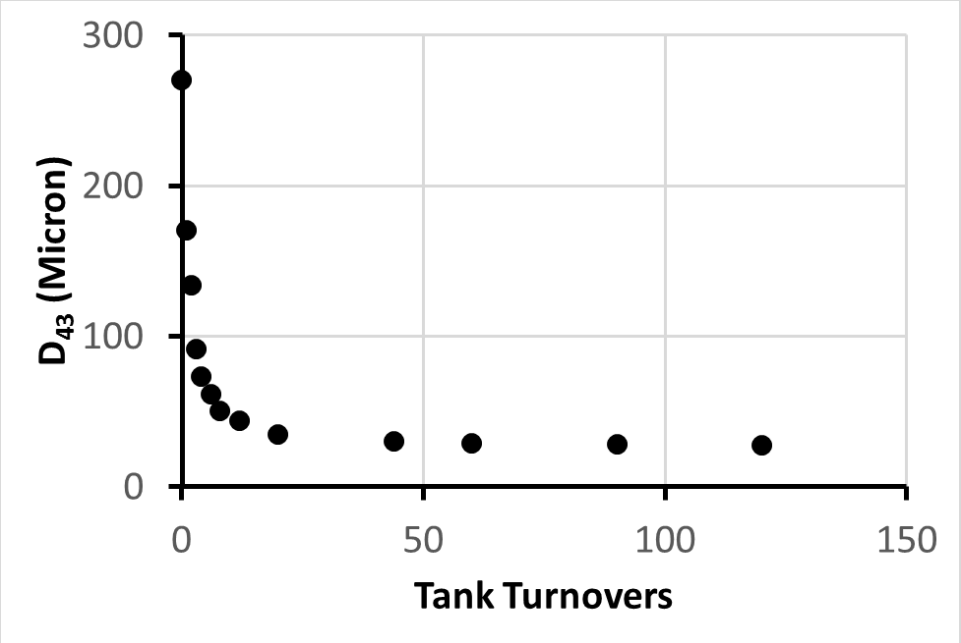

Figure C.3.6 – D_{43} versus milling time in tank turnovers for ascorbic acid/IPA wet milling at 8000 rpm and 4.2 lpm

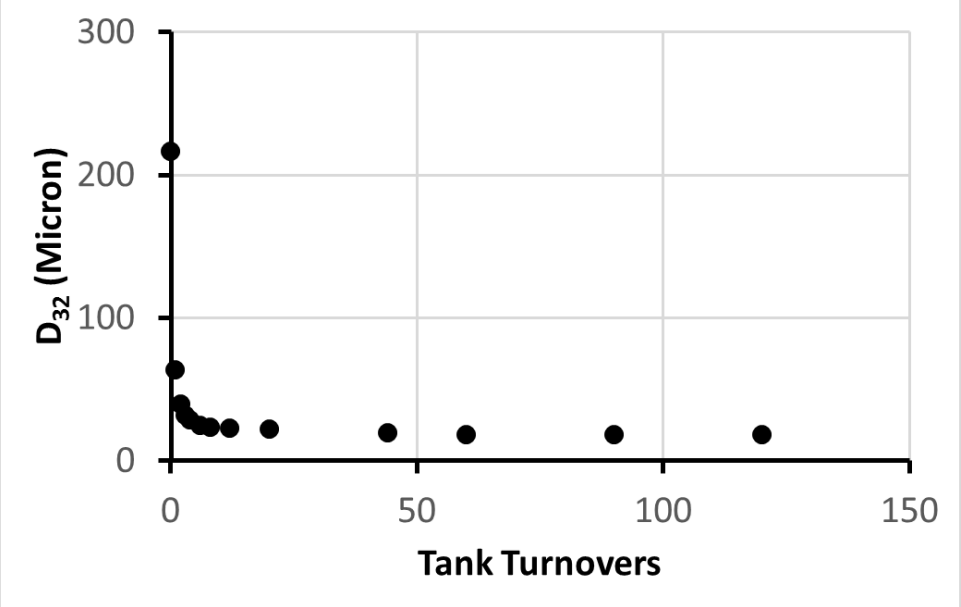

Figure C.3.7 – D_{32} versus milling time in tank turnovers for ascorbic acid/IPA wet milling at 8000 rpm and 4.2 lpm

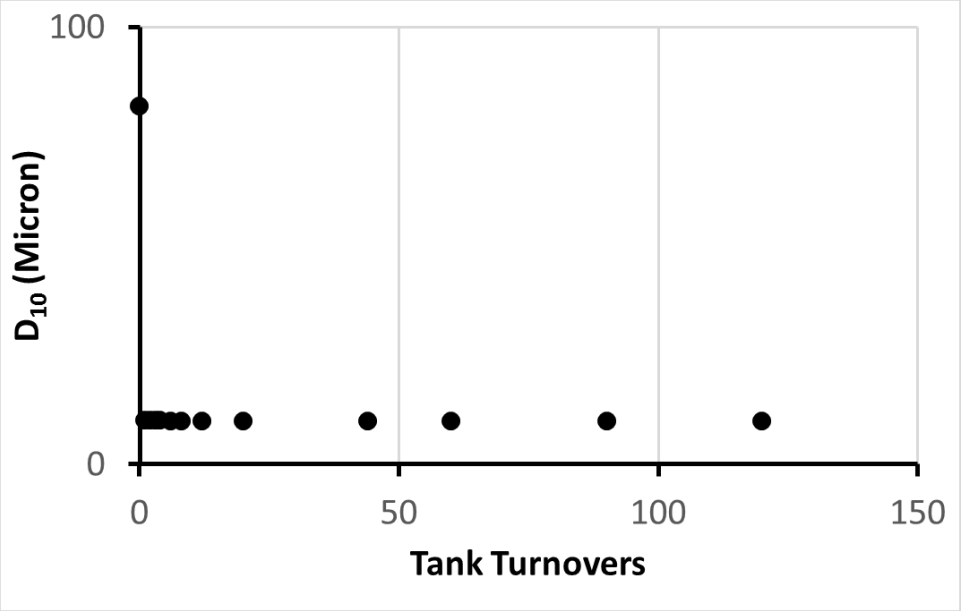

Figure C.3.8 – D_{10} versus milling time in tank turnovers for ascorbic acid/IPA wet milling at 8000 rpm and 4.2 lpm

Appendix D: Wet milling data measured with the FBRM probe for sucrose-IPA system in the Silverson L4R inline mixer with standard shear gap

Glycine crystals with 10% by weight, dispersed in 2 litres IPA, were fed to the Silverson L4R inline mixer with the standard shear gap at 5000 rpm and 2.1 lpm, 6500 rpm and 3.0 lpm, and 8000 rpm and 4.2 lpm. Extra milling time was provided to ensure that the equilibrium is achieved. Here, the experimental data acquired at different milling time are presented in terms of different cumulative diameters, D95, D90, D80, D50, and D10 versus milling time in tank turnovers.

D.1 –FBRM results of wet milling of sucrose/IPA at 5000 rpm and 3.0 lpm

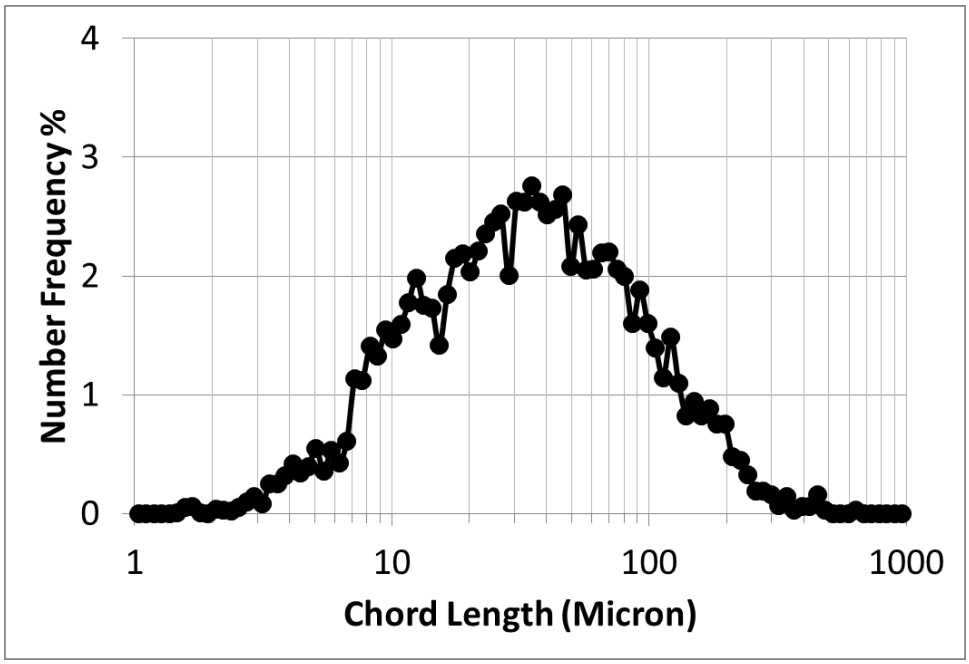

Figure D.1.1 - Initial chord length distribution of sucrose/IPA measured by FBRM probe

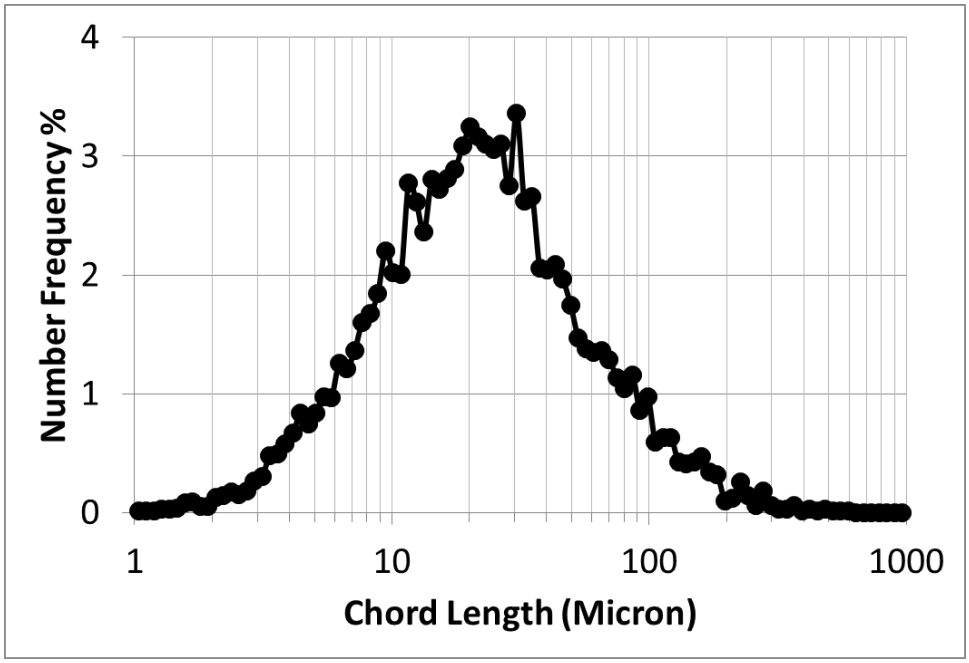

Figure D.1.2 - Wet milling of sucrose/IPA at 5000 rpm and 3.0 lpm – Chord length distribution at 2 tank turnovers measured by FBRM probe

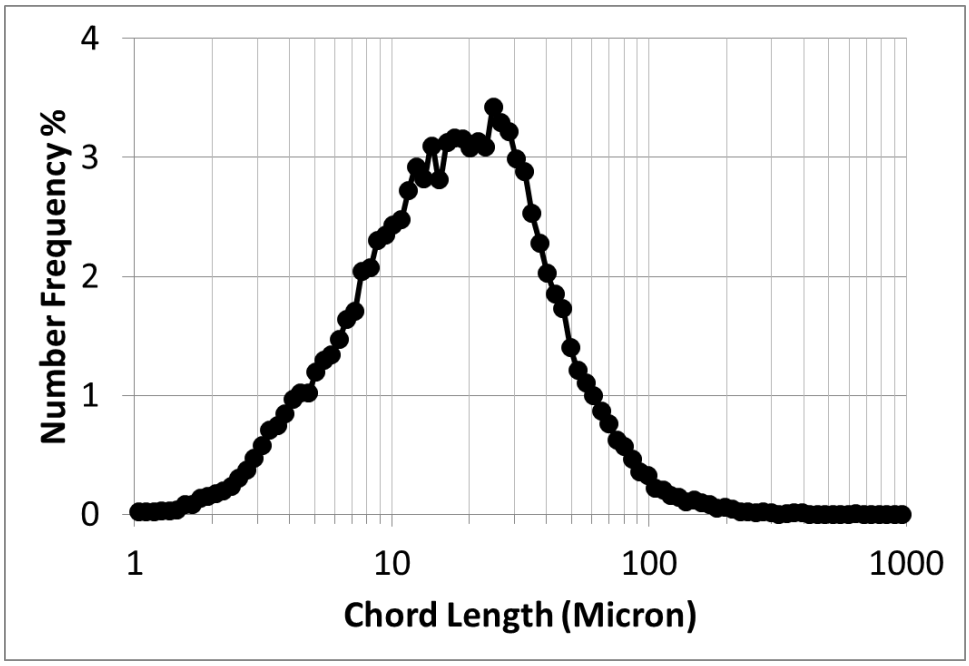

Figure D.1.3 - Wet milling of sucrose/IPA at 5000 rpm and 3.0 lpm – Chord length distribution at 4 tank turnovers measured by FBRM probe

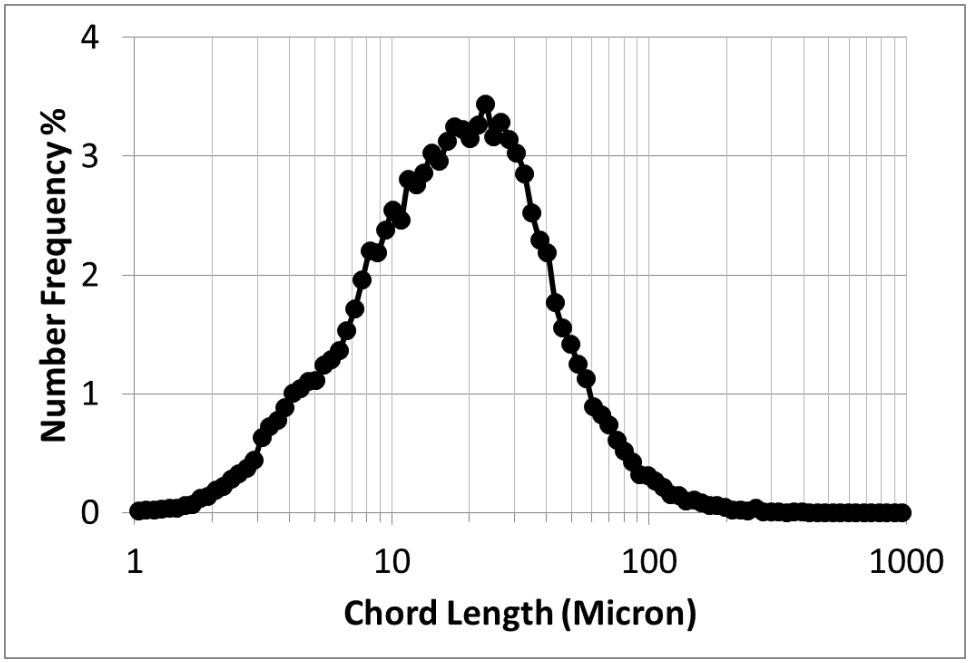

Figure D.1.4 - Wet milling of sucrose/IPA at 5000 rpm and 3.0 lpm – Final chord length distribution measured by FBRM probe

D.2 –FBRM results of wet milling of sucrose/IPA at 6500 rpm and 3.0 lpm

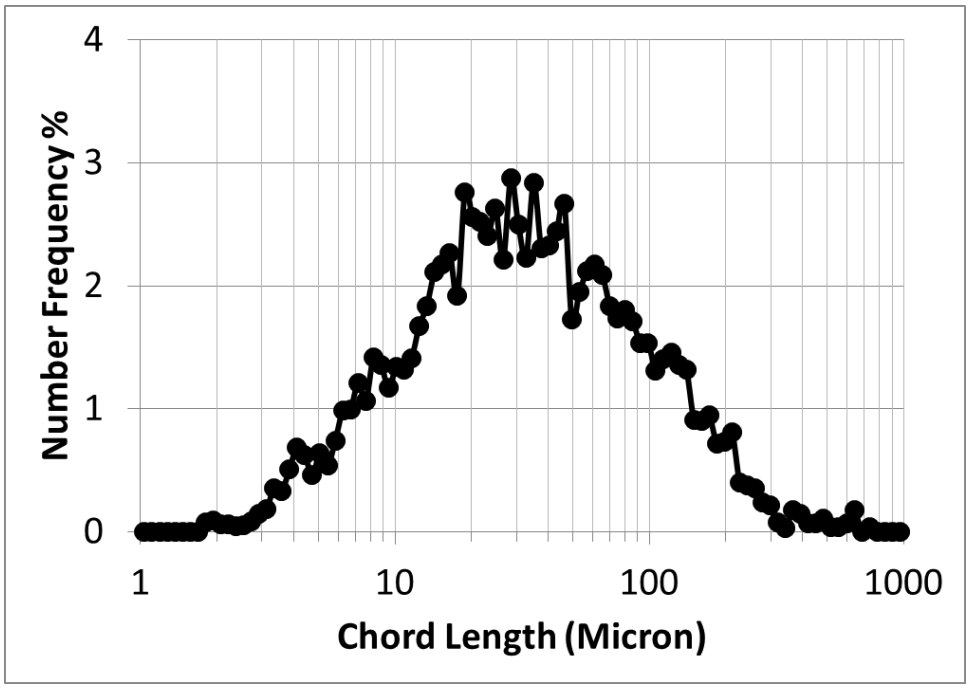

Figure D.2.1 – Initial chord length distribution of sucrose/IPA measured by FBRM probe

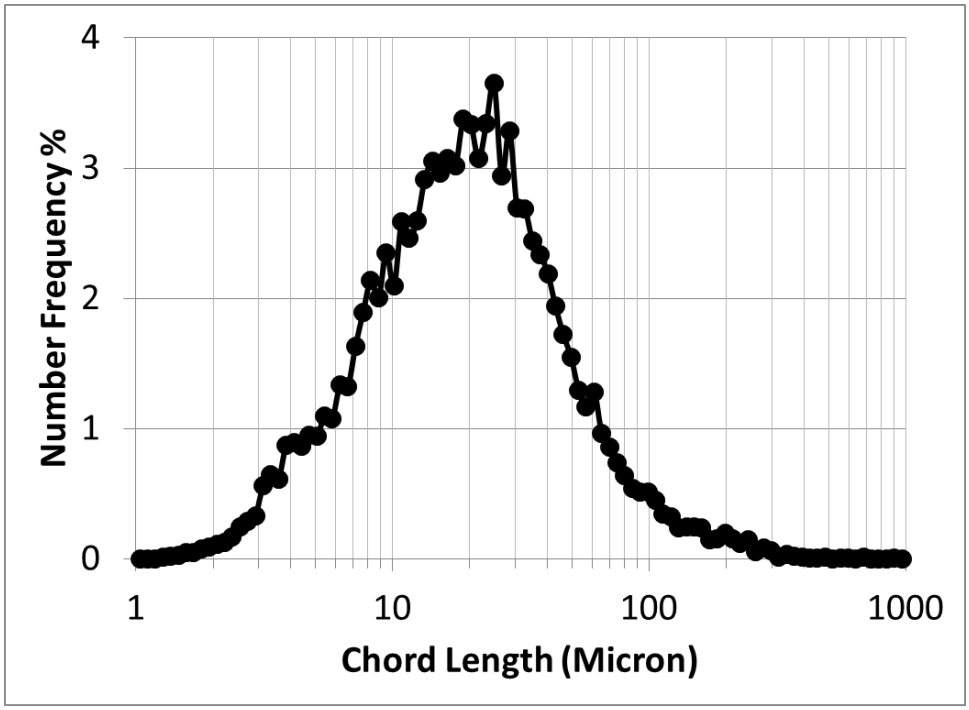

Figure D.2.2 – Wet milling of sucrose/IPA at 6500 rpm and 3.0 lpm – Chord length distribution at 2 tank turnovers measured by FBRM probe

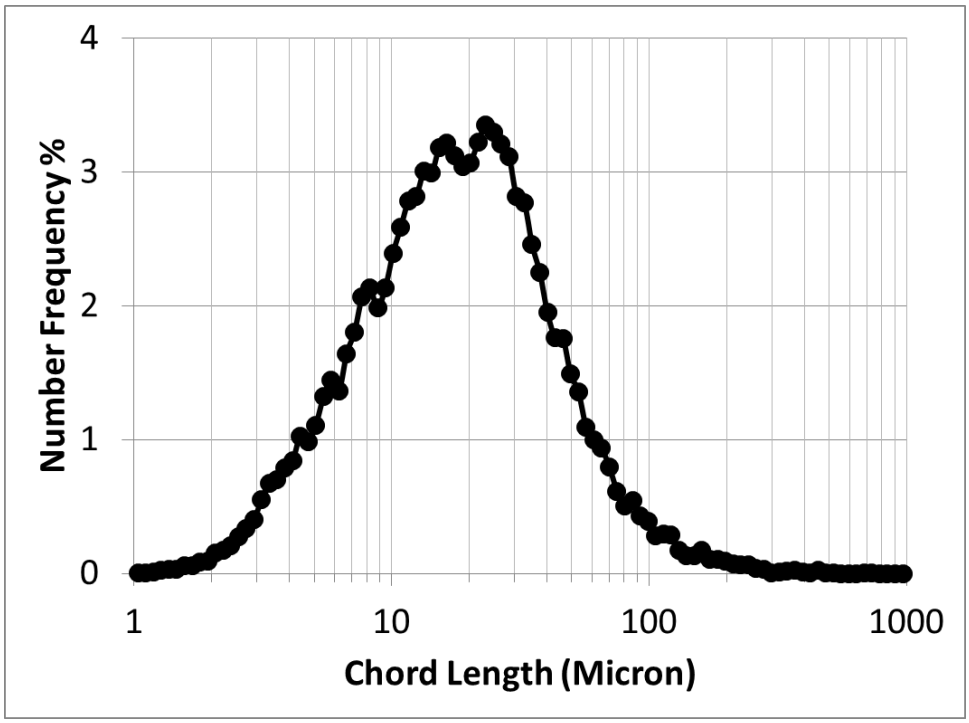

Figure D.2.3 - Wet milling of sucrose/IPA at 6500 rpm and 3.0 lpm – Chord length distribution at 4 tank turnovers measured by FBRM probe

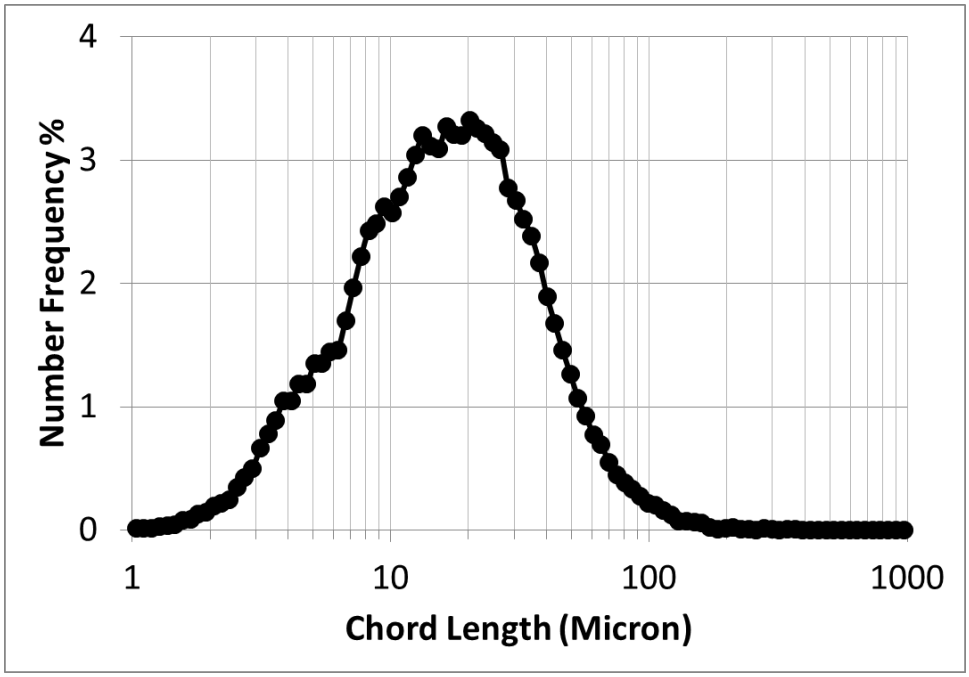

Figure D.2.4 - Wet milling of sucrose/IPA at 6500 rpm and 3.0 lpm – Final chord length distribution measured by FBRM probe

D.3 –FBRM results of wet milling of sucrose/IPA at 8000 rpm and 3.0 lpm

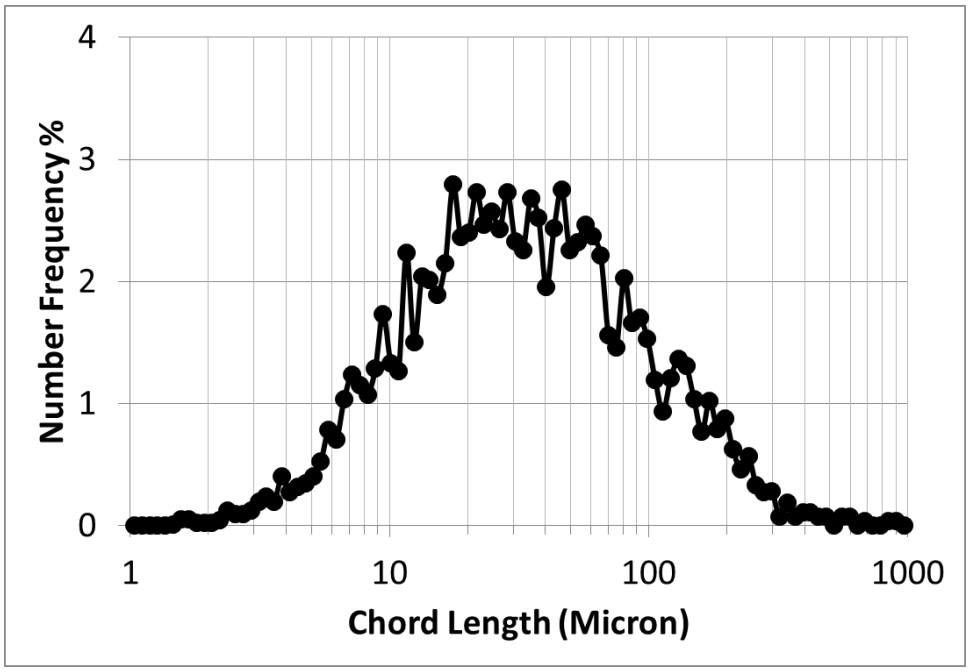

Figure D.3.1 - Initial chord length distribution of sucrose/IPA measured by FBRM probe

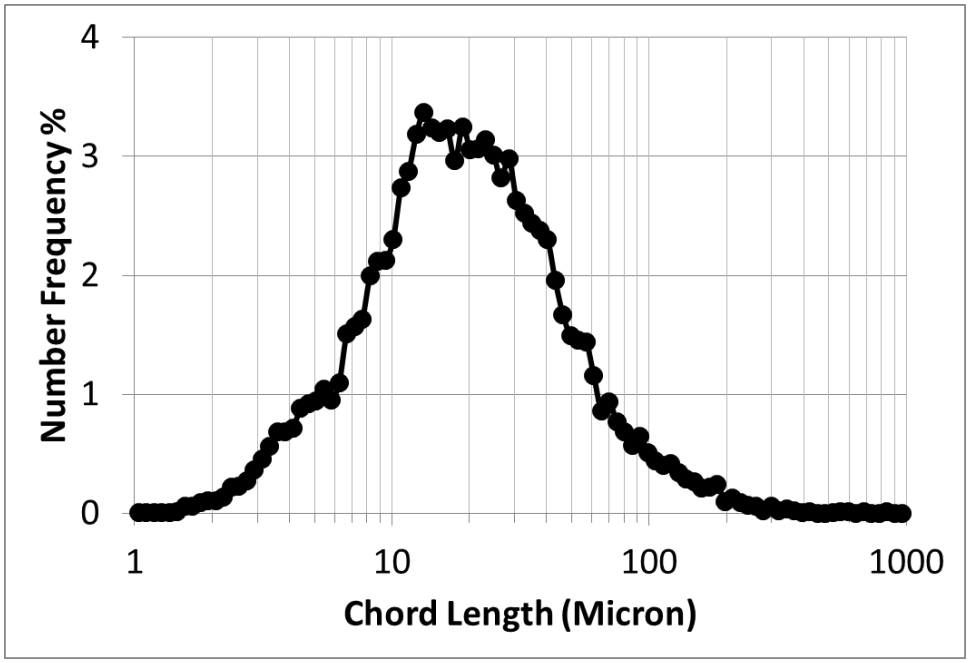

Figure D.3.2 - Wet milling of sucrose/IPA at 8000 rpm and 3.0 lpm – Chord length distribution at 2 tank turnovers measured by FBRM probe

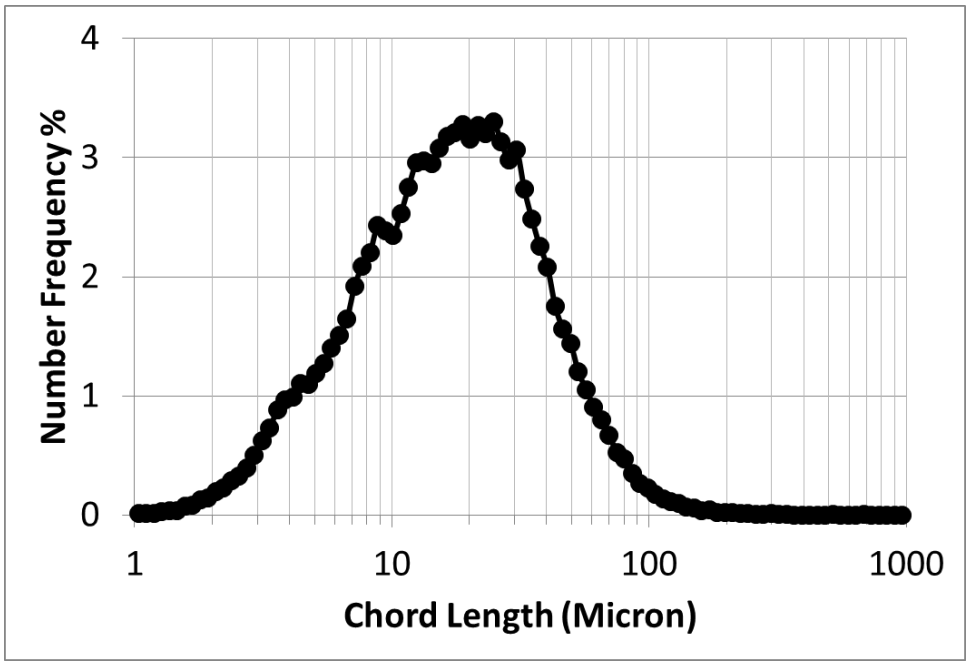

Figure D.3.3 - Wet milling of sucrose/IPA at 8000 rpm and 3.0 lpm – Chord length distribution at 4 tank turnovers measured by FBRM probe

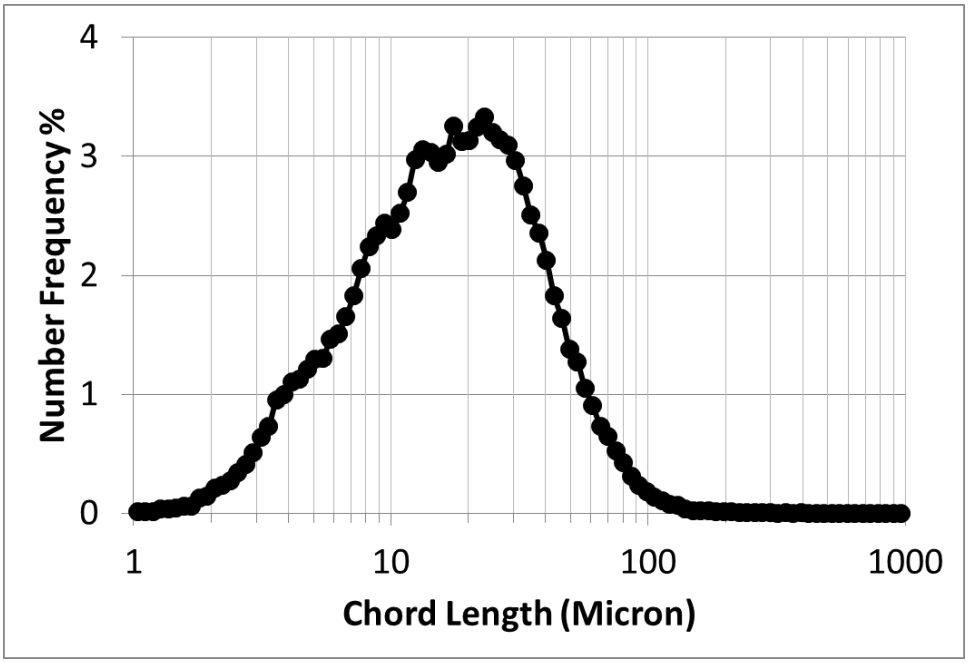

Figure D.3.4 - Wet milling of sucrose/IPA at 8000 rpm and 3.0 lpm – Final chord length distribution measured by FBRM probe

Appendix E: Flow Field Animations

Two flow field animations are provided in a CD. The captions to these animations are included here.

Animation 1 – The Silverson L4R inline mixer with the standard shear gap – Rotor speed of 8000 rpm - Mean velocity field colored by velocity magnitude in the XZ plane at y = 130 mm. Showing the center plane of rotor and stator. Pressure inlet, pressure outlet (free pumping), 7.8M cells, RANS simulations.

Animation 2 – The Silverson L4R inline mixer with the enlarged shear gap – Rotor speed of 8000 rpm - Mean velocity field colored by velocity magnitude in the XZ plane at y = 130 mm. Showing the center plane of rotor and stator. Pressure inlet, pressure outlet (free pumping), 7.8M cells, RANS simulations.

References

[1] T. Allen, Particle Size Measurement, 5th ed., Chapman & Ball, 2-6 Boundary Row, London SEl 8HN, UK, 1990.

[2] V.A. Atiemo-obeng, W.R. Penney, P. Armenante, Solid – Liquid Mixing, in: E.L. Paul, V.A. Atiemo-Obeng, S.M. Kresta (Eds.), Handb. Ind. Mix. Sci. Pract., John Wiley & Sons, Inc., 2004: pp. 543–584.

[3] M.D. Abràmoff, P.J. Magalhães, S.J. Ram, Image processing with imageJ, Biophotonics Int. 11 (2004) 36–41.

[4] Horiba, Horiba Partica LA950 User Manual, Irvine, CA, 2012.

[5] Mettler-Toledo, Lasentec D600 Hardware Manual, Redmond, WA, 2001.

[6] Mettler-Toledo, Lasentec PVM User Manual, Redmond, WA, 2002.

[7] F.C. Campbell, Fatigue and Fracture: Understanding the Basics, 2012.

[8] A.D. Salman, M.J. Hounslow, M. Ghadiri, handbook of powder technology, volume 12, particle breakage, 2007. doi:10.2165/2011121.

[9] D. Tabor, Indentation hardness : Fifty years on a personal view, Philos. Mag. A. 74 (1996) 1207–1212.

[10] G.R. Irwin, Analysis of Stresses and Strains Near the End of a Crack Traversing a Plate, J. Appl. Mech. (1957).

[11] C.B. Ponton, R.D. Rawlings, Vickers indentation fracture toughness test Part 1 Review of literature and formulation of standardised indentation toughness equations, Mater. Sci. Technol. 5 (1989) 865–872. doi:10.1179/mst.1989.5.9.865.

[12] A.J. Lynch, C.A. Rowland, The History of Grinding, 2015. doi:Book Review.

[13] L.G. Austin, A commentary on the Kick, Bond and Rittinger laws of grinding, Powder Technol. 7 (1973) 315–317.

[14] F.C. Bond, The third theory of comminution, Trans. AIME. 193 (1952) 484–494.

[15] V.R. Voller, A note on energy-size reduction relationships in comminution, Powder Technol. 36 (1983) 281–286. doi:10.1016/0032-5910(83)85014-1.

[16] P.C. Kapur, D.W. Fuerstenau, Energy-size reduction "laws" revisited, Int. J. Miner. Process. 20 (1987) 45–57. doi:10.1016/0301-7516(87)90016-0.

[17] E. Stamboliadis, Energy distribution in comminution, anew approach to the laws of Rittinger, Bond and Kick, Can. Metall. Q. 43 (2004) 249–258.

[18] H. Rumpf, Physical aspects of comminution and new formulation of a law of comminution, Powder Technol. 7 (1973) 145–159.

[19] C. Zhang, G.D. Nguyen, J. Kodikara, An application of breakage mechanics for predicting energy–size reduction relationships in comminution, Powder Technol. 287 (2015) 121–130. doi:10.1016/j.powtec.2015.09.040.

[20] R.R. Austin, L.G., Klimpel, The Theory of Grinding, Ind. Eng. Chem. 56 (1964) 18–29. doi:10.1021/ie50659a004.

[21] M. Rhodes, Introduction to Particle Technology – Second Edition Introduction to Particle Technology SECOND EDITION, 2008.

[22] A.A. Griffith, The Phenomena of Rupture and Flow in Solids, Philos. Trans. R. Soc. A Math. Phys. Eng. Sci. 221 (1921) 163–198. doi:10.1098/rsta.1921.0006.

[23] C.E. Inglis, Stresses in a plate due to the presnce of cracks and sharp corners, Trans. Inst. Nav. Arch. 55 (1913) 219–239.

[24] L.B. Freund, Dynamic Fracture Mechanics, 1st ed., Cambridge Monographs

On Mechanics And Applied Mathematics, 1990.
[25] D.B. Lawn, B. R., Marshall, Hardness, toughness and brittleness, an indentation analysis, J. Am. Ceram. Soc. 62 (1979) 347–350.
[26] M. Ghadiri, Z. Zhang, Impact attrition of particulate solids. Part 1: A theoretical model of chipping, Chem. Eng. Sci. 57 (2002) 3659–3669.
[27] W.C. Duncan-Hewitt, G.C. Weatherly, Evaluating the hardness, Young's modulus and fracture toughness of some pharmaceutical crystals using microindentation techniques, J. Mater. Sci. Lett. 8 (1989) 1350–1352. doi:10.1007/BF00721518.
[28] M. Ghadiri, K.R. Yuregir, H.M. Pollock, J.D.J. Ross, N. Rolfe, Influence of processing conditions on attrition of NaCl crystals, Powder Technol. 65 (1991) 311–320. doi:10.1016/0032-5910(91)80195-O.
[29] P.M. Vitvitskii, V. V. Panasyuk, S.Y. Yarema, Plastic deformation around crack and fracture criteria. A review, Eng. Fract. Mech. 7 (1975). doi:10.1016/0013-7944(75)90012-0.
[30] K.E. Puttick, The correlation of fracture transitions, J. Phys. D. Appl. Phys. 13 (1980) 2249. http://stacks.iop.org/0022-3727/13/i=12/a=011.
[31] C. Gahn, A. Mersmann, The brittleness of substances crystallized in industrial processes, Powder Technol. 85 (1995) 71–81. doi:10.1016/0032-5910(95)03008-W.
[32] C. Gahn, a Mersmann, Theoretical Prediction and Experimental Determination of Attrition Rates, Chem. Eng. Res. Des. 75 (1997) 125–131. doi:http://dx.doi.org/10.1205/026387697523570.
[33] C. Gahn, A. Mersmann, Brittle fracture in crystallization processes Part A. Attrition and abrasion of brittle solids, Chem. Eng. Sci. 54 (1999) 1273–1282. doi:http://dx.doi.org/10.1016/S0009-2509(98)00450-3.
[34] H. Rumpf, Physical aspects of comminution and new formulation of a law of comminution, Powder Technol. 7 (1973) 145–159.
[35] L. Vogel, W. Peukert, Breakage behaviour of different materials - Construction of a mastercurve for the breakage probability, Powder Technol. 129 (2003) 101–110. doi:10.1016/S0032-5910(02)00217-6.
[36] L. Vogel, W. Peukert, From single particle impact behaviour to modelling of impact mills, Chem. Eng. Sci. 60 (2005) 5164–5176. doi:10.1016/j.ces.2005.03.064.
[37] M. Meier, E. John, D. Wieckhusen, W. Wirth, W. Peukert, Influence of mechanical properties on impact fracture: Prediction of the milling behaviour of pharmaceutical powders by nanoindentation, Powder Technol. 188 (2009) 301–313. doi:http://dx.doi.org/10.1016/j.powtec.2008.05.009.
[38] L.J. Taylor, D.G. Papadopoulos, P.J. Dunn, A.C. Bentham, N.J. Dawson, J.C. Mitchell, M.J. Snowden, Predictive milling of pharmaceutical materials using nanoindentation of single crystals, Org. Process Res. Dev. 8 (2004) 674–679. doi:10.1021/op0300241.
[39] J.H. Michell, On distributions of stress in three dimensions, LondonMath Soc Proc. 32 (1900) 23–61.
[40] B. Marrot, B. Biscans, Impact of a single crystal in solution, on an immersed target, in conditions which simulate impact attrition in crystallizers, Powder Technol. 120 (2001) 141–150.
[41] B. Biscans, Impact attrition in crystallization processes. Analysis of repeated impacts events of individual crystals, Powder Technol. 143–144 (2004) 264–272. doi:10.1016/j.powtec.2004.04.025.

[42] Y. Asakuma, T. Tetahima, K. Maeda, M. Hideo, D. Fukeu, Attrition behavior by micro-hardness parameters in suspension-crystallization processes, Powder Technol. 171 (2007) 75–80. doi:10.1016/j.powtec.2006.10.001.
[43] M. Bravi, S. Di Cave, B. Mazzarotta, N. Verdone, Relating the attrition behaviour of crystals in a stirred vessel to their mechanical properties, Chem. Eng. J. 94 (2003) 223–229.
[44] Z. Zhang, M. Ghadiri, Impact attrition of particulate solids. Part 2: Experimental work, Chem. Eng. Sci. 57 (2002) 3671–3686. doi:10.1016/S0009-2509(02)00241-5.
[45] L.J. Taylor, D.G. Papadopoulos, P.J. Dunn, A.C. Bentham, J.C. Mitchell, M.J. Snowden, Mechanical characterisation of powders using nanoindentation, Powder Technol. 143–144 (2004) 179–185. doi:10.1016/j.powtec.2004.04.012.
[46] A.. Bentham, C.. Kwan, R. Boerefijn, M. Ghadiri, Fluidised-bed jet milling of pharmaceutical powders, Powder Technol. 141 (2004) 233–238. doi:10.1016/j.powtec.2004.01.024.
[47] W. Yang, C.C. Kwan, Y.L. Ding, M. Ghadiri, K.J. Roberts, Milling of sucrose, Powder Technol. 174 (2007) 14–17. doi:10.1016/j.powtec.2006.10.014.
[48] D. Olusanmi, K.J. Roberts, M. Ghadiri, Y. Ding, The breakage behaviour of Aspirin under quasi-static indentation and single particle impact loading: effect of crystallographic anisotropy., Int. J. Pharm. 411 (2011) 49–63. doi:10.1016/j.ijpharm.2011.03.039.
[49] Y. Cheng, C.-M. Cheng, Relatioships between hardness, elastic modulus, end the work of indentation, Appl. Phys. Lett. 73 (1998) 614–616. doi:10.1063/1.1218731063/1.120159.
[50] I. Lee, N. Variankaval, C. Lindemann, C. Starbuck, Rotor-stator milling of APIs - Empirical scale-up parameters and theoretical relationships between the morphology and breakage of crystals, Am. Pharm. Rev. 7 (2004). http://www.scopus.com/inward/record.url?eid=2-s2.0-19644401254&partnerID=tZOtx3y1.
[51] T. Kamahara, M. Takasuga, H.H. Tung, K. Hanaki, T. Fukunaka, B. Izzo, J. Nakada, Y. Yabuki, Y. Kato, Generation of fine pharmaceutical particles via controlled secondary nucleation under high shear environment during crystallization - Process development and scale-up, Org. Process Res. Dev. 11 (2007) 699–703. doi:10.1021/op700045j.
[52] A. Harter, L. Schenck, I. Lee, A. Cote, High-Shear Rotor–Stator Wet Milling for Drug Substances: Expanding Capability with Improved Scalability, Org. Process Res. Dev. 17 (2013) 1335–1344. doi:10.1021/op4001143.
[53] J. Engstrom, C. Wang, C. Lai, J. Sweeney, Introduction of a new scaling approach for particle size reduction in toothed rotor-stator wet mills, Int. J. Pharm. 456 (2013) 261–268. doi:10.1016/j.ijpharm.2013.08.084.
[54] C. V. Luciani, E.W. Conder, K.D. Seibert, Modeling-Aided Scale-Up of High-Shear Rotor–Stator Wet Milling for Pharmaceutical Applications, Org. Process Res. Dev. 19 (2015) 582–589. doi:10.1021/acs.oprd.5b00066.
[55] J. Baldya, W. Orciuch, L. Makowski, K. Malik, W. Eagles, G. Padron, Dispersion of Nanoparticle Clusters in a Rotor - Stator Mixer, Ind. Eng. Chemsitry Res. 47 (2008) 3652–3663.
[56] G. Padron, W.P. Eagles, G.N. Özcan-Taşkin, G. McLeod, L. Xie, G. Özcan-Taskin, G. McLeod, L. Xie, Effect of Particle Properties on the Break Up of Nanoparticle Clusters Using an In-Line Rotor-Stator, J. Dispers. Sci. Technol. 29 (2008) 580–586. doi:10.1080/01932690701729237.

[57] R. V. Calabrese, M.K. Francis, V.P. Mishra, S. Phongikaroon, Measurement and analysis of drop size in a batch rotor stator mixer, in: 10th Eur. Conf. Mix., Amsterdam, Netherland, 2000: pp. 149–156.
[58] R. V. Calabrese, M.K. Francis, K.R. Kevala, V.P. Mishra, G.A. Padron, S. Phongikaroon, Fluid Dynamics and Emulsification in High Shear Mixers, in: Proc. 3rd World Congr. Emuls., Lyon, France, 2002.
[59] P.E. Rueger, R. V. Calabrese, Dispersion of water into oil in a rotor–stator mixer. Part 1: Drop breakup in dilute systems, Chem. Eng. Res. Des. 91 (2013) 2122–2133. doi:10.1016/j.cherd.2013.05.018.
[60] P.A. Tanguy, J. Bertrand, C. Xuereb, Handbook of Industrial Mixing, Science and Practice, E.L. Paul, V.A. Atiemo-Obeng, S.M. Kresta (Eds.). John Wiley & Sons, Hoboken, NJ, (2003), ISBN: 0-471-26919-0, Chem. Eng. Sci. 60 (2005). doi:10.1016/j.ces.2004.12.002.
[61] T.N. Zwietering, Suspending of solid particles in liquid by agitators, Chem. Eng. Sci. 8 (1958) 244–253. doi:10.1016/0009-2509(58)85031-9.
[62] K.S. Pedersen, M.L. Michelsen, a. Firoozabadi, J.M. Prausnitz, J. Baldyga, J.R. Bourne, S. Kumar, D. Ramkrishna, Letters to the editor, AIChE J. 43 (1997) 1372–1374. doi:10.1002/aic.690430529.
[63] G.A. Padron, Measurement and comparison of power draw in batch rotor-stator mixers, University of Maryland, College Park, MD, USA, 2001.
[64] G. Özcan-Taşkin, D. Kubicki, G. Padron, Power and flow characteristics of three rotor-stator heads, Can. J. Chem. Eng. 89 (2011) 1005–1017. doi:10.1002/cjce.20553.
[65] J. Hinze, Fundamentals of the Hydrodynamic Mechanism of Splitting in Dispersion Processes, AIChE J. 1 (1955) 289–295.
[66] R. V. Calabrese, T.P.K. Chang, P.T. Dang, Drop breakup in turbulent stirred tank contactors. Part I: Effect of dispersed phase viscosity., AIChE J. 32 (1986) 657–666. doi:10.1002/aic.690320416.
[67] J.T. Davies, A physical interpretation of drop sizes in homogenizers and agitated tanks, including the dispersion of viscous oils, Chem. Eng. Sci. 42 (1987) 1671–1676. doi:10.1016/0009-2509(87)80172-0.
[68] M. Yang, CFD simulations for scale up of wet milling in high shear mixers, University of Maryland, College Park, MD, USA, 2011. http://hdl.handle.net/1903/11595.
[69] C.A. Coulaloglou, L.L. Tavlarides, Description of interaction processes in agitated liquid-liquid dispersions, Chem. Eng. Sci. 32 (1977) 1289–1297. doi:10.1016/0009-2509(77)85023-9.
[70] V.A. Atiemo-Obeng, R. V Calabrese, Rotor–Stator Mixing Devices, in: Handb. Ind. Mix., John Wiley & Sons, Inc., 2004: pp. 479–505. doi:10.1002/0471451452.ch8.
[71] K.R. Kevala, Sliding mesh simulation of a wide and narrow gap inline rotor-stator mixer, University of Maryland, College Park, MD, USA, 2001.
[72] F. Barailler, M. Heniche, P.A. Tanguy, CFD analysis of a rotor-stator mixer with viscous fluids, Chem. Eng. Sci. 61 (2006) 2888–2894. doi:10.1016/j.ces.2005.10.064.
[73] A.T. Utomo, M. Baker, A.W. Pacek, Flow pattern, periodicity and energy dissipation in a batch rotor-stator mixer, Chem. Eng. Res. Des. 86 (2008) 1397–1409. doi:10.1016/j.cherd.2008.07.012.
[74] A. Utomo, M. Baker, A.W. Pacek, The effect of stator geometry on the flow pattern and energy dissipation rate in a rotor-stator mixer, Chem. Eng. Res.

Des. 87 (2009) 533–542. doi:10.1016/j.cherd.2008.12.011.
[75] H.H. Mortensen, R. V. Calabrese, F. Innings, L. Rosendahl, Characteristics of batch rotor-stator mixer performance elucidated by shaft torque and angle resolved PIV measurements, Can. J. Chem. Eng. 89 (2011) 1076–1095. doi:10.1002/cjce.20587.
[76] D.I. Ko, Computational fluid dynamics simulations of an in-line slot and tooth rotor-stator mixer, University of Maryland, College Park, MD, USA, 2013. http://hdl.handle.net/1903/14206.
[77] J.W. Kim, Comparison between particle image velocimetry data and computational fluid dynamics simulations for an in-line slot and tooth rotor-stator mixer, University of Maryland, College Park, MD, USA, 2015. http://hdl.handle.net/1903/17243.
[78] T. Sparks, Fluid mixing in rotor/stator mixers, Cranfield University, Cranfield, UK, 1996.
[79] K.J. Myers, M.F. Reeder, D. Ryan, Power draw of a high-shear homogenizer, Can. J. Chem. Eng. 79 (2001) 94–99. doi:10.1002/cjce.5450790114.
[80] L. Doucet, G. Ascanio, P.A. Tanguy, Hydrodynamics Characterization of Rotor-Stator Mixer with Viscous Fluids, Chem. Eng. Res. Des. 83 (2005) 1186–1195. doi:10.1205/cherd.04254.
[81] A.J. Kowalski, An expression for the power consumption of in-line rotor-stator devices, Chem. Eng. Process. Process Intensif. 48 (2009) 581–585. doi:10.1016/j.cep.2008.04.002.
[82] M. Cooke, T.L. Rodgers, A.J. Kowalski, Power Consumption Characteristics of an In-Line Silverson High Shear Mixer, AIChE J. 58 (2012) 1683–1692. doi:10.1002/aic.
[83] J.R. Bourne, M. Studer, Fast reactions in rotor-stator mixers of different size, Chem. Eng. Process. 31 (1992) 285–296. doi:10.1016/0255-2701(92)87002-X.
[84] M.K. Francis, The development of a novel probe for the in situ measurement of particle size distributions, and application to the measurement of drop size in rotor–stator mixers, University of Maryland, College Park, MD, USA, 1999.
[85] S. Phongikaroon, Drop size distribution for liquid-liquid dispersions produced by rotor–stator mixers, University of Maryland, College Park, MD, USA, 2001.
[86] G.A. Padron, Effect of surfactants on drop size distribution in a batch, rotor-stator mixer, University of Maryland, College Park, MD, USA, 2004. http://hdl.handle.net/1903/2160.
[87] J.R. Walker, R. V. Calabrese, Analysis of surfactant laden liquid-liquid dispersion using an axisymmetric laminar jet, Can. J. Chem. Eng. 89 (2011) 1096–1103. doi:10.1002/cjce.20624.
[88] S. Hall, M. Cooke, A. El-Hamouz, A.J. Kowalski, Droplet break-up by in-line Silverson rotor-stator mixer, Chem. Eng. Sci. 66 (2011) 2068–2079. doi:10.1016/j.ces.2011.01.054.
[89] S. Hall, M. Cooke, A.W. Pacek, A.J. Kowalski, D. Rothman, Scaling up of silverson rotor-stator mixers, Can. J. Chem. Eng. 89 (2011) 1040–1050. doi:10.1002/cjce.20556.
[90] P.E. Rueger, R. V. Calabrese, Dispersion of water into oil in a rotor–stator mixer. Part 2: Effect of phase fraction, Chem. Eng. Res. Des. 91 (2013) 2134–2141. doi:10.1016/j.cherd.2013.06.010.
[91] M. Jasińska, J. Bałdyga, S. Hall, A.W. Pacek, Dispersion of oil droplets in rotor-stator mixers: Experimental investigations and modeling, Chem. Eng. Process. Process Intensif. 84 (2014) 45–53. doi:10.1016/j.cep.2014.02.008.

[92] C. Liu, M. Li, C. Liang, W. Wang, Measurement and analysis of bimodal drop size distribution in a rotor-stator homogenizer, Chem. Eng. Sci. 102 (2013) 622–631. doi:10.1016/j.ces.2013.08.030.
[93] J. Baldyga, W. Orciuch, L. Makowski, M. Malski-Brodzicki, K. Malik, Break up of nano-particle clusters in high-shear devices, Chem. Eng. Process. Process Intensif. 46 (2007) 851–861. doi:10.1016/j.cep.2007.05.016.